NORTHWESTERN UNIVERSITY

Modeling the Mechanical Properties of Intermetallic/Solder Interfaces

A DISSERTATION

SUBMITTED TO THE GRADUATE SCHOOL
IN PARTIAL FULFILLMENT OF THE REQUIREMENTS

For the degree

DOCTOR OF PHILOSOPHY

Field of Theoretical and Applied Mechanics

Department of Civil and Environmental Engineering

By

Yao Yao

EVANSTON, ILLINOIS

December 2008

ABSTRACT

Modeling the Mechanical Properties of Intermetallic/Solder Interfaces

Yao Yao

Solder joint integrity is recognized as a key issue in the reliability of flip chip and ball grid arrays in integrated circuit packages. Significant reductions in the solder-joint interconnect size results in both the increased volume fraction of brittle intermetallics in the joint and joule heating and electromigration failure due to high current density.

Based on cohesive fracture theory, a 3D computational model has been developed to predict the crack nucleation, propagation and interfacial damage of interconnects. Unified creep-plasticity theory and a cohesive zone model were incorporated to predict the creep and hysteresis effects on fatigue crack propagation in solder and the interfacial behavior between the solder bulk and the intermetallic layer, respectively. A thermo-electric numerical analysis was conducted to predict the electrical concentration and joule heating effects on the failure of solder under different applied current densities. The temperature and current density distribution in a solder joint with a crack that propagates near the interface of the bulk solder and intermetallic layer was predicted.

An approach based on phase transformation theory, micromechanics, and fracture mechanics has been developed to treat fatigue crack propagation in both lead rich and lead free eutectic solders. The predicted fatigue crack propagation rate using phase transformation theory was compared with experimental data for Sn-3.5Ag and Sn-37Pb eutectic solders. Reasonable agreement between theoretical predictions and experimental results was obtained.

With the reduction of the size of electronic devices, the current density is increasing rapidly and the electromigration effect becomes more critical to the failure of solder interconnects. The mechanism of electromigration effect to void propagation caused interconnect failure was studied in the research. A kinetic mass diffusion model was developed to predict void width and propagation speed near the interface of intermetallic and solder caused by electromigration. The model gives reasonable prediction to the void width and propagation velocity compared with experimental results.

Acknowledgements

I would like to express my special gratitude to my advisor, Professor Leon M. Keer, I sincere appreciate his valuable and patient guidance and support throughout my study at Northwestern University. Working with him is a wonderful experience that I will always treasure.

I wish to express my deep appreciation to Professor Morris E. Fine for advising and reviewing of the work. His inspirations and encouragement have always motivated me and helped me overcome the difficulties of research.

Sincere gratitude is expressed to Professor Semyon Vaynman, Professor Gautam Ghosh, and Mr. Brent Fiedler for good suggestions and use of their experimental data. It would not have been possible to write this dissertation without having access to their data.

I wish to thank Professor Jane Wang, Professor Yu Nie, Professor Brian Moran, Dr. Xiaoqin Jin, Dr. Shenmin Wen, Dr. Fan Wang, and the members of Professor Keer's group, Professor Fine's group and Professor Wang's group for their help and friendship. I wish to thank my relatives and friends for their support.

I gratefully acknowledge the financial support from Semiconductor Research Corporation through contract 1393, and from the Northwestern University McCormick Fellowship and Smith Final Year Fellowship.

I express my profound gratitude to my wife and son for their support, devotion and patience throughout my study.

Finally, I dedicate this work to my beloved grandparents and parents for their love. Without their support and love, I could never have succeeded.

Table of Contents

List of Figures

List of Tables

Chapter 1

Introduction and Literature Review

1.1 General Introduction and Background of Research

The continuing reduction in size of electronic device interconnects and the switch to lead-free solders moves fatigue failure prediction for these interconnects into the zone of insufficient data and experience. Previously, empirical approaches based on many years of experience were highly successful, but now a better scientific understanding of the fatigue failure processes is needed to assure reliability with minimum experimentation. It is found that more interconnects fail because of relative brittle failure near the interface of intermetallic compound and bulk solder which is not considered in the traditional design method, which usually considers the fatigue failure in bulk solder only. A scientific theory to predict interconnect failure should combine the creep-plasticity behavior in bulk solder with the mechanical failure mode of the interface and intermetallic compound. For interconnects operating under high current density, the electromigration effect plays the more important role and needs be considered. The present work is undertaken with the above in mind, trying to develop a scientific approach to predict the failure mode and behavior of interconnects under cyclic loading and high current density.

Although a significant amount of research has been performed with a goal to predict fatigue life of interconnects; however, a clear understanding of the physical meaning of interconnect fatigue failure is still incomplete and needs further research. A phase transformation theory has been developed and applied to fatigue crack propagation in an

interconnect, consisting solder, an intermetallic and the interface between them. Modeling the interconnect fatigue failure of this sub-system is one of the objects of the research in this dissertation.

During the past few decades, research has been conducted on fatigue analysis of solders, but those on Intermetallic Compound (IMC) of solder/Cu pad interface are limited. With the help of more advanced experimental methods, it is noted that most of the solder failures are due to the cracking on the interface of IMC/solder or within the IMC layer. Thus it is important to understand the mechanical properties and behavior of IMC under cyclic thermal-mechanical load. With higher current density, the effect of electromigration was found to play an important role in the failure of solder. To the author's best knowledge, there is no available model to predict the failure of solder by combining the effect of thermal-mechanical fatigue and electromigration. Failure of IMC in solder/Cu pad interface for flip-chips will be discussed in chapter one. Current research is focus on the behavior of solder and IMC behavior under thermal-mechanical cyclic load. Some observations from experiments on the behavior of IMC under thermal-mechanical load are reviewed in this chapter.

A 3D finite element model based on cohesive fracture mechanics and unified creep and plasticity theory is developed in chapter 2 to predict the crack initiation and propagation near the IMC/solder interface. The traction-separation law of a cohesive element at interface is applied in the finite element program, ABAQUS, and a numerical analysis of IMC related solder joint failure has been conducted. The cohesive-UCP finite element model is applied to analyze the effect of IMC layer thickness on solder joint failure. The growth of IMC layer thickness has a significant effect on solder joint failure. The von Mises stress required to initiate a crack is found lower for a thicker IMC layer and the solder joint lifetime decreases with increasing IMC

layer thickness. Since solder joint failure is a complex coupled problem caused by mechanical, thermal, and electrical loads, a coupled thermo-electric numerical analysis has been conducted to understand the phenomenon better. The electrical crowding and joule heating effects are found to play important roles on solder joint failure, especially when a crack propagates near the interface of IMC and solder. The temperature and electric current density distribution in Sn-2.5Ag-0.8Cu-0.5Sb solder under different applied currents has been predicted. It is found that there has pronounced temperature and electrical current concentration near the crack tip. Although the lead-free solders usually have higher melting temperatures as compared with lead-rich solder, the concentration of heat at the crack tip caused by joule heating may still melt the solder material under a high current density, which will enhance the propagation of crack and cause a circuit failure.

An approach to predict the fatigue crack propagation in solids is developed based on phase transformation theory and fracture mechanics in chapter 3 (Yao et al. 2008). The theory shows reasonable accuracy when compared with experimental data for steels and aluminum alloys (Izumi et al. 1979, 1981). Motivated by the experimental observations on fatigue failure of interconnects, this method is extended to interconnects. The required energy U to propagate a unit crack area in solder is determined from numerical analysis with the finite element model developed in chapter 2. The prediction of fatigue crack propagation rate for 63Sn-37Pb eutectic solder is compared with experimental data. The theory can be used to predict fatigue crack propagation for different types of interconnects under cyclic stress with the needed parameters for solder and intermetallics are available from experiment.

The background of electromigration effect on solder/IMC interconnect failure will be discussed in section 1.6. A kinetic mass diffusion model is developed in chapter 4 based on the

Einstein relation and mass conservation principle. The approach is applied to predict void width and propagation velocity near the solder/IMC interface caused by electromigration. Finite element analysis has been conducted to determine the current crowding parameter in the model.

This chapter starts with the literature review to the available fatigue theories.

1.2 Literature Review to Fatigue Theories and Analysis to Solder Interconnect

The word fatigue originated from the Latin expression fatigue which means 'to tire'. The terminology used in engineering refers to the damage and failure of materials under cyclic loads, including mechanical loads, thermal loads, etc. Major advances have been made during the past hundred years in fatigue analysis. However, the application of fatigue concepts to practical situations encounters many complicated conditions and is far from final solution. Different fatigue methods have been proposed in the past century and will be reviewed in this section.

There are two major fatigue theories widely adopted, one is the S-N curve theory, which is used when elastic deformation dominates, it is an empirical law to relate stress and fatigue failure cycles for metals. The other is the Coffin-Manson type relationship, which is used when substantial plastic deformation occurs in the material under cyclic loading, it is also an empirical law to relate the load cycle numbers cause fatigue failure to the plastic strain magnitude. It was proposed by Coffin (Coffin and Schenectady 1954) and Manson (1953), the method is convenient to use but a materials science basis and physical meaning of the formula is still not clear and need further research.

The Coffin-Manson type fatigue law is used for solder materials since solder alloys have inelastic strain at very low stress level, the law is in following form:

$$\Delta\varepsilon N_f^{\alpha} = C \tag{1.1}$$

where $\Delta\varepsilon$ is the inelastic strain range, N_f is the number of cycles to failure, α and C are material constants fitted from fatigue tests. The method is not applicable for case beyond experimental investigates range.

Another well known fatigue theory is the Paris law, which was proposed by Paris in the 1960's. The method is generally a defect-tolerant approach. The theory assumes pre-existing cracks and uses an empirical power law relationship between the crack propagation rate and range of stress intensity factor at the crack tip. The fatigue life is determined by the load cycle number to propagate the pre-existing crack to a critical crack length. There are many other versions of the Paris law type fatigue theory. Details can be referring to Paris's paper (1998).

Morrow (1964) concluded that both stress and plastic strain are required for fatigue damage. He proposed a plastic strain energy density to consider both stress and plastic strain:

$$\Delta W = W_f^{'}(2N_f)^n \tag{1.2}$$

where ΔW is the plastic strain energy density dissipated per cycle, which physically corresponding to the area in the hysteresis loop; N_f is the number of cycles to failure. Experimental results agreed with the formula reasonable with an exponent of $n = -0.65$.

Solomon (1986) developed a revised Coffin-Manson type relationship for 60Sn-40Pb solder:

$$\Delta\gamma_p N_f^{\alpha} = C \tag{1.3}$$

where $\Delta\gamma_p$ is the applied plastic strain range; N_f is the number of cycles to failure; α and C are constants that depend on temperature. To account for the influence of frequency on fatigue life of this solder, Eq. (1.3) was modified to:

$$\Delta\gamma_p\left(N_f\nu^{K-1}\right)^{\alpha} = C \tag{1.4}$$

Vaynman (1987) modified the Coffin-Manson type formula to a time-based empirical formula to predict the fatigue life:

$$N_f = \frac{C + D(t_{ht} + t_{hc})}{2t_r + t_{ht} + t_{hc}} \tag{1.5}$$

where subscripts r, h_t and h_c refer to ramp, tensile hold and compressive hold, respectively; C and D are constants that take into account the strain range effect, and N_f is the cycle number when the tensile load dropping occurs. The compressive hold time is incorporated in his model.

Clech et al. (1989) fitted the experimental data for different leaded packaging assemblies by using Morrow's approach:

$$N_f = C(\Delta W)^{1/n} \tag{1.6}$$

where N_f is the mean cyclic life; ΔW is the cyclic strain energy density; and the exponent n was determined to be -0.64 in their research.

Zubelewicz et al. (1990) presented a modified Coffin-Manson relationship based on micromechanical study:

$$N_f \left|\Delta\varepsilon_{\text{ov}}^{p}\right|^{n} = \left(\frac{\Delta\sigma^{\text{ov}}}{\tau_0 \eta_{\text{cr}}} - 1\right) / \kappa \tag{1.7}$$

where N_f is the instable deformation beginning cycle number; $\Delta\sigma^{\text{ov}}$ is the overall stress magnitude $\Delta\sigma^{\text{ov}}$; The theory includes micro structural evolution and it was applied to predict fatigue life of high lead and eutectic PbSn solder.

Dasgupta et al. (1992) proposed an energy-partitioning approach to study solder fatigue by applying Morrow's energy formula to elastic, plastic and creep strain energy terms respectively:

$$U_e = U_0 N_{fe}^{b},\ W_p = W_{p0} N_{fp}^{c},\ W_c = W_{c0} N_{fc}^{d} \tag{1.8}$$

where U_0, W_{p0}, and W_{c0} are material constants and can be determined from experiment. A Rankine type equation is used to predict failure cycle number:

$$N_f = \frac{1}{1/N_{fe} + 1/N_{fp} + 1/N_{fc}} \tag{1.9}$$

Here, N_f is the cycle number with 50% of load drop.

A stress-based fatigue formula is developed by Guo et al. (1992):

$$N_f = \frac{B}{\Delta\sigma - 4\sigma_f / \sqrt{3}} \tag{1.10}$$

where N_f is the cycle number at which the peak stress range acceleration start to decrease; B is a material constant; $\Delta\sigma$ is the peak stress range; σ_f is the flow stress in tension. His work is

based on a dislocation pile-up model and Mura's fatigue crack initiation theory. The formula was used to model thermomechanical fatigue of 63Sn-37Pb solder.

Wen and Ross (1995) proposed a revised Coffin-Manson relationship as following:

$$N_f\left(\sigma_m / S\right)^{\gamma} \Delta\varepsilon_p^{\,1/k} = C \tag{1.11}$$

where σ_m is the maximum flow stress amplitude; S is the reference ultimate stress. In their model, the failure criteria for N_f are based on electronic monitoring and visual inspection.

Ju et al. (1996) suggested the following approach through the J integral range:

$$\frac{da}{dN} = C\left(\Delta \mathrm{J}\right)^m \tag{1.12}$$

Here N is the cycle number and C is a material constant.

Since the plastic strain energy density is not uniform in a real solder structure, Akay et al. (1997) proposed a volume-weighted total strain energy criterion to predict fatigue life:

$$N_f = \left(\frac{\Delta \overline{W}_{total}}{W_0}\right)^{1/k} \tag{1.13}$$

$$\Delta \overline{W}_{total} = \left(\int \overline{\sigma}_{av} d\overline{\varepsilon}_{av}\right) \Sigma V^e, \text{ for a stabilized cycle} \tag{1.14}$$

where N_f is the cycle number when electrical open circuiting occurs, k is a mterail constant.

Stolkarts et al. (1999) proposed a formula based on percolation theory:

$$N_f\left(\Delta\gamma^{cycle}\right)^{\chi} = \overline{\omega}_c \tag{1.15}$$

where N_f is the cycle number at which accelerated decrease of peak tensile stress starts; $\Delta\gamma^{cycle}$ is the shear strain range per cycle; $\overline{\omega}_c$ is the critical microcrack density. The formula presents a strain-based Coffin-Manson type form and uses damage accumulation to determine fatigue life.

Recently at Northwestern University, Wen et al. (2002) proposed a unified creep and plasticity theory following McDowell et al.'s work (1994) to predict the fatigue life of solder, which shows reasonable agreement with experimental data. The model is adopted in current research.

From the literature review to the available fatigue theories introduced in this section, it can be seen that although lots of methods have been proposed to predict the fatigue life of interconnects, a scientific based method is still timely and of use to the electronics industry, which is the one of the major objects of this dissertation.

1.3 Constitutive Model for Solder

It should be noted that the fatigue formulas introduced in Section 1.2 usually requires the stress, strain or strain energy density as input for a real solder interconnect system. These quantities are not directly measured or controlled in the field situation. Usually they are estimated by numerical simulations, which depend on the constitutive model for solder materials. Thus, constitutive relationships for solder alloys should be incorporated into the solder life prediction methodology. The unified creep plasticity (UCP) model follows the materials science perspective that dislocation motion is the cause of both creep (time-dependent) and plastic (time-independent) deformation, and it uses inelastic deformation to include both. The total stain is expressed as follows:

$$\dot{\boldsymbol{\varepsilon}} = \dot{\boldsymbol{\varepsilon}}^{e} + \dot{\boldsymbol{\varepsilon}}^{in} + \dot{\boldsymbol{\varepsilon}}^{th} \tag{1.16}$$

where $\dot{\boldsymbol{\varepsilon}}^{in}$ is the inelastic strain rate. Some of the recently published and used models are described next.

McDowell et al. (1994) introduced a thermoviscoplastic internal state variable model to simulate the solder alloys. The inelastic strain rate $\mathbf{D}^{in}$ is defined as follows:

$$\mathbf{D}^{in} = \sqrt{\frac{3}{2}} A \left(\frac{\langle S_v \rangle}{D} \right)^{n} \exp\left(B \left(\frac{\langle S_v \rangle}{D} \right)^{n+1} \right) \Theta \mathbf{N} \tag{1.17}$$

$$S_v = \sqrt{\frac{3}{2}} \left\| \mathbf{S} - \boldsymbol{\alpha} \right\| - R \tag{1.18}$$

$$\mathbf{N} = \frac{\mathbf{S} - \boldsymbol{\alpha}}{\left\| \mathbf{S} - \boldsymbol{\alpha} \right\|} \tag{1.19}$$

$$\Theta = \exp\left(-\frac{Q}{R_G T} \right) \quad for \;\; T \geq \frac{T_m}{2} \tag{1.20}$$

$$\Theta = \exp\left(-\frac{2Q}{R_G T} \left[\ln\left(\frac{T_m}{2T} \right) + 1 \right] \right) \quad for \; T \leq \frac{T_m}{2} \tag{1.21}$$

where S_v is the viscous over stress, $\mathbf{S}$ is the deviatoric stress tensor, $\boldsymbol{\alpha}$ is the backstress that plays a primary role in the model to establish the non-linear mechanical behavior for solders, R is the yield stress radius, D is the drag strength, $\mathbf{N}$ is the direction of the inelastic strain rate, and Θ is a diffusivity parameter.

There are some other unified constitutive models been developed for solder materials. For instance, Desai et al. (1997) developed a temperature dependent yield function; Ju et al. (1996) proposed a scalar function to obtain the inelastic strain rate; Whitelaw et al. (1999) adopted isotropic hardening and directional hardening variable to obtain the inelastic strain rate. Recently, a modified unified creep and plasticity model was developed by Wen et al. (2001 2002) following McDowell's work (1994), which is adopted in current research and introduced in chapter 2 to simulate solder coupled creep-plastic behavior.

1.4 Failure of Interconnects near the Interface of Solder and Intermetallic Compound under Thermal-mechanical Cyclic Loading

It has been observed experimentally that solders fail by crack nucleation and propagation at or near the interface of Intermetallic Compound (IMC) and solder (Chan et al. 1997) (Zhang et al. 2006). To predict the failure mode of the solder-intermetallic interface and the interconnect lifetime, it is important to know the material properties of both solder and IMC materials. The material property and behavior of IMC under cyclic thermal and mechanical loading observed in experiments will be discussed in this section. In the past few decades, the behavior of solder in micro electro device has been analyzed by lots of researchers, however, only few research has been conducted on behavior of IMC in recent years. Some experimental observations and analyses will be introduced in this section.

The growth of IMC layer in solder joints is not only caused by a long reflow time and high reflow temperature during soldering, but also by aging, storage, and long term cyclic operation of the electronic assembly at room temperature including long dwell times in operation or sleep mode (Chan et al. 1997). The effects of Cu-Sn IMC on solder joint failure during

thermal shock can be summarized as follows: during thermal cycling, the IMC thickness increases almost linearly with the square root of cycle number. The flat IMC/solder boundary degrades the solder joint performance and the fatigue lifetime. Fatigue failure occurs mainly in the IMC/solder interface. The lifetime of solder joints decreases rapidly with the increase of IMC thickness during reflowing.

Generally it is found in experiments that most of the failure of solders is on the layer of IMC, namely, the crack usually initiate, and propagate in the IMC layer due to cyclic thermal-mechanical load and effect of electromigration (Gupta 2004). The effect of Cu-Sn IMC on the fatigue failure of solder joint has been studied by Chan et al. (1997). From statistics analysis, numerically the reliability R is the fraction of survivors and can be defined as:

$$R(x) = 1 - F(x) \tag{1.22}$$

where $F(x)$ is the lifetime distribution. Chan et al. (1997) found that the lifetime distribution of solder joints could be modeled by the two parameters Weibull cumulative distribution function, which has the following form:

$$F(x) = 1 - e^{-(x/Q)^B} \tag{1.23}$$

where x is the value of a random variable, which corresponds to number of load cycles to failure (N) of solder joints, B is the Weibull shape parameter relate to Weibull slope, and Q is the scale parameter (characteristic value). The "best fit" Weibull parameters can be obtained from experimental data fitting. Thus, the effect of the IMC layer on joint fatigue lifetime can be expressed as a function of Weibull parameters B and Q. Obviously, the bigger Q will cause

longer probable lifetime. In Chan's work, the x value corresponding to $F(x)$=0.5 is called the number of cycles to failure at 50% failure rate ($N_{50\%}$). $N_{50\%}$ is an important parameter to express fatigue lifetime. The fatigue lifetime of solder joints can be characterized using the parameters Q and $N_{50\%}$ for the study of the effect of intermetallic growth on the shear thermal-mechanical cycling failure of solder joints. It is found that the thinner the IMC layer, the larger number of cycles to failure as the Weibull distribution curve moves to higher N. The lifetime distribution is characterized by the scale parameter Q.

Some experiments on solder and IMC behavior under cyclic load have been conducted by Chan et al. (1997) and observed by using Scanning Electron Microscope (SEM). SEM is a type of electron microscope capable of producing high resolution images of a sample surface. Due to the manner in which the image is created, SEM images have a characteristic three-dimensional appearance and are useful for judging the surface structure of the sample. Chan found that with the increasing of aging time and temperature, the thickness of IMC grows thicker, and it will have worse effect on the failure of solder joint. The IMC layer has higher stiffness than the bulk solder, so the shear stress will be concentrated on the IMC/solder interface. The dislocations and vacancies that exist at the smooth boundary of the IMC gather gradually, and then the crack forms, grows, and gives rise to joint failure (Chan et al.1997). After the crack initiated, it propagates fast and fracture quickly (100 cycles), and generally the fracture behavior of solder joints after major crack initiated appears to be brittle. Since the stress is generated mainly due to the development of cyclic strains by temperature fluctuations and a mismatch in thermal expansion coefficients (TEC) between component and Printed Circuit Board (PCB). The crack initiates and grows in η-phase (Cu_6Sn_5) or the boundary of ε-phase (Cu_3Sn) and η-phase.

Therefore, it can be concluded that the cracks mainly initiate and propagate along the IMC/bulk solder interface. This conclusion matches the observations from other researches (Gupta 2004).

It has also been found in Chan's experiments (1997) that the ε-phase is formed between Cu-pad and η-phase (Cu_6Sn_5), and grows faster than the η-phase. The intermetallic reduces the solder joint lifetime, the lower solder joint lifetime with greater IMC thickness and aging time. The lifetime with a thickness of IMC around 2.8ηm is corresponding to 62% of lifetime of an unaged sample. The decreasing rate of lifetime with increase of IMC thickness gradually slows because The IMC/solder interface becomes flat. In conclusion, solder joint fatigue lifetime is affected by the morphology of the Cu–Sn intermetallic compounds/bulk solder interface for shear cycling.

Although the ε -phase is formed between Cu-pad and η -phase, and grows more quickly than the η-phase, it has little effect on failure of IMC. The IMC thickness increases linearly almost with the square root of aging time, and the IMC/bulk solder interface becomes gradually flatter. Chan et al. (1997) proposed a simplified equation to predict the thickness of IMC as a function of aging time. Similar formula has been proposed by Tu et al. (1999) as well.

$$k = \sqrt{\alpha t} \tag{1.24}$$

where k is the thickness of IMC layer; t is hold time at constant temperature, proportional to cyclic number N (hold at 125˚C in Chan's experiment); α is diffusion coefficient define as:

$$\alpha = \alpha_0 e^{(-\frac{Q}{\gamma T})} \tag{1.25}$$

where α_0 is a diffusion constant equals to $1.68\times10^{-4}m^2/s$, which can be modified for different cases; Q is a diffusion coefficient (1.09ev in Chan's experiment); γ is Boltzmann constant (1.38×10^{-23} joules/kelvin); and T is the absolute temperature.

In conclusion, the effects of Cu-Sn IMC on solder joint failure during thermal shock can be summarized as follows (Chan et al. 1997): at the beginning the IMC/solder interface is uneven, but the IMC layer flattens gradually at the interface of IMC/solder. Under reflowing, the Cu_6Sn_5 IMC is formed between the Cu-pad and the solder joint, longer reflowing time causes thicker IMC layer and rougher the IMC/solder boundary. During thermal cycling, the IMC thickness increases almost linearly with the square root of cycle number. The flat IMC/solder boundary degrades the solder joint performance and the fatigue lifetime. The fatigue failure occurs mainly in the IMC/solder interface. The Cu_3Sn ε-phase between Cu-pad and η-phase formed during the thermal cycling is found to have little influence on the lifetime. The lifetime of solder joints goes down rapidly with the increase of IMC thickness during reflowing.

Although some experiments have been conducted on IMC growth under thermal aging, very few of them provided the material properties of IMC, which is useful in developing the mechanical failure models for IMC failure. Recently, Ghosh (2004) has performed a series of experiments to analyze the electric properties, hardness, and indentation fracture toughness of IMC relevant to electronic packaging. Some of his experimental data for IMC materials are used in the cohesive zone mechanical model developed in chapter 2.

Ghosh (2004) found that indentation crack propagation in Cu_3Sn, Cu_6Sn_5, and $NiSn_4$ are similar to the brittle materials and varies by factor of 2. Ag_3Sn is relatively ductile compare with other intermetallics. By knowing the material properties of IMC material, the objective of

current research is to find a mechanical model to predict the behavior of IMC layer under thermal-mechanical cyclic load as well as high current density. Generally the materials show ductile fracture with high fracture toughness and brittle failure with low fracture toughness. It is noted that IMC layer materials range from quasi-brittle to semi-ductile. Thus cohesive zone model is applicable for IMC materials, which will be introduced in next section.

1.5 Failure Analysis to Solder under Cyclic Load Using Cohesive Zone Model

Recently, the cohesive zone model (CZM) has been used to predict failure of Pb and Pb-free solder joints. The damage mechanics incorporated in the model is introduced in this section. The model can be applied to predict the IMC layer thickness and Young's modulus effects on crack initiation stress of solder interconnects.

Yang et al. (2004) proposed a cohesive zone model to predict the low cycle fatigue life of solder joints plastically deformed under cyclic loading. Damage mechanics is incorporated into the cohesive law to account for deterioration of stiffness and strength of solder materials under cyclic loading. The damage evolution law is assumed to be a simple function of accumulated plastic strain in their paper. However, only plastic-induced damage is considered in their work, the strain rate and temperature effects are not considered. They used a simplified method to obtain D with a form of $a(\gamma_p)^b$ by curve fitting experimental data, where γ_p is the accumulated plastic shear strain, a and b are constant curve fitted from experimental data. Since most solder joints are subjected mainly to in-plane shear deformations, only the mode-II (pure shear) of the cohesive zone model is considered in their paper.

The fatigue crack path consists of normal and tangential components. The interfacial failure can be modeled by normal (n) and tangential (t) traction-separation with springs in CZM. As shown in Fig. 1.1, the cohesive tractions in normal and shear T_n and T_t can be calculated by:

$$T_n = \sigma_{\max,0} e \exp(-\frac{\Delta u_n}{\delta_0}) \left\{ -\frac{\Delta u_n}{\delta_0} \exp(-\frac{\Delta u_n^2}{\delta_0^2}) + (1.0-q)\frac{\Delta u_n}{\delta_0}\left[1.0-\exp(-\frac{\Delta u_n^2}{\delta_0^2})\right]\right\} \quad (1.26)$$

$$T_t = 2\sigma_{\max,0} eq(\frac{\Delta u_n}{\delta_0})(1+\frac{\Delta u_n}{\delta_0})\exp(-\frac{\Delta u_n}{\delta_0})\exp(-\frac{\Delta u_n^2}{\delta_0^2}) \quad (1.27)$$

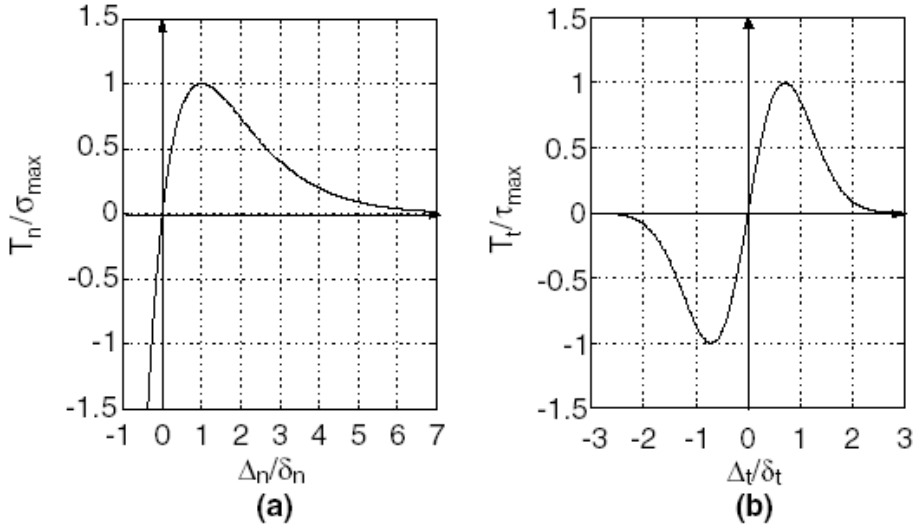

Figure 1.1 Normal and tangential components of cohesive traction (Roe and Siegmund 2003)

To consider cyclic loading, the effect cohesive zone traction tensor can be defined by:

$$\overline{T}_{CZ} = \frac{\beta T_{CZ}}{(1-D_\alpha)} \quad (1.28)$$

$$T_\alpha = k_\alpha (1-D_\alpha)^n \Delta_\alpha \quad (1.29)$$

where $\beta = (\frac{x}{x_0})^m$, k is the initial stiffness, Δ is the opening displacement of crack,

The current cohesive strengths are:

$$\sigma_{\max} = \alpha\sigma_{\max,0}(1-D) \tag{1.30}$$

$$\tau_{\max} = \alpha\tau_{\max,0}(1-D) \tag{1.31}$$

To develop a damage evolution law, essentially the following requirements should be obeyed (Roe and Siegmund, 2003): 1) an endurance stress limit σ_f under which the cyclic load will never cause the solder joint failure; 2) a critical deformation δ_0, the damage starts to accumulate only if the deformation greater than δ_0; 3) the rate of damage variable $\dot{D}$ is a function including traction T, separation vector across the cohesive zone Δu, and damage variable D. 4) the increment of damage is related to the increment of deformation with respect to load level. Based on the principles, the evolution law is suggest by Baqi et al. (2005):

$$\dot{D}_\alpha = c_\alpha \left|\dot{\Delta}_\alpha\right| (1-D_\alpha + r)^m \left(\frac{|T_\alpha|}{1-D_\alpha} - \sigma_f\right) \tag{1.32}$$

where c_α is a constant which controls the damage accumulation, $\dot{\Delta}_\alpha$ is the rate of the relative opening of the cohesive zone, r and m are constants which control the decay of the reaction force at the final stage of damage and σ_f is the cohesive zone endurance limit.

The cohesive zone model has been adopted in current research to simulate the interfacial behavior between IMC and solder bulk; details are introduced in chapter 2.

1.6 Electromigration Effect on IMC Growth and Solder Failure

Electromigration is the transport of material caused by the gradual movement of the ions in a conductor due to the momentum transfer between conducting electrons and diffusing metal atoms. The effect is important in applications where high current densities are used, such as in microelectronics and related structures. As the structure size in electronics such as integrated circuits (ICs) decreases nowadays, the practical significance of this effect increases.

Initial research on the failure mechanisms of electromigration in thin metal conductors has been conducted by James R. Black (Black 1969) in 1960s. He found that the lifetime of a thin metal conductor is inversely proportional to the square of the current density and has an exponential component with activation energy consistent with grain boundary diffusion. He proposed the following median time to failure equation:

$$t_{50} = \frac{A}{j^n} \exp(\frac{E_a}{kT}) \tag{1.33}$$

where t_{50}, median time to failure (MTTF), is defined as the time at which 50% of a large number of identical devices have failed, A is a empirical material constant, j is the current density, n is the current density exponent and is found to be 2 in Black's experiments, E_a is the activation energy, k is Boltzman's constant, and T is the absolute temperature. This equation is known as Black's Equation. Black's experiments suggest that grain boundary diffusion is the major diffusion mechanism and electromigration failure is controlled by grain boundary diffusion. The activation energy of time to failure coincides with the grain boundary diffusion activation energy. The single mode of distribution of aluminum thin film structure has been widely accepted. However, Black's law ignores the influence of thermal gradient across the specimen, it only provide an empirical formula to roughly estimate the MTTF value.

Gan and Tu (2002) have conducted a series of experiments to analyze electromigration effect on IMC behavior under high current density. They found that IMC is comprised mainly of Cu_3Sn compound rather than Cu_6Sn_5 compound. Besides, copper has much better electromigration resistance than Aluminum; they found in the experiment that void started to appear in the solder part just in front of the solder/IMC cathode interface after 21 hours and grow bigger after 87 hours. Based on the solder V-groove samples experimental observation, H. Gan and K.N.Tu (2002) proposed a method to consider the electromigration effect on IMC formation. In their model, the general form of the atomic flux J can be described as:

$$J = J_{chem} + J_{em} + J_{\sigma} = -D\frac{\partial C}{\partial x} + C\frac{D}{\gamma T}Z^{*}ej\rho - C\frac{D}{\gamma T}\frac{d\sigma\Omega}{dx} \tag{1.34}$$

where C is the concentration $=1/\Omega$ for pure metal, Ω is the atomic volume; D is the diffusivity; γ is the Boltzmann constant; T is the absolute temperature; Z^* is the effective charge number; e is the electron charge; ρ is the resistivity; j is the current density; J_{chem} is the diffusion term and J_{em} is the drift term due to electron momentum transfer effect (electron wind force); J_{σ} is the back stress term due to electromigration.

The growth rate of IMC at the anode can be calculated as:

$$\frac{dx}{dt} = GD\frac{\Delta C_{\eta}}{\Delta x} + GC\frac{D}{kT}\frac{\Delta\sigma\Omega}{\Delta x} - GJ'_{em} - G_2 J_{em} \tag{1.35}$$

C_{η} is the Cu concentration in the Cu_6Sn_5 compound.

$$G = G_1 + G_2 = \frac{1}{C_{Cu} - C_{\eta}} + \frac{1}{C_{\eta} - C^{*}} \tag{1.36}$$

Eq. (1.45) can be simplified as:

$$\frac{dx}{dt} = \frac{A}{\Delta x} + b = \frac{a + a^*}{\Delta x} + b \tag{1.37}$$

a^* and $b>0$ for anode; a^* and $b<0$ for cathode.

where $a^* = GC\frac{D}{kT}\Delta\sigma\Omega$ $a = GD\Delta C_\eta$ $b = G_2 J_{em} - GJ'_{em}$

The grow rate *dx/dt* depends on chemical potential, electron wind force and back stress due to electromigration, which corresponds to *a/Δx, a*/Δx, b* term respectively. It should be noted that when the linear term b=0, the growth of IMC layer has parabolic dependence with time. For no current case, the growth rate is smaller at the cathode, larger at anode. It can be found that there is a thicker layer of Cu_6Sn_5 formed at the anode side and a thinner layer at the cathode side. The difference is due to the polarity of electric current and local current crowding (Gan and Tu 2002).

Generally, for interconnects under high current density that cause electromigration, vacancy diffusion is driven by four forces: 1) electrical current field forces, which is due to momentum exchange between moving electrons and host ions, 2) stress gradient, due to localization of accumulation and depletion of mass, 3) temperature gradient, due to joule heating, 4) vacancy concentration gradient. At high current densities, void formation becomes important. The chemical potential, electron wind force, and thermal stress effects will be investigated numerically. Based on the well known Einstein relation (Einstein 1905), the actual flux is proportional to the thermal dynamic force. For solder interconnect, the thermal dynamic force has contributions mainly from electron wind force, capillary force, and thermal stress gradient.

Electric crowding and joule heating effects also play important roles. The electron wind force corresponding to the electromigration effect can be predicted using a dislocation core diffusion model. The surface energy term corresponding to capillary force can be determined based on Herring's formula (Herring 1951). The thermal stress field distribution will be determined either experimentally or numerically. It is noted that in both IMC layer and bulk solder, electromigration and stress migration forces are generally at the same order of magnitude, and the electromigration force is stronger than stress migration force under very high applied current density. The terms of the Einstein relation for the interconnect system can be determined, and the kinetic mass diffusion model to predict the void growth in interconnects will be available by combining with available experimental data. A kinetic mass diffusion model is developed in chapter 4 to predict the electromigration effect on interconnect failure under high current density.

1.7 Objectives of the Study

Based on the literature review of previous research works performed by different researchers, the ultimate objective of this dissertation is to develop a materials science based theory for interconnects combine intermetallic compound failure mode and interfacial behavior. The following investigations are undertaken to achieve this goal:

Firstly, a 3D computational model is developed including cohesive zone model and unified creep and plasticity theory to simulate the interfacial behavior and creep-plastic behavior of solder, respectively. Thermal-mechanical analysis is also conducted using the 3D solder/IMC interconnect model. Secondly, an energy based phase transformation theory is developed based on fracture mechanics and micromechanics to predict the fatigue crack nucleation and propagation in solids, experimental data for steels, aluminum alloys, and solder alloys are

compared with the prediction of the theory. Some parameters in the theory are obtained from numerical analysis using the proposed computational model. Finally, a kinetic mass diffusion theory is developed to predict the electromigration effect on interconnect failure. The predicted void width and propagation speed are compared with experimental data. Application of the proposed theory has no size limitation, is applicable to various solder materials, allows data sharing, is able to handle high current effect, avoids choosing fatigue location or predefining crack parameters, and, more importantly, gives metallurgical directions so that necessary measures can be taken to optimize the microstructure and achieve longer lifetime.

1.8 Outline of the Dissertation

The solder and IMC behavior under thermal-mechanical cyclic load is studied in this dissertation; some theoretical and experimental works on solder interconnect failure have been reviewed. It is found that most of the solder joints failure is caused by failure near the interface of IMC and bulk solder. A cohesive zone-UCP mechanical model is applied to predict the crack initiation and propagation at the interface of solder/IMC or in IMC layer. Thermal mechanical fatigue analysis to IMC related solder failure is conducted. An energy based phase transformation model is developed to predict fatigue crack propagation. A kinetic mass diffusion model is proposed to predict the electromigration effect on interconnect failure.

Chapter 1 introduces the background of current research and gives literature review to research works conducted by previous researchers. Chapter 2 develops the cohesive-UCP computational model for solder interconnect including intermetallic layers. Both mechanical and thermal-electric numerical analyses have been conducted. Chapter 3 investigates the physical damage process within solder/IMC system. Based on experimental findings, a fatigue theory

with its failure criterion based on physical damage mechanism is developed for interconnects. The theory applies phase transformation concept and energy-based micromechanical fatigue model to the solder structure. Fatigue crack propagation rate has been accurately predicted for different steels, aluminum alloys, and solder alloys. Chapter 4 develops a kinetic mass diffusion model to predict the electromigration effect on solder failure under high current density. Void width and growth speed can be predicted using the proposed model; reasonable agreement is obtained compared with experimental data. Chapter 5 concludes the dissertation and suggests the future research directions. Appendix lists the ABAQUS code for the cohesive-UCP interconnects structure; the derivation to apply the phase transformation theory to ellipsoidal crack; a method to incorporate the electrical current effect into phase transformation theory; and numerical analysis to ball grid array (BGA) electric packaging under drop impact.

Chapter 2

Mechanical and Thermo-Electrical Computational Analysis to Interfacial Failure of Solder Joint

Based on cohesive fracture theory and continuum mechanics, a 3D computational model has been developed in this chapter to predict the crack nucleation, propagation and interfacial damage of interconnects. Unified creep-plasticity theory is incorporated in the model to predict the creep and hysteresis effects on fatigue crack propagation in solder. In addition the cohesive zone model is adopted to predict the interfacial behavior between the solder bulk and the intermetallic layer. Using the cohesive-UCP finite element model, the intermetallic-layer growth effect on crack initiation stress has been studied for different solders. A thermo-electric finite element analysis has been conducted to predict the electrical concentration and joule heating effects on the failure of Sn-2.5Ag-0.8Cu-0.5Sb solder under different applied current densities. The temperature and current density distribution in a solder joint with a crack that propagates near the interface of the bulk solder and intermetallic layer has been predicted. Pronounced temperature and electrical current concentration is observed near the crack tip. Although the Pb-free solder is usually regarded as having a higher melting temperature compared with Pb-Sn eutectic solder, the concentration of heat at the crack tip caused by joule heating may still melt the solder material under high current density. The crack propagation will be enhanced and

cause a circuit failure. The developed numerical model will be applied to predict some parameters for phase transformation theory, detail will be introduced in chapter 3.

2.1 Introduction

It has been observed experimentally that solders fail by crack nucleation and propagation at or near the interface of Intermetallic Compound (IMC) and solder (Mattila and Kivilahti 2006) (Zhang et al. 2006). To predict the failure mode of the solder-intermetallic interface and the interconnect lifetime, it is important to know the material properties of both solder and IMC materials. The objective of this chapter is to develop a finite element model predicting the interconnect behavior including IMC layer and IMC/solder interface by knowing the thermal, electrical, and mechanical properties of the interconnect system materials, including IMCs. Initial emphasis will be on the IMC and IMC/solder interface failure. The fracture toughness of various materials compared to IMC's is given in Table 2.1 by Ghosh (2004). Generally the materials show ductile fracture with high fracture toughness and brittle failure with low fracture toughness. It is noted that IMC layer materials range from quasi-brittle to semi-ductile.

Table 2.1 Fracture toughness of different materials Ghosh (2004)

Material	$MPa\sqrt{m}$
Soda-lime-glass	0.7-0.8
Polystyrene	0.8-1.1
Cu_6Sn_5 (η)	2.22-3.38
Cu_6Sn_5 (η')	2.37-2.83
Cu_3Sn	4.86-6.58
$AuSn_4$	2.15-2.85
Ni_3Sn_4	3.77-4.67
An aluminum alloy	36
A steel alloy	50

During the past four decades, several methods have been proposed to predict the failure of solder joints. Typically the most widely used empirical method is the ‘‘Coffin-Manson’’ law. However, the approach is not useful for cases beyond the experimental range investigated. Another empirical method is to apply the rate- and temperature-dependent constitutive model (rate independent inelastic deformation such as plasticity is incorporated in unified creep-plasticity (UCP) theories) combined with mechanical continuum damage mechanics (CDM) (McDowell et al. 1994) (Wen et al. 2001 2002) (Wang et al. 2004). The theory gives accurate predictions to the constitutive relationship of solder materials, typically a large number of experimentally determined material constants are needed to describe the mechanical behaviors and damage evolution to achieve a reasonable accuracy. However, both of the methods are not useful to predict the interfacial failure of solder/IMC. Thus, an advanced method to predict solder/IMC interfacial failure is required besides applying UCP theory for solder materials.

Recently, the cohesive zone model (CZM) has been used to predict failure of Pb and Pb-free solder joints (Baqi et al. 2005) (Yang et al. 2001) (Roe and Siegmund 2003) (Nguyen et al.

2001) (Yang et al. 2004) (Towashiraporn et al. 2005) (Cavalli et al. 2004) (Yu et al. 2006) (Yao and Shang 1996). The cohesive zone method is a numerical tool for the mechanics of interfaces; initially it was developed to model crack initiation and growth in quasi-brittle materials. This method treats fracture as a gradual process in which separation between incipient material surfaces is resisted by cohesive tractions. Compared with the traditional empirical method, the CZM can be applied from micro- to macro-scale, as long as the parameters, cohesive strength and critical separation displacement, are determined by careful fracture experiments. The model can predict the entire fracture process from crack initiation to propagation accurately for any joint geometry and under any applied loads. Crack initiation and propagation are natural outcomes of a CZM analysis and has been adopted in this chapter through the finite element program, ABAQUS. The damage mechanics incorporated in the model is introduced and the damage initiation and evolution conditions are defined. The model is applied to predict the effects of IMC layer thickness and Young's modulus on crack initiation stress of solder joints.

Since the solder joint failure is a coupled thermo-electric-mechanical problem, in addition to a mechanical analysis, a thermo-electric analysis to solder joint with a crack propagating near the interface of bulk solder and intermetallic layer has been conducted. The temperature and current density distribution in a solder joint with interfacial crack propagation has been predicted numerically. The current concentration and joule heating effects are discussed based on experimental observation and computational analysis results.

2.2 Cohesive Zone Modeling and Finite Element Mechanical Analysis to Simulate Interfacial Behavior of Solder/IMC

To incorporate a cohesive zone model into the finite element model, the principle of virtual work can be modified to (Roe and Siegmund 2003):

$$\int_V \widetilde{P} : \delta\widetilde{F} dV - \int_{S_i} \vec{T}_{CZ} \cdot \delta\Delta\vec{u} dS = \int_{\partial V} \vec{T}_e \cdot \delta\vec{u} dS \qquad (2.1)$$

where $\widetilde{P}$ is the nominal stress tensor which equals $\widetilde{F}^{-1}\det(\widetilde{F})\widetilde{\sigma}$, $\widetilde{F}$ is the deformation gradient, $\widetilde{\sigma}$ is the Cauchy stress tensor, V is the control volume, $\vec{u}$ is the displacement vector, $\vec{T}_{CZ}$ is the cohesive zone traction vector, $\vec{T}_e$ is the traction vector on the external surface of the body, S_i is the internal boundary, and ∂V is the external boundary of V.

A quadratic nominal stress criterion to predict damage initiation is adopted in this chapter. Damage is assumed to initiate when a quadratic interaction function involving the nominal stress ratios reaches unity. This criterion is represented as (ABAQUS documentation 6.6.3 2006):

$$\left(\frac{\langle t_n \rangle}{t_n^0}\right)^2 + \left(\frac{t_s}{t_s^0}\right)^2 + \left(\frac{t_t}{t_t^0}\right)^2 = 1 \qquad (2.2)$$

where t_n, t_s, t_t refer to the normal, the first, and the second shear stress components; t_n^0, t_s^0, t_t^0 represent the peak values of the nominal stress when the deformation is either purely normal to the interface or in the first or the second shear direction. The symbol $\langle\ \rangle$ is the usual

Macaulay bracket interpretation, used to signify that a purely compressive deformation or stress state does not initiate damage. It should be noted that the damage initiation can also be predicted by using the energy based phase transformation theory, which is introduced in chapter 3.

The damage evolution for mixed mode failure is defined based on Benzeggagh-Kenane fracture criterion (Benzeggagh and Kenane 1996), when the critical fracture energies during deformation along the first and the second shear directions are similar; i.e. $G_s^C = G_t^C$, the criteria is given by:

$$G_n^C + (G_s^C - G_n^C)(\frac{G_S}{G_T})^\eta = G^C \tag{2.3}$$

where the mixed-mode fracture energy $G^C = G_n + G_s + G_t$. G_n, G_s, and G_t refer to the work done by the traction and its conjugate relative displacement in the normal, the first, and the second shear directions, respectively, and G_n^C, G_s^C and G_t^C refer to the critical fracture energies required to cause failure in the normal, the first, and the second shear directions, respectively. Here, $G_S = G_s + G_t$, $G_T = G_n + G_S$, and η is a material parameter.

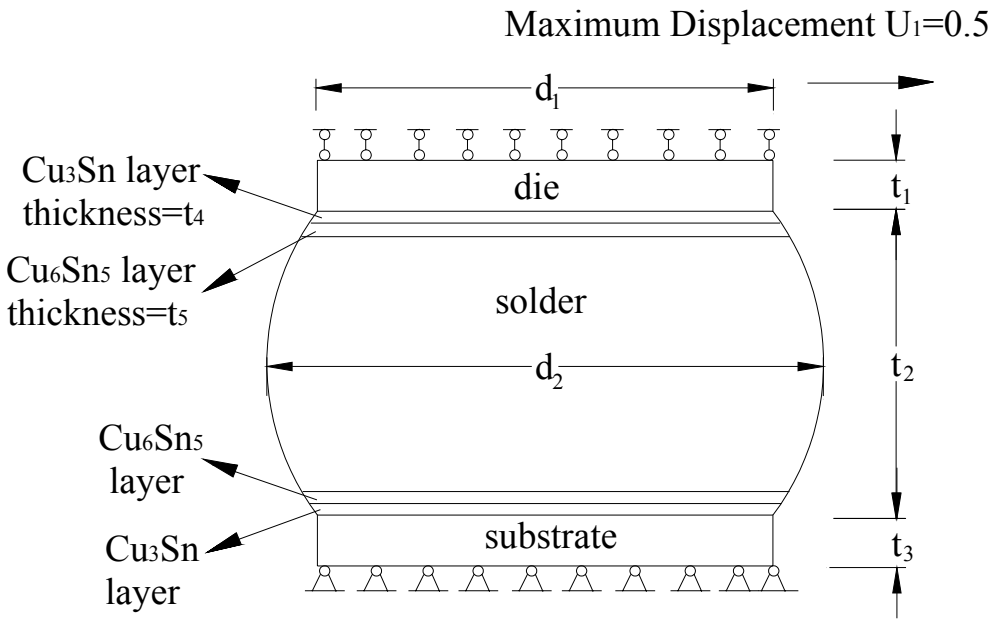

Figure 2.1 Description of finite element model (XZ plane for 3D model)

A 3D finite element solder joint model has been developed incorporating the CZM and UCP model using ABAQUS, the detail of the UCP theory will be introduced in next section. The geometrical and boundary conditions are shown in Fig. 2.1. Two layers of IMC, Cu_6Sn_5 and Cu_3Sn are included in the model. Sinusoidal displacement is applied with a maximum magnitude of 0.5μm to simulate the shear load due to mismatch of the coefficient of thermal expansion (CTE). The solder, intermetallic layer and silicon die properties are given in Table 2.2 (Ghosh 2004) (NIST database 2002) (Lau 1996).

Table 2.2 Material properties used in finite element model
(Ghosh 2004) (NIST database 2002) (Lau 1996)

	Young's modulus (GPa)	Poisson's ratio	Yield Stress(MPa)
Solder: Sn-3.5Ag-0.7Cu Eutectic	56	0.36	30.6
Solder: Sn-2Ag-46Bi-4Cu	33.8	0.36	67.6
Solder: Sn-37Pb Eutectic	35	0.36	30.2
η-phase Cu_6Sn_5	96.9	0.309	-
ε-phase Cu_3Sn	123.2	0.319	-
Ag_3Sn	81.4	0.347	-
Silicon die layer	131.0	0.3	-

Note: Solder yield stress obtained from NIST database for solder properties with Emphasis on new lead-free solders release 4.0

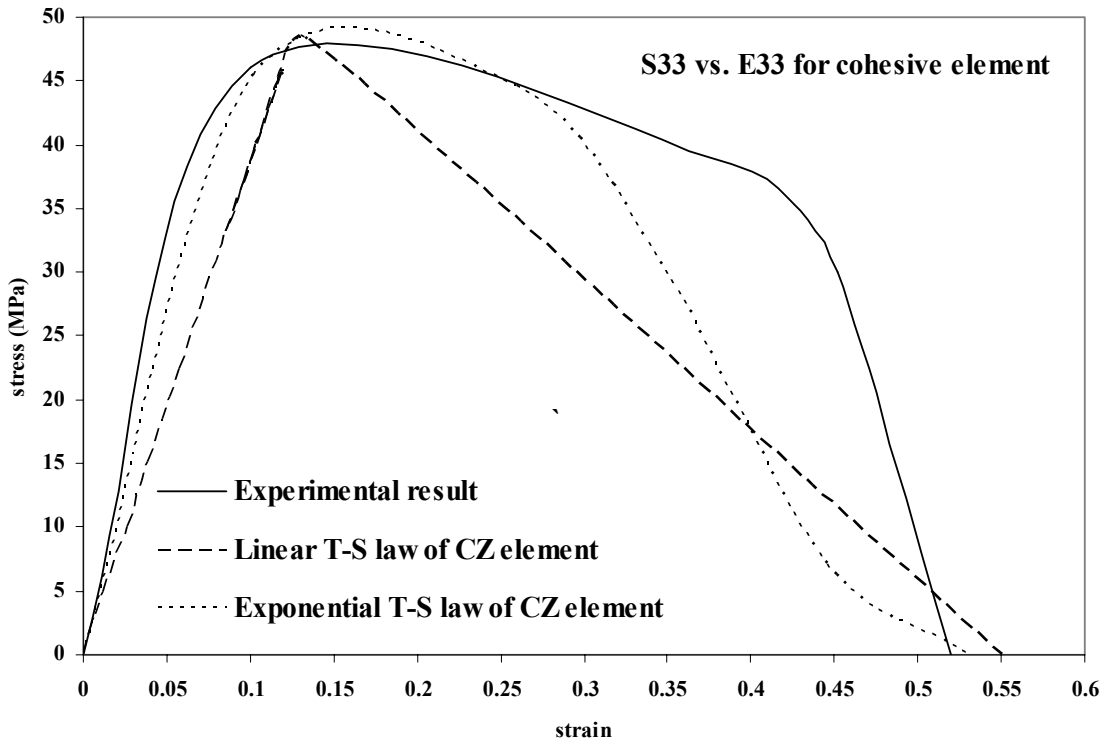

Figure 2.2 Traction-separation law of cohesive element for 95.5Sn-3.8Ag-0.7Cu solder compared with experimental result

For simplicity an exponential traction-separation (T-S) law of the interfacial cohesive element is assumed, and the model is applied to simulate 95.5Sn-3.8Ag-0.7Cu solder, for which experimental data is available (Ren et al. 2005). The stress-strain relationship for the cohesive element is compared with experimental results, as in Fig. 2.2, which shows acceptable accuracy using an exponential T-S law.

2.3 Unified Creep and Plasticity Model to Simulate Behavior of Solder Materials

For solder materials, the UCP theory is adopted in the finite element model based on the dual backstress thermoviscoplasticity model proposed by McDowell et al. (1994) and Wen et al. (2001 2002). The relationship between stress rate $\dot{\boldsymbol{\sigma}}$ and strain rate can be written as:

$$\dot{\boldsymbol{\sigma}} = \mathbf{C}(T) : (\dot{\boldsymbol{\varepsilon}} - \dot{\boldsymbol{\varepsilon}}^{in} - \chi \dot{T}\,\mathbf{I}) + \mathbf{C}^{-1} : \boldsymbol{\sigma} : \frac{\partial \mathbf{C}}{\partial T}\dot{T} \tag{2.4}$$

where $\boldsymbol{C}$ is the matrix of the elastic constants and is a function of Poisson's ratio v and Young's modulus $E(T)$, which is also a function of absolute temperature T; $\dot{\boldsymbol{\varepsilon}}$ is the total strain rate; $\dot{\boldsymbol{\varepsilon}}^{in}$ is the inelastic strain rate; χ is the coefficient of thermal expansion and $\mathbf{I}$ is the unit tensor. Here, the term $\chi \dot{T}\,\mathbf{I}$ refers to the thermal strain rate.

The form of the flow rule for inelastic strain rate is given by:

$$\dot{\boldsymbol{\varepsilon}}^{in} = \sqrt{\frac{3}{2}} A \left(\frac{S_v}{d} \right)^n \exp\left(D \left(\frac{S_v}{d} \right)^{n+1} \right) \Theta(T)\mathbf{N} \tag{2.5}$$

where d is the drag strength; A and D are material constants; the diffusivity term $\Theta(T) = \exp(-Q/(kT))$; Q is the apparent activation energy; k is the universal gas constant, equal to 8.314J/Kmole; $\boldsymbol{N}$ is a unit vector in the direction of the deformation loading, defined by:

$$\mathbf{N} = (\mathbf{S} - \boldsymbol{\alpha}) / \left\| \mathbf{S} - \boldsymbol{\alpha} \right\| \tag{2.6}$$

where $\mathbf{S}$ is the deviatoric tensor, $\mathbf{S} = \boldsymbol{\sigma} - tr(\boldsymbol{\sigma})/3$; S_v is the viscous overstress defined by:

$$S_v = \left\langle \sqrt{\frac{3}{2}} \left\| \mathbf{S} - \boldsymbol{\alpha} \right\| - R \right\rangle \tag{2.7}$$

where R is the yield stress radius; $\boldsymbol{\alpha}$ is the deviatoric back stress

The evolutionary law for $\boldsymbol{\alpha}$ is defined as:

$$\dot{\boldsymbol{\alpha}} = \mu \left\| \dot{\boldsymbol{\varepsilon}}^{in} \right\| \mathbf{N} - \beta \boldsymbol{\alpha} \tag{2.8}$$

where μ and β are material constants. Eq. (2.8) is similar to Prager's flow law (Prager 1956) in plasticity, and it is noted that $\boldsymbol{\alpha}$ reaches a saturated value along with the loading process.

To determine the R term in Eq. (2.7),

$$R = R_{initial} + R_{add} \tag{2.9}$$

$$\dot{R}_{add} = \varpi \dot{\chi} \tag{2.10}$$

where ϖ is a material constant; χ is the hardening from the dislocation increment within the material, which is defined as:

$$\dot{\chi} = \mu \left\| \dot{\varepsilon}^{in} \right\| (\overline{\chi} - \chi) \tag{2.11}$$

where $\overline{\chi}$ is the sutured value of χ; μ is a material constant.

The material constants for the model were obtained through analysis of the material behavior and by fitting to the experimental data (Vaynman and Zubelewicz 1990) (Vaynman and McKeown 1993) (Wen 2001) (Wen et al. 2002) (Wang et al. 2004). For the Sn-3.5Ag eutectic solders, the values of the parameters were determined as: E=45GPa, A=5.81×10^{3}s^{-1}, α=0, D=0.001, n=2, d=70MPa, R=8.0MPa, μ=16, β=0.009s^{-1}, Q=38000J/mole. For the 63Sn-37Pb eutectic solders, the values of the parameters were determined as: A=0.009, α=0, D=0.001, n=1.2, d=70MPa, $R_{initial}$=2.0MPa, μ=8, $\overline{\chi}$=8MPa, $\varpi = 0.085$, Q=22000 J/mole.

2.4 Case Study and IMC Layer Thickness Effect on Solder Failure

A 3D finite element model for an interconnect has been developed incorporating CZM and UCP theories to simulate solder/IMC interfacial behavior and hysteresis effect in solder bulk, respectively (Yao et al. 2008). The model has been programmed into the commercial software, ABAQUS, through a user defined subroutine using FORTRAN language. The ABAQUS code for the model is given in Appendix A.

The main process of building a model is as follows:

a. Defining the job title and units

b. Creating the model geometry

c. Defining parts, section and material properties (User defined subroutine are combined into the model to include CZM and UCP theory)

d. Defining element type and property, cohesive element and solid stress elements are used for 2D/3D stress analysis; electrical-thermal element is used for joule heating analysis

e. Meshing

f. Defining the analysis type and analysis options

g. Applying loads and boundary conditions

h. Specifying load step options

i. Initiating the solution

j. Review the results

Fig. 2.3a shows the stress analysis with typical elastic-plastic solder modeling applied to the solder/IMC interconnect system, where the von Mises stress distribution is predicted. Fig. 2.3b shows the analysis to solder/IMC using the combined CZM and UCP theory. A cohesive layer with traction-separation type cohesive element has been defined at the interface of the solder and IMC to predict the interfacial failure. In addition to the von Mises stress distribution, the crack nucleation and propagation near the solder/IMC interface can be predicted in a cohesive element model with the defined damage initiation and evolution law. Figure 2.4 shows the von Mises Stress distribution in a Sn-3.5Ag-0.7Cu eutectic solder joint with a crack propagating near the interface of solder/IMC under cyclic loading, here A_c is the crack area and A_t is the total cross section area.

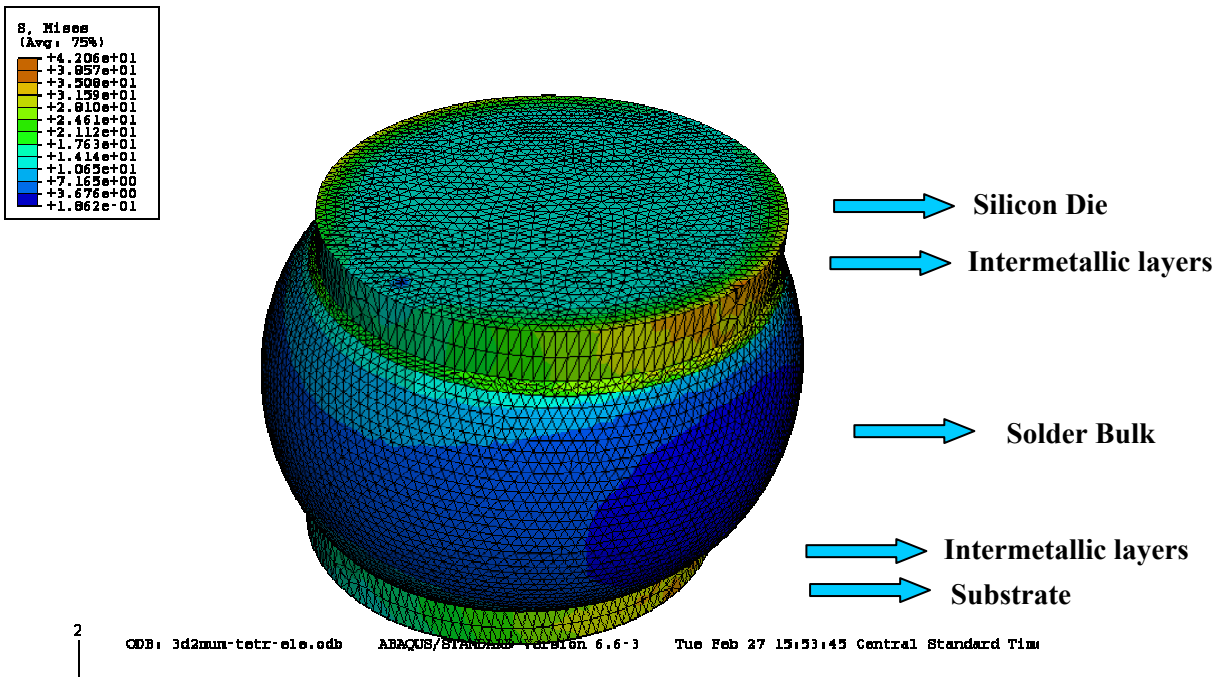

Figure 2.3a Von Mises Stress distribution in a solder joint using elastic-plastic model (MPa)

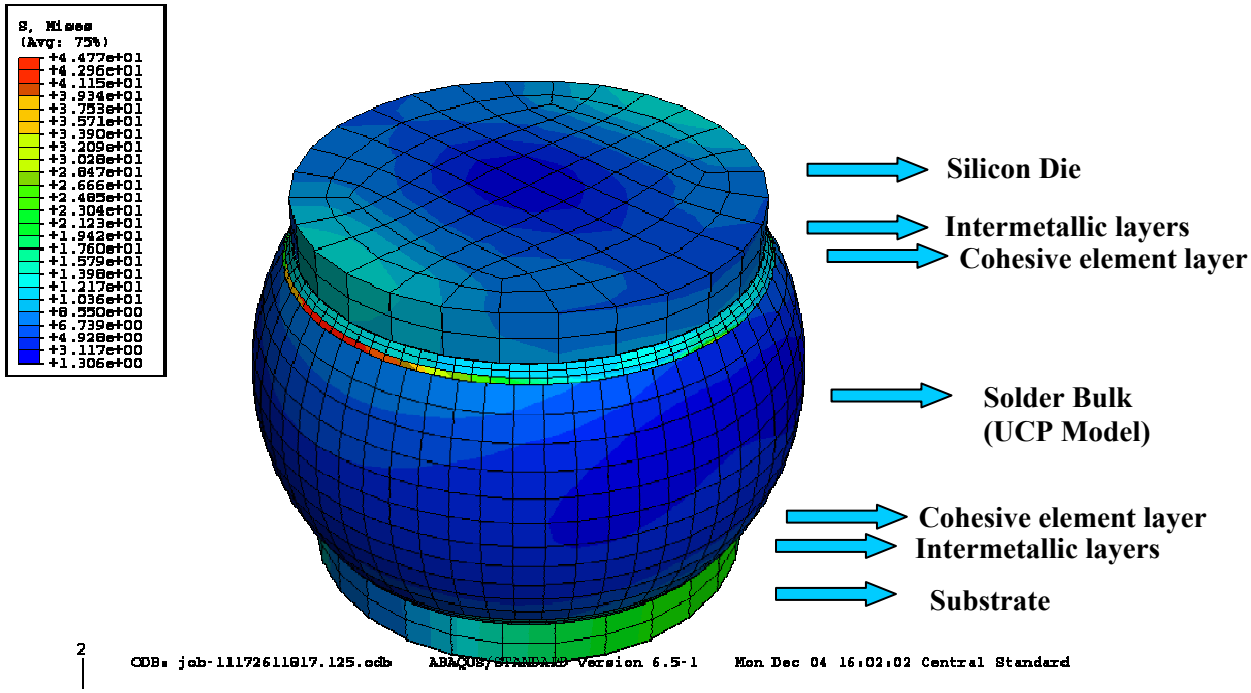

Figure 2.3b Von Mises Stress distribution in a SnAgCu solder joint combining cohesive zone and UCP model (MPa)

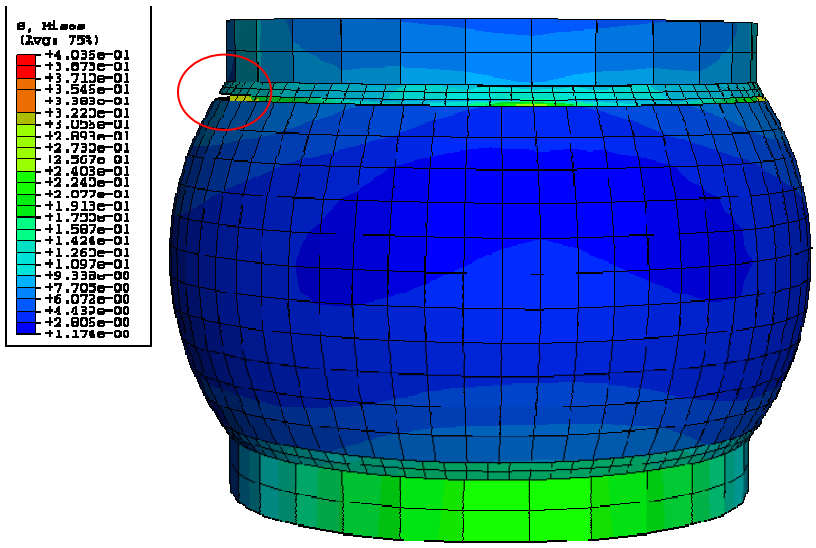

Figure 2.4a von Mises stress distribution when A_c/A_t=3%

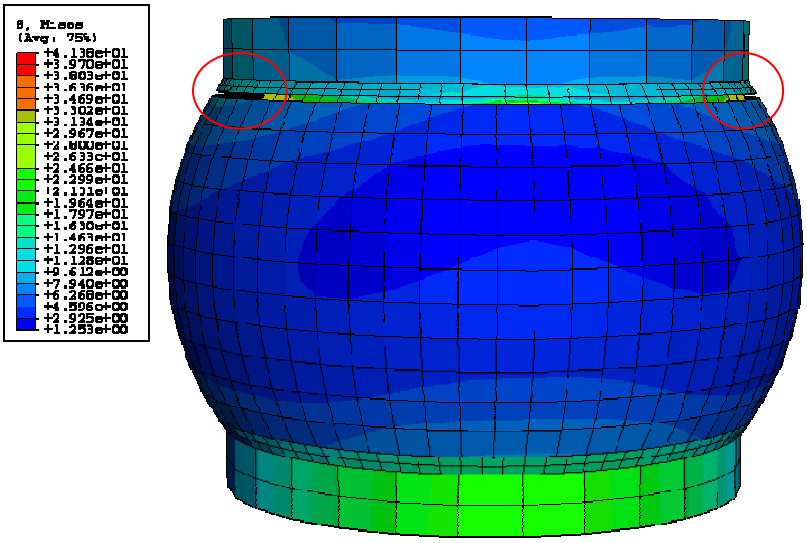

Figure 2.4b von Mises stress distribution when A_c/A_t=10%

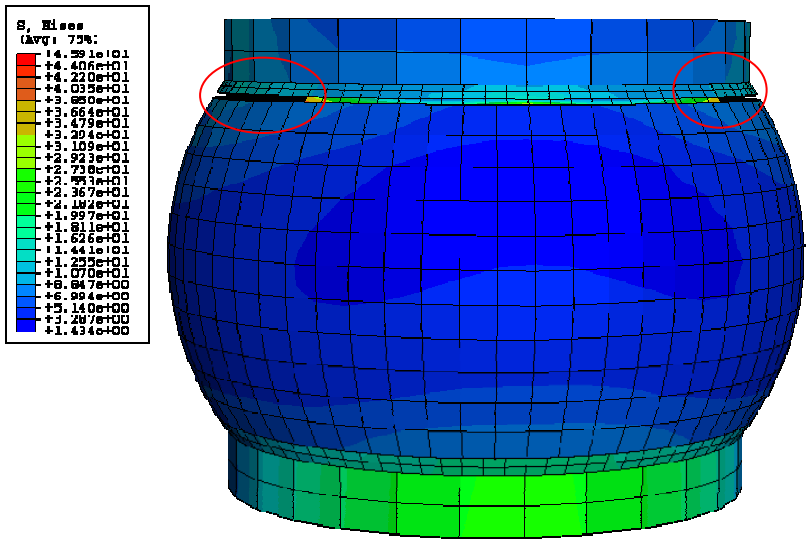

Figure 2.4c von Mises stress distribution when A_c/A_t=20%

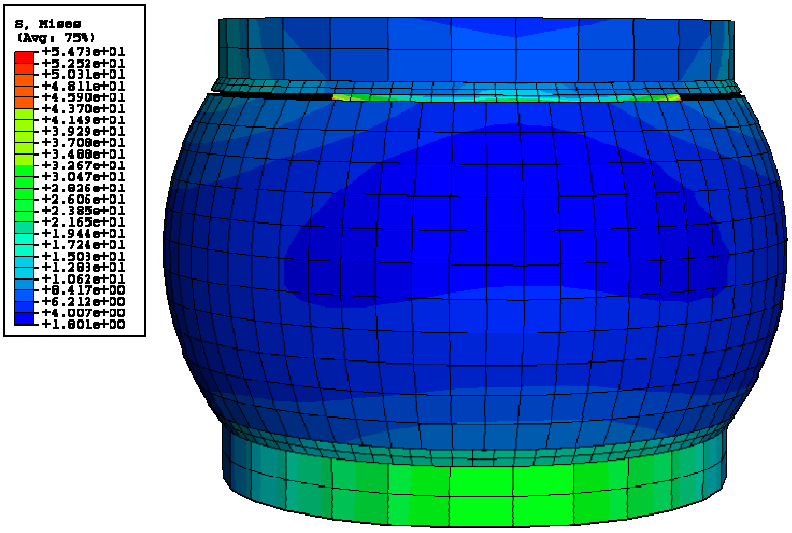

Figure 2.4d von Mises stress distribution when A_c/A_t=30%

Figure 2.4 von Mises Stress distribution in a Sn-3.5Ag-0.7Cu eutectic solder joint with a crack propagating near the interface of solder/IMC under cyclic loading

The proposed cohesive-UCP finite element model is applied to predict the effect of IMC layer thickness on the crack initiation stress of a solder joint. The growth of an IMC layer in solder joint is caused not only by a long reflow time and high reflow temperature during soldering, but also by aging, storage, and long term cyclic operation of the electronic assembly at room temperature, including long dwell times during operation or sleep mode at higher temperatures. It is found experimentally that the IMC thickness increases linearly, almost with the square root of aging time (Chan et al. 1997) (Gan and Tu 2002) (Xu et al. 2006).

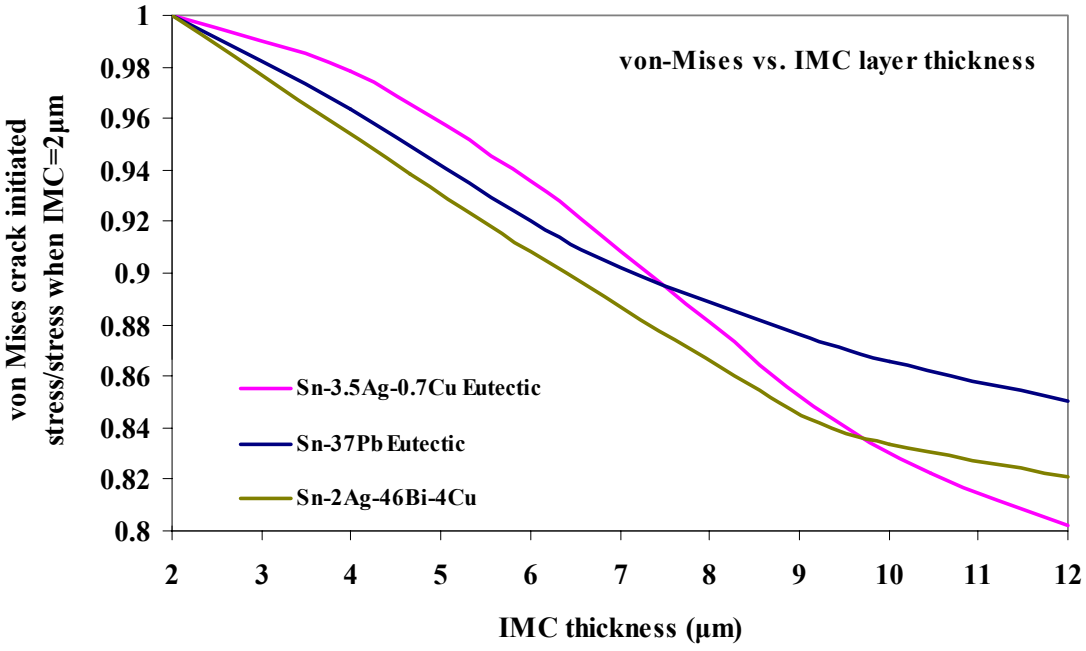

Figure 2.5 Effect of intermetallic layer thickness on crack initiation stress

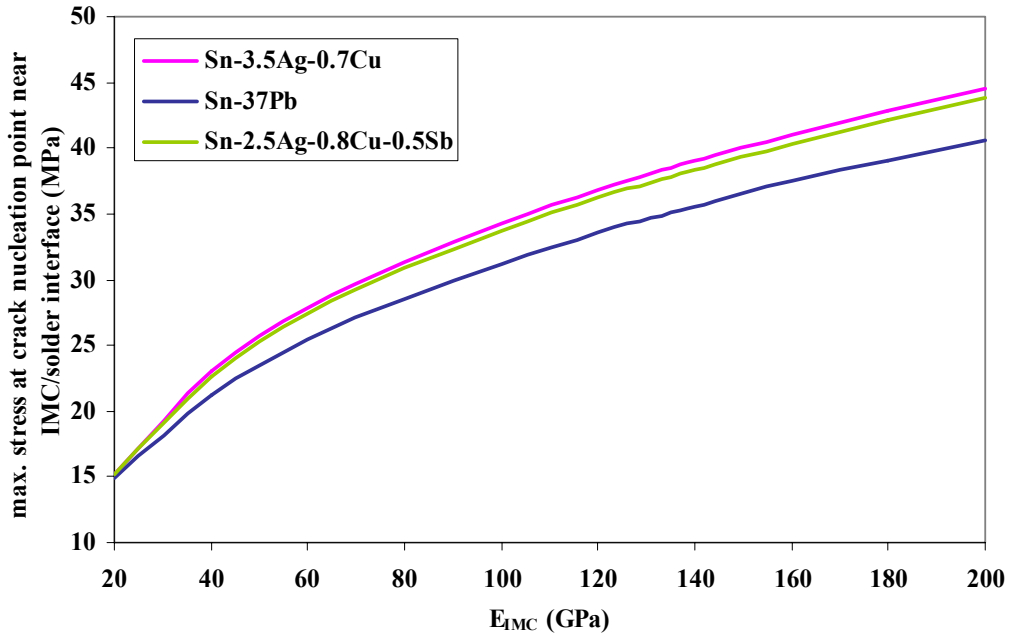

Figure 2.6 IMC Young's modulus effect on maximum von Mises stress at solder/IMC interface (crack nucleation point)

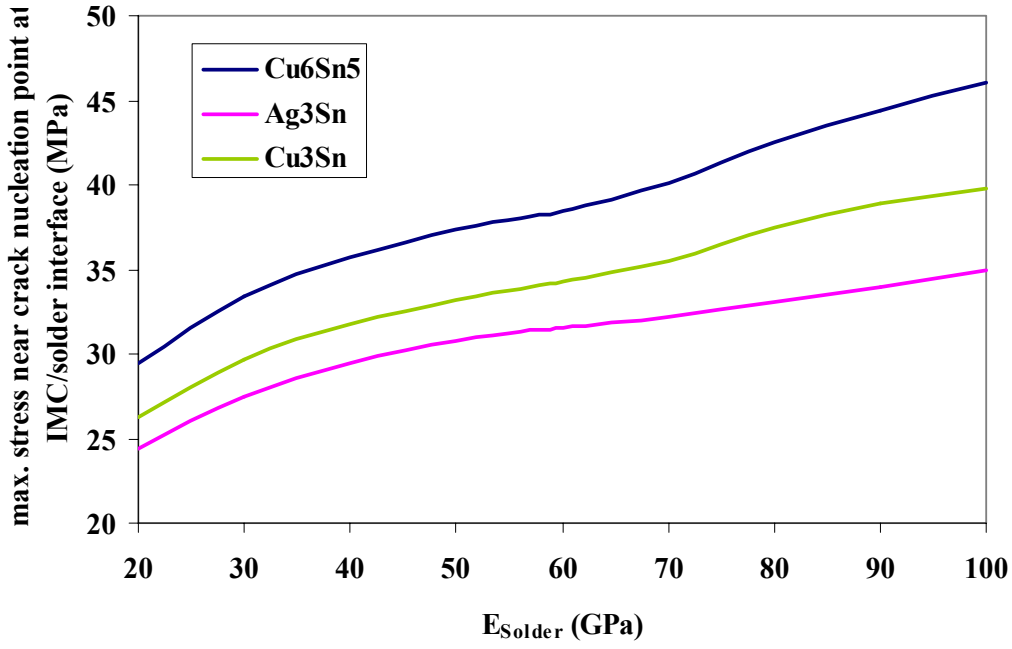

Figure 2.7 Solder Young's modulus effect on maximum von Mises stress at solder/IMC interface (crack nucleation point)

Although some experiments have been performed on IMC growth under thermal aging, limited material properties of IMC are available for use in developing mechanical failure models for IMC failure. Recently, a series of experiments to analyze the electric properties, hardness, and indentation fracture toughness of IMC relevant to electronic packaging has been conducted at Northwestern University (Ghosh 2004). Based on these experimental results, a finite element analysis has been conducted to analyze the effect of IMC thickness upon solder joint failure. Different layer thicknesses of Cu_3Sn and Cu_6Sn_5 are incorporated in the cohesive finite element model, and Fig. 2.5 shows the effects of intermetallic layer thickness on crack initiation stress for three different solders. It is found that the required von Mises stress for a crack to initiate is lower for thicker IMC layers; i.e. it is easier for a crack to initiate with thicker IMC layers. During thermal cycling, failure occurs mainly near the IMC/solder interface, and the lifetime of solder joints decreases with an increase of IMC thickness. The observation matches the experimental observations (Chan et al. 1997) (Gan and Tu 2002) (Xu et al. 2006). Fig. 2.6 and Fig. 2.7 show the IMC and solder Young's modulus effects on the maximum von Mises stress at solder/IMC interface, respectively. It can be seen that with the increase of Young's modulus of IMC or solder, the maximum stress at the solder/IMC interface increase, which will cause crack nucleate. It also shown that lead free solder such as Sn-3.5Ag-0.7Cu and Sn-2.5Ag-0.8Cu-0.5Sb has higher stress than Pb rich solder under the same load condition, which means it is easier for crack to nucleate in Sn-3.5Ag-0.7Cu and Sn-2.5Ag-0.8Cu-0.5Sb eutectic solder than Pb rich solder under the same load condition.

2.5 Coupled Thermo-Electric Analysis to Solder Joint with Crack Propagation near the Interface of Bulk Solder and Intermetallic Layer

Since the failure of solder joint is a coupled thermo-electric-mechanical problem, a thermo-electric analysis is necessary in addition to the mechanical analysis to understand the interconnect failure mechanism. When a crack propagates near the interface between solder and IMC, an important issue affecting solder joint failure is joule heating, which arises when the energy dissipated by an electrical current flowing through a conductor is converted to thermal energy. The effect has been researched experimentally (Alam et al. 2006) (Ye et al. 2003) (Nah et al. 2005) (Liang et al. 2006) (Chiu et al. 2006). However, the joule heating effect on solder joint failure with interfacial crack propagation is still not clear. In this section finite element analysis is conducted to analyze the joule heating and electrical concentration near the crack tip. The thermo-electric coupling arises from two sources: the temperature dependent conductivity in the electrical problem, and the internal heat generated, which is a function of electric current.

The flow of electrical current is described by Ohm's law. Since a potential rise occurs when a charged particle moves against the electrical field, the direction of the gradient is opposite to that of the electric field. Using this definition of the electrical field, Ohm's law is written as:

$$j = \sigma^E \cdot \hat{E} \tag{2.12}$$

Here j is the current density (A/cm^2); $\sigma^E(T, f^\alpha)$ is the electrical conductivity matrix; T is the temperature; and f^α, α = 1, 2…are any predefined field variables. The conductivity can be isotropic, orthotropic, or fully anisotropic. The electrical field intensity $\hat{E}$ can be defined as:

$$\hat{E} = -\frac{\partial \varphi}{\partial x} \tag{2.13}$$

where φ is the electric potential field.

$$\rho j = \hat{E} \tag{2.14}$$

ρ is the resistivity (μΩcm);

From conservation of charge, $\nabla \hat{E} = \nabla^2 \varphi = 0$

The electric field in a conducting material is governed by Maxwell's conservation of charge equation (ABAQUS documentation 6.6.3 2006). Assuming steady-state direct current, the equation is:

$$\int_S \vec{j} \cdot \vec{n} dS = \int_V r_c dV \tag{2.15}$$

where V is any control volume whose surface is S, $\vec{n}$ is the outward normal to S, $\vec{j}$ is the electrical current density (current per unit area), $j = -\vec{j} \cdot \vec{n}$ is the current density entering the control volume across S, and r_c is the internal volumetric current source per unit volume.

The equivalent weak form is obtained by introducing an arbitrary electrical potential field, $\delta\varphi$, and integrating over the volume. Appling the chain rule, divergence theorem and Ohm's law, the governing conservation of charge Eq. (2.15) becomes:

$$-\int_V \frac{\partial \delta\varphi}{\partial \vec{x}} \cdot \tilde{\sigma}^E \cdot \frac{\partial \varphi}{\partial \vec{x}} dV = \int_S \delta\varphi j dS + \int_V \delta\varphi r_c dV \tag{2.16}$$

where $\tilde{\sigma}^E$ is the electrical conductivity matrix.

Based on Eq. (2.16), a coupled thermo-electric finite element analysis is conducted to determine the joule heating effect, temperature concentration and electrical current concentration with a crack propagating near the interface of solder and IMC. The finite element model is used first to predict the average temperature in a solder joint under different applied currents, and the results match well when compared with experiment (Chiu et al. 2006), as shown in Fig. 2.8.

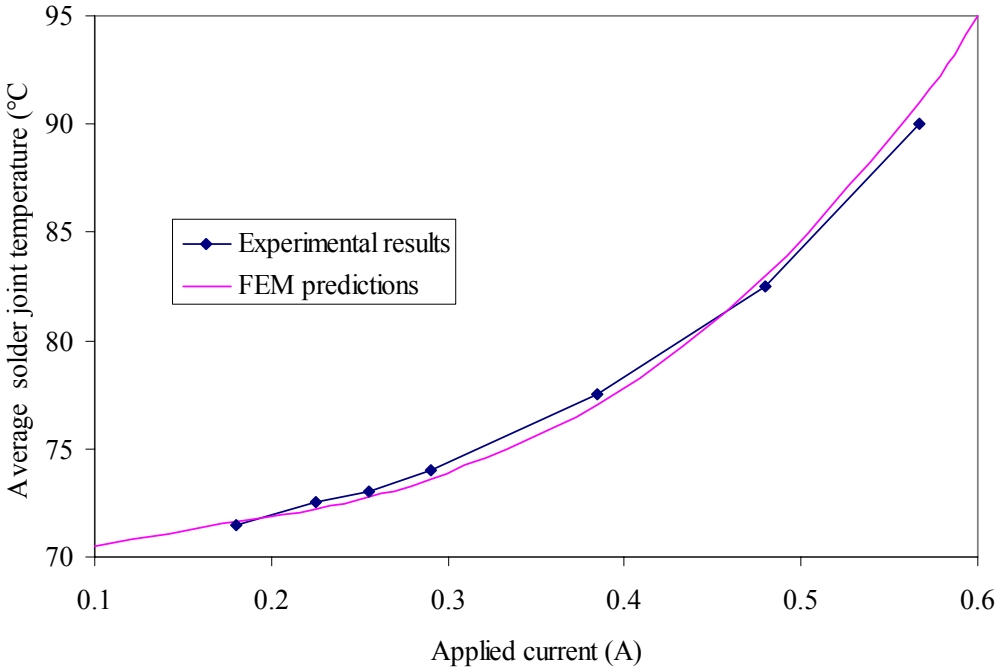

Figure 2.8 Simulation of applied current density versus average temperature in a solder joint

Because of limited experimental data for thermal and electrical properties of solders and IMC materials, Castin™ (Sn-2.5Ag-0.8Cu-0.5Sb) solder is analyzed here. The thermal and electrical properties of solder and IMC materials for Castin™ solder are given in Table 2.3 and 2.4 (NIST database 2002). Fig. 2.9 and 2.10 show the electric current density and temperature distribution of a solder joint with a crack propagating near the interface of solder bulk and IMC

layer. Temperature and current density concentration are observed near the crack tip; it is noted that the current density at the crack tip can be one order of magnitude higher than the average current density in a solder ball, which can induce more thermal energy and higher temperature near the crack tip.

Table 2.3 Thermal and electrical properties of Castin™ solder (Sn-2.5Ag-0.8Cu-0.5Sb) (NIST database 2002)

Melting Point	215 – 217 °C
Thermal Diffusivity	35.82 +/- 0.18 mm^2/s
Specific Heat	218.99 J/(kg.K)
Thermal Conductivity	57.26 W/(m.K)
Electrical Resistivity	12.1 μΩ.cm
Electrical Conductivity	8.25 MS/m

Table 2.4 Pure copper, Tin and Nickel, and their intermetallics: room-temperature physical and thermal properties (NIST database 2002)

Property	Cu	Sn	Cu_6Sn_5	Cu_3Sn
Electrical Resistivity (μΩ·cm)	1.7	11.5	17.5	8.93
Thermal Conductivity (W/m·K)	3.98	0.67	34.1	70.4
Thermal Diffusivity (cm^2/s)	-	-	0.145	0.24
Specific Heat (J/kg·K)	0.385	0.227	286	326
Thermal Expansion ($10^{-6}/K$)	17.1	23	16.3	19.0

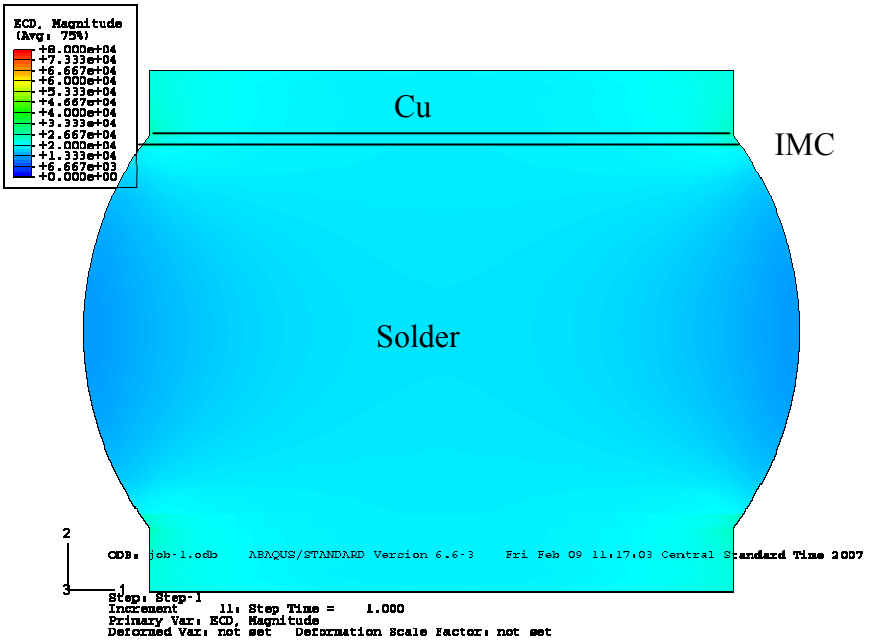

2.9a. current distribution when crack length=0μm

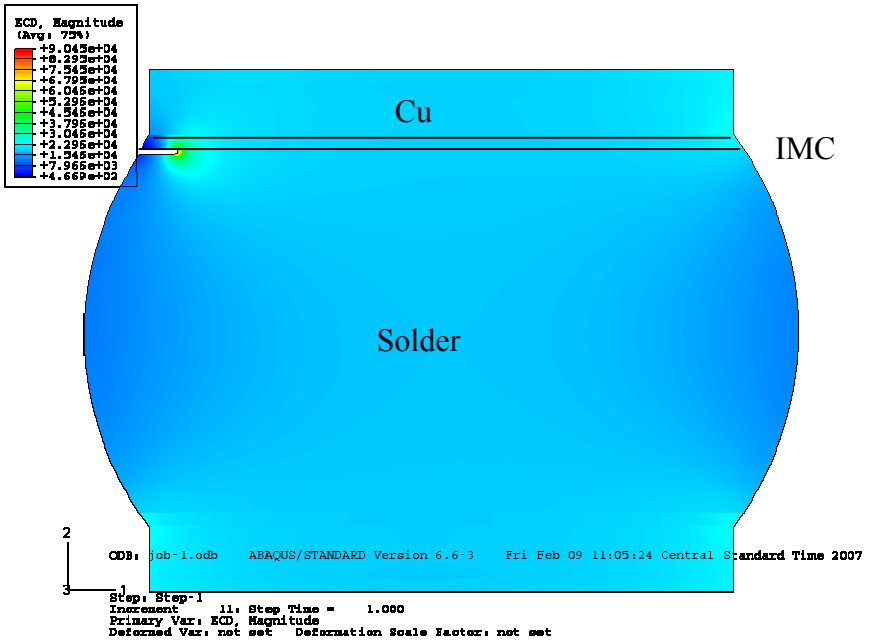

2.9b. current distribution when crack length=5μm

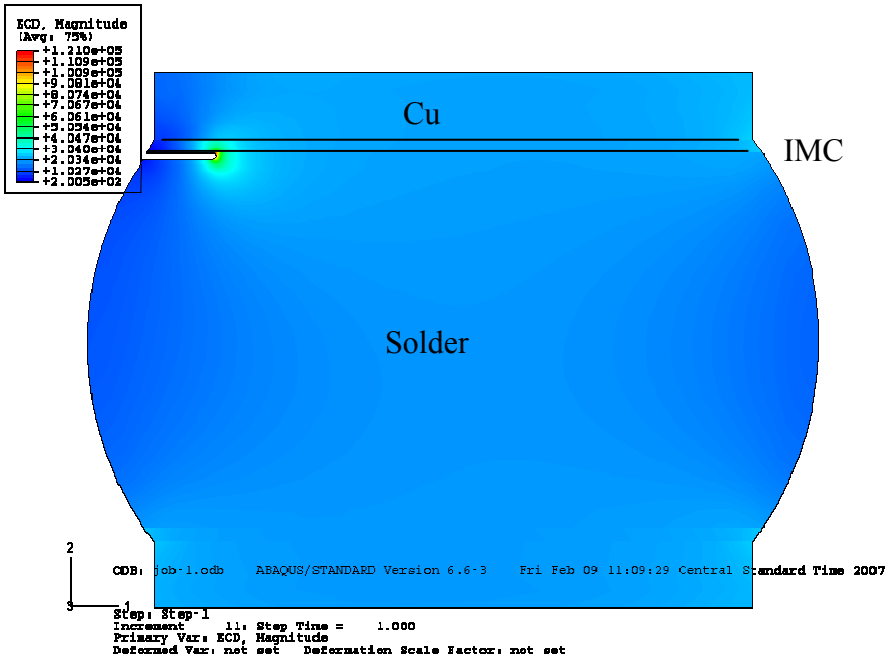

2.9c. current distribution when crack length=10μm

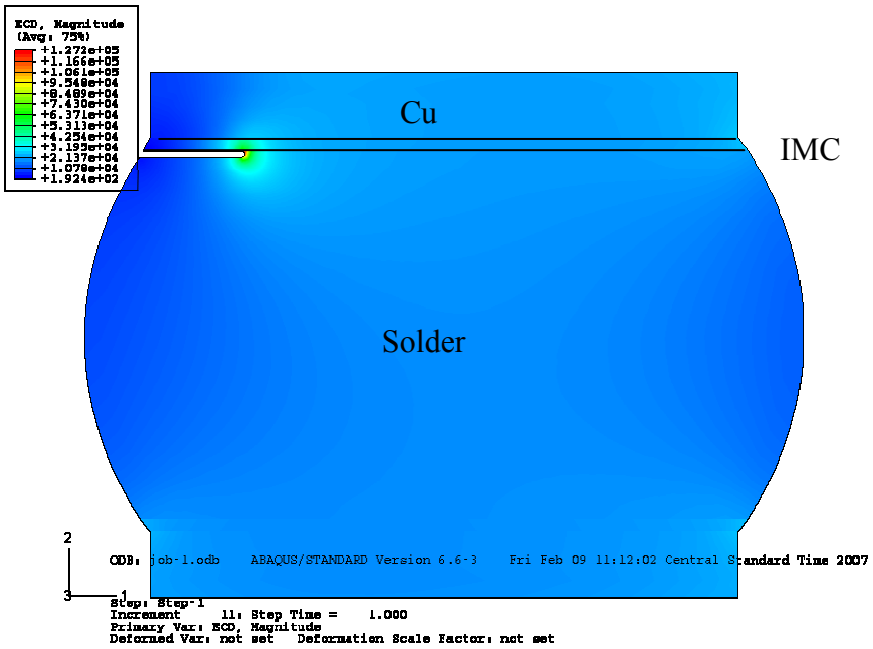

2.9d.current distribution when crack length=15μm

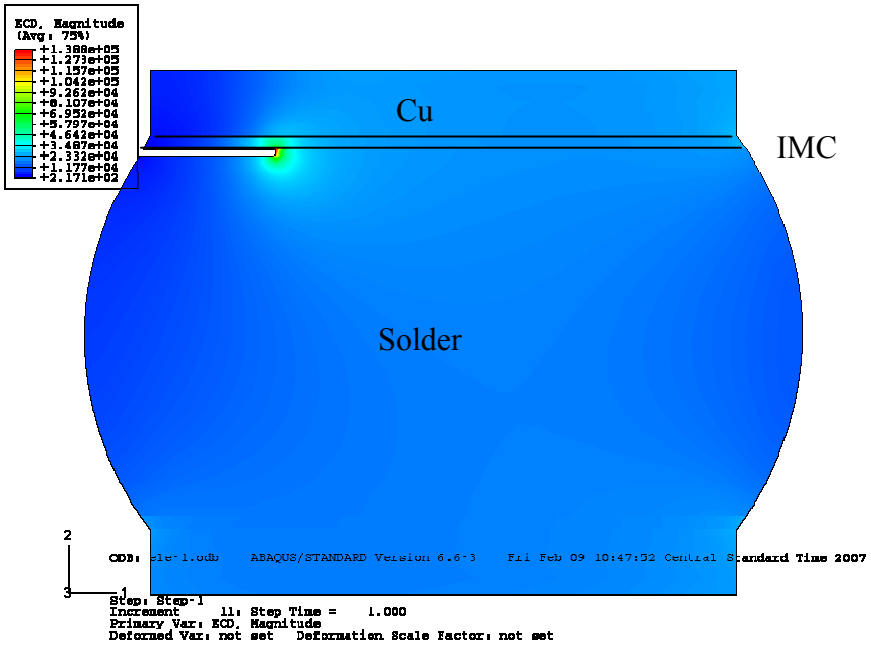

2.9e. current distribution when crack length=20μm

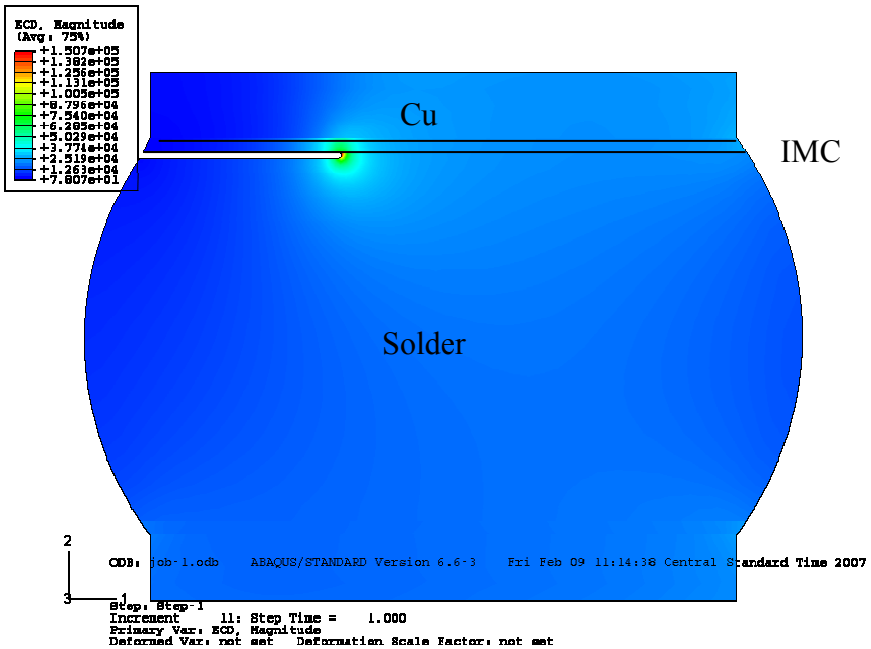

2.9f. current distribution when crack length=30μm

Figure 2.9 Current density distribution in a Sn-2.5Ag-0.8Cu-0.5Sb solder joint under applied current density of 10^4 A/cm^2 with a void propagating near the interface of solder/IMC

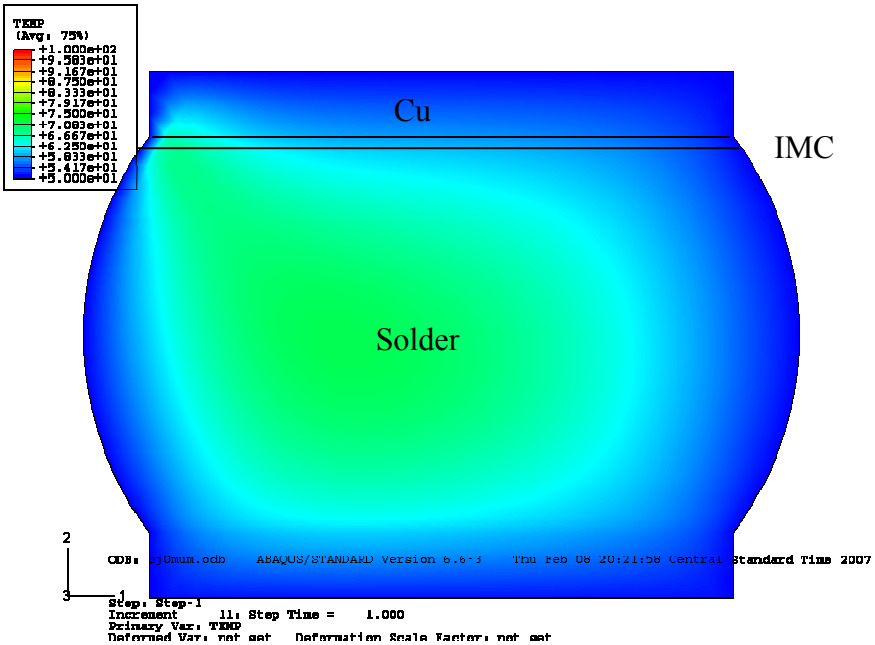

2.10a. temperature distribution when crack length=0μm

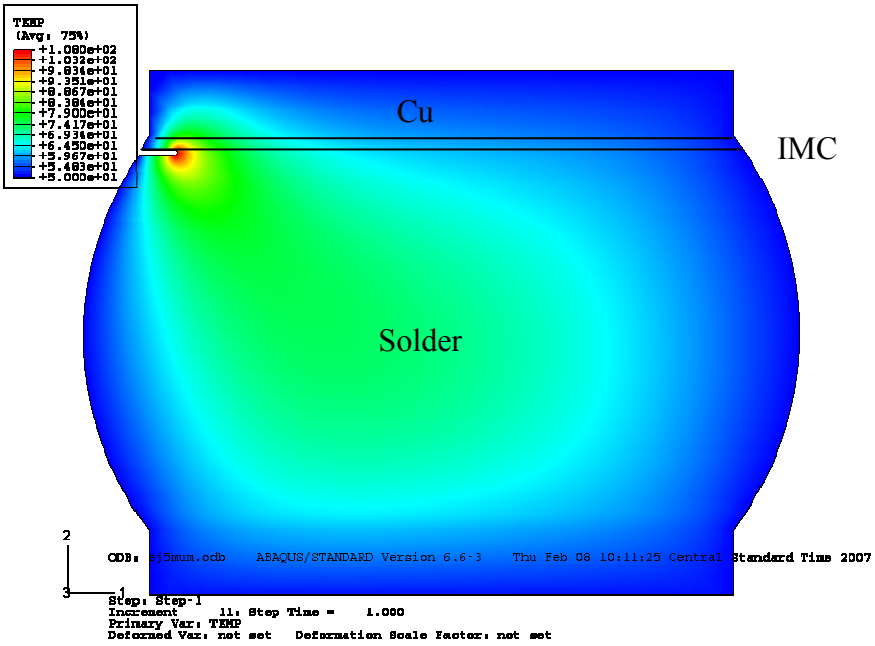

2.10b. temperature distribution when crack length=5μm

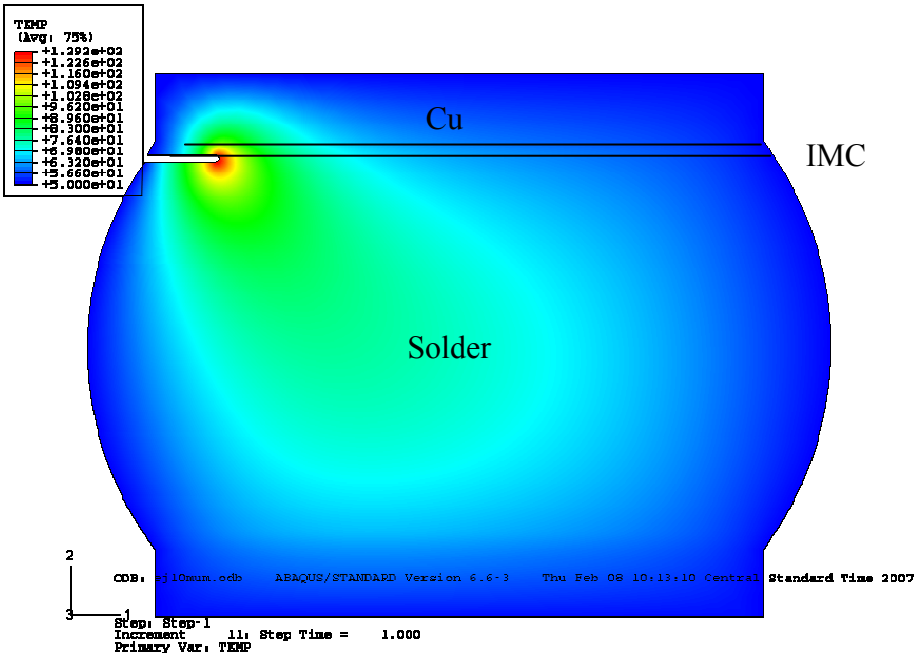

2.10c. temperature distribution when crack length=10μm

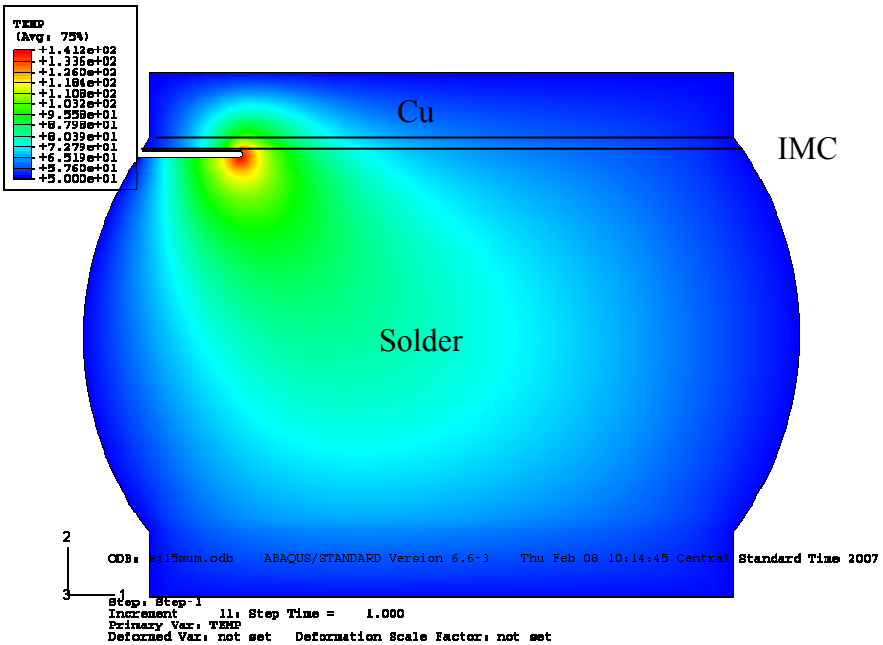

2.10d. temperature distribution when crack length=15μm

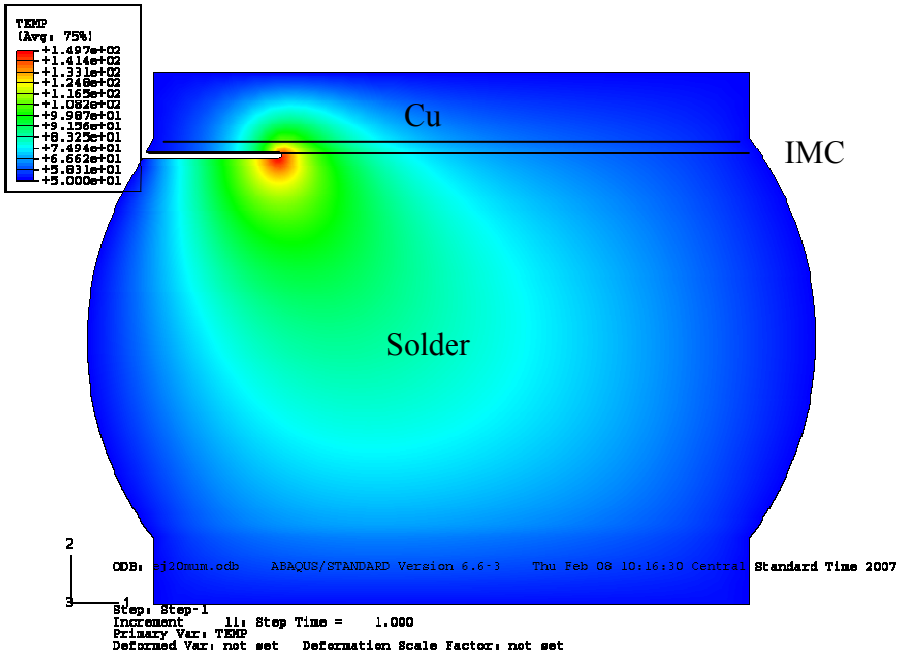

2.10e. temperature distribution when crack length=20μm

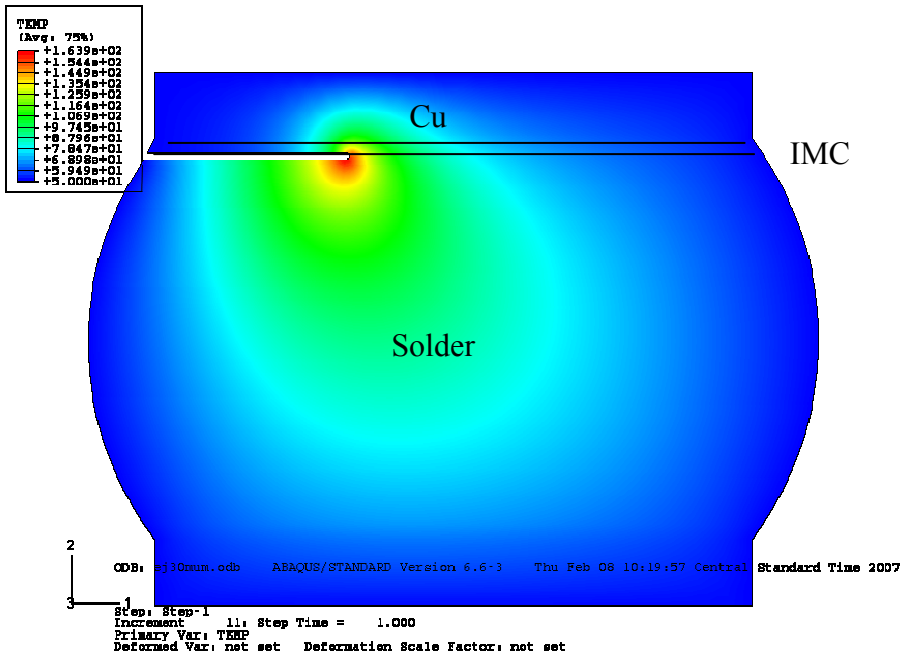

2.10f. temperature distribution when crack length=30μm

Figure 2.10 Temperature distribution in a Sn-2.5Ag-0.8Cu-0.5Sb solder joint under applied current density of 10^4 A/cm^2 with a void propagating near the interface of solder/IMC

Fig. 2.11 shows the crack tip temperature of Sn-2.5Ag-0.8Cu-0.5Sb solder under different current densities. The crack tip temperature increases with the propagation of a crack and may enhance the crack propagation speed and cause circuit failure. For Sn-2.5Ag-0.8Cu-0.5Sb solder, the temperature is found to be caused by joule heating that may melt the material near the crack tip with a current density in the solder ball higher than 5×10^4 A/cm^2.

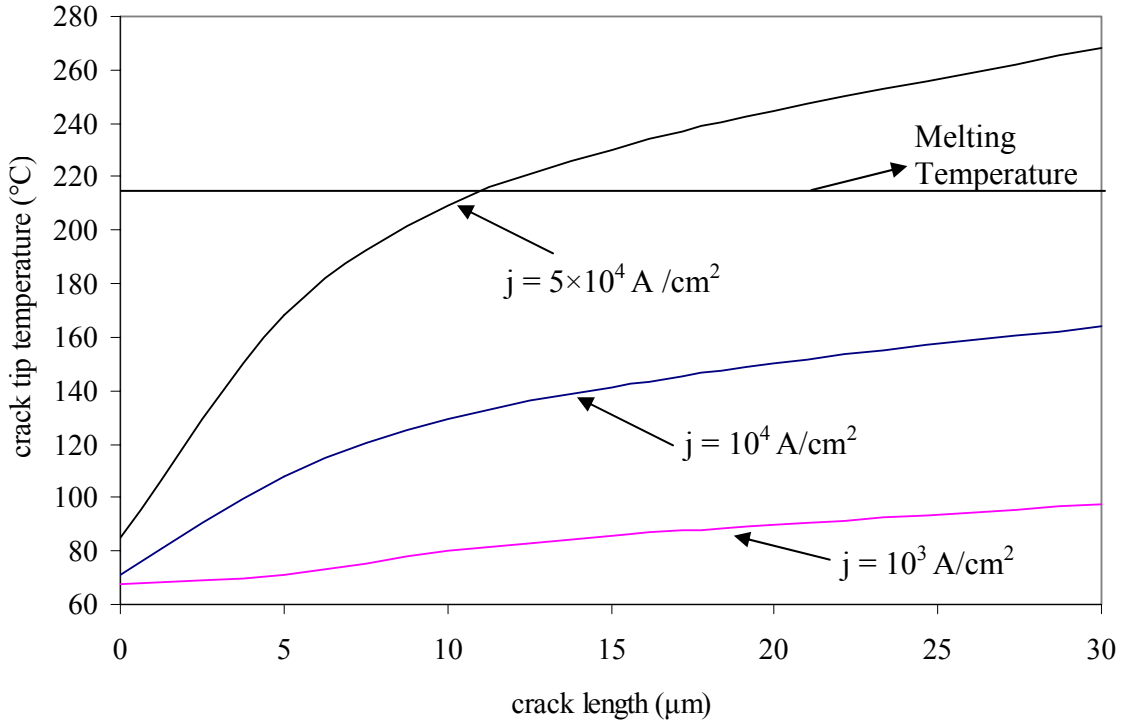

Figure 2.11 Temperature at the crack tip of Sn-2.5Ag-0.8Cu-0.5Sb solder with an interfacial crack propagating under different current densities

In general, the numerical analysis shows that when a crack propagates near the interface of IMC and solder, there is a pronounced temperature and electrical current concentration near the crack tip. Moreover, by comparing with the experimentally measured solder melting

temperature, as given in Fig. 2.12 (NIST database 2002), the concentration of heat at the crack tip caused by joule heating may high enough to melt the solder.

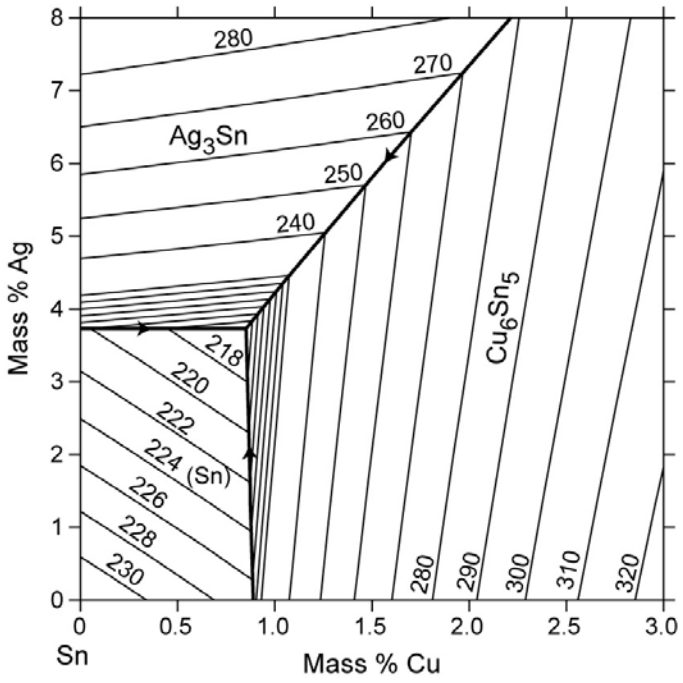

Figure 2.12 Liquidus surface for Ag-Cu-Sn system (NIST database 2002)

2.6 Solder and IMC Thermal and Electrical Conductivities Effects on Crack Tip Temperature

For solder and IMC materials, the thermal and electrical conductivities effects on crack tip temperature are analyzed using the developed finite element model. The crack tip temperatures with respect to different solder and IMC thermal and electrical conductivities for different crack lengths are shown in Fig. 2.13 and Fig. 2.14. In current research, the solder and IMC's thermal conductivity ranges from 10 to 100W/mK, and electrical conductivity ranges from 2 to 20MS/m. The solder joints are under the current density of 10^4 A/cm^2.

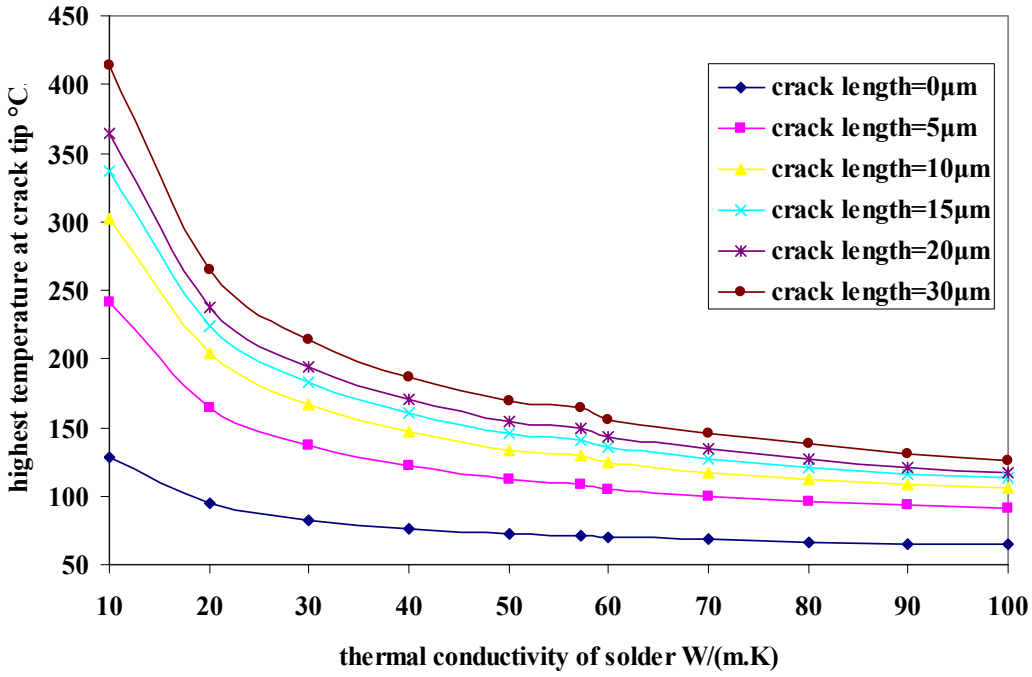

2.13a) Solder TC VS crack tip temperature

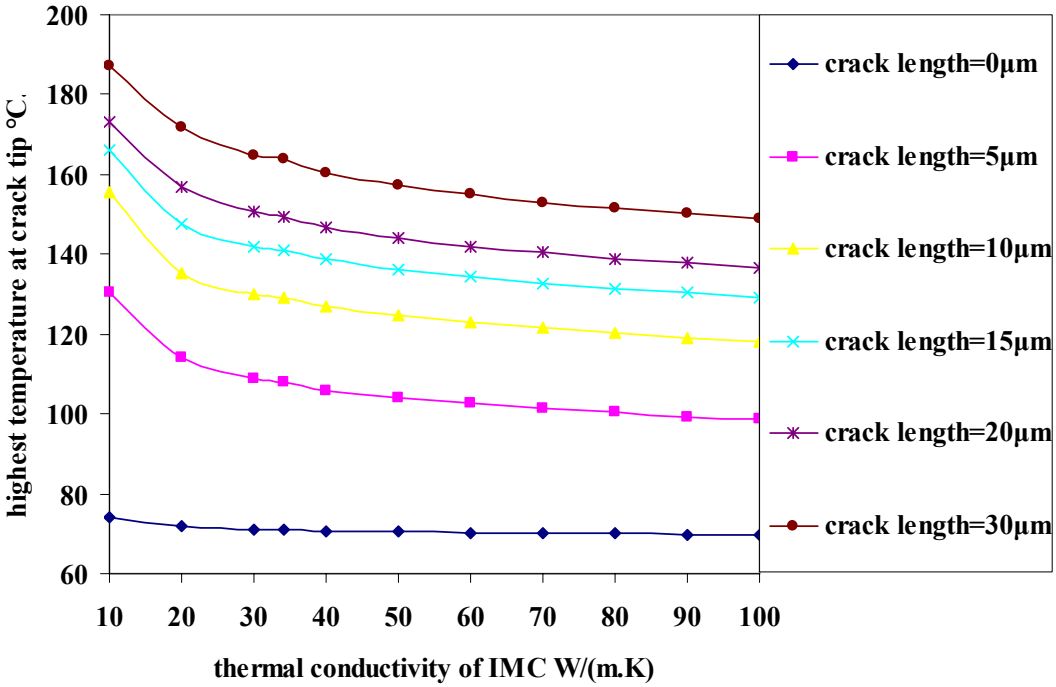

2.13b) IMC TC VS crack tip temperature

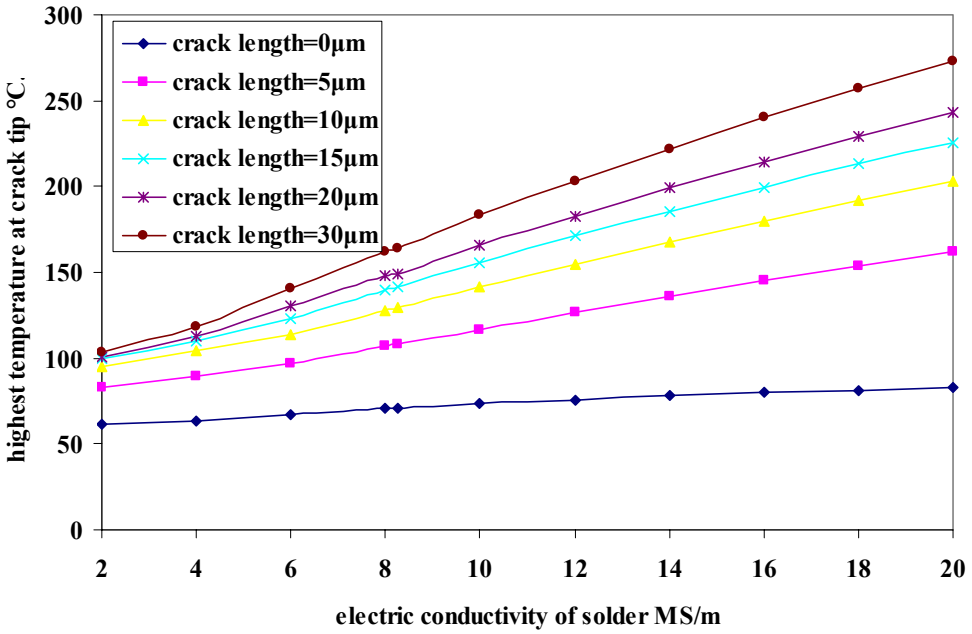

2.13c) Solder EC VS crack tip temperature

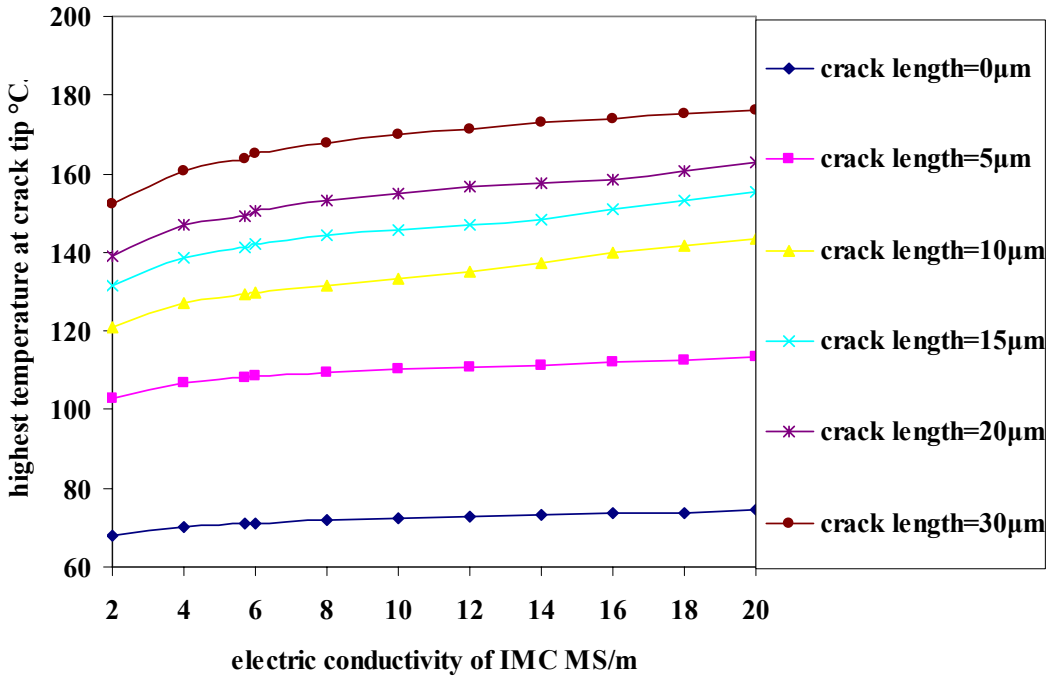

2.13d) IMC EC VS crack tip temperature

Figure 2.13 Solder and IMC thermal and electrical conductivities effects on crack tip temperature for different crack lengths

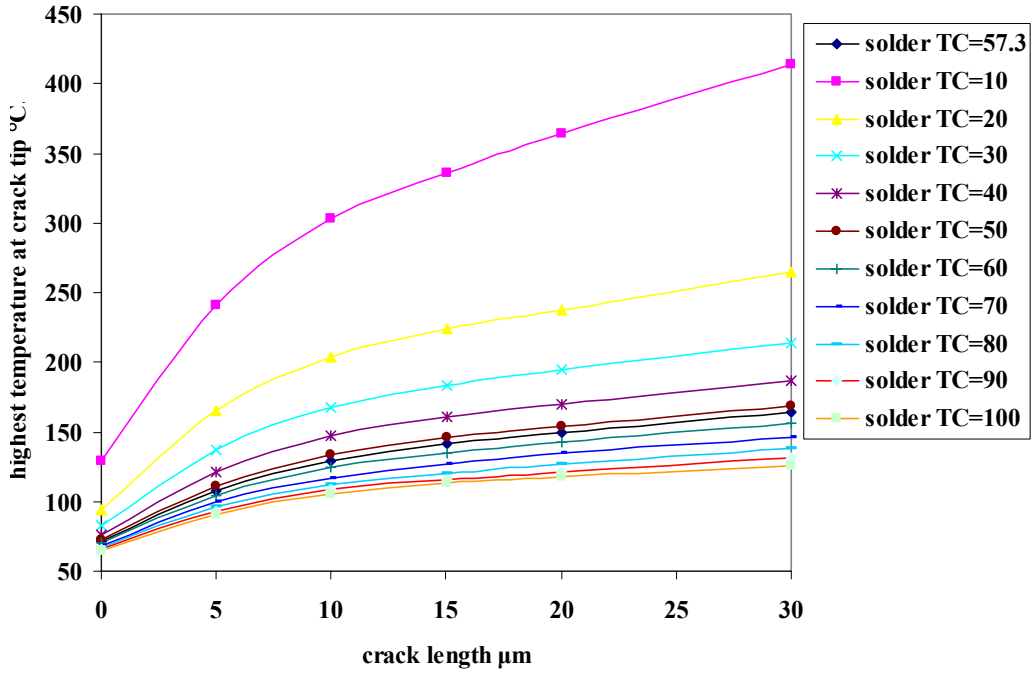

14a) Crack lengths VS crack tip temperature for different Solder TC

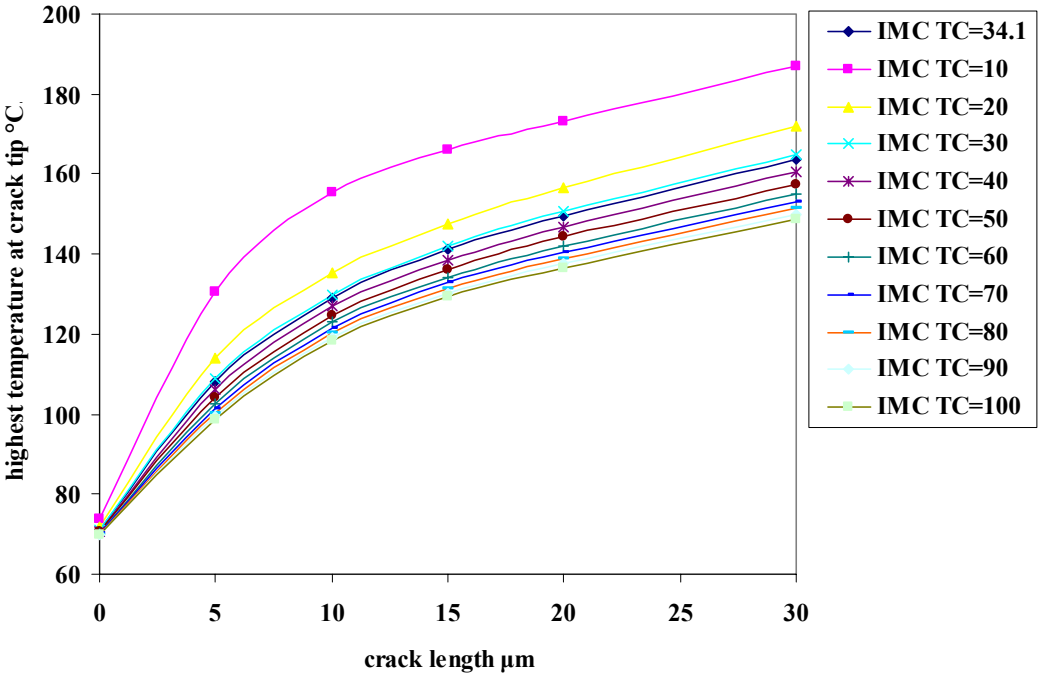

14b) Crack lengths VS crack tip temperature for different IMC TC

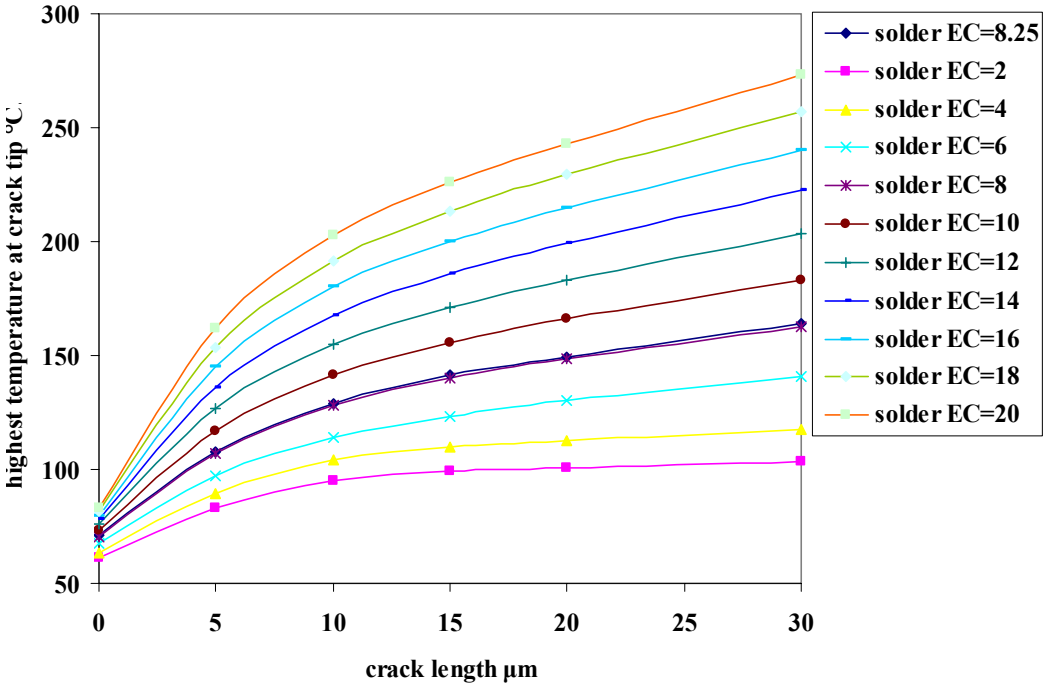

14c) Crack lengths VS crack tip temperature for different Solder EC

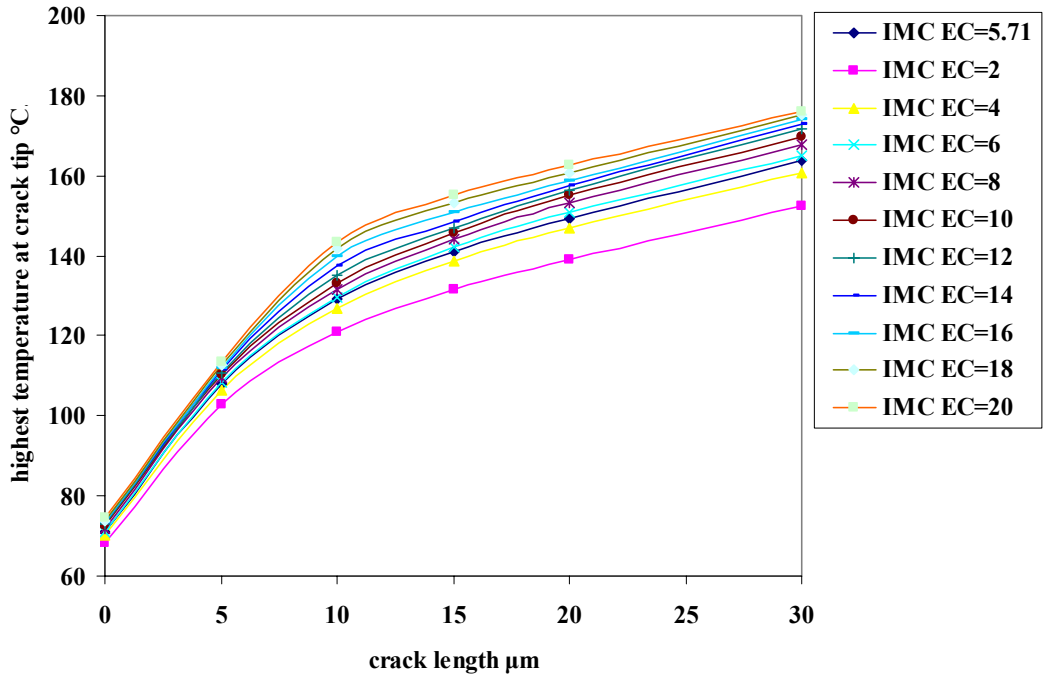

14d) Crack lengths VS crack tip temperature for different IMC EC

Figure 2.14 Solder and IMC thermal and electrical conductivities effects on crack tip temperature with crack propagation predicted using FEM

It is found that the crack tip temperature increases with crack growth. Larger thermal conductivity leads lower crack tip temperature because of better heat dissipation. With larger electrical conductivity, the crack tip temperature is higher because more electrons pass through the cross section. At the initial stage of crack propagation, the slope is larger than that at the later stage of crack propagation, which means crack tip temperature increases faster at the beginning stages of crack propagation. The research is thus focus on initial stages of crack propagation. The importance of the effects on crack tip temperature is found to be: solder's thermal conductivity > solder's electrical conductivity > IMC's thermal conductivity > IMC's electrical conductivity. For solder and IMC materials, thermal conductivities from 20 to 100W/mK can be regarded as a band and crack tip temperature increase consistently with smaller thermal conductivities; however, when solders' thermal conductivity changes from 20 to 10 W/mK, the increase of crack tip temperature will be much serious.

2.7 Wiedemann-Franz-Lorenz Relation for Solder and Intermetallic Materials

Due to the limitation of available experimental data for thermal conductivity of solder and IMC materials, the Wiedemann-Franz-Lorenz (WFL) law is a possible solution to predict thermal conductivity with known electrical conductivity. The thermal and electrical conductivities of Sn and Sn rich solder and intermetallic materials are studied in this section. The WFL law is obeyed well in Sn, however, there is a positive deviation from the theoretical Lorenz number. In metals the WFL law is written as:

$$\kappa = L_0 \sigma T \tag{2.17}$$

For metal and alloy materials, the thermal conductivity mainly consists of two parts:

$$\kappa = \kappa_e + \kappa_l \tag{2.18}$$

κ_e is the electronic conductivity and κ_l is the lattice conductivity. The electrical and thermal conductivities are related by the Wiedemann-Franz-Lorenz law:

$$\kappa = L_e \sigma T + \kappa_l \tag{2.19}$$

where L_e is the Lorenz factor, σ is the electrical conductivity, and T is the absolute temperature.

It is interesting to investigate how well the theory is obeyed for Sn and Sn rich solder alloys. Table 2.5 gives the predicted Lorenz factors for different materials.

Table 2.5a Lorenz factor for different materials (Austin 1942) (NIST database 2002)

Metal	Temp.(K)	EC:$\sigma(10^8/\Omega m)$	σ *T	TC:κ(W/mK)	Lorenz factor
Cu	293	0.588	172.284	398	2.310139
Cu	293	0.588	172.284	393	2.281117
Cu	293	0.588	172.284	401	2.327552
Sn	293	0.087	25.491	67	2.628379
Sn	293	0.087	25.491	73	2.863756
Sn	90	0.294	26.46	82	3.099017
Sn	273	0.0763	20.8299	64	3.072506
Sn	293	0.087	25.491	64	2.51069
Sn	364	0.0549	19.9836	59	2.952421
Sn	449	0.0424	19.0376	59	3.09913
Sn	498	0.0455	22.659	61	2.692087
Ni	293	0.128	37.504	90.5	2.413076
Ni	293	0.147	43.071	92	2.136008
Ni	293	0.147	43.071	91	2.112791
Ag	293	0.625	183.125	418	2.282594
Ag	293	0.625	183.125	429	2.342662
Al	293	0.2326	68.1518	240	3.52155
Cr	293	0.05	14.65	66	4.505119
Au	293	0.4545	133.1685	297	2.230257
Mo	293	0.192	56.256	146	2.595279
Pd	293	0.0926	27.1318	70	2.579998
Pt	293	0.0943	27.6299	71	2.56968
W	293	0.182	53.326	200	3.750516
FeNi	293	0.0217	6.3581	11	1.730077
Kovar	293	0.02	5.86	17	2.901024
Ag-Pd	293	0.05	14.65	150	10.23891
Au-Pt	293	0.0333	9.7569	130	13.3239
Au-20Sn	293	0.0625	18.3125	57	3.112628
Pb-5Sn	293	0.0526	15.4118	63	4.087777
Cu-W(20%Cu)	293	0.4	117.2	248	2.116041
Cu-Mo(20%Cu)	293	0.417	122.181	197	1.612362
IMC					
Cu_6Sn_5	293	0.057	16.701	34.1	2.041794
Cu_3Sn	293	0.112	32.816	70.4	2.145295
Ni_3Sn_4	293	0.035	10.255	19.6	1.911263
Solder					
Sn-2.5Ag-0.8Cu-0.5Sb	293	0.0825	24.1725	57.26	2.368808
Sn-2.8Ag-20.0In	293	0.0588	17.2284	53.5	3.105338
Sn-37Pb(eutectic)	293	0.0685	20.0705	50.9	2.53606
	293	0.069	20.217	50.9	2.517683

Table 2.5b Lorenz factor for different materials (Sorted)

Materials	Absolute Temp.(K)	Elec.Conduc. $\sigma(10^8/\Omega m)$	σ *T	Ther.Conduc. κ(W/mK)	Lorenz factor
Cu-Mo(20%Cu)	293	0.417	122.181	197	1.612362
FeNi	293	0.0217	6.3581	11	1.730077
Ni_3Sn_4	293	0.035	10.255	19.6	1.911263
Cu_6Sn_5	293	0.057	16.701	34.1	2.041794
Ni	293	0.147	43.071	91	2.112791
Cu-W(20%Cu)	293	0.4	117.2	248	2.116041
Ni	293	0.147	43.071	92	2.136008
Cu_3Sn	293	0.112	32.816	70.4	2.145295
Au	293	0.4545	133.1685	297	2.230257
Cu	293	0.588	172.284	393	2.281117
Ag	293	0.625	183.125	418	2.282594
Cu	293	0.588	172.284	398	2.310139
Cu	293	0.588	172.284	401	2.327552
Ag	293	0.625	183.125	429	2.342662
Sn-2.5Ag-0.8Cu-0.5Sb	293	0.0825	24.1725	57.26	2.368808
Ni	293	0.128	37.504	90.5	2.413076
Sn	293	0.087	25.491	64	2.51069
Sn-37Pb(eutectic)	293	0.069	20.217	50.9	2.517683
Sn-37Pb(eutectic)	293	0.0685	20.0705	50.9	2.53606
Pt	293	0.0943	27.6299	71	2.56968
Pd	293	0.0926	27.1318	70	2.579998
Mo	293	0.192	56.256	146	2.595279
Sn	293	0.087	25.491	67	2.628379
Sn	498	0.0455	22.659	61	2.692087
Sn	293	0.087	25.491	73	2.863756
Kovar	293	0.02	5.86	17	2.901024
Sn	364	0.0549	19.9836	59	2.952421
Sn	273	0.0763	20.8299	64	3.072506
Sn	90	0.294	26.46	82	3.099017
Sn	449	0.0424	19.0376	59	3.09913
Sn-2.8Ag-20.0In	293	0.0588	17.2284	53.5	3.105338
Au-20Sn	293	0.0625	18.3125	57	3.112628
Al	293	0.2326	68.1518	240	3.52155
W	293	0.182	53.326	200	3.750516
Pb-5Sn	293	0.0526	15.4118	63	4.087777
Cr	293	0.05	14.65	66	4.505119
Ag-Pd	293	0.05	14.65	150	10.23891
Au-Pt	293	0.0333	9.7569	130	13.3239

Fig. 2.15 shows the distribution of Lorenz factor for different materials. Figure 2.16 to Fig. 2.18 gives the predicted Wiedemann-Franz-Lorenz law for Cu, Ni, Sn, and different solder and IMC materials.

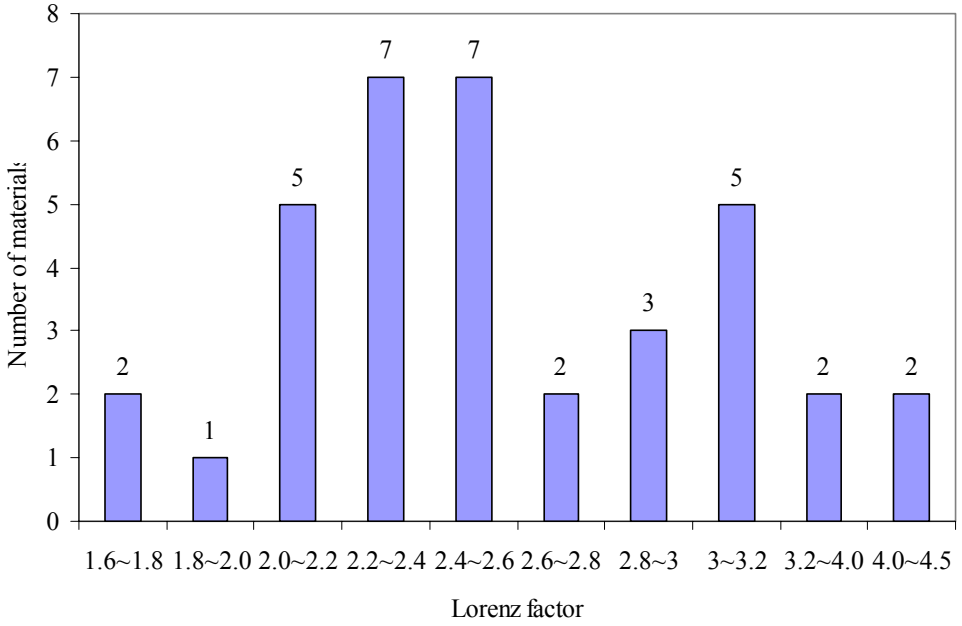

(Including every data point)

Figure 2.15a Distribution of Lorenz factor for different materials

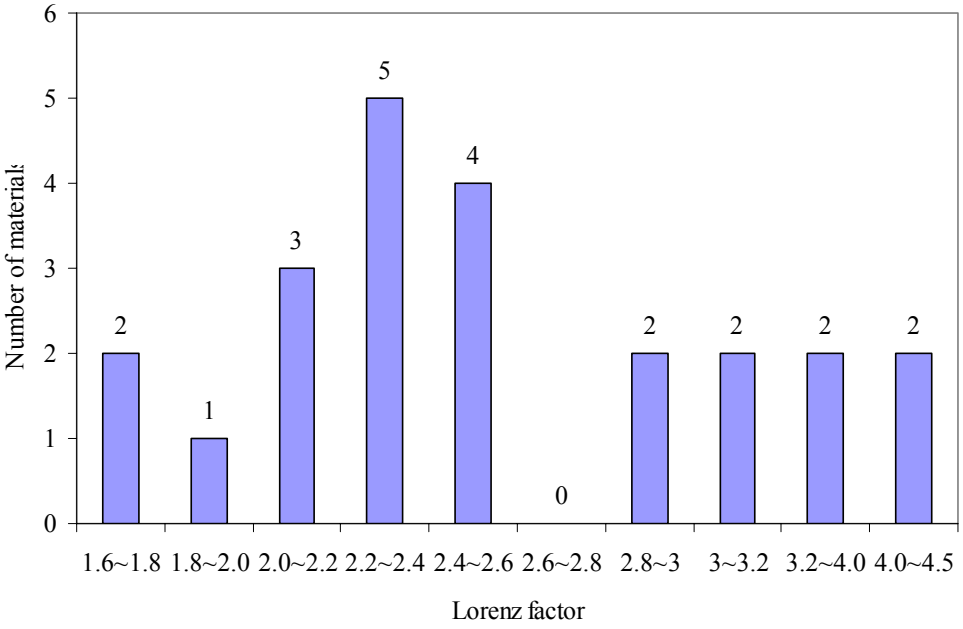

Figure 2.15b Distribution of Lorenz factor for Cu, Sn, Ag, Ni, and Sn-37Pb)

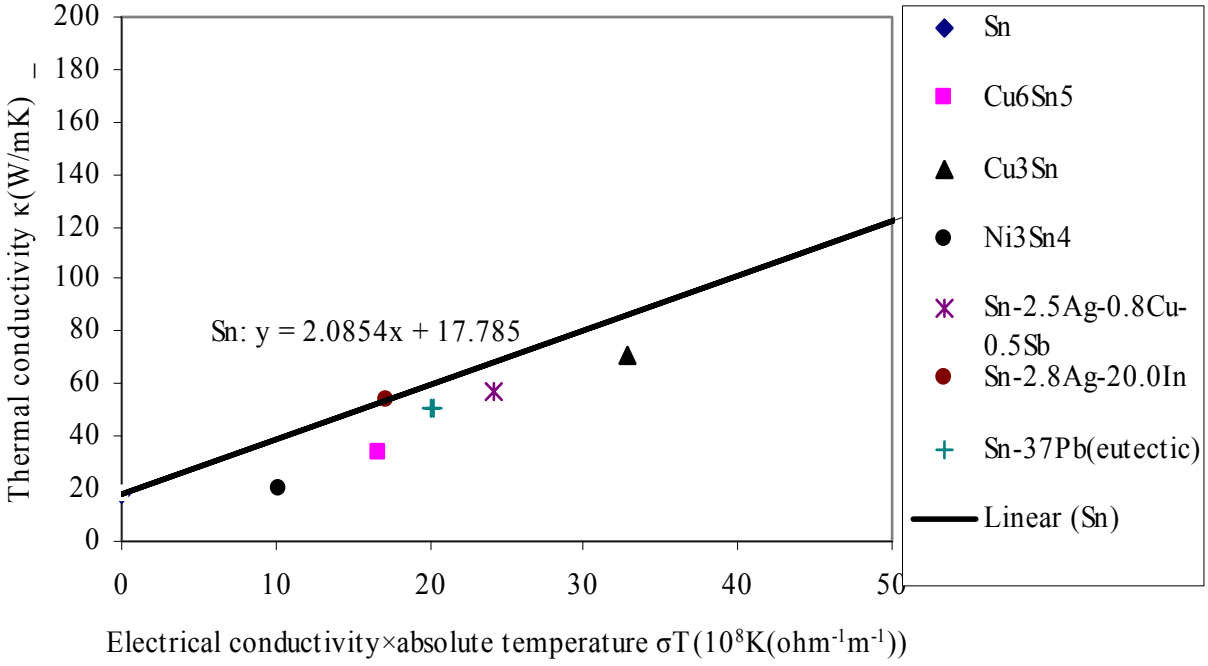

Figure 2.16 WFL law for Sn, IMC, and some solders

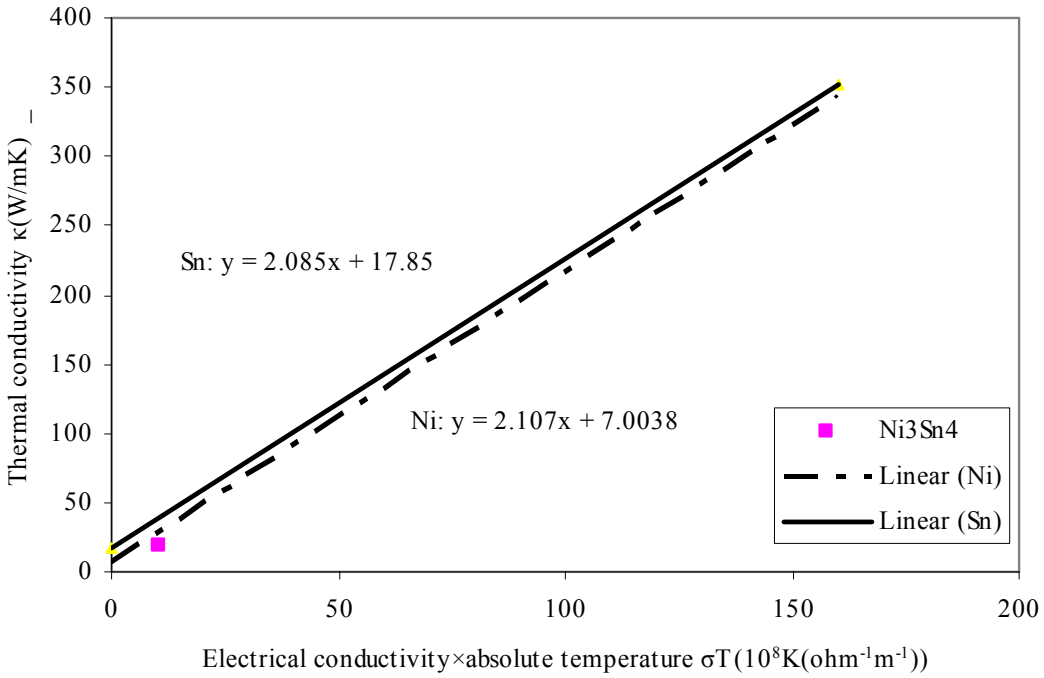

Figure 2.17 WFL law for Sn, Ni, and Ni_3Sn_4

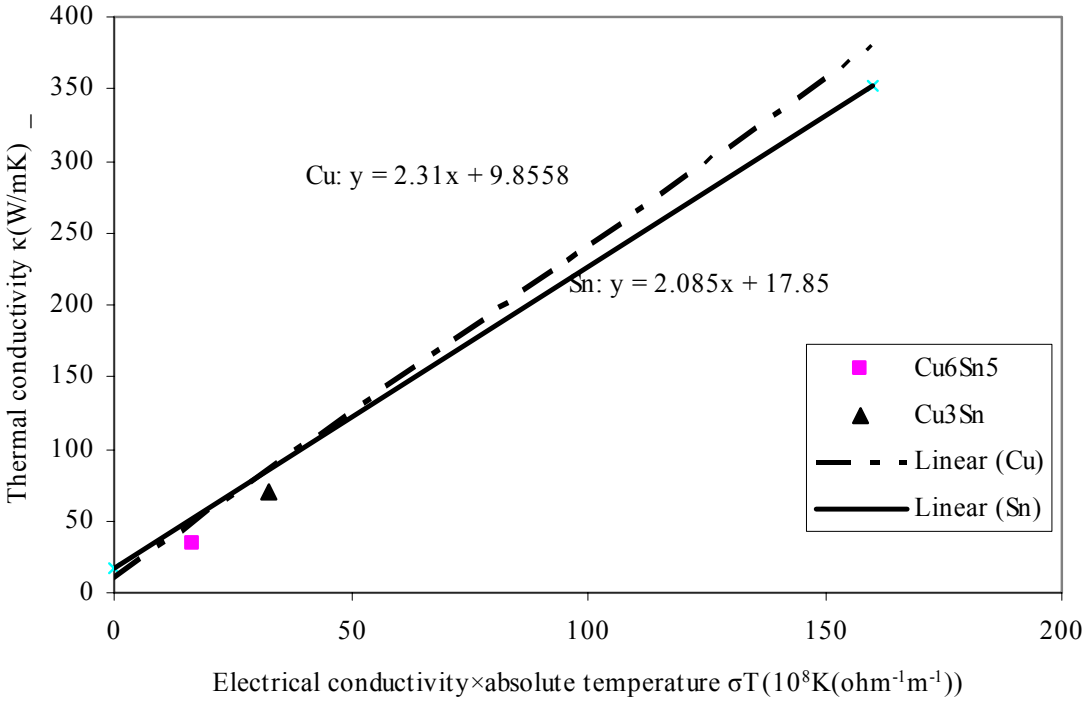

Figure 2.18 WFL law for Sn, Cu Cu_3Sn and Cu_6Sn_5

Table 2.6 Thermal conductivity predicted using WFL law of Sn for different materials

IMC	WFL (Sn) predicted TC (W/mK)	TC measured from experiment (W/mK)	Factor of prediction
Cu_6Sn_5	52.61327	34.1	1.5
Cu_3Sn	86.21949	70.4	1.2
Ni_3Sn_4	39.17078	19.6	2
Solder			
Sn-2.5Ag-0.8Cu-0.5Sb	68.19433	57.26	1.2
Sn-2.8Ag-20.0In	53.71311	53.5	1.0
Sn-37Pb(eutectic)	59.64002	50.9	1.2

Table 2.6 shows the thermal conductivities predicted using WFL law of Sn for different materials. Generally, the analysis to the experimental data shows that the Wiedemann-Franz-Lorenz law is obeyed in both solder alloy and intermetallic materials especially matches close to

the law for Sn. Thus, with the available electrical conductivity data, which is more easily measured, the thermal conductivity can be obtained based on the Wiedemann-Franz-Lorenz law.

2.8 Conclusion

It has been experimentally observed that solder joints fail near the IMC/solder interface. A 3D computational model based on cohesive fracture and continuum mechanics has been developed to predict the crack initiation and propagation near the IMC/solder interface. The traction-separation law of a cohesive element at interface is applied in the finite element program, ABAQUS; UCP theory is incorporated in the model to simulate the creep-plastic solder behavior. A numerical analysis of IMC related solder joint failure has been conducted. The cohesive-UCP finite element model is applied to analyze the effect of IMC layer thickness on solder joint failure. The growth of IMC layer thickness has a significant effect on solder joint crack initiation. The von Mises stress required to initiate a crack is found lower for a thicker IMC layer and the solder joint lifetime decreases with increasing IMC layer thickness. A coupled thermo-electric numerical analysis has been conducted. The electrical concentration and joule heating effects are found to play important roles on solder joint failure, especially when a crack propagates near the interface of IMC and solder. The temperature and electric current density distribution in Sn-2.5Ag-0.8Cu-0.5Sb solder under different applied currents has been predicted. Pronounced temperature and electrical current concentration was found near the crack tip. Although the lead-free solders usually have higher melting temperatures as compared with lead-rich solder, the concentration of heat at the crack tip caused by joule heating may still melt the solder material under a high current density, which will enhance the propagation of crack and cause a circuit failure. The effect of thermal and electrical conductivity of solder and IMC on

crack tip temperature are analyzed using the proposed finite element model. The Wiedemann-Franz-Lorenz (WFL) law is found to be well obeyed in IMC and solder alloys, which can save big amount of experimental work to determined thermal conductivity for solder and IMC materials.

Chapter 3

Phase Transformation Theory Applied to Predict Fatigue Crack Propagation

Mechanical deformation of a solid during fatigue cycling is broadly defined a phase transformation, because defects are produced that increase its internal energy. Change in the defect structure, crack initiation and growth are also examples of phase transformations. Many of the concepts of phase transformation theory are applicable to fatigue crack nucleation and propagation. Phase transformation theory was applied to penny-shaped crack nucleation in interconnects in previous research (Fine et al. 1999, 2000). The physical meaning of fatigue crack nucleation in solid materials was previously studied by Fine et al. (2000) using energy considerations. This chapter extended the treatment to fatigue crack propagation. Phase transformation theory is applied to predict the fatigue crack propagation rate in metals, alloys, and solder materials. The fatigue crack propagation rates predicted is compared with experimental data for different steels, aluminum alloys, and solder materials to demonstrate that the prediction of the theory agrees reasonably well with experimental results. The theory is applicable to predict fatigue crack propagation in interconnects under cyclic loading with corresponding experimental data for different solder and intermetallics.

Fatigue experiments were carried out on plastic ball grid array (PBGA) solder interconnects at Northwestern University by B. Fiedler, which prove the applicability of the

proposed theory on interconnect failure. Fatigue experiments on Sn-3.5Ag solder alloys were conducted at Northwestern University by S. Vaynman. With the stress intensity factor range determined from numerical analysis, the effect of stress intensity factor range on fatigue crack propagation is discussed. The relationship between stress intensity factor range and crack propagation rate is obtained.

Solder alloys operate at high homologous temperatures, usually around 50% of their melting temperatures, and thus combined creep and plasticity effects play important roles in interconnect failure and need to be considered in the analysis. The 3D cohesive-UCP finite element interconnect model developed in Chapter 2 is used to predict the required energy U to increase the crack by a unit area. With U determined numerically, the predicted fatigue crack propagation rate using phase transformation theory is compared with available experimental data for Sn-3.5Ag and 63Sn-37Pb eutectic solder eutectic solder. Reasonable agreement between theoretical predictions and experimental results is obtained.

3.1 Introduction

The continuing reduction in size of electronic device interconnects and the switch to lead-free solders moves fatigue failure prediction for these interconnects into the zone of insufficient data and experience. Previously, empirical approaches based on many years of experience were highly successful, but now a better scientific understanding of the fatigue failure processes is needed to assure reliability with minimum experimentation. The present research is undertaken with the above in mind, and the results are applicable to solders and intermetallics and the interfaces between them in the interconnect.

Over the years research has been conducted on predicting fatigue crack nucleation, propagation, and structural life under cyclic loading for different materials both theoretically (Rice 1967; Weertman 1973; Ellyin 1997; Huang et al. 1997; Paris 1998; McDowell 1999; Ritchie 1999; Yi et al. 1999; Laz et al. 2001; Deshpande and Needleman 2002; Klingbeil and Nathan 2003) and experimentally (Lang and Larsen 1999; Harlow and Wei 1999; Mars and Fatemi 2003; Korhonen et al. 2004; Soboyejo et al. 2004). However, the fundamental physical meaning of fatigue crack nucleation and propagation is still not resolved and requires further research. Mura and co-workers showed that the initial fatigue crack formation is a nucleation process as there is an energy barrier to the formation of a fatigue crack (Funabashi et al. 1978; Lin et al. 1986). As in Griffith's theory for fracture of brittle solids, the energy barrier is due to the energy required to create new surfaces. The energy release on crack formation is due to release of elastic energy from the applied load and loss of lattice defects at the nucleation site. The model of Mura et al. (Mura and Lin 1974; Kwon et al. 1988; Mura 1994) is a two dimensional one, where the crack is modeled as a line. In the model dislocation dipoles are assumed to accumulate along closely spaced parallel slip bands during fatigue cycling and are emitted or lost when the energy of the accumulation reaches the critical value, ΔW, versus cycle number N given by a maximum in the curve of the work to form a crack. At this value of $\Delta W = \Delta W^*$, a fatigue crack spontaneously nucleates. Mura's theory used the dislocation dipole accumulation model to give a ΔW vs. N relation and then finds the maximum by setting $d\Delta W/dN$ equal to zero and solving for N_i, the critical number of cycles to crack initiation.

By extending Mura's ideas, a thermodynamic approach to predict fatigue crack nucleation was developed by Fine et al. (Izumi et al. 1981; Fine 2000). In their method, the

increase in internal energy from damage accumulation was theoretically investigated. Thermally assisted fatigue crack nucleation was treated and applied to the kinetics of fatigue crack nucleation for a Sn-Pb eutectic solder. The melting temperature is 183 °C (456 K). The operating temperature of interconnects is about 0.7 of the absolute melting temperature and thermal activation is expected to play an important role in the nucleation kinetics. The intermetallic layer between the solder and the chip or chip carrier will have a much higher melting temperature and thermal activation plays a smaller role. The η phase in the Sn-Cu system, for example, melts at 415 °C, while Sn_4Ni_3 melts at 795 °C.

The elastic contribution for penny-shaped cracks was expanded to three dimensions and fatigue at elevated temperatures was treated to include thermal activation as well as accumulation of defects. This approach was applied to fatigue of Sn-Pb eutectic solder at room and elevated temperatures. At high homologous temperatures such as for this solder at room temperature, recovery reduces the dislocation pile up rate so that after some initial cycling a steady state dislocation structure at the maximum stress in the cycle was assumed to be established, which may result in a constant rate of crack nucleation. The dislocation energy released on crack formation was assumed constant with cycling due to recovery, and the differentiation was carried out with respect to a, the radius of the virtual crack, where $d\Delta W/da = 0$ yielded the critical crack radius, a^*. Reaction rate theory was then used to determine the crack nucleation rate assisted by thermal energy, i.e., energy from thermal vibrations of the atoms. The cracks that form on fatigue of Sn-Pb eutectic solder are on interfaces.

Based on Fine's theory, the increase in internal energy from damage accumulation is a measurable quantity that can be theoretically investigated. Thermally assisted fatigue crack nucleation was treated and applied to the kinetics of fatigue crack nucleation in tin-lead eutectic

solder. Recently, the theory has been extended to lower temperatures where thermal activation is smaller and shows reasonable accuracy compared with experimental data (Bhat and Fine 2001). The proposed phase transformation theory is applied to predict fatigue crack propagation in this chapter combined with fracture mechanics from energy considerations. Fatigue cracking in the broad sense is regarded as a phase transformation in that there is a reduction in internal energy on fatigue cracking. The theoretical crack propagation work presented in this chapter is based on extensive experimental work on fatigue of metals and solder alloys. The objective of present research is to find a science based equation including measurable quantities related to microstructural processes occurring in the material during fatigue. The predictions are compared with experimental data of different steels and aluminum alloys.

Motivated by the experimental observations on fatigue failure of interconnects, this chapter applied the phase transformation theory to interconnects. The required energy U to propagate a unit crack area in solder is determined from numerical analysis, and a 3D finite element model has been developed to simulate the behavior of an interconnect under cyclic loading. The unified creep and plasticity (UCP) theory and cohesive zone model (CZM) are incorporated in the finite element model as introduced in chapter 2 to predict the hysteresis effect and interfacial behavior of solder, respectively. The prediction of fatigue crack propagation rate for 63Sn-37Pb and Sn-3.5Ag eutectic solder is compared with experimental data. The theory can be applied to predict fatigue crack propagation for various Pb-rich or Pb-free solders under cyclic stress if the needed parameters for solder and intermetallics are provided.

The chapter starts with experimental observation on solder failure and follows with a discussion of crack nucleation and propagation.

3.2 Experimental Observations and Numerical Analysis on Solder Interconnects Failure at Northwestern University (Experiments Conducted by B. Fiedler, 2007)

Experiments were conducted by B. Fiedler in 2007 at Northwestern University (Fiedler et al. 2007), the experiments physically support the application of phase transformation theory to solder interconnect. In his experiments, observation of the phase transformation theory was carried out in modern plastic ball-grid-array (PBGA) lead free solder interconnects. Fig. 3.1a shows a diagram of a cross-section of the joints used in his work. Solder balls nominally 600 μm in diameter with a 1.0mm pitch were reflowed onto 300 μm Cu pads with an electroless nickel-gold (ENIG) surface finish. The average joint height after reflow was 500 μm and the glass-epoxy laminate is 1.5mm thick. The specimens were made up of 288 solder joints daisy-chained together in series, set up on a 23 mm square as shown in Fig. 3.1b. These components were made by Practical Components of Los Alamitos, CA and assembled by Lace Technologies in St. Charles, IL.

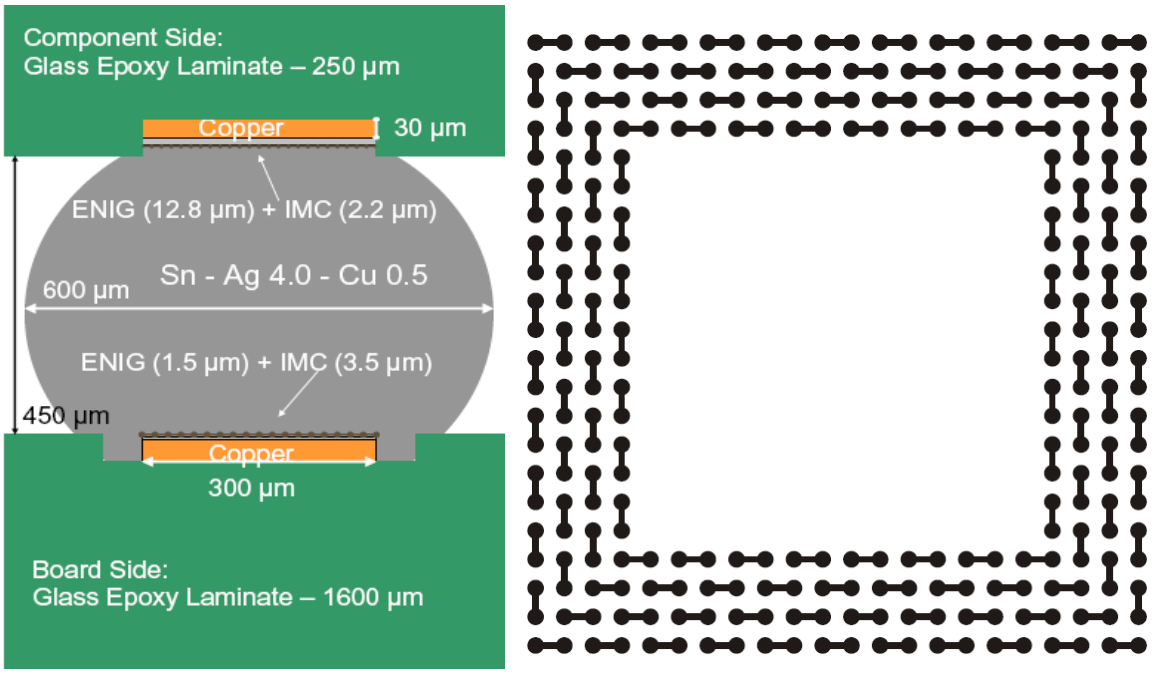

Figure 3.1 (a) cross-section diagram of specimens used in monotonic and cyclic loading tests for this study; (b) the arrangement of 288 interconnects on 23mm square surface
Notes: Adjoining lines represent Cu connecting paths used to daisy chain the component. The printed circuit board (PCB) has complementary Cu connections. (B. Fiedler, 2007)

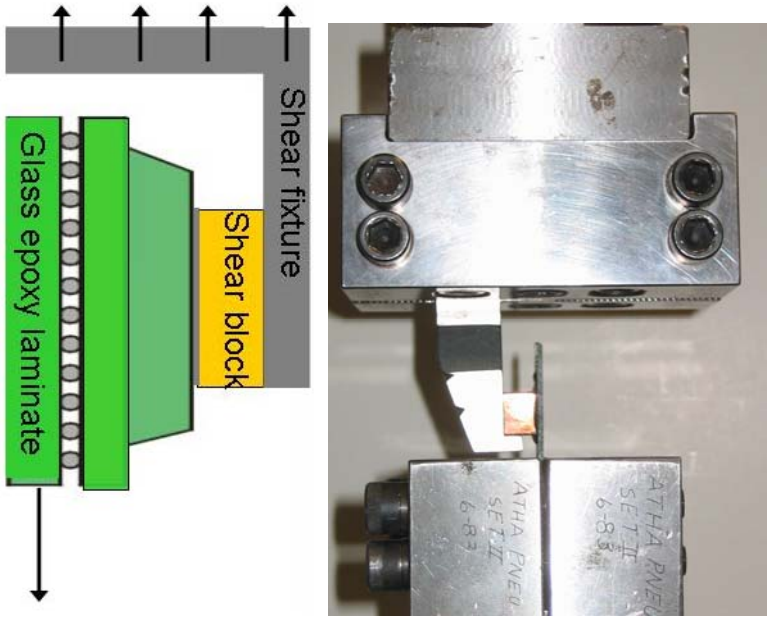

Figure 3.2 Test fixtures for mode II loading in fatigue and monotonic shear tests (B. Fiedler, 2007)

Low-cycle, mechanical fatigue experiments were carried out on a MTS 810 hydraulically actuated testing system. The experiments were displacement controlled with cycle limits set from 5-50 µm, which corresponds to a strain range of 0.01 to 0.10. A cycle frequency of 0.1 Hz was used which linearly strained the samples at a rate of 0.018 /s. The rigid grips of the MTS810 were aligned to within ± 0.1 mrad (0.6 °) to maximize mode II loading. The glass-epoxy laminate was directly secured on one side and on the other, a brass block was glued to the surface, then fastened into a fixture designed to eliminate the bending moment, as shown in Fig. 3.2. Monotonic shear and tensile tests were also conducted on an MTS model Sintech 20g electromechanical unit. The purpose was to compare fracture surfaces between static and dynamic loading conditions. A similar setup to that shown in Fig. 3.2 was used, only a different machine was used. The strain rate used for monotonic tests was 0.002 /s.

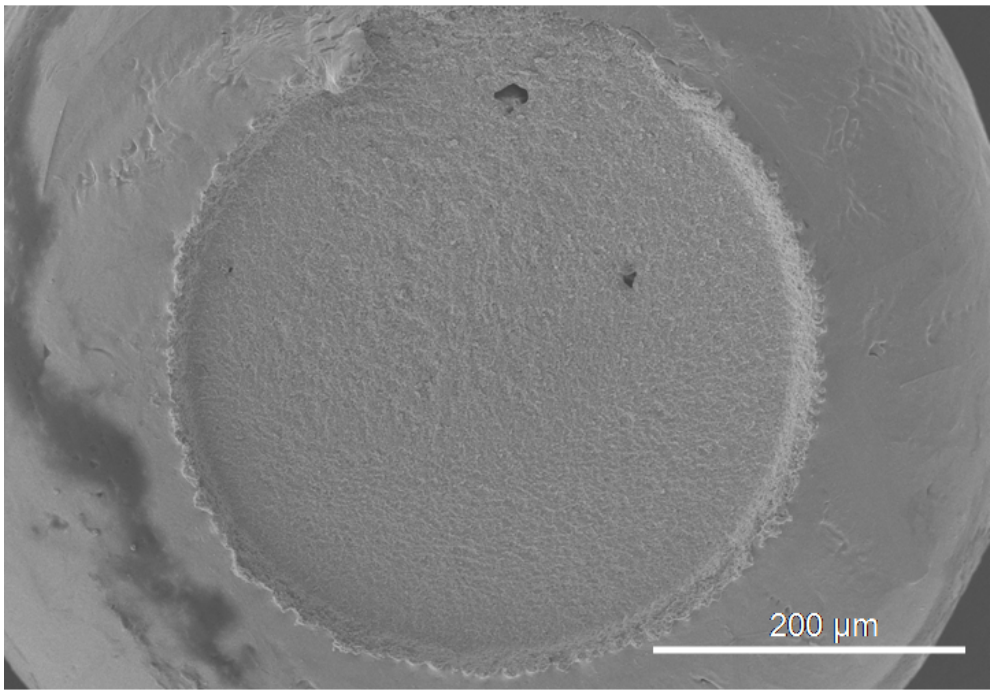

Figure 3.3 Sudden failure fracture surface seen in monotonic shear and tensile tests

(B. Fiedler, 2007)

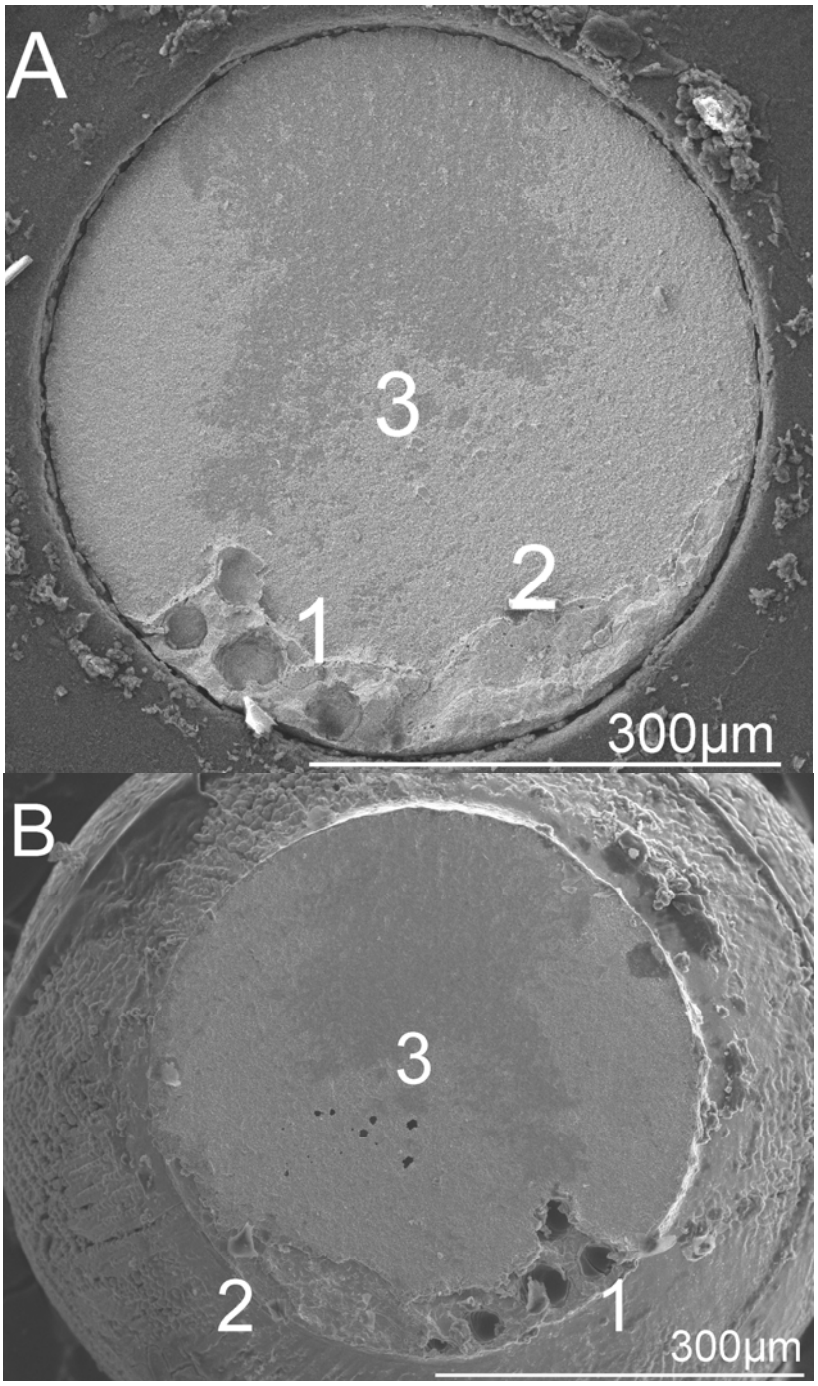

Figure 3.4 Fatigue fracture surfaces of Sample A, (a) board fracture surface; (b) ball fracture surface Note: Regions 1 and 2 are fatigue crack initiation sites. (B. Fiedler, 2007)

A marked difference between monotonic and fatigue fracture surfaces may be seen by comparing Figs. 3.3 and 3.4. Fig. 3.3 shows the sudden failure mode which was observed between the IMC and solder in monotonic shear and tensile tests. This sample was tested in as-flowed condition, without any further heat treatment. The average intermetallic compound (IMC) layer thickness for the monotonically tested specimen was 3 μm. Sample A, shown in Fig. 3.4 underwent a 96 hr heat treatment at 125 °C, which resulted in the IMC at the interface reaching an average thickness of 4 μm. Sample A also experienced 5000 cycles of mode II, stroke controlled fatigue loading in the aforementioned displacement profile, after which time it was pried apart to expose the fatigue fracture surfaces. Hysteresis loops were recorded at set intervals in order to monitor sample degradation. Hysteresis from monitoring the stress and strain of this sample was first seen after 1000 cycles. Fig. 3.4a and 3.4b are mirror images of opposite fracture surfaces on the same joint. Two semi-circular (thumbnail shaped) regions of fatigue crack can clearly be seen. Region 1 shows numerous voids contributing to the formation of a crack, while region 2 is free of these defects. The intergranular (between grain) failure characteristic of LCF failure can clearly be seen in the bulk solder of regions 1 and 2. Region 3 is the planar, rapid failure area.

Both regions 1 and 2 are the crack nucleation and propagation regions known as phase I and phase II. The majority of the sample lifetime consists of these microcrack formation, conglomeration (or aggregation) and propagation phases. Region 2 displays a thumbnail shape characteristic of fatigue cracking in phases I and II. Region 1 shows 4 large voids of 25-35 μm in diameter within 55 μm of the edge of the joint and 1 smaller void of 12.5 μm diameter with its center only 9 μm from the interconnect edge. The size and location of voids or inclusions has been shown to have a significant effect on the fatigue lifetime of metals. Seniw et al. (2000)

observed that larger voids nearer to the center of a specimen may have less of an effect on fatigue life than a smaller void located closer to a stress concentration in cast aluminum samples. The numerous voids in region 1 frustrate the thumbnail shaped growth as each void may be nucleating cracks simultaneously.

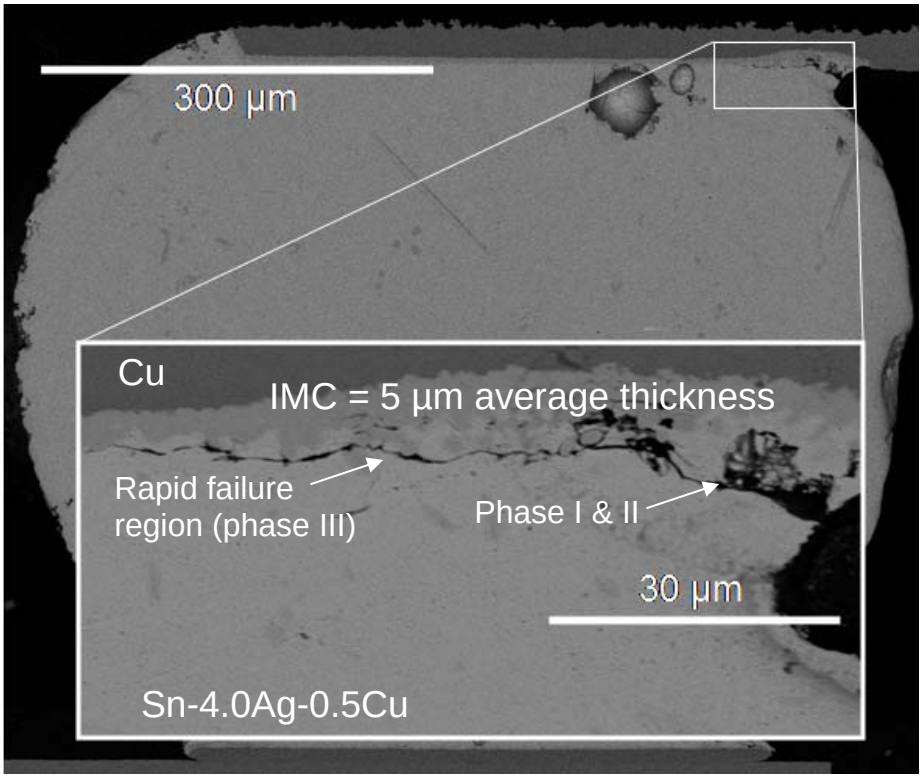

Figure 3.5 Fatigue fracture cross-section showing the crack path of Sample B

(B. Fiedler, 2007)

Figure 3.5 shows a cross section view of a crack path in sample B which underwent 168hr heat treatment at 125 °C resulting in an average IMC layer thickness of 5 µm. The total length of the fatigue crack path measures 88µm. This increase in length, compared to sample A is due to some phase III crack growth occurring at the solder / IMC interface. The sections of phase I, II and III cracking are labeled as such. Phase II growth progresses immediately after microcracks from phase I come together and form a crack. This development can be seen

through the bulk solder as it progresses towards the IMC interface at a 30° angle, for 30 μm. This angled path toward the interface is due to the butterfly shaped plastic zone ahead of the crack tip (Fig. 3.6) which generates dislocations. These then accumulate at solder IMC interface leading to cracking along this brittle portion of the solder joint. There is a transition region of 10 μm before the final 48 μm of phase III cracking between the solder and IMC.

Given the crack length of 61 μm in region 2 and that sample A underwent 5000 cycles. Sample B experienced 4400 cycles and had an 88 μm crack, giving a whole test average crack growth rate of 20 nm / cycle. This agrees with the value from Sample A and shows that a slower average crack propagation rate occurs during phase I and II. Additionally, these data suggest the majority of the sample lifetime is contained within these regions of early stage crack growth.

Thus, from the experimental observation, the interconnect failure may be divided into three phases. Phase I corresponds to crack nucleation plus dislocation and micro crack accumulation in the solder. Phase II corresponds to the crack propagating in the bulk solder to the intermetallic and the interfaces of the intermetallic with the solder and the copper pad. Phase III corresponds to the crack propagating at the interfaces or within IMC layer. Since K_c values in the interfaces and intermetallic are very small, brittle crack propagation and rapid fracture will occur once phase III is reached. The fatigue life time of an interconnect is mainly during phase I and II. Phase III constitutes a very small fraction of the fatigue life of a single interconnect. The physical meaning can be explained from Eq. (3.7) in next section, in which U is a major parameter to determine the process of interconnects failure. The U value for a crack propagating in bulk solder is much larger than the U in IMC layer. Thus, the fatigue propagation rate, da/dN, of phase II is much smaller than that of phase III, and the fatigue life during the crack propagation stage (phase II plus phase III) will be almost exclude during phase II. Based on the

phase transformation theory, the current work extends Fine et al's work (1999, 2000) on crack nucleation (phase I) in interconnects to crack propagation (phase II).

Fig. 3.6 shows the von Mises Stress distribution in a Sn-4.0Ag-0.5Cu eutectic solder joint with a crack propagating in solder. The J-integral value and the range of stress intensity factor can be determined from numerical analysis, which is useful for the development of phase transformation theory in next section. The details of the numerical analysis and modeling setup will be introduced in section 3.5.

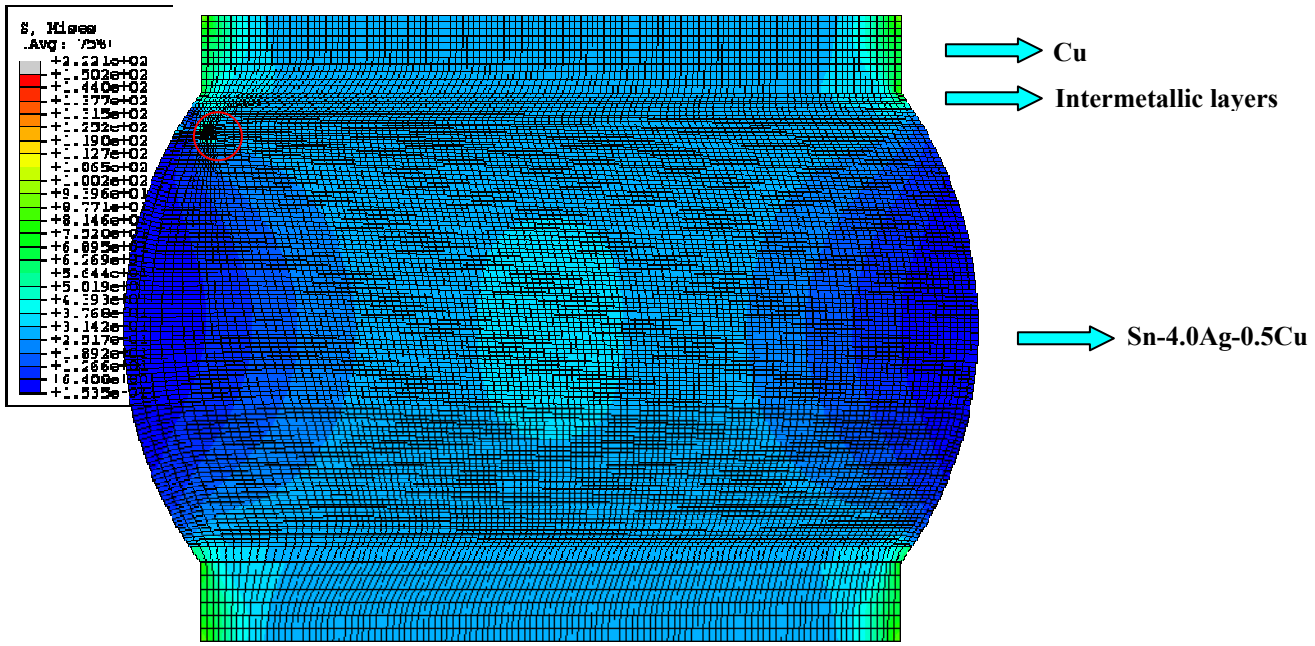

3.6a) a von Mises stress distribution in a Sn-4.0Ag-0.5Cu solder interconnect

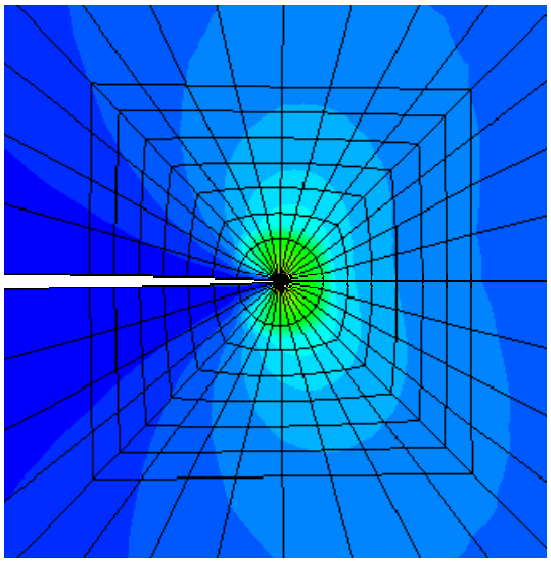

3.6b) von Mises stress distribution ahead of crack tip

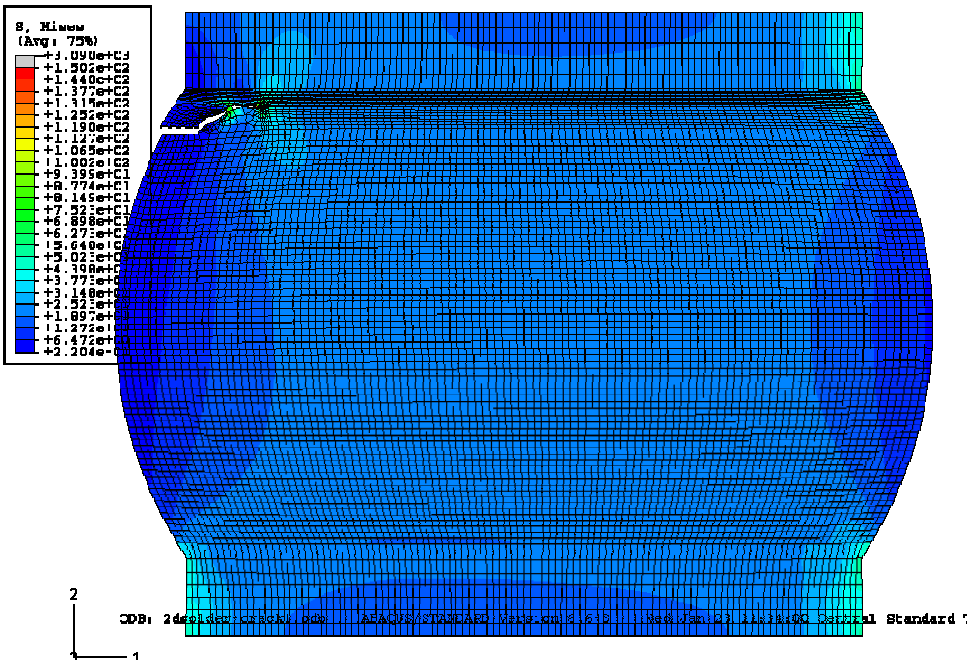

3.6c) von Mises stress distribution in a Sn-4.0Ag-0.5Cu solder interconnect with crack propagation

Figure 3.6 von Mises stress distribution of a Sn-Ag-Cu interconnect predict from finite element analysis (MPa)

3.3 Phase Transformation Theory to Predict Fatigue Crack Nucleation

The accumulated damage from fatigue loading is essentially an increase in dislocation density but dynamic recovery (due to thermally activated diffusion-like processes like dislocation climb) sets in immediately, where dislocations of opposite sign annihilate and a stable steady-state dislocation structure forms if thermal energy is sufficiently high and the activation energy for dislocation motion is not too high. For example, in Al fatigued at room temperature a dislocation cell structure forms but dislocation tangles form at liquid nitrogen temperature (Williams and Fine 1985). While a stable steady state dislocation structure is expected to form after a transient during fatigue cycling of solder, fatigue cracks nucleate from the point with local concentration of dislocations and here damage continues to increase at some rate per cycle.

When a crack forms in a solid material or at an interface, defects are released at the new surfaces along with a reduction in internal energy and stored elastic energy. These counteract the energy increase due to the increase in surface area. The change in energy ΔW to form a crack of area A is (Fine 2000):

$$\Delta W = -\delta A - \Delta W_2 + \gamma_T A \qquad (3.1)$$

where δ = stored energy in defects per unit area of crack, which is smaller if the material is brittle, as in most intermetallics;

ΔW_2 = stored elastic energy;

$\gamma_T = 2\gamma$ = total surface energy per unit area of crack, where the parameter 2 indicates two surfaces are created; if the crack is at a pre existing interface, the surface energy term $\gamma_T = 2\gamma - \gamma_i$, and γ_i is the interfacial energy per unit area.

For a penny-shaped crack, ΔW_2 can be obtained based on eigenstrain theory by Mura (1991):

$$\Delta W_2 = \frac{8(1-\nu^2)\sigma^2 a^3}{3E} \tag{3.2}$$

where σ = the maximum stress in the cycle;

E = the Young's modulus;

ν = Poisson's ratio;

a = crack radius.

A simplified solution for crack nucleation for this case can be defined as:

$$\Delta W = -\pi a^2 \delta - \frac{8(1-\nu^2)\sigma^2 a^3}{3E} + \pi a^2 \gamma_T \tag{3.3}$$

Bhat and Fine (2001) defined the parameter δ related to hysteresis loop parameters as:

$$\delta(N^*) = ftN^* \Delta\sigma \Delta\varepsilon_p \tag{3.4}$$

where f = efficiency factor (efficiency in storing defects caused by fatigue);

t = sum of the thicknesses of materials on each side of the crack that are drained of defects when the crack is formed;

N^* = critical number of cycles for crack nucleation;

$\Delta\sigma \Delta\varepsilon_p$ are the stress and plastic strain ranges of the fatigue cycling.

Eq. (3.4) is an extension of the ideas advanced by Mura and coworkers (Mura and Lin 1974; Izumi et al. 1981; Mura 1994) based on the concept of Gibbs free energy change accompanying the transition from the bulk deformation stage (in this stage, cyclic deformation during which the repeated applications of stress or strain condition the metal for the subsequent stages) to that containing microcracks (in this stage, crack initiation during which microcracks nucleate and coalesce to form macrocracks). The term *f* is taken as a constant for the material and specific combination of test conditions. The term *ft* may be looked upon as an indicator of the energy that is stored from cycle to cycle.

Differentiating Eq. (3.3) with respect to *a* with *N** constant gives:

$$\left(\frac{d}{da}\Delta W\right)_{N^*} = 0 \rightarrow a^* = \frac{E\pi(\gamma - \delta(N^*))}{4(1-\nu^2)\sigma^2} \tag{3.5}$$

where a^* = critical crack radius; N^* can be predicted by:

$$N^* = \frac{\pi E\gamma - 4\sigma^2 a^*(1-\nu^2)}{\pi E f t \Delta\sigma\Delta\varepsilon_p} \tag{3.6}$$

There are a number of unknowns in Eq. (3.6) and experimental determination of these parameters is the key to the applicability of these equations. The value of a^* is limited by our ability to detect small cracks, which is a function of the experimental techniques used to monitor crack initiation. For a penny-shaped crack, a conservative value for a^* is assumed to be 250 nm although smaller cracks have been observed by examining shadowed surface replicas in the electron microscope. For simplicity the assumption of a penny-shaped crack is adopted in

present research, which is reasonable for many fatigue crack nucleation and propagation situations in steel or aluminum alloy (Williams and Fine 1985; Bhat and Fine 2001).

3.4 Phase Transformation Theory to Predict Fatigue Crack Propagation

The main focus of current research is to apply phase transformation theory to predict fatigue crack propagation. An equation similar to Eq. (3.1) is used as a basis for discussing fatigue crack growth.

$$\Delta W = -\Delta W_{1a}\Delta A - \Delta W_2 + \Delta W_{1b}\Delta A + \Delta W_3\Delta A + \gamma_T \Delta A \qquad (3.7)$$

where ΔW = the energy required to increase the crack area by ΔA;

ΔW_{1a} = the gain in energy per unit area due to loss of defects as the crack advances by ΔA. Under constant ΔK (the stress intensity range) this gain is negated by ΔW_{1b} due to the plastic zone extension and the attendant increasing defect density in the extension.

ΔW_{1b} = the energy per unit area consumed by the extension of the plastic zone;

ΔW_2 = the stored elastic energy;

ΔW_3 = the plastic work per unit area transferred to heat for each cyclic loading step. ΔW_3 may be regarded as a "frictional" term, measured by the hysteresis between the loading and unloading stress strain curves. This is the mechanical energy converted to heat that raises the specimen temperature and is lost to the surroundings.

Normally $\Delta W_3 > \Delta W_{1a}$ because f <<1 (for example, for an HSLA steel, f = 0.0006, Bhat and Fine 2001). Whether the fatigue is under constant stress or constant strain control but increasing ΔK, the plastic zone will grow in length and ΔW_{1b} will be numerically larger than ΔW_{1a}, but the

difference will be small. Thus, we may assume $\Delta W_3 >> (\Delta W_{1b} - \Delta W_{1a})$ and $(\Delta W_{1b} - \Delta W_{1a})$ can be neglected.

The surface energy term is least for crack growth on an interface such as a grain boundary or interface between phases, such as between a solder and an intermetallic layer in an interconnect. Many examples of fast fatigue crack propagation at grain boundaries and interfaces exist in the interconnect literature. In addition the hysteretic work term is much smaller in a brittle intermetallic than in a ductile alloy with the same yield stress and the crack propagation rate is expected to be faster in the intermetallic.

Since crack growth is an irreversible process. ΔW_2 must exceed very slightly the sum of $\gamma_T \Delta A$, and $\Delta W_3 \Delta A$ for the crack to grow spontaneously. To calculate dA/dN, the crack area growth per cycle, we assume that $d\Delta W$ is negligibly small. By equating the two sums:

$$\Delta W_{1a} dA/dN + \Delta W_2 = \Delta W_{1b} dA/dN + \Delta W_3 dA/dN + \gamma_T dA/dN \tag{3.8}$$

where dA/dN = area of crack growth per cycle;

By neglecting $(\Delta W_{1a} - \Delta W_{1b})$, solving for dA/dN gives:

$$\frac{dA}{dN} = \frac{\Delta W_2}{\gamma_T + (\Delta W_{1b} - \Delta W_{1a}) + \Delta W_3} \approx \frac{\Delta W_2}{\gamma_T + \Delta W_3} \tag{3.9}$$

For a solid material under cyclic loading, the energy release rate G (energy released per unit area) is assumed to consist mainly of two parts in the absence of an electrical field and can be defined by:

$$G \approx G_L + G_h \tag{3.10}$$

Here, G_L corresponds to the Griffith-Irwin energy dissipation mechanism (energy to create the new crack surfaces), which corresponds to the material's surface energy γ_T and is equivalent to the J-integral value of J calculated from Fracture Mechanics (J/m^2). The term G_h corresponds to energy dissipation by conversion of mechanical energy to heat, ie. internal friction previously associated with the dislocation motion in the plastic zone ahead of the crack as shown in Fig. 3.7.

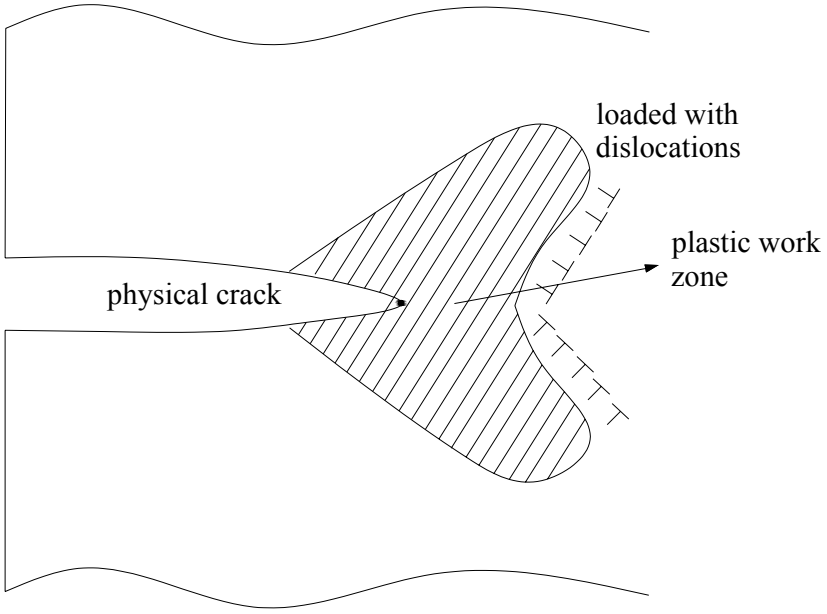

Figure 3.7 Schematics of plastic zone ahead of crack tip

Since we assume $\Delta W_3 >> (\Delta W_{1b} - \Delta W_{1a})$, the hysteretic fracture energy loss release rate $G_h \approx \Delta W_3$. Thus, we assume,

$$G \approx J + G_h \approx \gamma_T + \Delta W_3 \tag{3.11}$$

Here, the generalized force acting on the tip of a crack can be expressed in terms of J-integral of the Maxwell energy-momentum tensor P_{lj} of elasticity taken over a surface (Mura

1981), and the three-dimensional expression of J-integral can be defined by (Rice 1967; Weertman 1973):

$$J_l = -\int_{\Gamma} \sigma_{ij} n_j u_{i,l} dS + \int_{\Gamma} W n_l dS = \int_{\Gamma} P_{lj} n_j dS \tag{3.12}$$

where $P_{lj} = W\delta_{lj} - \sigma_{ij} u_{i,l}$; $W = \int_0^{\varepsilon_{ij}} \sigma_{ij} d\varepsilon_{ij}$ and $W_{,l} = \sigma_{ij} \varepsilon_{ij,l}$; $\varepsilon_{ij} = \frac{1}{2}(u_{i,j} + u_{j,i})$; the integration path Γ is an arbitrary closed contour followed counterclockwise surrounding the crack tip in a stressed body; σ_{ij} is the stress and ε_{ij} is the strain; u_i is the displacement; and n_j is the normal vector on the boundary *dS*.

For homogeneous, isotropic materials, the J-integral value can be simplified and calculated as follows (Suo and Hutchinson 1990). For a crack within a material:

$$J = \frac{1}{\overline{E}}(K_I^2 + K_{II}^2) + \frac{1}{2\mu} K_{III}^2 \tag{3.13}$$

where K_I, K_{II}, and K_{III} are the stress intensity factors for fracture modes I, II, and III, respectively; μ is the shear modulus; $\overline{E} = \frac{E}{1-\nu^2}$ for plane strain.

For a crack in the interface between two layers of materials:

$$J = \frac{1-\beta^2}{E^*}(K_I^2 + K_{II}^2) + \frac{1}{2\mu^*} K_{III}^2 \tag{3.14}$$

Here, $\frac{1}{E^*} = \frac{1}{2}(\frac{1}{\overline{E}_1} + \frac{1}{\overline{E}_2})$, $\frac{1}{\mu^*} = \frac{1}{2}(\frac{1}{\mu_1} + \frac{1}{\mu_2})$, where the shear modulus $\mu_1 = \frac{E_1}{2(1+\nu_1)}$,

$\mu_2 = \frac{E_2}{2(1+\nu_2)}$.

The Dundur's parameter can be determined by (Dundurs 1969):

$$\beta = \frac{\mu_1(\kappa_2 - 1) - \mu_2(\kappa_1 - 1)}{\mu_1(\kappa_2 + 1) - \mu_2(\kappa_1 + 1)}, \tag{3.15}$$

where $\kappa = 3 - 4\nu$ for plain strain

The physical meaning of the theory can be explained from energy considerations. Assume a crack propagates under external load F_i in a solid with domain of V, external boundary of S and internal crack boundary of A. When an existing crack with area of A extends to an area of δA, from the first law of thermodynamics and using Gauss theorem,

$$\int_S F_i \delta u_i dS = \int_S \sigma_{ij} n_j \delta u_i dS = \int_V (\sigma_{ij} \delta u_i)_{,j} dV - \int_{A+\delta A} \sigma_{ij} n_j \delta u_i dS \tag{3.16}$$

where δu_i is the displacement; n_j is the normal vector on the boundary.

From the equations of equilibrium, $\sigma_{ij,j} = 0$ in V; assume a free surface, i.e. $\sigma_{ij} n_j = 0$ on A; and Eq. (3.16) is simplified as:

$$\int_S F_i \delta u_i dS = \int_V \sigma_{ij} \delta u_{i,j} dV - \int_{\delta A} \sigma_{ij} n_j \delta u_i dS \tag{3.17}$$

Based on the assumption of small strains, the total strain consists of elastic strain e_{ij} and plastic strain ε_{ij}^p :

$$\frac{1}{2}(u_{i,j}+u_{j,i})=e_{ij}+\varepsilon_{ij}^{p},\ \frac{1}{2}(\delta u_{i,j}+\delta u_{j,i})=\delta e_{ij}+\delta\varepsilon_{ij}^{p} \tag{3.18}$$

Substituting Eq. (3.18) into Eq. (3.17) gives:

$$\int_S F_i\delta u_i dS=\int_V \sigma_{ij}\delta e_{ij}dV+\int_V \sigma_{ij}\delta\varepsilon_{ij}^{p}dV-\int_{\delta A}\sigma_{ij}n_j\delta u_i dS=U\delta A \tag{3.19}$$

Here, $\int_S F_i\delta u_i dS$ is the potential energy of external load; $\int_V \sigma_{ij}\delta e_{ij}dV$ is the elastic strain energy corresponding to the stored elastic energy; $\int_V \sigma_{ij}\delta\varepsilon_{ij}^{p}dV$ is the plastic work term and $(-\int_{\delta A}\sigma_{ij}n_j\delta u_i dS)$ corresponds to the surface energy and equals to the value of J-integral (Izumi et al. 1981). The energy to propagate a unit area fatigue crack surface is U(J/m^2), which can be determined from experiment (Liaw et al. 1981).

For the plasticity and hardening model, Weertman (1973) and Mura and Lin's (1974) work extending BCS crack theory is followed in this chapter. Considering the plastic part $\int_V \sigma_{ij}\delta\varepsilon_{ij}^{p}dV$ and noting that $\delta\varepsilon_{ij}^{p}\propto\frac{(\Delta K)^2}{\mu\sigma_y}$ and the plastic domain $\propto\frac{(\Delta K)^2}{\sigma_y^2}$, by neglecting the work done on the new crack surface, a generally accepted equation for the crack growth per cycle for a ductile material is obtained:

$$\frac{dA}{dN}\propto\frac{\Delta K^4 b}{\mu U\sigma_y^2} \tag{3.20}$$

where σ_y = yield stress;

b = specimen thickness;

Eq. (3.20) is obtained by extending the Griffith fracture theory to fatigue crack propagation problem by defining the Gibbs free energy of solids under cyclic loading. In the analysis stress rather than cumulative displacement or cumulative damage is the quantity whose critical value controls the crack growth. The assumption is that the material at the tip of a fatigue crack progressively work hardens until the stress reaches a critical value.

Based on Eq. (3.7) and (3.19), relating Eq. (3.20) to phase transformation theory gives:

$$\Delta W = U\frac{dA}{dN} = -\Delta W_2 + B\frac{\Delta K^4 b}{\mu\sigma_y^2} + J\frac{dA}{dN} \tag{3.21}$$

where B is a dimensionless constant;

The area of fatigue crack propagated per cycle can thus be obtained by:

$$\frac{dA}{dN} = \frac{B\dfrac{\Delta K^4 b}{\mu\sigma_y^2} - \Delta W_2}{(U-J)} = \frac{B\Delta K^4 b}{\mu\sigma_y^2(U-J)} - \frac{\Delta W_2}{(U-J)} \tag{3.22}$$

Eq. (3.22) provides a theoretical basis to predict the fatigue crack propagation rate for both brittle and ductile solid materials. To verify the theory, Eq. (3.22) is applied to different materials and compared with experimental data in next section.

Based on Eq. (3.7), an equation to predict the length of fatigue crack propagated per cycle can be derived similarly:

$$\frac{da}{dN} = \frac{B\Delta K^4}{\mu\sigma_y^2(U-J)} - \frac{\Delta W_2}{(U-J)b} \text{ (if } \Delta K < \Delta K_c\text{)} \tag{3.23}$$

where *da/dN* is the area of crack growth per cycle; *B* is a dimensionless constant; *J* is the value of J-integral; σ_y is yield stress; *b* is specimen thickness; ΔK is the range of stress intensity factor; ΔK_c is the critical stress intensity factor and μ is shear modulus. A formula to predict the dimensionless constant *B* is suggested by:

$$B = l \times (mag(\Delta K))^m \tag{3.24}$$

where $mag(\Delta K)$ is the dimensionless magnitude of stress intensity range, which equals $\Delta K / K_{unit}$, and $K_{unit} = 1$ MN/m$^{3/2}$; here *l* and *m* are material constants.

3.5 Experimental and Computational Analysis on Fatigue Crack Propagation of Sn-3.5Ag Eutectic Solder at Northwestern University (experiments conducted by S. Vaynman, 2007)

To verify the proposed phase transformation theory, experiments on fatigue crack propagation in Sn-3.5Ag solder alloy have been conducted by S. Vaynman at Northwestern University, 2007. In his experiments, fatigue crack propagation in solder in Mode I loading was studied utilizing a solder-joint plate specimen with a single edge notch (Fig. 3.8). Two copper plates were joined by Sn–Ag eutectic solder. Prior to soldering, the copper plates were polished with 600-grit emery chapter and cleaned with diluted nitric acid, rinsed in distilled water and dried with methanol. The copper surface to be soldered was coated with $SnCl_2$ solution, placed in a fixture and pre-heated to 260°C on hot plate. The solder was melted in the gap between the copper plates. The fixture was removed from the hot plate ten minutes after the joint was formed and was cooled down to room temperature. The excess solder was removed from the specimen surface by grinding/polishing. The notch was introduced by wire in the electro-discharge

machine. Fatigue crack propagation tests were performed in air at room temperature in a servo-hydraulic fatigue machine (MTS-810) in load control (sinusoidal waveform, 5 Hz) with maximum load of 2,400N and the load ratio of 0.1. The crack growth was monitored by a traveling microscope. Scanning electron microscopy (SEM) and optical microscope examinations were performed directly on the specimens.

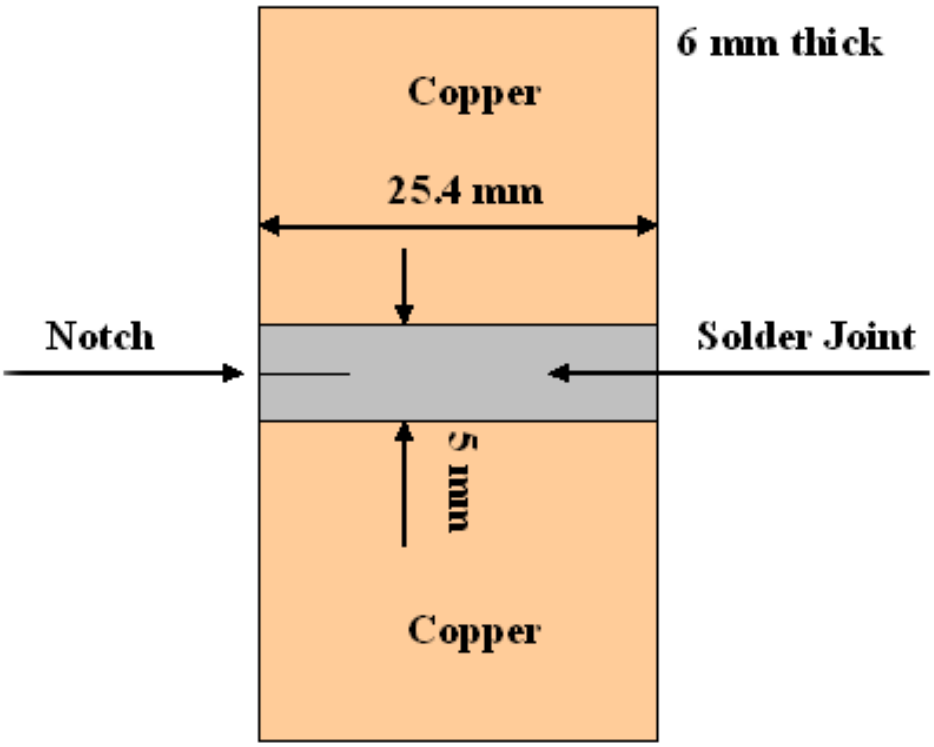

Figure 3.8 Schematic of the fatigue tests specimen (S. Vaynman 2007)

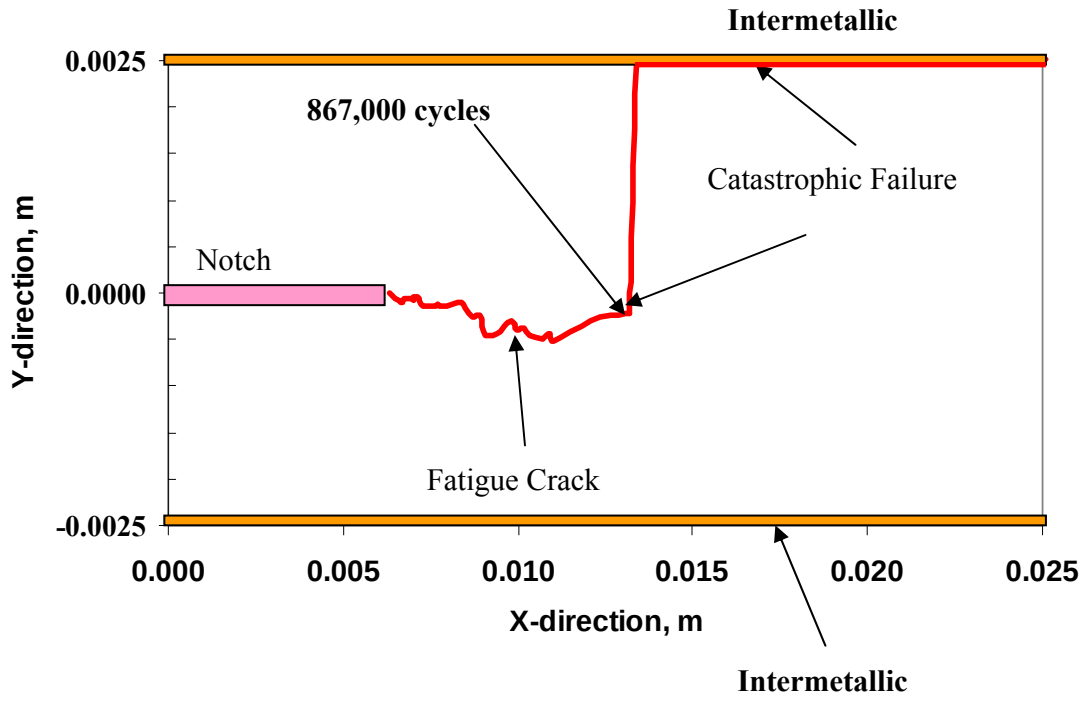

Figure 3.9 Fatigue crack propagation path in Sn-3.5Ag Solder during cyclic loading (S. Vaynman 2007)

The fatigue crack propagation path in Sn-3.5Ag Solder during fatigue cyclic is shown in Fig. 3.9. It is found that the crack gradually propagates in a direction approximately perpendicular to the stress direction through the region with accumulation of dislocation. When after 867000 cycles, the crack grew to approximately 13mm in the horizontal direction; the crack migrated to the copper/solder interface resulting in sudden catastrophic failure. Fig. 3.10 is optical micrograph of the crack. Different phases of fatigue failure, fatigue crack initiation, propagation and catastrophic failure are observed. Fig. 3.11 is a SEM micrograph of fatigued solder specimen surface. There is a wire-cut surface of the solder on the left. The crack starts and then propagates to the right.

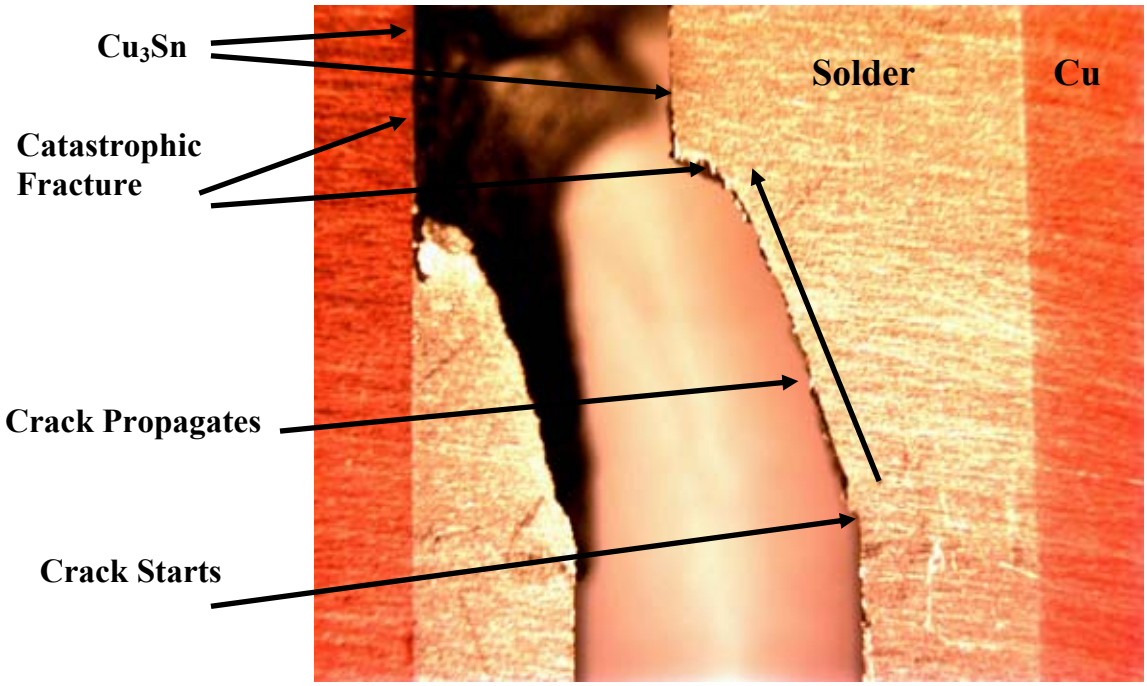

Figure 3.10 Fatigue Crack in Sn-3.5Ag Solder (two sides of crack are shown) Sample aged 10 minutes in liquid state (S. Vaynman 2007)

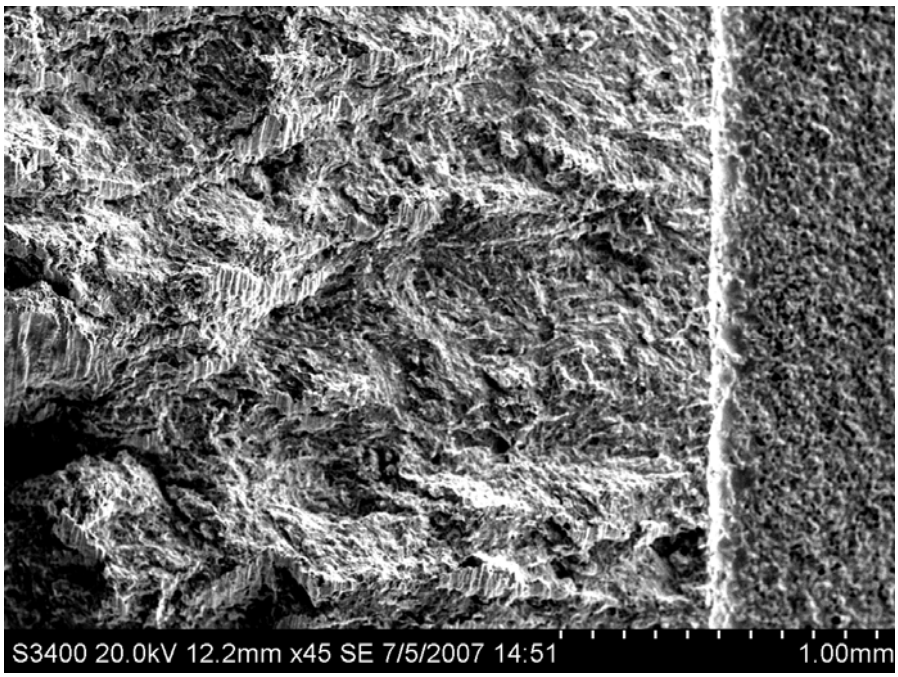

Figure 3.11 SEM micrograph of fatigued solder specimen surface (S. Vaynman 2007)

A finite element model has been developed to predict the range of stress intensity factor ΔK for the experiment. The CPS8R element in ABAQUS was used for the analysis, and the square root and $1/r$ singularities were built into finite element meshes using standard elements. To simulate the singularity at the crack tip, a ring of collapsed quadrilateral elements were used to perform the modeling there. The mid-side nodes on the sides connected to the crack tip were moved to the 1/4 point nearest the crack tip, and a quarter point spacing with second-order isoparametric elements was created. Fig. 3.12 shows the distribution of von Mises stress for solder/IMC predicted by using the finite element model; a stress concentration is predicted ahead of crack tip and higher stress is also observed near the interface between solder and the IMC layer. Fig. 3.13 shows the relationship between stress intensity factor range ΔK and crack length ratio a/W. With the increase of crack length, the stress intensity factor range increases. The relationship between cycle number and crack length for two different specimens is shown in Fig. 3.14. It is found for the specimen before 600000 cycles the crack length increases linearly, after 600000 cycles, the crack length increases exponentially and much faster. Fig. 3.15 shows the relationship between stress intensity factor range and crack propagation rate. The experimental results are used to validate the prediction of fatigue crack propagation rate using phase transformation theory in section 3.7.

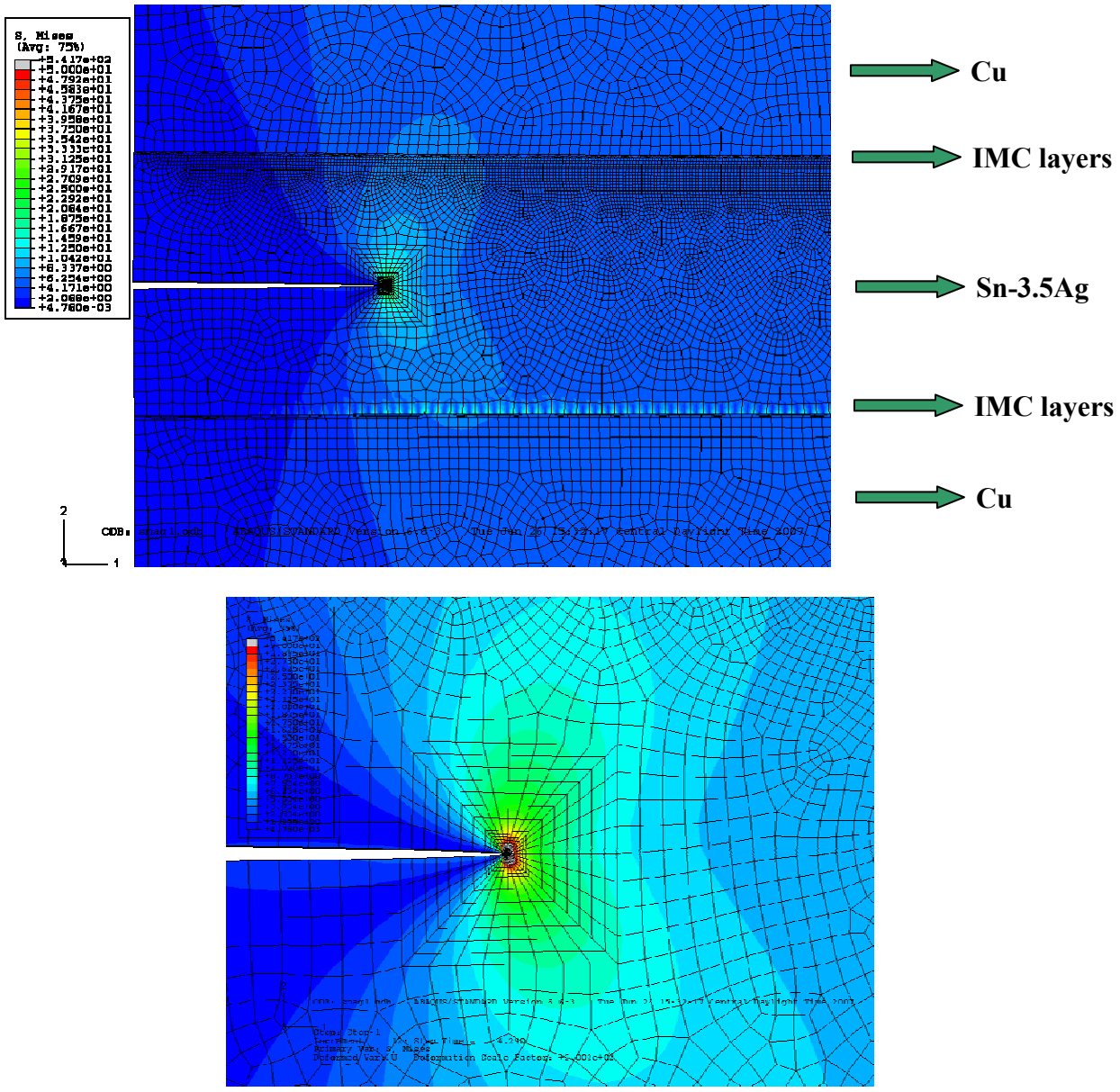

Figure 3.12 von Mises stress distribution for the experiment predicted using FEM

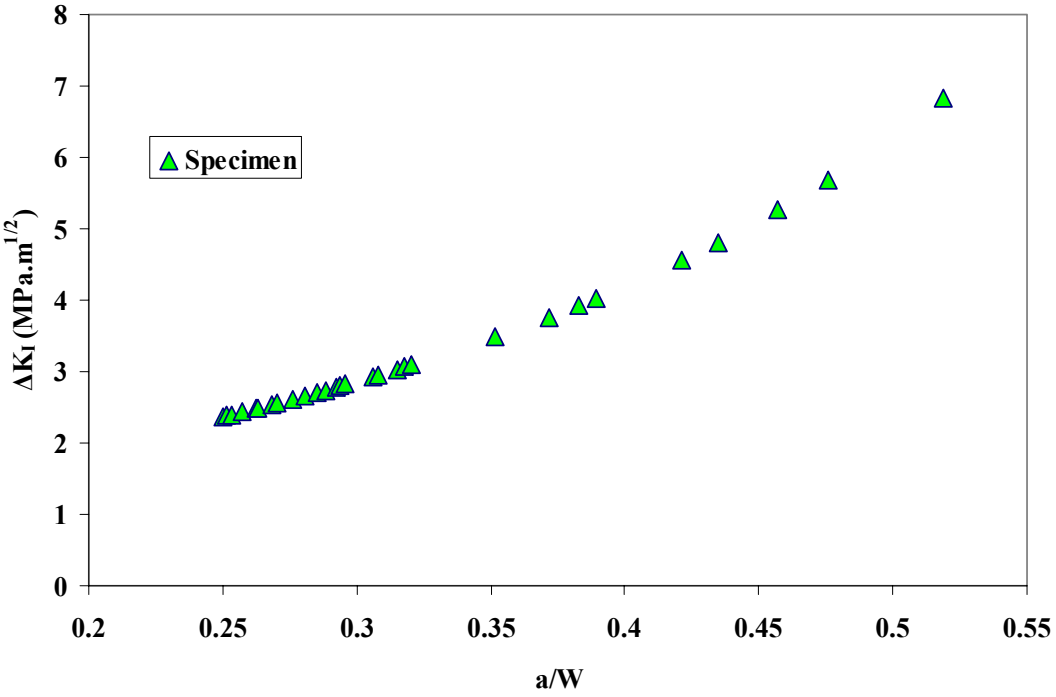

Figure 3.13 Relationship between stress intensity factor range and crack length ratio *a/W*

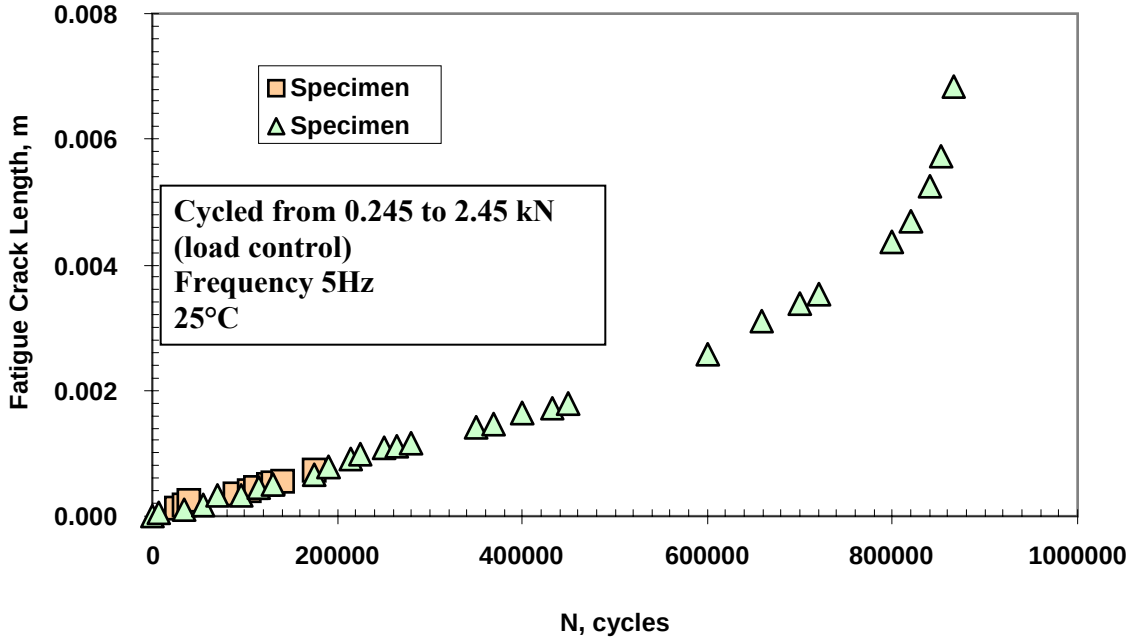

Figure 3.14 Relationship between cyclic number and crack length

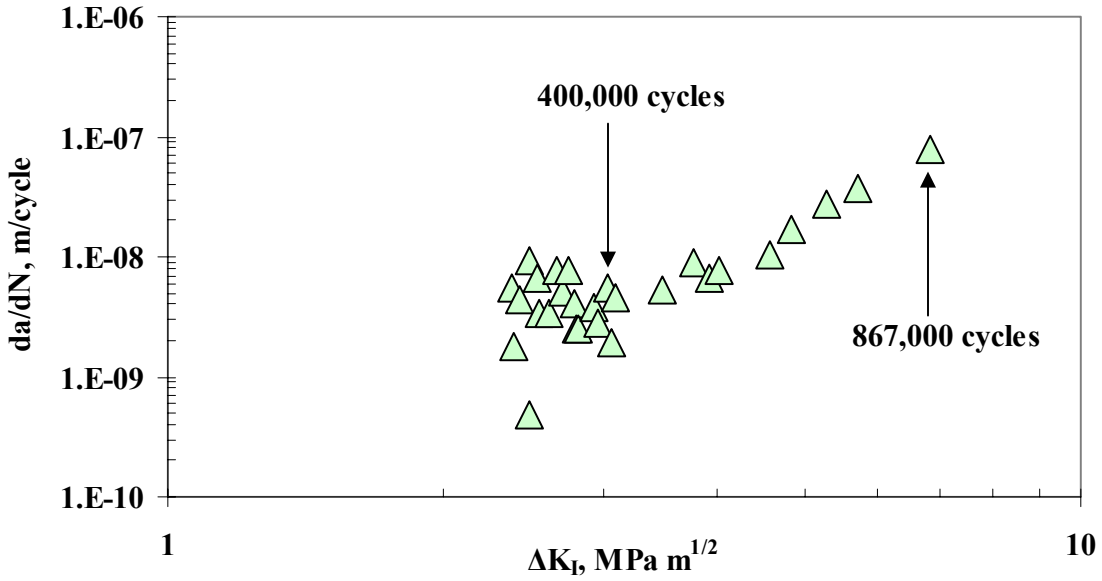

Figure 3.15 Relationship between stress intensity factor range and crack propagation rate

3.6 Computational Analysis to Determine the Energy to Propagate a Unit Fatigue Crack Surface *(U)* Value for Solder Materials

To the author's knowledge, there are only few experimental data or theoretical models available to obtain the value of U in Eq. (3.7) for solder materials. Klingbeil (2003) suggested that U equals the monotonic critical energy release rate G_C ; however, the hysteresis effect, which is found to be important for fatigue crack propagation predictions, is not incorporated in his model. Motivated by Klingbeil's work, finite element analysis was conducted to determine the U value in this chapter, obtaining it from the hysteresis stress-strain curve of an interconnect under cyclic loading with a crack propagating in the solder near the interface of solder and IMC layer.

To determine the value of U in Eq. (3.7) for a solder, as introduced in Chapter 2, a 3D finite element model for an interconnect has been developed incorporating CZM and UCP theories to simulate solder/IMC interfacial behavior and hysteresis effect in solder bulk, respectively. The model is programmed into the commercial software ABAQUS through a user defined subroutine using FORTRAN language. Two layers of IMC, Cu_6Sn_5 and Cu_3Sn, are included in the 3D finite element model. A cohesive layer with a traction-separation type cohesive element has been defined at the interface of the solder and IMC to predict the interfacial behavior. An exponential traction-separation (T-S) law of the interfacial cohesive element is assumed, and a quadratic nominal stress criterion to predict damage initiation is adopted. The damage evolution for mixed mode failure is defined based on the Benzeggagh-Kenane fracture criterion. For solder, the UCP theory is adopted based on the dual backstress thermo-plasticity model proposed by McDowell et al. (1994) and Wen et al. (2002), which is introduced in Chapter 2 in detail. To simulate realistic operating conditions of an interconnect, sinusoidal displacement is assumed with a maximum magnitude of 0.5μm to simulate the shearing load caused by thermal mismatch of the coefficients of thermal expansion (CTE). The solder, IMC layer and silicon die properties are given in Table 3.1 (NIST database 2002) (Kanchanomai et al. 2005). The distribution of von Mises stress for solder/IMC predicted using the proposed finite element model, higher stress is observed near the interface of bulk solder and IMC layer.

Table 3.1 material properties used in finite element model

(NIST database 2002) (Kanchanomai et al. 2005)

	Young's modulus (GPa)	Poisson's ratio	Yield Stress(MPa)
Solder: 63Sn-37Pb	32	0.32	18.1
Solder: Sn-3.5Ag	45	0.36	30.6
Cu	117	0.33	70
IMC close to solder: η-phase Cu_6Sn_5	96.9	0.309	-
IMC close to Cu:ε-phase Cu_3Sn	123.2	0.319	-

Since very few experimental data of fatigue crack propagation available for interconnects operating under thermal-mechanical shear. To verify the proposed approach, the boundary and loading condition of finite element model was modified to simulate the test condition of experiments for 63Sn-37Pb (Kanchanomai et al. 2005) and Sn-3.5Ag eutectic solder by Vaynman as introduced in previous section (refer to Yao et al. 2008) under mode I loading. Cyclic sinusoidal tensile loading rather than shear loading was applied with a frequency of 10 Hz, and the results should be viewed as the first approximation for application of the phase transformation theory to predict fatigue crack propagation in interconnects. More experimental data for fatigue crack propagation in interconnects under realistic operating conditions are required for future research. Under mode I loading, similar to the shear loading case, the crack was found to nucleate and propagate in solder bulk near the interface of solder and IMC layer, which matches the experimental observation.

The stress-strain relationship predicted using UCP model for Sn-3.5Ag eutectic solder under cyclic loading is compared with experimental data (Wen 2001), (Fig. 3.16), which shows stable matching with experimental data. The area within the hysteresis loop was integrated numerically, and assumed in this method to be approximately equal to the value of U

($U \approx 1.80 \times 10^5$ J/m^2 for Sn-3.5Ag eutectic solder). For 63Sn-37Pb eutectic solder, the value of U is found to be approximately equals to 1.85×10^5 J/m^2.

The value was substituted into Eq. (3. 23) to determine the fatigue crack propagation rate in interconnect and compared with experimental data in next section.

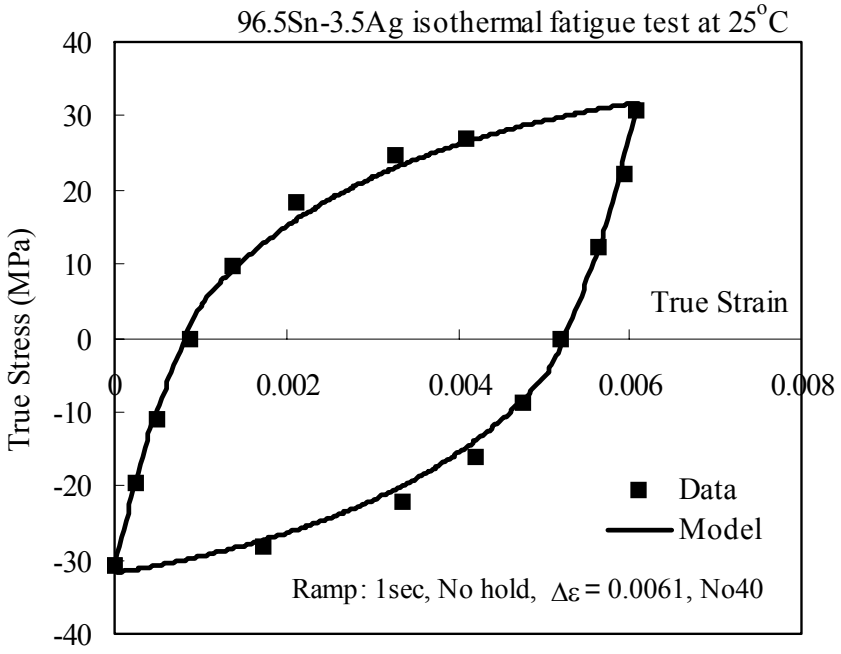

Figure 3.16 Stress-strain relationship of Sn-3.5Ag eutectic solder under cyclic loading predicted from numerical analysis compared with experimental data (Wen 2001)

3.7 Case Studies and Discussion

Eq. (3.22) predicts the fatigue crack propagation rate *dA/dN* from measurable properties and a dimensionless parameter *B*. Complete sets of experimental data for a group of steels and aluminum alloys are given in Table 3.2 (Izumi and Fine 1979; Liaw et al. 1981; McKittrick et al. 1981; Fine et al. 1999).

Table 3.2 Experimental results used to verify phase transformation theory

(Izumi and Fine 1979; Liaw et al. 1981; McKittrick et al. 1981; Fine et al. 1999)

Steels	ΔK(MN/m$^{3/2}$)	σ_y(MN/m^2)	U(J/m^2)	dA/dN(m^2/cycle)
0.05 wt pct C steel	8	170	5.30×10^{6}	4.50×10^{-12}
HY80	20	521	7.70×10^{5}	1.05×10^{-10}
HY130	20	868	2.20×10^{5}	1.50×10^{-10}
Nb-HSLA(Hot-rolled)	9.3	340	6.00×10^{5}	9.00×10^{-12}
Nb-HSLA(Hot-rolled)	12.4	340	1.20×10^{6}	2.40×10^{-11}
Nb-HSLA(Hot-rolled)	15.5	340	8.00×10^{5}	5.10×10^{-11}
Nb-HSLA(Hot-rolled)	19.5	340	1.20×10^{6}	1.11×10^{-10}
Nb-HSLA(400ºC temper.)	20	600	3.00×10^{6}	1.80×10^{-11}
Nb-HSLA(550ºC temper.)	20	688	7.60×10^{5}	4.50×10^{-11}
1.46 wt pct Cu-0.45 wt pct C Steel 500ºC 200min)	19.5	780	1.30×10^{5}	1.68×10^{-10}
Aluminum Alloys				
99.99Al (cold-rolled)	2.5	42	1.80×10^{6}	4.80×10^{-12}
1100Al (Annealed)	2.8	49	1.20×10^{6}	8.70×10^{-12}
2219 Al-T861	7.8	370	2.40×10^{5}	4.50×10^{-11}
2219 Al-T861	15.5	370	1.60×10^{5}	7.50×10^{-10}
2219 Al (overaged)	9.3	260	2.10×10^{5}	2.04×10^{-10}
2024 Al-T4	7.8	390	2.60×10^{5}	4.80×10^{-11}
2024 Al-T4	15.5	390	3.20×10^{5}	4.20×10^{-10}
T4	12.4	230	5.80×10^{5}	1.41×10^{-10}
7050 Al-T4	12.4	410	5.00×10^{4}	9.00×10^{-10}
7050 Al-T76	15.5	510	6.00×10^{4}	9.00×10^{-10}
MA87	10	553	1.70×10^{4}	4.80×10^{-10}
MA87	17	553	4.30×10^{4}	1.68×10^{-9}
Al 6.3 w/o Cu	12.4	230	5.80×10^{5}	1.41×10^{-10}
Al 6.3 w/o Cu	9.3	230	1.05×10^{6}	3.60×10^{-11}
7050 Al-T76	15.5	510	6.30×10^{4}	9.00×10^{-10}
7075 Al-T4	12.4	410	5.40×10^{4}	9.00×10^{-10}
Ni 7.2 w/o Al Aged 2 days temper.=625ºC	15.5	670	4.80×10^{5}	6.00×10^{-11}

where shear modulus $\mu = 7.8\times10^{4}$ MN/m^2 for steel and 2.6×10^{4} MN/m^2 for aluminum alloys and σ_y is the 0.2% offset cyclic yield stress; $dA/dN=b\times dc/dN$, which is the fatigue crack propagation rate (area per cycle) for a given ΔK. Here, specimen thickness b=3mm.

First the value of B was determined for each data set by equating the theoretical dA/dN to the measured value and solving for B. The B values varies from 1.46×10^{-3} to 4.37×10^{-3} for steels and 1.23×10^{-3} to 4.43×10^{-3} for aluminum alloys. The mean value of B, *mean(B)*, is

3.08×10^{-3} and 2.85×10^{-3} for steels and aluminum alloys, respectively. The distribution of *B/mean(B)* for steels and aluminum alloys is given in Fig. 3.17 with ΔK varies from 2.5 to 20 $MN/m^{3/2}$. Various theoretical models have been proposed to predict the dimensionless constant *B* by different researchers (Mura and Lin 1974; Irving and McCartney 1977; Izumi et al. 1981). The values of *B* calculated from the theoretical models are generally 5 to 10 times higher than the measured experimental values. The difference between the prediction of the theoretical model and experimental measurement may be explained by the fact that crack propagation is a nonreversible and spontaneous process, and the hysteresis effect is not incorporated in the theoretical models. From the experimental data, the *mean(B)* values are substituted into Eq. (3.22) to predict *dA/dN* for steels and aluminum alloys, respectively. As shown in Fig. 3.18, compared with experimentally measured *dA/dN*, the mean of predicted *dA/dN* is 1.062 and the coefficient of variation (COV) is 0.255 for steels; the mean is 1.185 and the coefficient of variation is 0.286 for aluminum alloys. Here, the coefficient of variation is a measure of dispersion of a probability distribution, which defined as the ratio of the standard deviation to the mean.

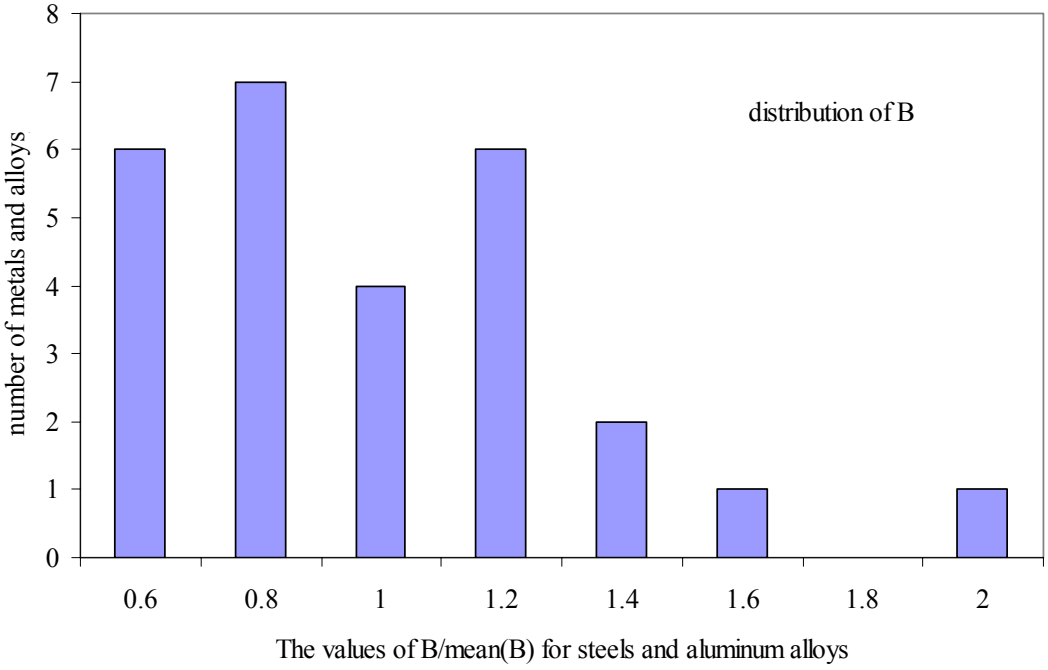

Figure 3.17 Distribution of the values of *B*/*mean(B)* for steels and aluminum alloys (ΔK varies from 2.5 to 20 MN/m$^{3/2}$)

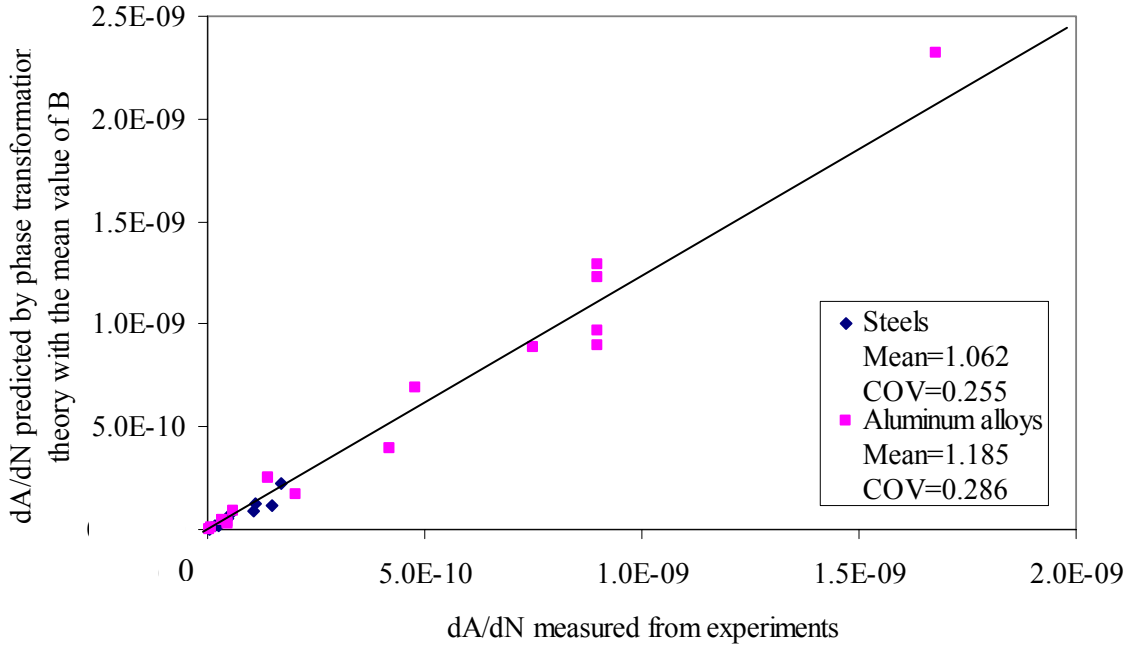

Figure 3.18 Predictions of fatigue crack propagation rate *dA/dN* for case study using Eq. (3.22) and the mean values of *B*

Note: here, 2.0E-09 *stands for* 2.0×10^{-9}

Analysis of the data shows that the values of B are related to the magnitude of ΔK rather than being a universal constant. Thus, instead of using the mean value of B, least-squares regression of a plot of B vs. $mag(\Delta K)$ is given in Fig. 3.19, yields the following empirical equation:

$$B = 0.0045 \times (mag(\Delta K))^{-0.15} \tag{3.25}$$

where $mag(\Delta K)$ is the dimensionless magnitude of stress intensity range, which equals to $\Delta K / K_{unit}$, and $K_{unit} = 1$ MN/m$^{3/2}$.

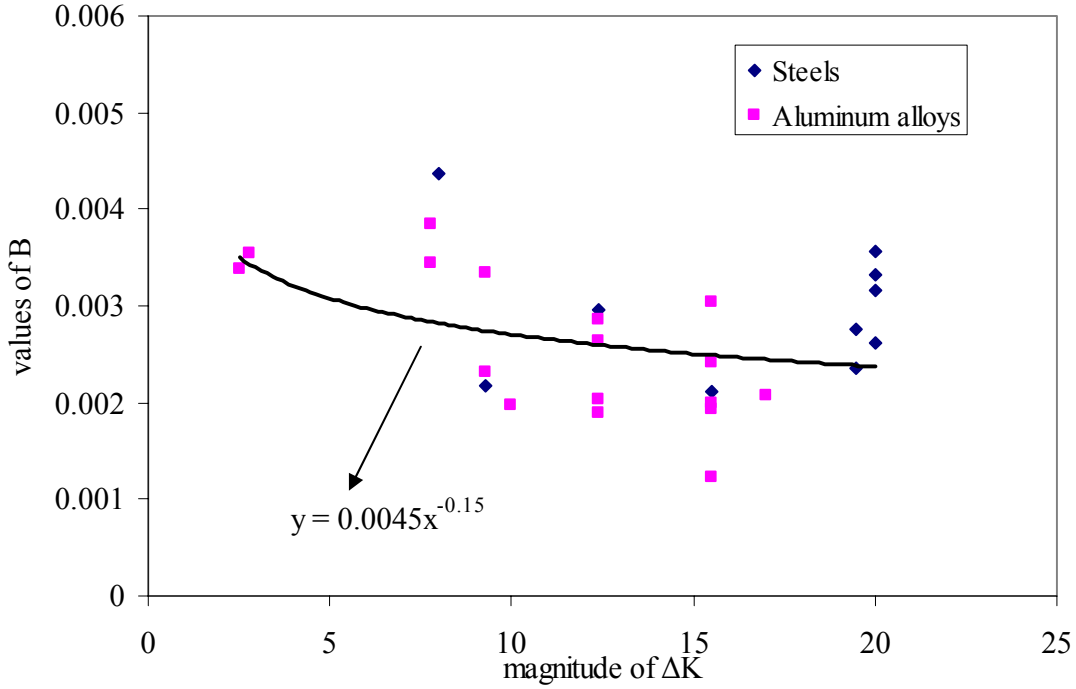

Figure 3.19 Values of B with respect to the magnitude of ΔK for materials in Table 3.2

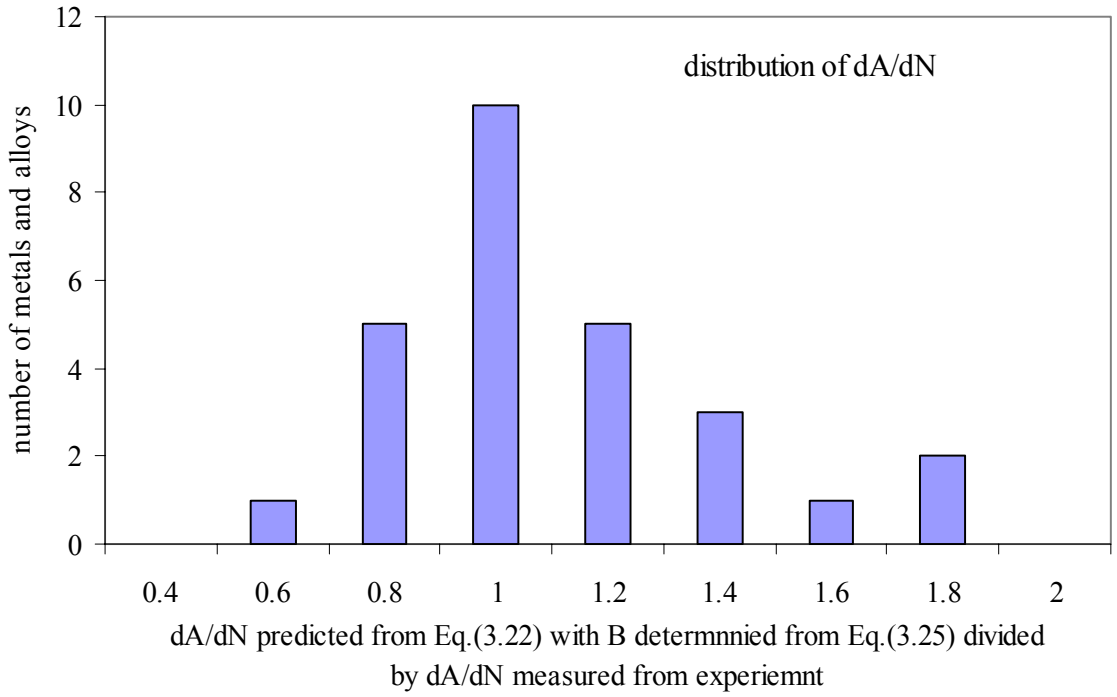

Figure 3.20 Distribution of *dA/dN* from Eq. (3.22) with *B* determined from Eq. (3.25) compared with experimental data of steels and aluminum alloys

Fig. 3.20 shows the distribution of *dA/dN* predicted from Eq. (3.22) with *B* determined from Eq. (3.25). The proposed approach gives relatively accurate predictions of *dA/dN* for both the steels and aluminum alloys. As shown in Fig. 3.21, compared with experimental data, the predicted *dA/dN* has a mean of 1.028 and the coefficient of variation is 0.264 for steels, the mean is 1.310 and the coefficient of variation is 0.253 for aluminum alloys. In general the phase transformation theory predicts fatigue crack propagation rate conservatively with reasonable accuracy. It should be noted that Eq. (3.25) are only applicable to steels and aluminum alloys and may not applicable to brittle or quasi-brittle materials such as glass or intermetallics. Most of the materials analyzed in the case study are relatively ductile, and the value of *dA/dN* depends

mostly on the first term on the right-hand side of Eq. (3.22). For a very ductile material, the second term on right hand side of Eq. (3.22) can be neglected, although it could play an important role on fatigue crack propagation in brittle materials.

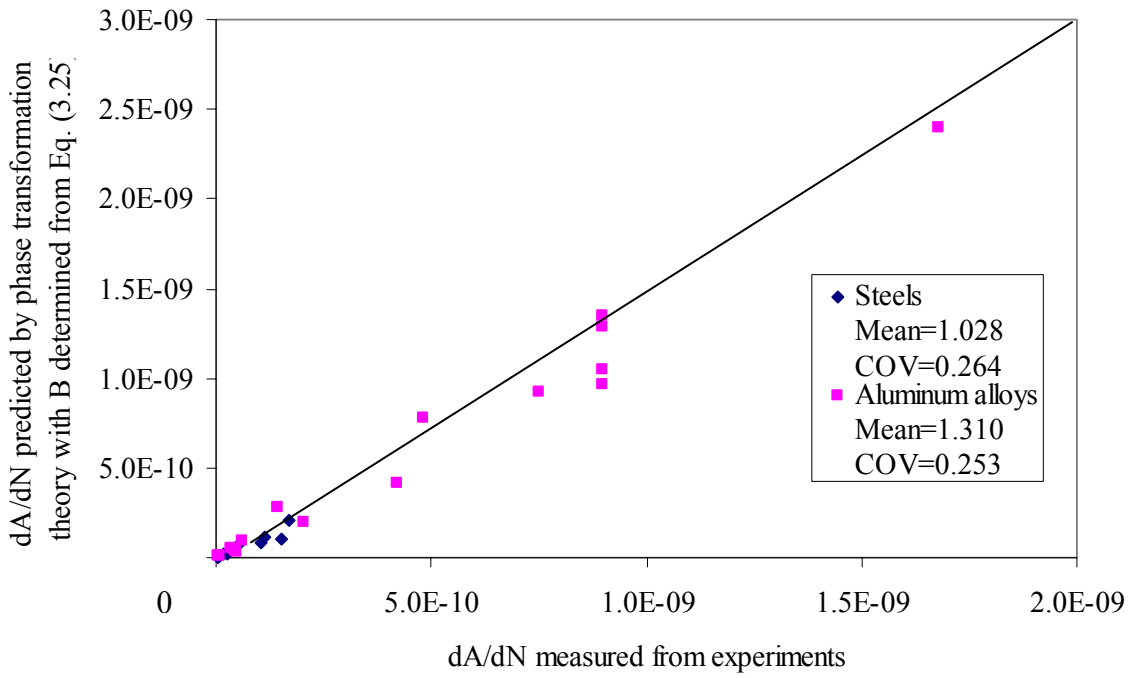

Figure 3.21 Predictions of fatigue crack propagation rate *dA/dN* for case study using Eq. (3.22) with *B* determined from Eq. (3.25)

The proposed theory can be applied to predict fatigue crack propagation in interconnects if corresponding experimental data for solder and intermetallics materials are available. Compared with solder, the intermetallics are expected to be relatively brittle, so the value of *U* will be smaller and the crack propagation rate will be higher in intermetallics based on Eq. (3. 23). In addition less energy is required for a crack to nucleate and propagate at an interface (heterogeneous nucleation) such as in Sn-Ag-Cu eutectic solder or at the interface between the

solder and an intermetallic sub-layer. The interfacial failure caused by fatigue crack propagation between bulk solder and intermetallic layers is expected to be an important failure mode of interconnects.

Eq. (3.23) was applied to predict the fatigue crack propagation rate *da/dN* of solder with the value of *U* determined numerically. The material constants *l* and *m* in Eq. (3.24) were obtained through analysis of the material behavior and by fitting to the experimental data. For 63Sn-37Pb eutectic solder, the material constants values were suggested to be: $l = 8.5 \times 10^{-4}$ and *m*=-1.5. For Sn-3.5Ag eutectic solder, the values for the material constants were suggested as: $l = 3.0 \times 10^{-4}$ and *m*=-1.3. Fig. 3.22 shows the distribution of *da/dN* predicted using the phase transformation theory. It is seen that the proposed approach gives relatively accurate predictions of *da/dN* for both Sn-Ag and Sn-Pb solders. Compared with the experimental data of fatigue crack propagation rate of Sn-3.5Ag and 63Sn-37Pb eutectic solder, Fig. 3.23, the predicted *da/dN* has mean values of 1.15 and1.10 and the coefficient of variation of 0.412 and 0.272 for Sn-3.5Ag and 63Sn-37Pb eutectic solder, respectively. The phase transformation theory predicts fatigue crack propagation rate conservatively and with reasonable accuracy. With enough experimental data to determine the material constants, the theory can be applied to different types of Pb-rich and Pb-free solders.

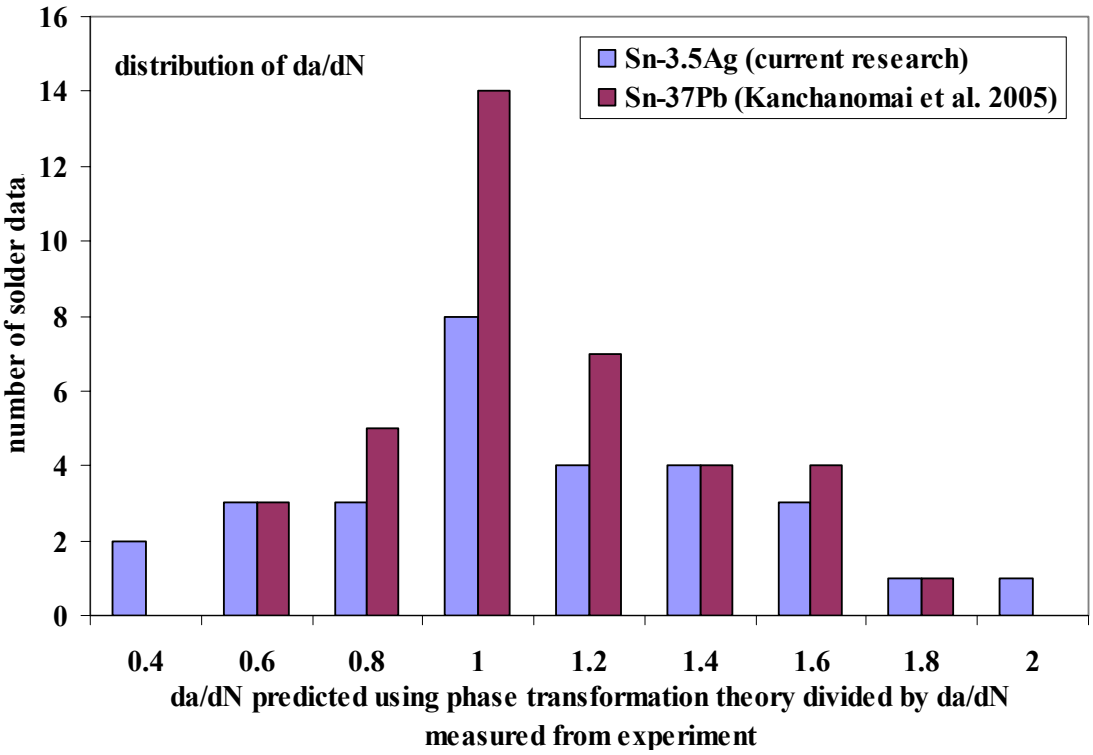

Figure 3.22 Distribution of *da/dN* using phase transformation theory compared with experimental data of Sn-3.5Ag and 63Sn-37Pb eutectic solders (Kanchanomai et al. 2005)

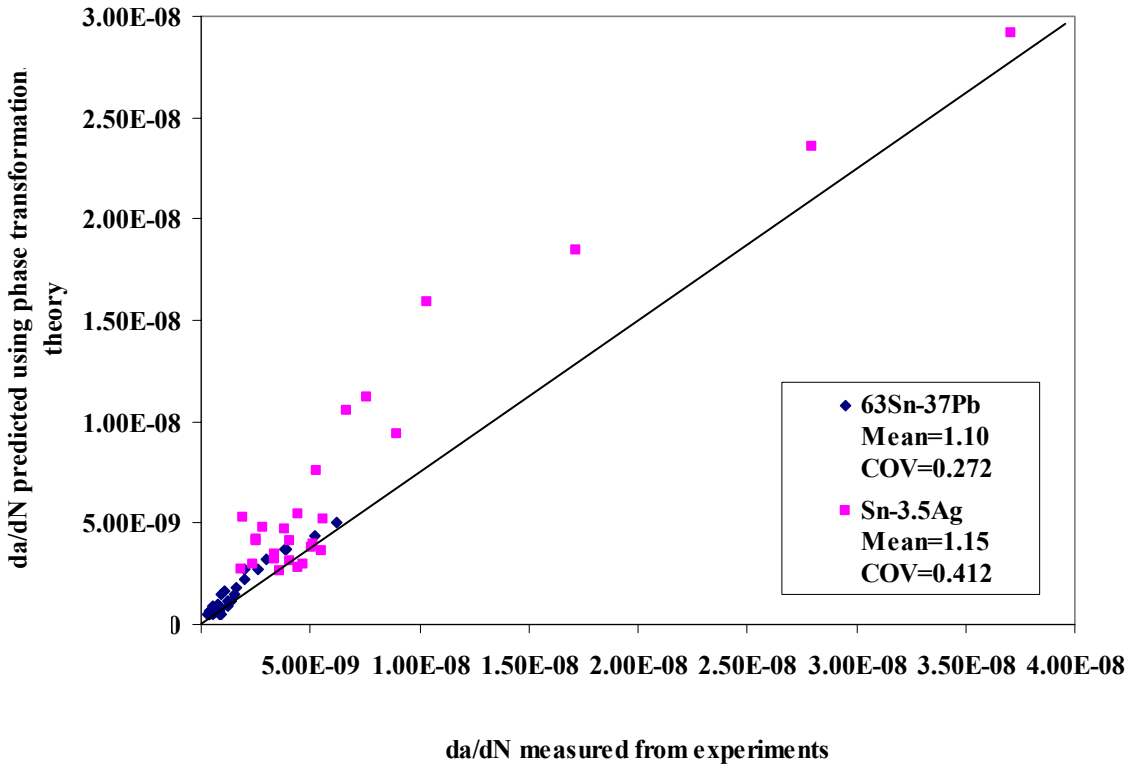

Figure 3.23 Predictions of fatigue crack propagation rate *da/dN* for case study using phase transformation theory (experimental data from Vaynman's experiments and Kanchanomai et al. 2005)

3.8 Conclusion

Fatigue damage of solid materials consists mainly of dislocation and microcrack accumulation. The fatigue crack nucleation and propagation significantly depends on the accumulation of dislocations and other lattice defects at nucleation sites. Based on phase transformation theory and fracture mechanics, a theoretical approach to predict crack nucleation has been extended to predict fatigue crack propagation. The theory is applied to predict the fatigue crack propagation rate for different materials. Compared with experimental data, the prediction of the proposed approach has a mean of 1.028 to 1.062 and the coefficient of variation

is 0.255 to 0.264 for steels, the mean is 1.185 to 1.310 and the coefficient of variation is 0.253 to 0.286 for aluminum alloys. Fatigue experiment on solder interconnects was conducted by B. Fiedler at Northwestern University. Based on experimental and finite element analysis, phase transformation theory was applied to predict fatigue crack propagation in interconnects. Fatigue experiments on Sn-3.5Ag solder alloy were conducted by S. Vaynman at Northwestern University, and crack propagation rate is characterized successfully by stress intensity factor range ΔK. The fatigue crack was found to initiate in the solder alloy and migrate to the solder/IMC layer interface; the crack propagated near the interface and caused catastrophic failure. Finite element analysis incorporating UCP theory and CZM was applied to determine the required energy U to propagate a unit crack area in solder. Interconnects failure caused by fatigue crack nucleation and propagation under cyclic loading was analyzed. Phase transformation theory was applied to predict the fatigue crack propagation rate of Sn-3.5Ag and 63Sn-37Pb eutectic solder. Compared with experimental data, the prediction of the proposed approach has a mean of 1.15 and 1.10 and the coefficient of variation of 0.412 and 0.272 for Sn-3.5Ag and 63Sn-37Pb eutectic solder, respectively. The results show that the phase transformation theory is not only accurate and consistent but also conservative. The proposed theory provides a scientific basis for a theoretical examination to fatigue crack nucleation and propagation in interconnects.

Chapter 4

Electromigration Effect on Void Propagation near the Interface of Solder and Intermetallic Compound

4.1 Introduction

As the size of electronic devices and solder interconnects reduces, the current density is rapidly increasing and the electromigration effect becomes more critical to interconnect failure. For next generation of chips, the solder interconnect size goes into micron and nanometer scale (SEMATECH 1999) as shown in Fig. 4.1.

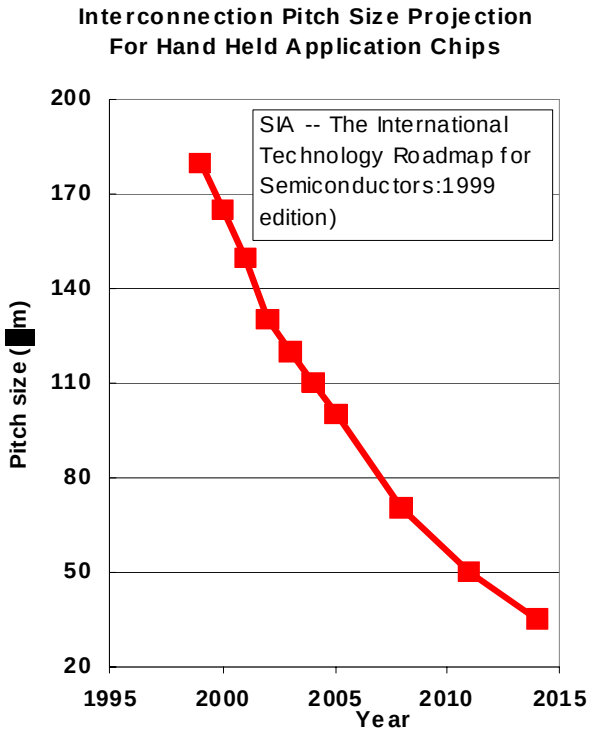

Figure 4.1 Projection of interconnect sizes in μm (SEMATECH 1999)

The mechanism of electromigration effect on solder/IMC interfacial void propagation and interconnect failure is studied in this chapter. A kinetic mass diffusion model is developed to predict void width and propagation speed near the interface of IMC and solder caused by electromigration. The current concentration effect at void tip is considered by using computational analysis. The model gives reasonable prediction to the void width and propagation velocity compared with experimental observations.

4.2 Kinetic Mass Diffusion Model to Predict Electromigration Effect for Pancake Type Void Propagation

The trend of minimization of electronic devices results in higher operating current densities in interconnects. Electromigration plays an important role in interconnect failure mechanisms under high current density (Zhang et al. 2006). Generally electromigration is the transport of material caused by the gradual movement of the ions in a conductor due to the momentum transfer between conducting electrons and diffusing metal atoms. As the structure size in electronic devices decreases, the physical significance of this effect increases. Experimental research relating the electromigration effect on interconnect failure has been performed by different investigators in the past decade. Gan and Tu (2002) conducted a series of experiments to analyze the electromigration effect in IMC and bulk solder under different current densities. They found that voids began to appear in the solder part just in front of the solder/IMC cathode interface and grew toward the interface between the IMC and solder bulk. Similarly, Miyazaki and Omata (2006) observed that voids nucleate from the current crowding point and then propagated through the interface between the solder and IMC. They concluded that the polarity and tilting effects are key factors to the electromigration effect on solder behavior.

Hauschildt et al. (2007) conducted statistical analysis to electromigration lifetimes and void evolution in copper interconnects. Recently, Gee et al. (2005) observed pancake type voids at the interface of IMC and bulk solder caused by electromigration under high current density; Fig. 4.2 shows the scanning electron microscope (SEM) micrographs of void formation in the flip chip 95.5Sn-4Ag-0.5Cu solder. Until recently, two types of electromigration failure modes in solder interconnects were observed in experiments from different researchers: cotton or pancake type voids (Lee et al. 2006). The void types were related to the size and location of defects in interconnects, and the applied electric currents. High current density causes a pancake type void, while medium current density or more defects in an interconnect causes a cotton type void. Once a crack exists in an interconnect, the void mechanism caused by cracking dominates the cotton type void; the void mechanism caused by current crowding dominates the pancake type void.

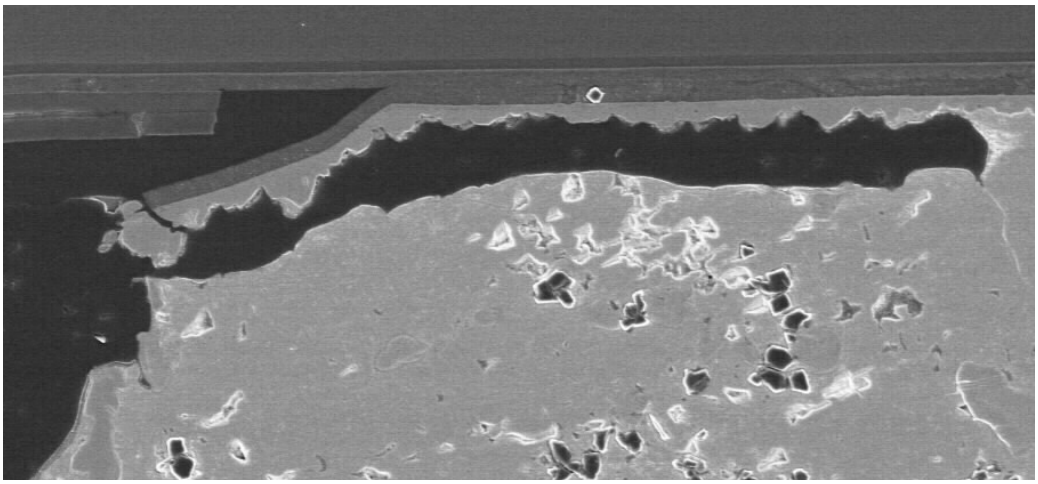

Figure 4.2 SEM micrographs of void formation in flip chip 95.5Sn-4.0Ag-0.5Cu solder (Gee et al. 2005)

Theoretical research has been conducted on electromigration caused failure of different materials during the past thirty years (Rice and Chuang 1981) (Bower and Freund 1993)

(Thouless et al. 1996) (Gungor and Maroudas 2007). Suo et al. (1994, 1996) developed a model to predict electromigration effect related to void caused damage in aluminum lines based on mass diffusion theory; Zhang et al. (2006) developed an approach to predict voids in a interconnect, considering the Gibbs-Thomson effect and mass conservation in the interconnect, however, the chemical potential gradient effect on void propagation is not included in their model. Based on the research conducted by Professor Suo et al. and the group led by Professor K.N. Tu, a kinetic mass diffusion model is developed in this chapter to predict effect of electromigration on interfacial failure between solder and intermetallic compound (IMC) of an interconnect. The electromigration, chemical potential gradient, and electric current crowding effects are all incorporated in the model. The model is applied to predict the void width and propagation speed near the IMC/solder interface caused by electromigration. The predictions are compared with experimental observations, and the electric current crowding effect ahead of void tip is considered using finite element analysis.

A crack in a solder joint is caused by dislocation processes accelerated by stress concentration and defects such as voids. However, the circular void is not a stable phase; under high current density and thermal stress, a void will grow by atomic flux. From diffusion theory, the flux of atoms is driven by both variations in chemical and electrical potentials. At high current densities, void formation and propagation become important. Based on the well known Einstein relation (Einstein 1905), the actual flux is proportional to the thermal dynamic force. For solder interconnects, the thermal dynamic force has contributions derived from the electron wind force and stress gradient caused by the mismatch of thermal expansion coefficients of different materials. Current crowding and joule heating effects also play important roles in interconnect failure. Based on Herring's formula (Herring 1951), the surface energy

corresponding to capillary force can be determined. The thermal stress field distribution and stress gradient can be determined numerically. Thus, the kinetic mass diffusion model based upon the Einstein relation to predict void growth in an interconnect is available.

For a Sn-Ag-Cu eutectic solder interconnect with a void defect, the stress gradient can be determined from 3D finite element analysis, as shown in Fig. 4.3. Cyclic shear loading is applied to simulate the thermal-mechanical loading caused by the thermal expansion coefficient mismatch of the different materials. The variation of stress with distance from void defect point along Y axis (vertical) is given in Fig. 4.4. The stress gradient in bulk SnAgCu eutectic solder and the Cu_6Sn_5 IMC layer is equal to 0.37 MPa/μm and 2.48 MPa/μm, respectively.

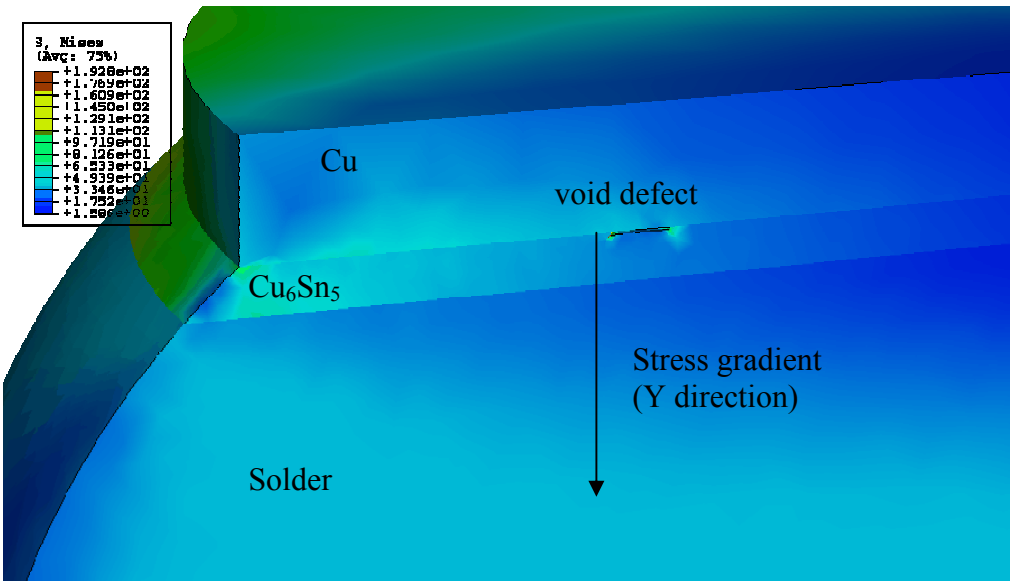

Figure 4.3 von Mises stress distribution in interconnects with void defect under shear loading

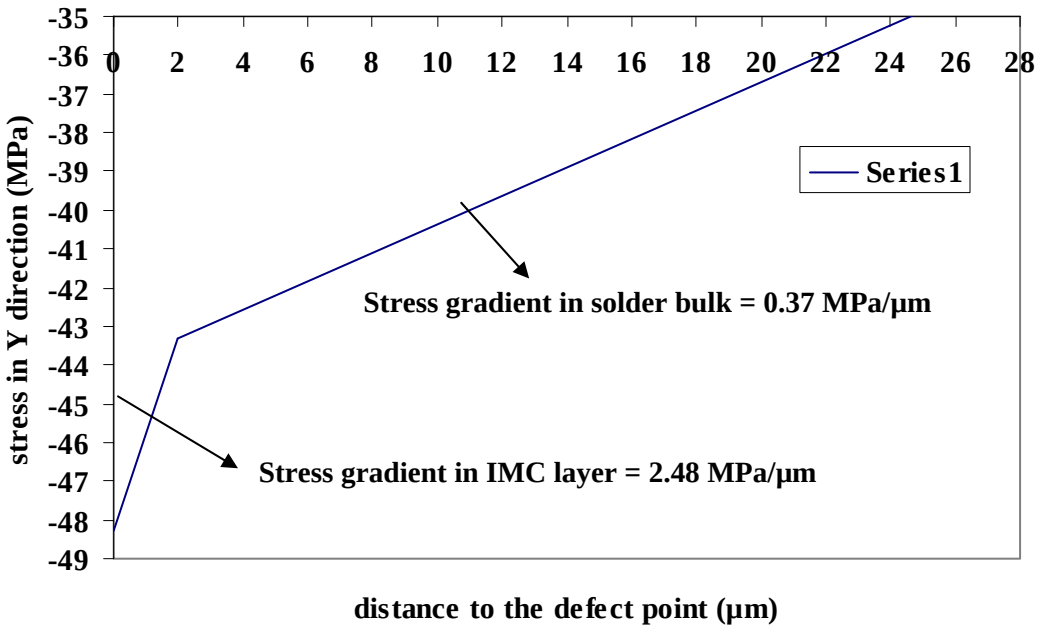

Figure 4.4 Variation of stress with the distance from void defect point in Y direction (MPa)

From the Einstein relation, the actual atomic flux $J = \frac{D_s \delta_s}{\Omega k T} F$, where D is the diffusivity (cm^2/s); Ω is the atomic volume (cm^3); k is the Boltzmann constant (1.38×10^{-23} joules/kelvin); T is the absolute temperature (K); δ_s is thickness of diffusion layer, which assumed equal to 0.5nm for the interface of solder/IMC (Zhang et al. 2006); F is the thermal dynamic force which consists of electromigration and stress migration forces. The electromigration force per atom, written as $F_E = -eE_t Z^* = -e\rho j Z^*$, where Z^* is the effective charge number, which includes the electric field and momentum exchange effects; e is the electron charge (1.6×10^{-19} Coulomb/electron); ρ is the resistivity (μΩcm); j is the current density (A/cm^2); E_t is the electric field projected on the surface: the electric field component tangent to the dislocation line. From the experimental results of Ye and Tu (2000), Wu et al. (2004), the effective charge number is Z_{Sn}^* =17 for Sn and Z_{η}^* =50 for Cu_6Sn_5. The resistivity of Sn is ρ_{Sn}=13.25 μΩcm and that of

Cu_6Sn_5 is ρ_η=17.5 μΩcm; the atomic volume Ω is taken as 2.0×10^{-23} cm^3. With the above experimental data, the electromigration and stress migration force of atoms can be determined. For example, with an applied current density equal to 1.5×10^4 A/cm^2, in a IMC layer, the electromigration force $F_{em} = -Z_\eta^* e\rho_\eta j = 21\times10^{-17}$ N, and the stress migration force: $F_{sm} = \Omega\frac{\partial\sigma}{\partial y} = 4.96\times10^{-17}$ N; in bulk solder, the electromigration force $F_{em} = -Z_{Sn}^* e_{Sn}\rho_{Sn} j = 5.4\times10^{-17}$ N; stress migration force: $F_{sm} = \Omega\frac{\partial\sigma}{\partial y} = 0.74\times10^{-17}$ N.

It is noted that in both IMC layer and bulk solder, electromigration and stress migration forces are generally in the same order of magnitude, and the electromigration force is stronger than the stress migration force under the applied current density of 1.5×10^4 A/cm^2. The results prove that the electromigration effect provides an important contribution to the interconnect failure mechanism under high current density.

Under electromigration the atoms in a solder interconnect will be driven to the anode and a corresponding vacancy flux will return to cathode interface; because the bonding energy in Cu_6Sn_5 is larger, the flux of vacancy that enters IMC layer is small, and a flux divergence of vacancy occurs at the interface, which leads to vacancy supersaturation, void nucleation, and finally void propagation at the solder/IMC interface.

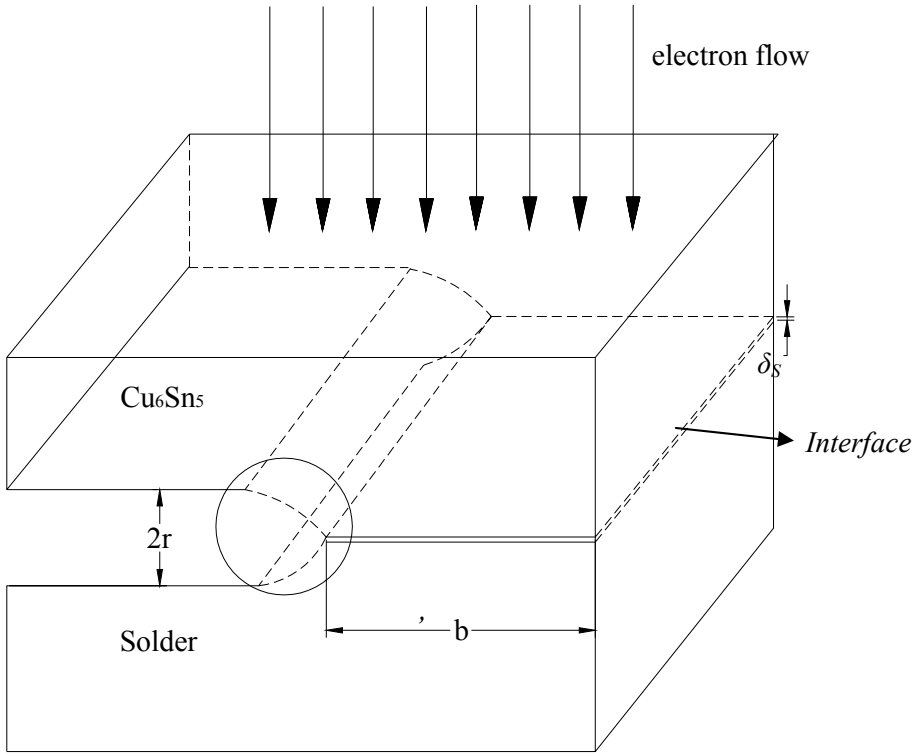

Figure 4.5 3D schematics of void propagation along interface of IMC and solder

To predict void propagation at the solder/IMC interface under high current, the schematics of void propagation along interface of IMC and solder is shown in Fig. 4.5. It is assumed that the flux of atoms is driven by variations in both chemical potential and electromigration, and the void width is assumed to be 2*r*. The fracture process zone, which is the zone contributed to the atom diffusion ahead of the void tip, is *b'*. The chemical potential μ per atom on the surface is approximated as: (Bower and Freund 1993):

$$\mu = \mu_0 + \Omega[\phi - \gamma_s \kappa] = \mu_0 + \Omega[\phi - \sigma_t] \tag{4.1}$$

where μ_0 is the potential of the bulk; $\phi = \frac{1}{2}\sigma_{ij}\varepsilon_{ij}$ is the elastic energy strain density; γ_s is the surface energy (J/m^2); κ is the curvature of the surface of the void tip. The stress acts normal to the grain boundary is σ_t.

In Eq. (4.1), there are two contributions to the chemical potential of an atom on a free surface: the surface energy term and the elastic strain energy term. Rice and Chuang (1981) showed that for most cases the elastic strain energy effect can be neglected, and this assumption is adopted in current research. Eq. (4.1) can thus be simplified to:

$$\mu = \mu_0 - \Omega\gamma_s\kappa = \mu_0 - \Omega\sigma_t \tag{4.2}$$

The flux on the void surface due to the chemical potential is expressed as:

$$J_s = -\frac{D_{\text{int}}}{\Omega kT}\frac{\partial\mu}{\partial s} = \frac{D_{\text{int}}\gamma_s}{kT}\frac{\partial\kappa}{\partial s} = \frac{D_{\text{int}}}{\Omega kT}\frac{\partial\sigma}{\partial y} \tag{4.3}$$

where $\frac{\partial\mu}{\partial s}$ denotes the gradient of chemical potential along the void surface; $\frac{D}{kT}$ is the atomic mobility; and $\frac{\partial\sigma}{\partial y}$ is the stress gradient along the direction of electron flux.

The curvature κ of the surface of the void tip in Eq. (4.3) is obtained as:

$$\kappa = -\frac{d\theta}{ds} \approx -\frac{d\tan\theta}{ds} = -\frac{dX}{dsdY} = -\frac{d\sin\theta}{dY} \tag{4.4}$$

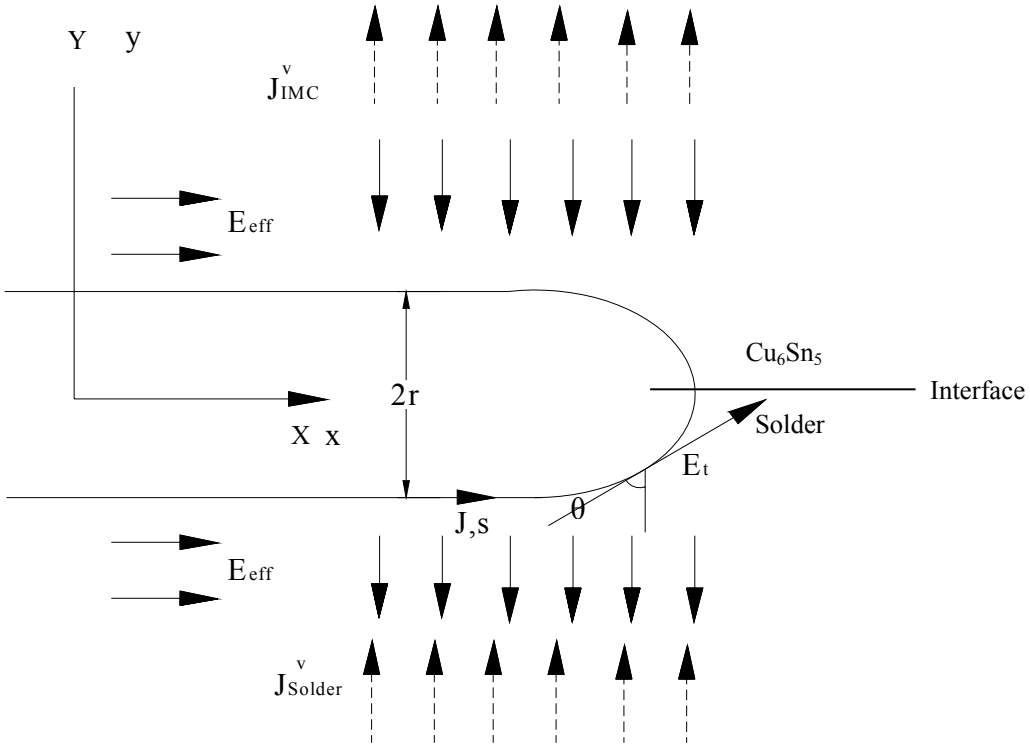

Figure 4.6 2D schematics of void tip at the interface of IMC and solder

The schematics of the pancake type void tip at the interface of IMC and solder in Fig. 4.5 can be simplified to a 2D case, as shown in Fig. 4.6. The solid arrows represents the current crowding that pushes atoms from the top to the bottom, and the dashed arrows represents the vacancies that go back from the solder to IMC layer (Cu_6Sn_5). The effective electric field is E_{eff}. The void flux on the void surface due to electromigration can be expressed as (Suo et al. 1994):

$$J_s = \frac{D_s \delta_s}{\Omega k T}(-eE_t Z_s^* + \Omega \gamma_s \frac{d\kappa}{dl}) \qquad (4.5)$$

The first term in Eq. (4.5) corresponds to the electron wind force and the second term to capillary force, based on Herring's formula (Herring 1951). Physically the electric field projected on the void surface tends to move atoms away from the void tip and extends the void.

Surface energy tends to move atoms toward a free surface. The propagation of the void is determined by the competition between the electric field and surface energy.

Assume κ is a function of Y only, the curvature gradient is determined by:

$$\frac{d\kappa}{ds} = -\frac{d^2 \sin\theta}{dY^2}\cos\theta = \sin\theta\cos\theta(\frac{d\theta}{dY})^2 - \cos^2\theta(\frac{d^2\theta}{dY^2}) \tag{4.6}$$

From mass conservation and by assuming the flux J is a function of Y, then $J(Y) = Yv/\Omega$. Substituting Eq. (4.6) into Eq. (4.5), and defining $y=Y/r$, gives (Suo et al. 1994):

$$\frac{1}{\mu}\frac{d^2 \sin\theta}{dy^2}\cos\theta + \sin\theta + y = 0 \tag{4.7}$$

The void shape for the composite is assumed to be the same as that in Suo et al.'s work (1994). With the following initial conditions: $\sin\theta = 1$, $d\sin\theta/dy = 0$, at $y = -1$, r, the radius of the void equals $d/2$, where d is the width of the void.

By approximating the void tip curvature as $\kappa \approx 1/r$, the curvature gradient is of order $\approx 1/r^2$, and a dimensionless coefficient is defined based on Eq. (4.5):

$$\eta = \frac{\overline{Z}^* e\overline{\rho}j' r^2}{\gamma_S \Omega} \tag{4.8}$$

where $\overline{Z}^* = a_{Sn}Z^*_{Sn} + a_\eta Z^*_\eta$, $\overline{\rho} = b_{Sn}\rho_{Sn} + b_\eta\rho_\eta$, $a_{Sn} + a_\eta = 1$, $b_{Sn} + b_\eta = 1$. For simplicity, $\overline{Z}^* = \frac{Z^*_{Sn} + Z^*_\eta}{2}$; $\overline{\rho} = \frac{\rho_{Sn} + \rho_\eta}{2}$ are defined here; further experimental work will be required to accurately determine the value of unitless constant $a_{Sn}, a_\eta, b_{Sn}, b_\eta$, which determine the fraction of Sn or Cu_6Sn_5 atoms passing through the interface. Here η is equal to 5.743 for the pancake type void, which is determined from solution of Eq. (4.7) using a fourth-order Runge-

Kutta method, and perturbation analysis is conducted to obtain the eigen-solution of Mathieu's equation in Suo's analysis (Suo et al. 1994).

The definition of the vacancy flux of Cu_6Sn_5 and solder by Zhang et al. (2006) is adopted here:

$$J_\eta^v = \frac{C_\eta^{bulk} D_\eta}{kT} Z_\eta^* e \rho_\eta j' \tag{4.9}$$

$$J_{Sn}^v = \frac{C_{Sn}^{bulk} D_{Sn}}{kT} Z_{Sn}^* e \rho_{Sn} j' \tag{4.10}$$

where J_η^v and J_{Sn}^v are the vacancy flux of Cu_6Sn_5 and solder respectively; C is the concentration, $C=1/\Omega$ for pure metal ($1/cm^3$);

Assuming the pancake type void extends steadily, i.e., the front moves with an invariant shape and has speed v relative to the lateral X direction. From the mass conservation principle, the increasing void volume vd is equal to the volume of atoms diffusing out at the fracture process zone in front of the void, where the fracture process zone is the region in which electronmigration caused atom flux contribute to the void formation.

$$vd = \Omega J_v = (C_{Sn}^{bulk} D_{Sn} Z_{Sn}^* \rho_{Sn} - C_\eta^{bulk} D_\eta Z_\eta^* \rho_\eta) \frac{ej'\Omega}{kT} b' \tag{4.11}$$

Here b' is the fracture process zone width. By estimating the width of b' considering the Gibbs-Thomson effect, Zhang et al. (2006) have calculated that the width of b' varies from 10.2% to 17.7% of solder diameter for a 95.5Sn-4Ag-0.5Cu eutectic solder, and 15% of the solder diameter is suggested as the value of b'; this assumption is adopted here. The current density j' in Eq. (4.11) is taken as the average current density in the fracture process zone rather than the original applied current density.

Thus, the void opening width d can be determined from Eq. (4.8) with η=5.743,

$$d = 2r = 4.793\sqrt{\frac{\gamma_S \Omega}{\overline{Z}^* e \overline{\rho} j'}} \tag{4.12}$$

The void propagation velocity v is determined from Eq. (4.11) as:

$$\begin{aligned} v &= \frac{\sqrt{\overline{Z}^* e \overline{\rho} j'}}{4.793\sqrt{\gamma_S \Omega}} (C_{Sn}^{bulk} D_{Sn} Z_{Sn}^* \rho_{Sn} - C_{\eta}^{bulk} D_{\eta} Z_{\eta}^* \rho_{\eta}) \frac{ej'\Omega}{kT} b' \\ &= \frac{0.209(ej')^{3/2} (\overline{Z}^* \overline{\rho} \Omega)^{1/2} b'}{\gamma_S^{1/2} kT} (C_{Sn}^{bulk} D_{Sn} Z_{Sn}^* \rho_{Sn} - C_{\eta}^{bulk} D_{\eta} Z_{\eta}^* \rho_{\eta}) \end{aligned} \tag{4.13}$$

Here the value 0.209 in Eq. (4.13) arises from dimensionless parameter η and can be varied for different void shapes.

4.3 Computational Analysis to Consider the Current Concentration Effect

Computational analysis is conducted to analyze the current concentration effect near the void tip. The effective current density *j'* can be determined based on the thermal-electrical finite element analysis as introduced in Chapter 2. The current density distribution in a Sn-Ag solder joint under applied current density of 10^4 A/cm^2 with a void propagating near the interface of solder/IMC is shown in Fig. 4.7. Here A_v is the void area and A_t is the interconnect cross section area. The void area can be related to crack length by:

$$A_v = R^2 \arccos(L/R) - L\sqrt{R^2 - L^2} \tag{4.14}$$

where R is the radius of solder bulk and $L = d/2 - C$, d is the pad opening. (Gee et al. 2005).

Fig. 4.8 shows the solder/IMC interface current density and temperature distribution in the solder interconnect with void nucleation at the upper left corner, where current crowding occurs. The cross-section is plotted on the X-Y plane and the current density is plotted along the

Z axis. The electrical current density ECD has units in A/cm^2, and X, Y are the nodes coordinates in μm. Higher temperature caused by joule heating was observed near the void nucleation plot. Fig. 4.9 shows the corresponding IMC/solder interfacial current density distribution with a void propagation under the applied current density of 1.5×10^4 A/cm^2.

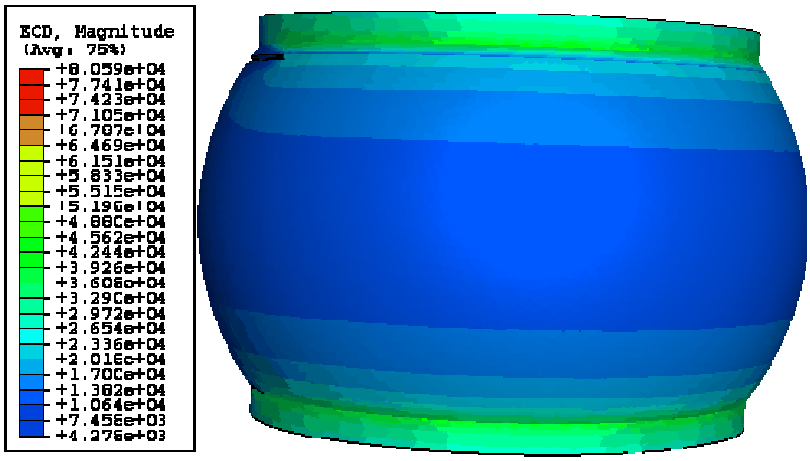

A_v/A_t = 0.6%

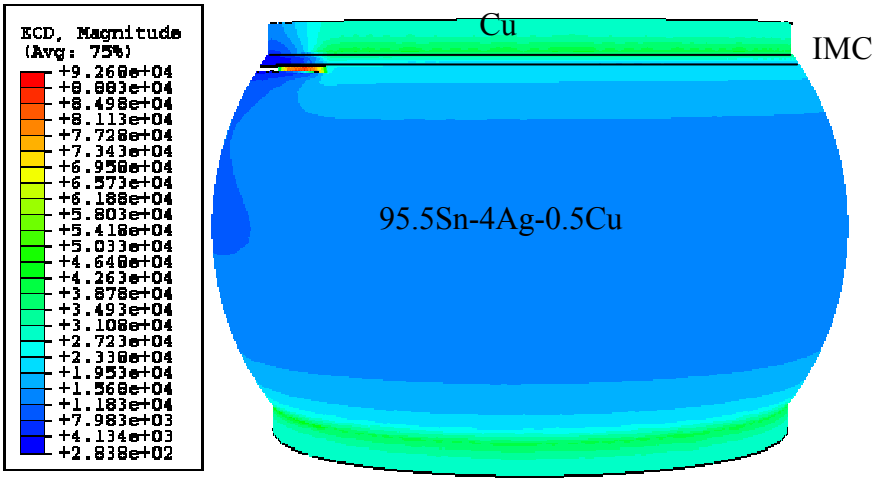

A_v/A_t = 2.2%

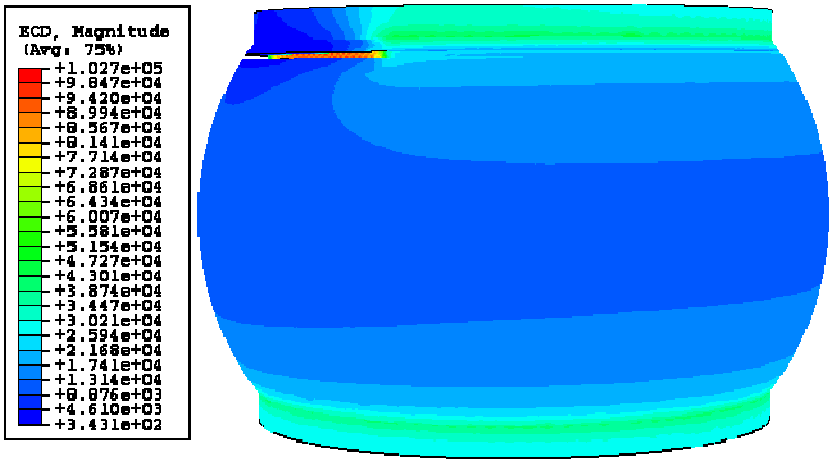

A_v/A_t = 6.1%

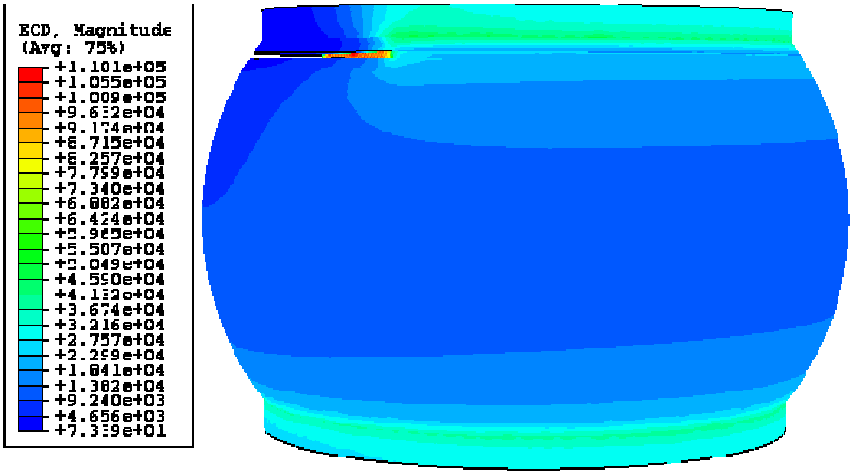

A_v/A_t = 11.0%

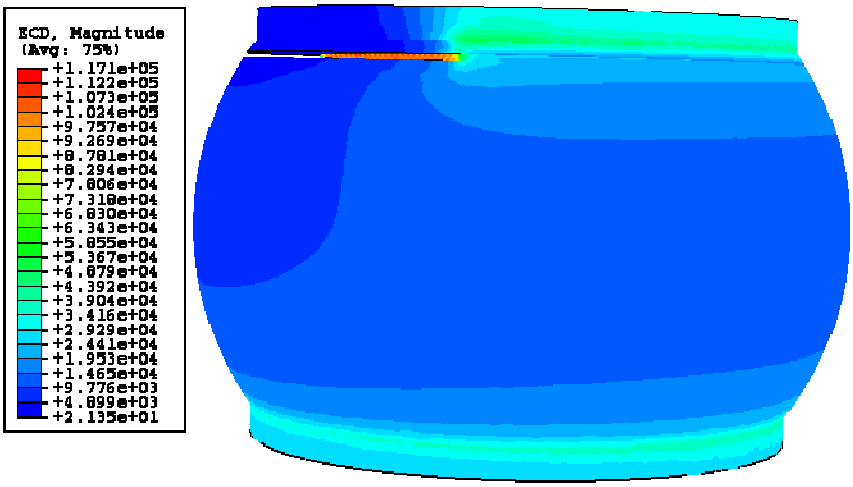

A_v/A_t = 16.5%

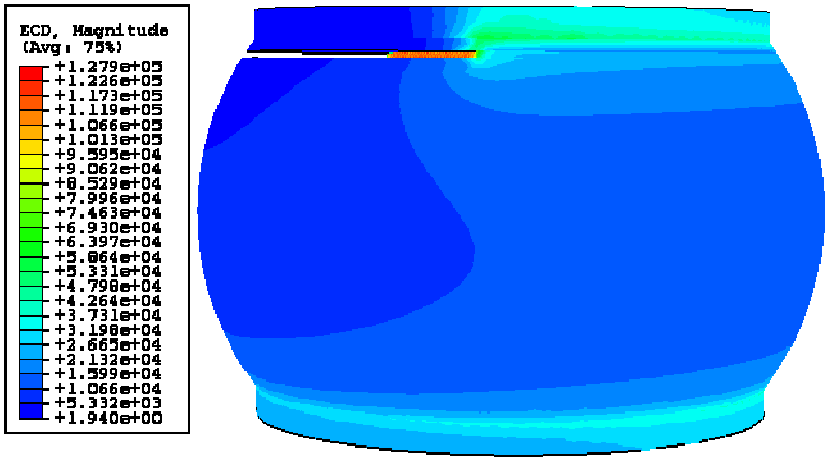

A_v/A_t = 29.2%

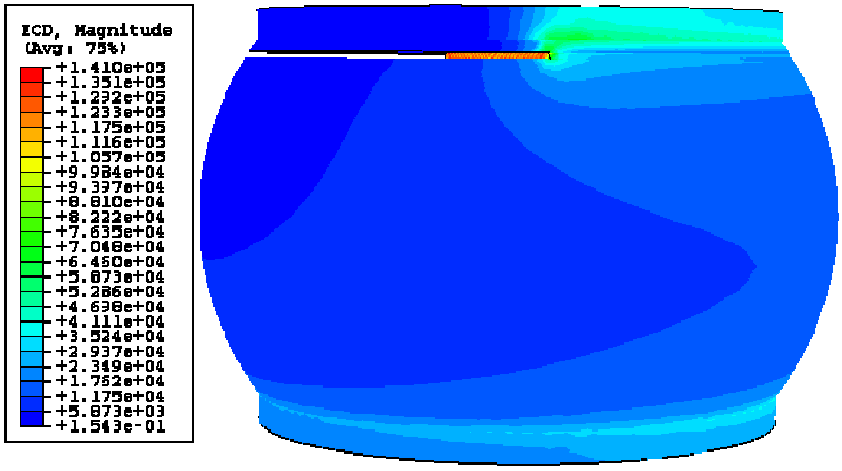

A_v/A_t = 42.9%

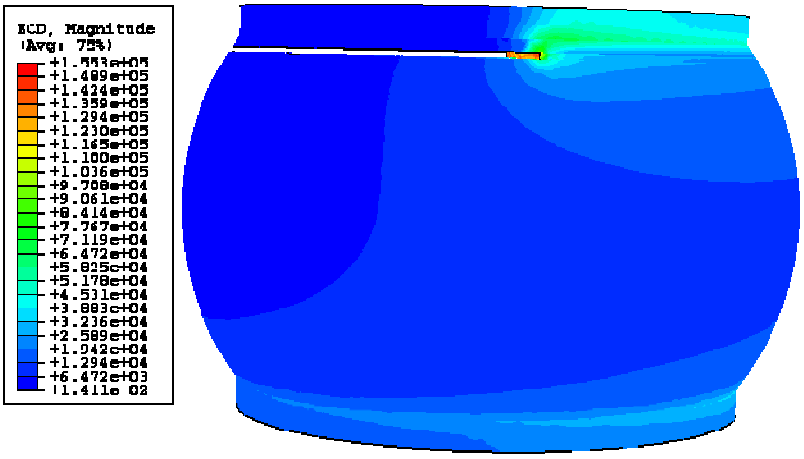

A_v/A_t = 57.1%

Figure 4.7 Current density distribution in a lead free solder joint under applied current density of 1.5×10^4 A/cm^2 with a void propagating near the interface of solder and IMC

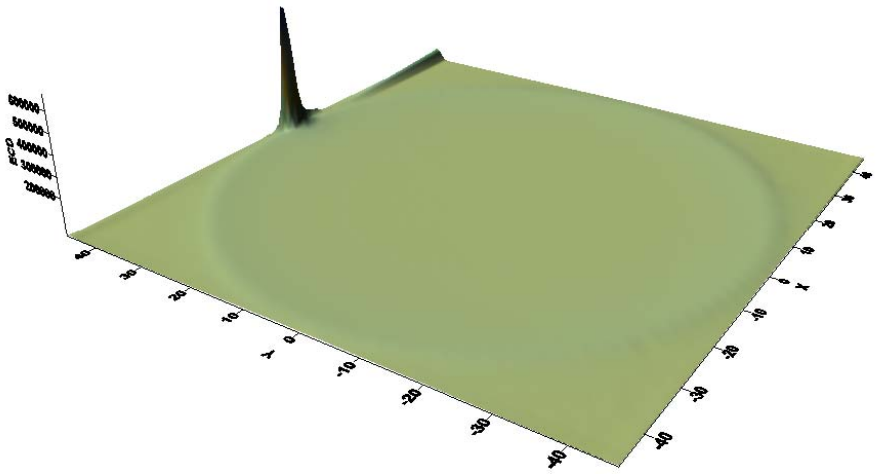

ECD (electrical current density A/cm^2)

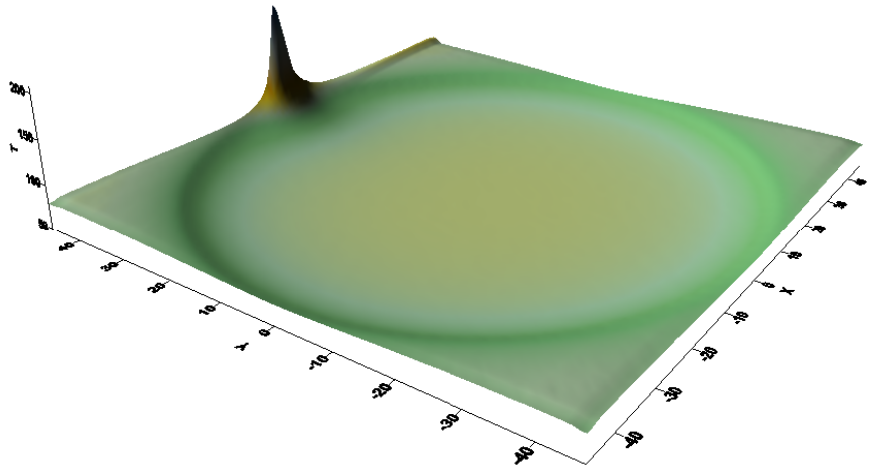

T (temperature ˚C)

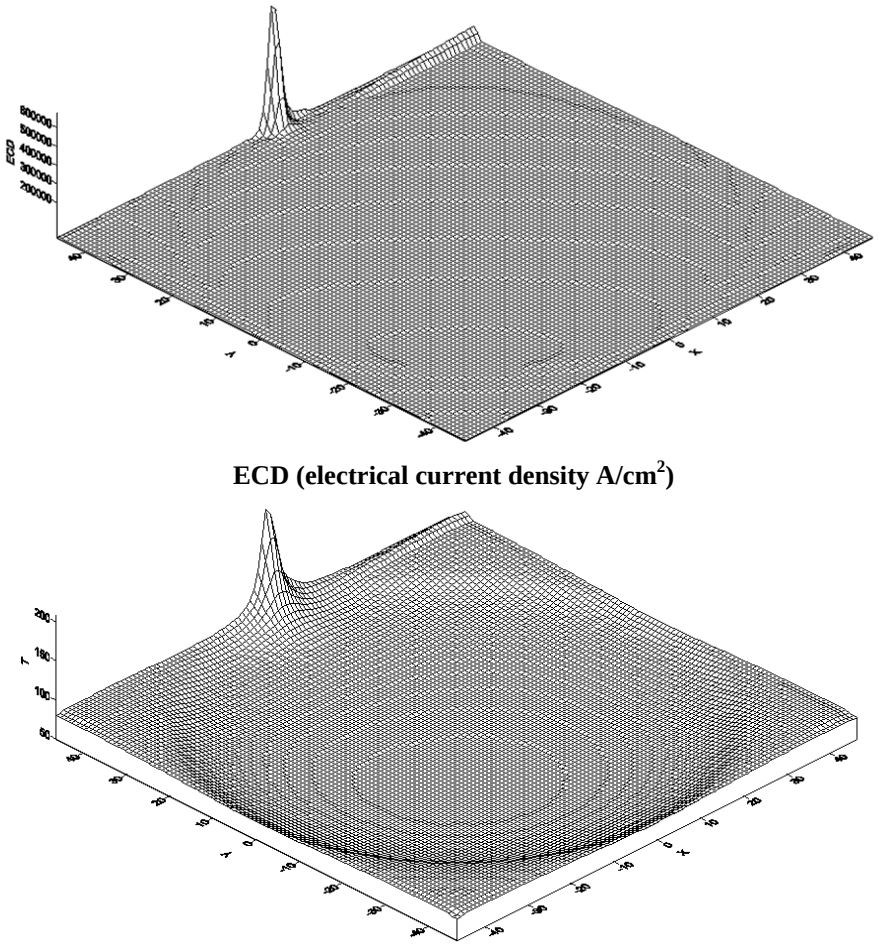

ECD (electrical current density A/cm^2)

T (temperature ˚C)

Figure 4.8 Solder/IMC interface current density and temperature distribution in a 95.5Sn-4Ag-0.5Cu eutectic solder interconnect with a void nucleation at the upper left corner

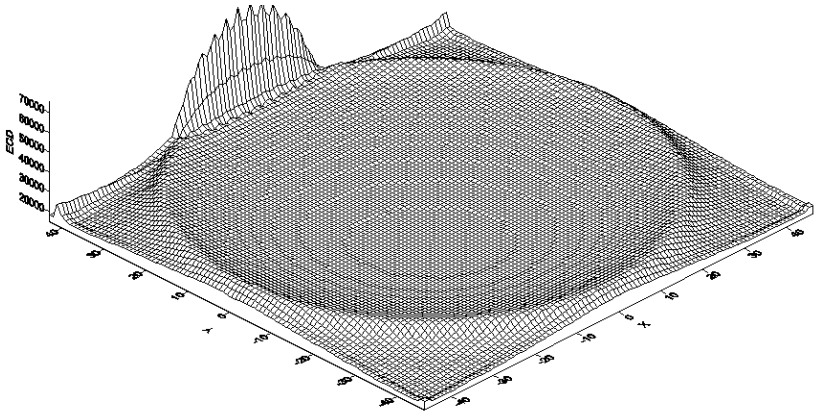

A_v/A_t = 0.6% (j_{max}=8.059×10^{4}A/cm^2)

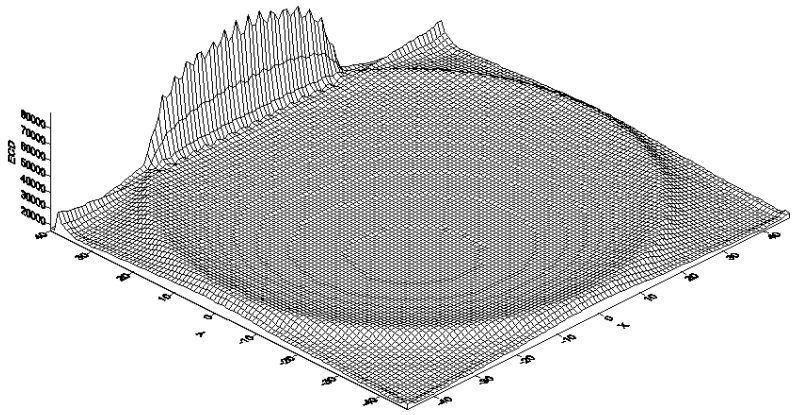

A_v/A_t = 2.2% (j_{max}=9.268×10^{4}A/cm^2)

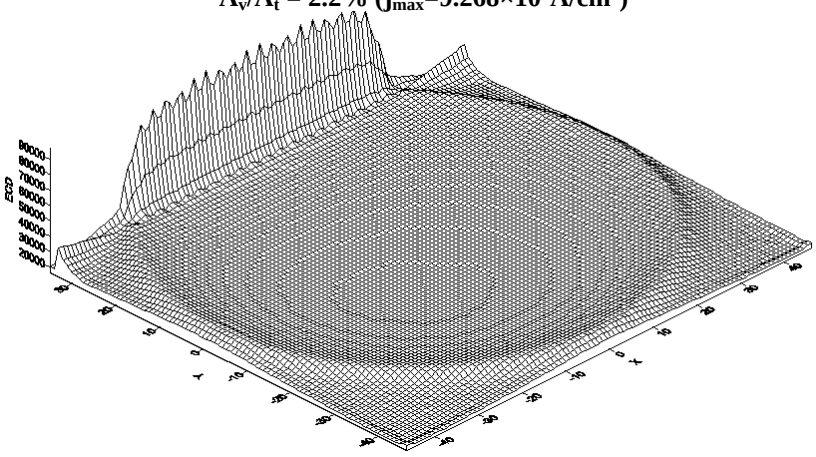

A_v/A_t = 6.1% (j_{max}=10.27×10^{4}A/cm^2)

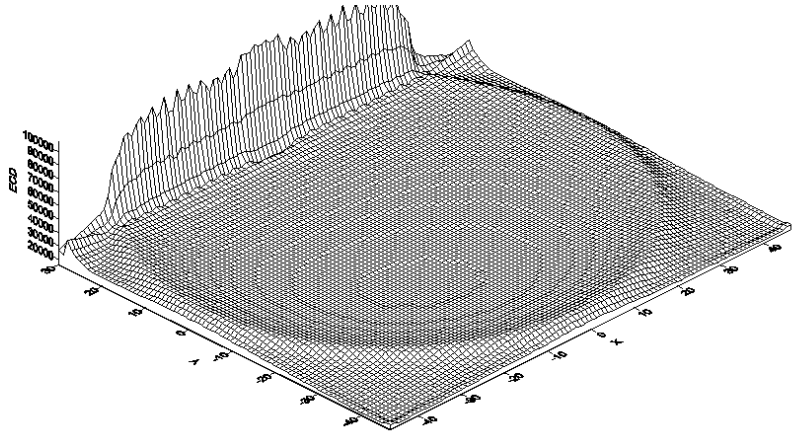

A_v/A_t = 11.0% (j_{max}=11.01×10^4A/cm^2)

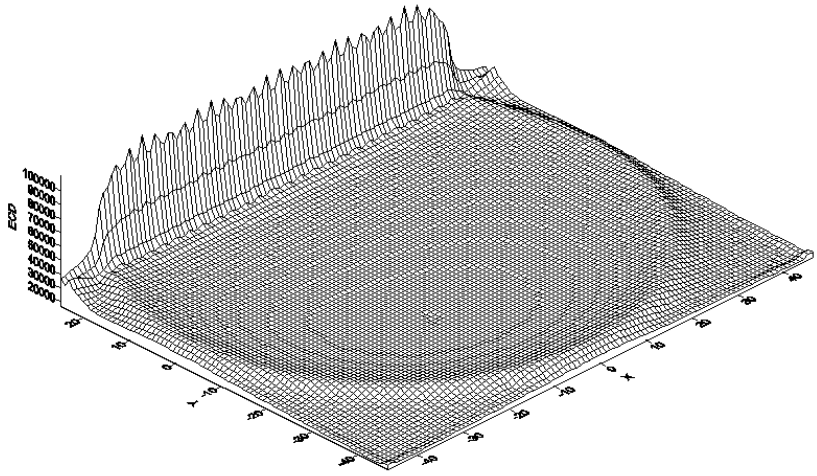

A_v/A_t = 16.5% (j_{max}=11.71×10^4A/cm^2)

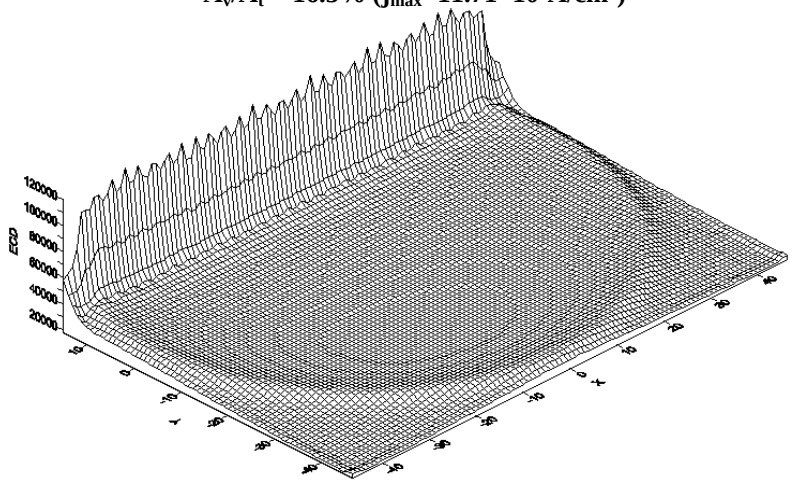

A_v/A_t = 29.2% (j_{max}=12.79×10^4A/cm^2)

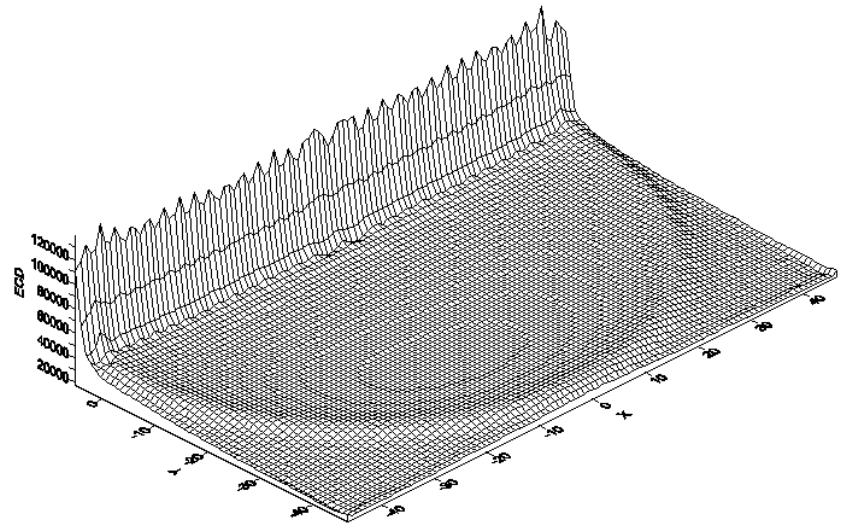

A_v/A_t = 42.9% (j_{max}=14.10×10^{4}A/cm^2)

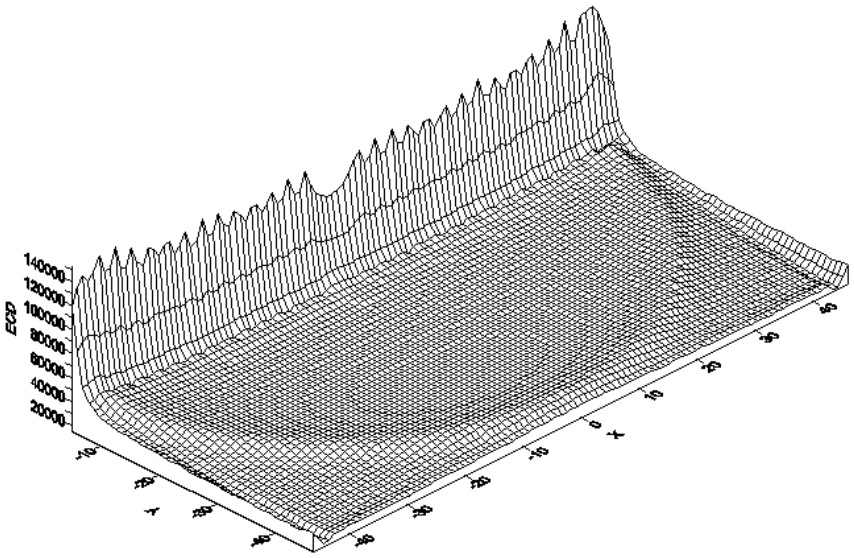

A_v/A_t = 57.1% (j_{max}=15.53×10^{4}A/cm^2)

Figure 4.9 Solder/IMC interface current density distribution in the 95.5Sn-4Ag-0.5Cu solder interconnect with a void propagating near the solder/ IMC interface

(note: ECD is electrical current density in A/cm^2, X, Y is the coordinate in μm)

Figure 4.10 shows the maximum current density at the void tip; the average electric current density in the fracture process zone *b'* and in the whole interconnect with the propagation

of void under different nominal current densities (1.5×10^4 A/cm^2 and 3.67×10^3 A/cm^2**)**. Based on the analysis, *j'* in Eq. (4.12) and (4.13) is defined as $j'=\alpha j$ to consider the current crowding effect, where α is the ratio of current density in the fracture process zone to the average current density in solder. From numerical analysis, the current crowding factor α is found to be approximately equal to 3 by assuming fracture process zone *b'* equals to 15% of solder diameter. If *b'* is close to zero, the current crowding effect will focus on the void tip, which corresponds to the upper bound value of α equals to j_{tip}/j_{ave}; here j_{tip} is the current density at void tip and j_{ave} is the average current density in interconnect. If *b'* equals to the solder diameter, the value of α will be close to the lower bound value 1 (j_{ave}/j_{ave}).

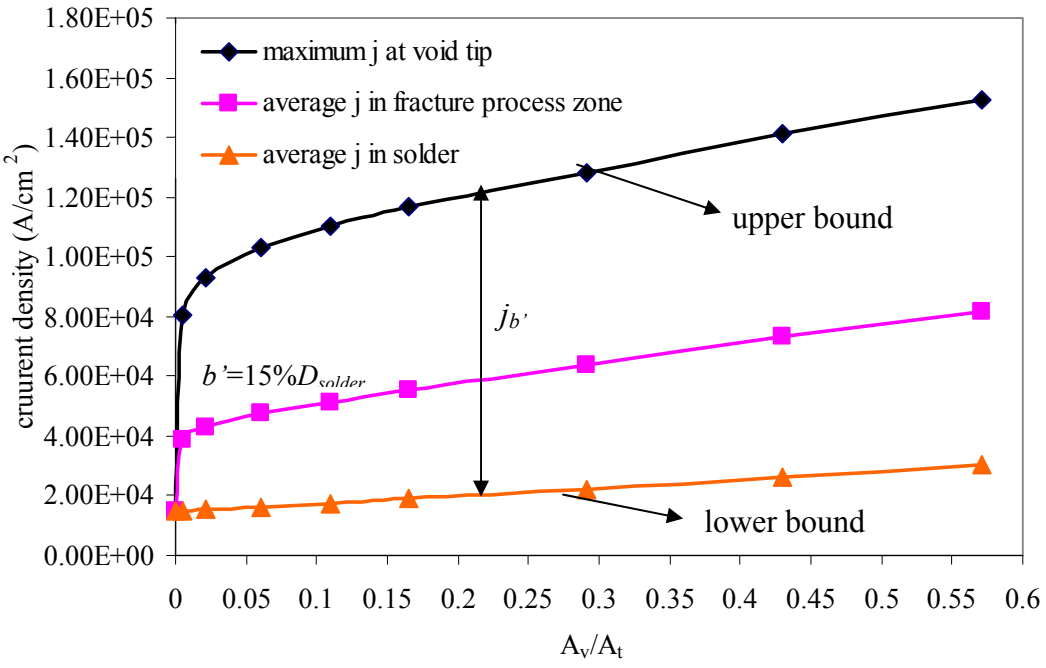

Applied current density = 1.5×10^4 A/cm^2

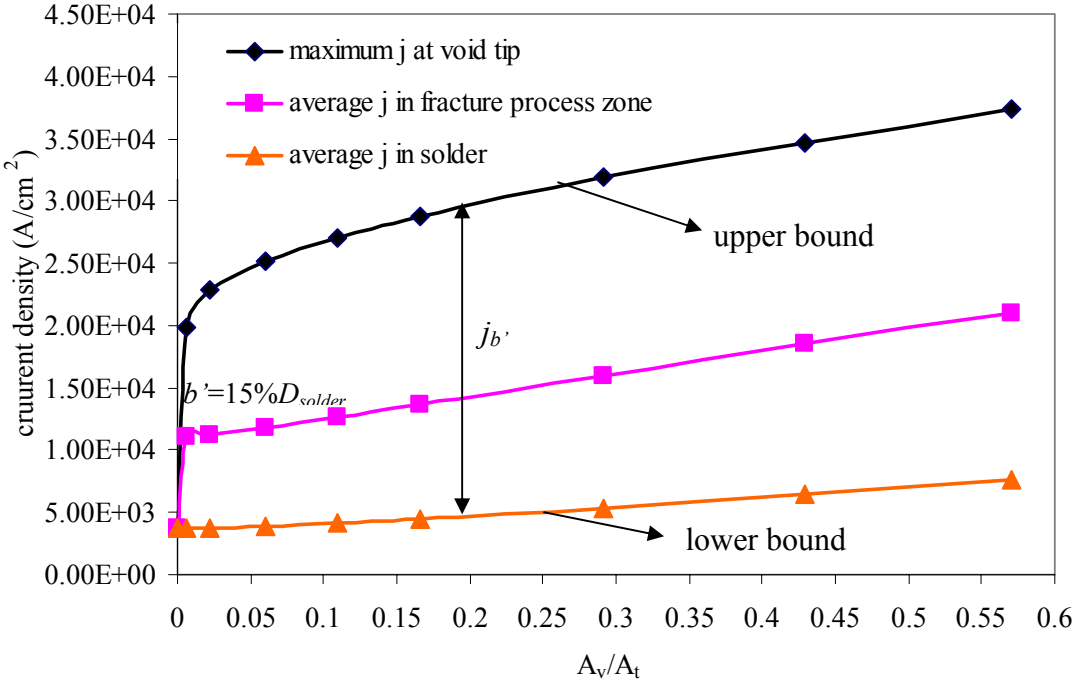

Applied current density = 3.67×10^3 A/cm^2

Figure 4.10 Maximum and average electric current density with the propagation of void at the interface of solder and IMC

4.4 Case Study by Comparing with Experimental Results

The proposed model is verified by using experimental results collected from literature. The following experimental data are obtained from Gee et al. (2005) and Zhang el al. (2006). In their experiments, the void width d is measured as 2.44μm. The test temperature is 146 °C, the electric current density is about 3.67×10^3 A/cm^2, the void length is 26.4μm, the void propagation process is 6 hours, and therefore the average void growth velocity is about 4.4μm/h. The fracture process zone $b' = 0.15\times250 = 37.5\mu m$ for the interconnect used in the experiment. The diffusivity is $D_{Sn}=1.3\times10^{-10}$ cm^2/s for Sn and $D_\eta = 2.76\times10^{-13}$ cm^2/s for Cu_6Sn_5, and the

diffusivity of the interface is taken to be 4.2×10^{-5} cm^2/s. The surface energy $\gamma_S = 10^{15}\,\text{eV/cm}^2 = 1.6\,\text{J/m}^2$ (Wu et al. 2004).

Defining the material constant $\lambda = C_{Sn}^{bulk} D_{Sn} Z_{Sn}^* \rho_{Sn} - C_{\eta}^{bulk} D_{\eta} Z_{\eta}^* \rho_{\eta} = 1.453\times10^9$ (Ω/s), and substituting the corresponding experimental determined values into Eq. (4.12) and (4.13), yields:

$$d = 2r = 4.793\times\sqrt{\frac{1.6\times2\times10^{-29}}{33.5\times1.6\times10^{-19}\times15.375\times10^{-8}\times3\times3.67\times10^{7}}} = 2.847\mu m\,,$$

$$v = \frac{1.453\times10^{9}\times1.6\times10^{-19}\times3\times3.67\times10^{7}\times2\times10^{-29}\times37.5\times10^{-6}}{1.38\times10^{-23}\times419\times2.847\times10^{-6}} = 1.166\times10^{-9}\,m/s = 4.198\mu m/h$$

The predictions match the experimental results (Zhang et al. 2006) well, which are the void width d=2.44μm and void growth velocity v=4.4 μm/h.

It is interesting to discuss the effects of fracture process zone *b'* and effective charge number $\overline{Z}^*$ on the accuracy of predictions. By varying the range of *b'* from 5% to 50% of the solder diameter, the current crowding parameter α is changed accordingly from numerical analysis. By applying Eq. (4.12) and (4.13), the predicted void width d varies from 2.20 to 4.41 μm and void growth velocity v varies from 3.01 to 5.45 μm/h. With the increasing IMC layer, more Cu_6Sn_5 atoms will flux through the interface, which also has important effect on the void formation and propagation in the interconnect. For the value of $\overline{Z}^* = a_{Sn} Z_{Sn}^* + a_{\eta} Z_{\eta}^*$, Eq. (4.8), if a_{Sn} = 0, a_{η} = 1, only the Cu_6Sn_5 atoms flux matters, $\overline{Z}^* = Z_{\eta}^* = 50$ (upper bound), then the predicted v=5.13 μm/h, d=2.33 μm. If a_{η} =0, a_{Sn} =1, only the Sn atoms flux matters, $\overline{Z}^* = Z_{Sn}^* = 17$ (lower bound), then the predicted v=2.99 μm/h, d=3.99 μm.

It should be noted that the void shape depends on the value of η in Eq. (4.8). Fig. 4.11 shows the mode I and mode II post-bifurcation steady-state shapes corresponding to different

eigenvalues of η by Yang et al. (1994). The bifurcation analysis performed by Yang et al. is based on Lyapunov's stability theory (Lyapunov 1966), the assumption adopted is that a circular loop will bifurcate if a shape perturbation exists so that the loop never returns to the circular shape. A circular void in solder may be developed from defects; it will distort, drift and evolve into a noncircular shape, and finally migrate to a fixed shape under the electron wind force. If η is small, the surface energy dominates the failure mode and the void will remain circular in shape and drift in the electron wind. If η is larger than 5.743, the electric field dominates and the cavity buckles to a noncircular shape. The void buckles when η=10.65, and becomes infinitely long and finger-like when η drops back to 5.743. The range 5.743< η <10.65 corresponds to mode-I (lateral) steady-state shapes, while the range 10.65 < η < 14.91 correspond to mode-II (vertical) steady-state shapes, where the loops elongate normal to the electric field, when $\kappa(0) \to 0$, η =14.91. For pancake-type void, the value of η is assumed to be 5.743.

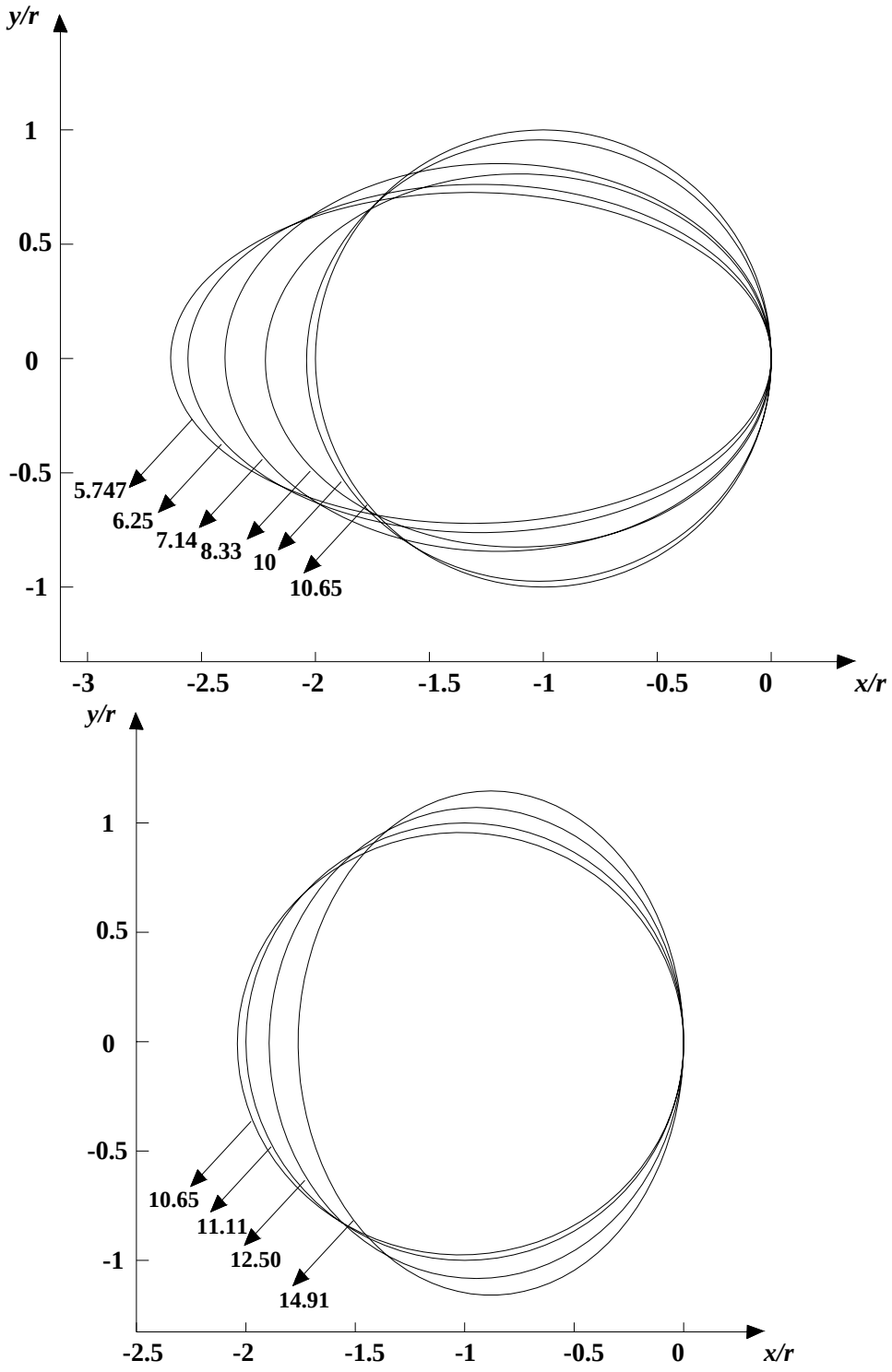

Figure 4.11 Mode I (lateral) and mode II (vertical) steady-state shapes corresponding to different η values (Yang et al. 1994)

With the proposed method, the prediction of void growth velocity and void width with respect to various η values from 5.74 to 10.65 (corresponding to different void shapes) under current densities from 2×10^3 to 2×10^4 A/cm^2 are given in Fig. 4.12 and Fig. 4.13. Fig. 4.14 and Fig. 4.15 predict the void growth velocity and void width under current densities from 2×10^3 to 2×10^4 A/cm^2 with different η values. From the parametric analysis, it is found that with increasing η value, the void growth velocity v decreases and void width d increases, which matches the physical observation and numerical analysis as in Fig. 4.11 by Yang et al. (1994). While with the increasing of current density j, void growth velocity increases and void width decreases (finally to a slit like failure).

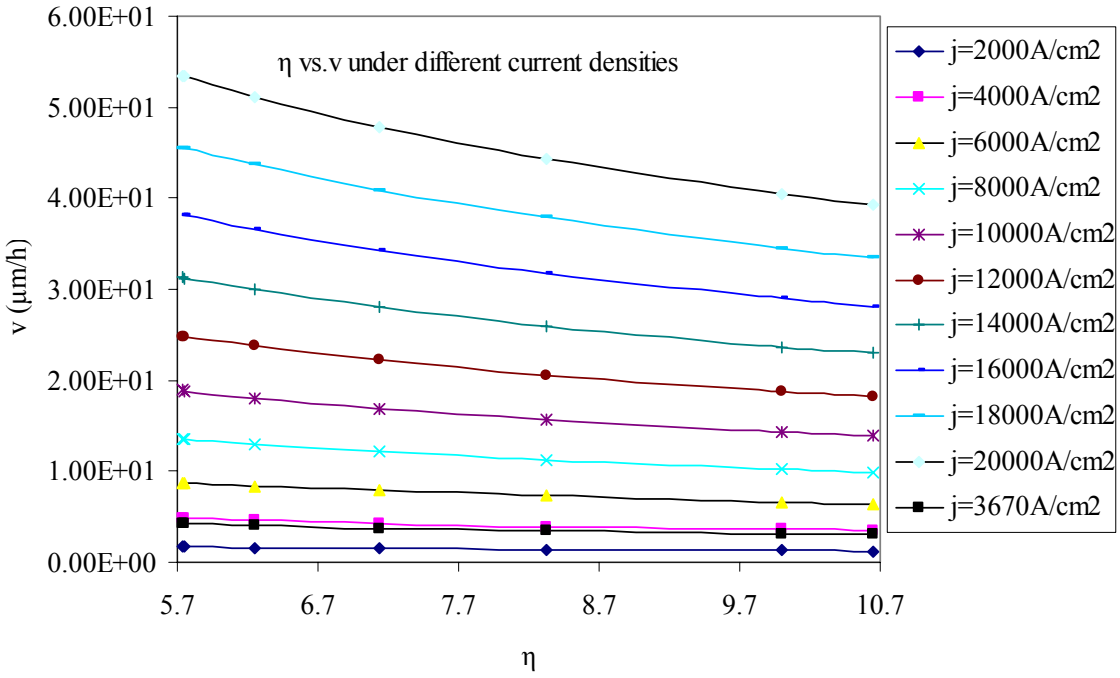

Figure 4.12 η vs. void growth speed v under different current densities

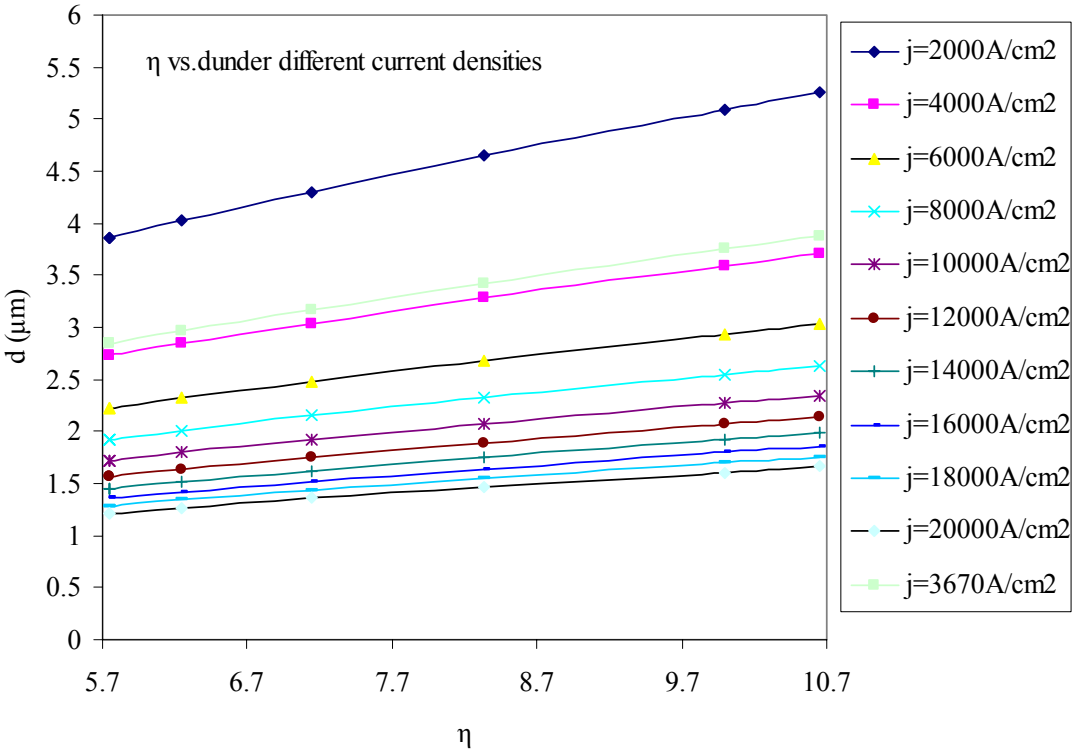

Figure 4.13 η vs. void width d under different current densities

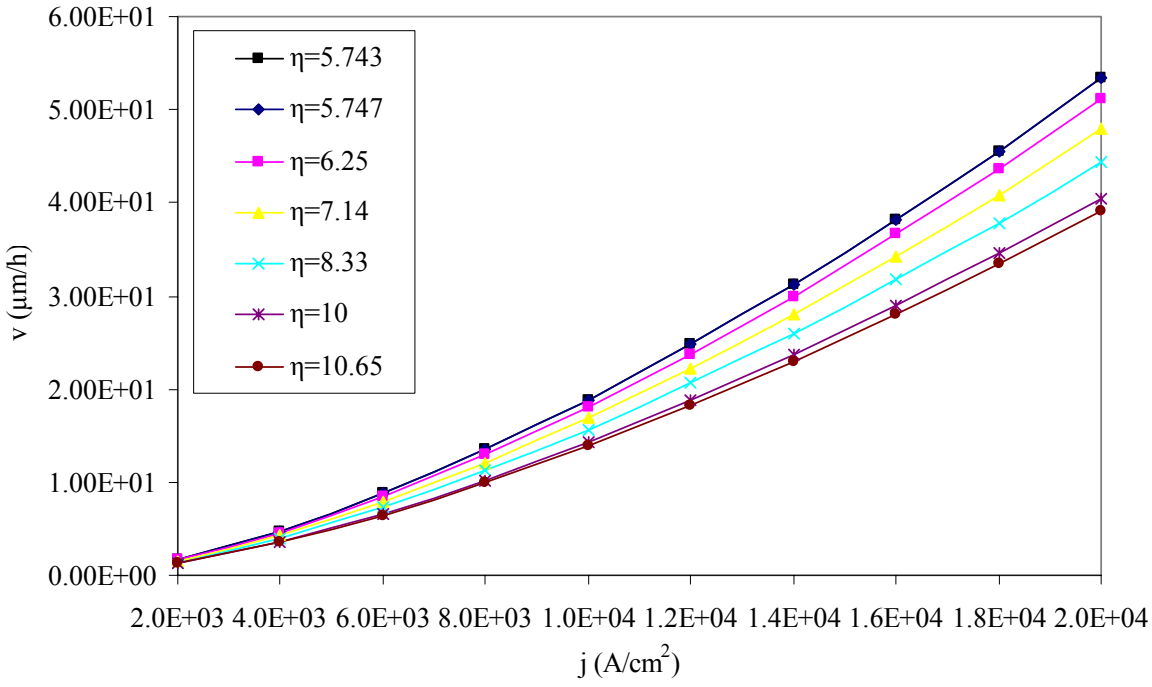

Figure 4.14 current density j vs. v for different η values

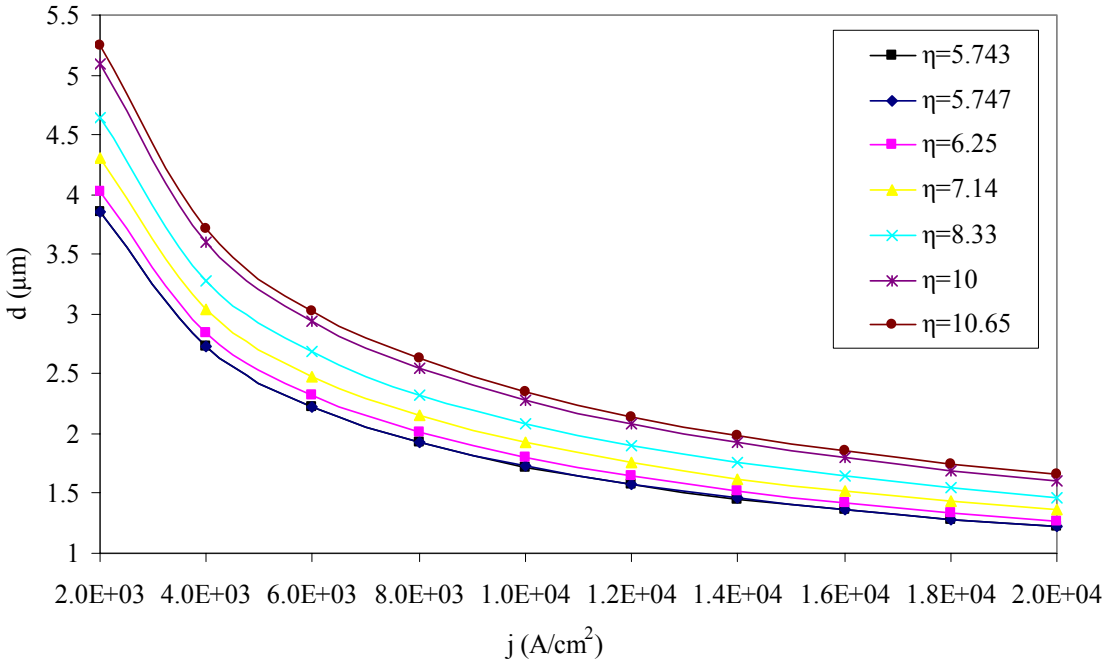

Figure 4.15 current density j vs. d for different η values

Table 4.1 shows the predicted void width d and propagation speed v by varying different parameters in the model, including b', j, $\overline{Z}^*$, and η. Effects of different parameters on the theoretical predictions are calculated and given in the table. It is shown that the theoretical calculations are consistent and in reasonable agreement with the experimental observations (Gee et al. 2005, Zhang el al. 2006).

Table 4.1 Effects of different parameters on the theoretical predicted void width *d* and propagation speed *v*

	d (μm)	*v* (μm/h)
b' varies from 5 to 50%D_{sodler} (with $\overline{Z}^*$ =33.5, j=3.67×10^{3}A/cm^2, η = 5.743)	2.20 ~ 4.41	3.01~ 5.45
$\overline{Z}^*$ varies from 17 to 50 (with *b'*=15%D_{sodler}, j=3.67×10^{3}A/cm^2, η = 5.743)	2.33~3.99	2.99~5.13
j varies from 2×10^3 to 2×10^{4}A/cm^2 (with *b'*=15%D_{sodler}, $\overline{Z}^*$ =33.5, η = 5.743)	1.22~3.86	1.69~53.4
η varies from 5.743 to 10.65 (with *b'*=15%D_{sodler}, $\overline{Z}^*$ =33.5, j=3.67×10^{3}A/cm^2)	2.847~3.88	3.08~4.198
Predicted value (with *b'*=15%D_{sodler}, $\overline{Z}^*$ =33.5, j=3.67×10^{3}A/cm^2, η = 5.743)	2.847	4.198
Experimental value (j=3.67×10^{3}A/cm^2)	2.44	4.4

It should be noted that the void propagation in interconnects is a complex phenomenon controlled by multiple factors. Under high current density, the momentum transfer from electrons to atoms will play an important role in IMC formation and growth.

Furthermore, the electromigration effect on IMC formation becomes insignificant at higher temperature (Alam et al. 2007). At temperatures near the melting temperature of Sn, the contribution from chemical potential gradient on the interfacial reaction rate is more important than the electromigration force. The increase of the IMC layer under current stressing and joule heating effect may also play important role in mass diffusion caused void.

4.5 Conclusion

It has been observed experimentally that most of the solder joints failure is near the IMC/solder interface under high current density. Electromigration effects on interconnect failure mechanism is discussed in the chapter. From numerical analysis, it is found that the electromigration force contributes more to void formation than stress migration force under high current density. A kinetic mass diffusion model is developed based on the Einstein relation and mass conservation principle. The approach is applied to predict void width and propagation velocity at the solder/IMC interface caused by electromigration. Computational analysis has been conducted to determine the current crowding parameter in the model. The predicted void width and propagation velocity matches experimental results reasonably well.

Chapter 5

Conclusion

5.1 Conclusion

It has been experimentally observed that solder joints fail near the IMC/solder interface. A 3D computational model based on cohesive fracture mechanics and continuum mechanics has been developed in the dissertation to predict the crack initiation and propagation near the IMC and solder interface. The traction-separation law of a cohesive element at interface is included in the finite element program, ABAQUS. Unified-creep-plasticity Model is incorporated in the model to simulate creep-plastic behavior of solder materials. A numerical analysis of IMC related solder joint failure has been conducted. The cohesive-UCP finite element model is applied to analyze the IMC layer thickness effect on solder joint failure. The growth of IMC layer thickness is found to have a significant effect on solder joint failure. The von Mises stress required to initiate a crack is found lower for a thicker IMC layer and the solder joint lifetime decreases with increasing IMC layer thickness. Higher Young's modulus of IMC tends to cause crack nucleation at interface. Since solder joint failure is a complex coupled problem caused by mechanical, thermal, and electrical stresses, a coupled thermo-electric numerical analysis has been conducted to understand better the phenomenon. The electrical concentration and joule heating effects are found to play important roles on solder joint failure, especially when a crack propagates near the interface of IMC and solder. The temperature and electric current density distribution in Sn-2.5Ag-0.8Cu-0.5Sb solder under different applied currents has been predicted. It is found that there has pronounced temperature and electrical current concentration near the

crack tip. Although the lead-free solders usually have higher melting temperatures as compared with lead-rich solder, the concentration of heat at the crack tip caused by joule heating may still melt the solder material under a high current density, which will enhance the propagation of crack and cause a circuit failure.

Fatigue damage of solid materials consists mainly of dislocation and microcrack accumulation. The fatigue crack nucleation and propagation significantly depends on the accumulation of dislocations and other lattice defects at nucleation sites. Based on phase transformation theory, micromechanics, and fracture mechanics, a theoretical approach has been developed to predict fatigue crack propagation in solid materials. The theory is first applied to predict the fatigue crack propagation rate in steels and aluminum alloys, where the required energy U to propagate a unit crack area in steel and aluminum alloys is determined by experimental analysis from Professor Fine's group at Northwestern University. Compared with experimental data, the prediction of the proposed approach has a mean of 1.028 to 1.062 and the coefficient of variation is 0.255 to 0.264 for steels, the mean is 1.185 to 1.310 and the coefficient of variation is 0.253 to 0.286 for aluminum alloys. Based on experimental and finite element analysis, the proposed phase transformation theory is extended to predict fatigue crack propagation in interconnects. Fatigue experiments on Sn-3.5Ag solder alloy conducted by S. Vaynman at Northwestern University is used to verify the approach. Fatigue crack propagation rate is characterized successfully by stress intensity factor range ΔK. The fatigue crack was found to initiate in the solder alloy and to migrate to the solder/ IMC layer interface; the crack propagated near the interface and caused catastrophic failure. The developed computational model incorporating UCP theory and CZM was applied to determine the required energy U to propagate a unit crack area in solder. With U determined numerically, phase transformation

theory was applied to predict the fatigue crack propagation rate of Sn-3.5Ag and 63Sn-37Pb eutectic solder. Compared with experimental data, the prediction of the proposed approach has a mean of 1.15 and 1.10 and the coefficient of variation of 0.412 and 0.272 for Sn-3.5Ag and 63Sn-37Pb eutectic solder, respectively. The results show that the phase transformation theory is not only accurate and consistent but also conservative. The proposed theory provides a basis for a theoretical examination to fatigue crack propagation in interconnects.

With the reduction of electronic device size, interconnects will operate under higher current density; eletromigration will play a more important role to interconnect failure in the near future. From numerical analysis, it is found that the electromigration force contributes more to void formation than stress migration force under high current density. A kinetic mass diffusion model is developed based on the Einstein relation and mass conservation principle to predict the electromigration effect on solder/IMC interfacial failure. The predicted void width and propagation speed shows reasonable agreement with experimental data.

5.2 Future Research

For future research, the electrical current effect could be included into the phase transformation theory; a possible method is proposed in Appendix C, which still in a preliminary development stage. More theoretical and experimental research works are needed on the coupled fatigue, joule heating and electromigration effects to failure of small-scale solder joints. Electromigration effect can also be included in the computational model, combined with the UCP theory. Since void nucleation and growth are the dominant damage mechanisms in electromigration induced failure, the electromigration research efforts on damage failure prediction will focus on these effects in future research. To simulate the damage process, initial

thermal and electrical fields are required. The current field distribution sometimes is a dominant feature and thermal expansion coefficient mismatch of different materials will also contribute to the stress field. For a 3-D solder joints computational model, a coupled system is needed to solve the displacement-diffusion problem. Boundary conditions, which include diffusion and displacement fields, will be considered in future research. Plastic strain accumulation is also an important factor in the void nucleation and growth process. The dislocation accumulation at second phase particles in the matrix phase is a source for void nucleation and growth. In order to accurately simulate the damage process, both plasticity (due to the high homologous temperature of the solder at ambient temperature) and creep must be considered. Plastic deformation will also contribute to the main damage phenomenon, which is void nucleation at the cathode side. Plastic deformation by grain boundary sliding produces high stress localization when the slip band intersects with particles at a grain boundary, which is a favorite site for void nucleation. The complexity of this problem arises from the coupling terms between diffusion governing partial differential equations and force equilibrium governing partial differential equations. In order to determine Jacobian contributions (stiffness matrix contribution) a material constitutive equation is needed. Because of the nonlinear material behavior, a local integration scheme is also needed; for example, a return mapping algorithm can be used. To validate the analysis, an ABAQUS user defined element subroutine can be developed for 3D thermal-mechanical-electromigration analysis and a computational solution of the governing partial differential equations will be obtained. With the program developed, void nucleation kinetics under coupled thermal-electrical load can be predicted. Furthermore, the mean time to failure of an interconnect can be determined from this process. The computational prediction will need to be compared with experiment, where parameters in the model having clear physical meaning can be

determined. With the program developed, a significant amount of experimental work can be saved. Anisotropic properties can be included in the developed finite element model with the material properties determined experimentally; if necessary molecular dynamic based technology can be applied to simulate the inter-grain interactions. A 3D computational model using a multi-physics analysis package can be developed in future research to predict the thermal stress, current crowding, and joule heating effects. The material properties used in the model need to be determined from experiments.

References

ABAQUS documentation 6.6.3 (2006)

Akay, H. U., Paydar N. H. and Bilgic, A., “Fatigue life predictions for thermally loaded solder joints using a volume-weighted averaging technique”, Journal of Electronic Packaging 119:228-235, (1997)

Alam, M. O., Wu, B.Y., Chan, Y. C. and Tu, K. N. “High electric current density-induced interfacial reactions in micro ball grid array (μBGA) solder joints.” Acta Materialia, v54, n3, Feb., p613-621 (2006)

Austin J. B., “The flow of heat in metals”, American Society for Metals, Cleveland, Ohio, (1942)

Baqi, A. A., Schreurs, P. J. G. and Geers, M. G. D., “Fatigue damage modeling in solder interconnects using a cohesive zone approach” International Journal of Solids and Structures, 42, 927–942 (2005)

Benzeggagh, M. L. and Kenane, M., “Measurement of mixed-mode delamination fracture toughness of unidirectional glass/epoxy composites with mixed-mode bending apparatus”, Composites Science and Technology, Volume 56, Number 4, April, pp. 439-449(11), (1996)

Bhat, P. S. and Fine, M. E., “Fatigue crack nucleation in iron and a high strength low alloy steel”, Material Science and Engineering A314 90-96, (2001)

Black, J.R., “Electromigration-A Brief Survey and Some Recent Results”, IEEE Transactions on Electron Devices, Vol. ED-16(No. 4):p. 338 347, April, (1969)

Blech, I. A. and Herring, C., “Stress generation by electromigration “, Appl. Phys. Lett. 29, 131 (1976).

Bower, A. F. and Craft, D., “Analysis of failure mechanisms in the interconnect lines of microelectronic circuits”, Fatigue and Fracture of Engineering Materials & Structures, v 21, n 5, May, p 611-630, (1998)

Cavalli, M. N. Thouless, M. D. and Yang, Q. D., “Cohesive-zone modeling of the deformation and fracture of weld-bonded joints”, Welding Journal (Miami, Fla), v 83, n 4, April , p 133-139, (2004)

Chan, Y. C., Tu, P. L., So, A. C. K. and Lai, J. K. L., “Effect of Intermetallic Compounds on the Shear Fatigue of Cu/63Sn–37Pb Solder Joints” IEEE Transaction on Components, Packing, and Manufacturing Technology —Part BVol. 20, No. 4, (1997)

Chiu, S. H., Liang, S. W., Chen, C., Yao, D. J. and Hsu, C. Y., "Infrared microscopy of hot spots induced by Joule heating in flip-chip SnAg solder joints under accelerated electromigration" Appl. Phys. Lett. Volume 88, 022110 (2006)

Clech, J. M., Werner, E. and Robert, W. K. ,"Reliability figures of merit for surface-soldered leadless chip carriers compared to leaded packages", IEEE Transactions On Components Hybrids and Manufacturing Technology 12, 449 – 458, (1989)

Coffin, L. F. J. and Schenectady, N. Y., "A Study of the Effects of Cyclic Thermal Stresses on a Ductile Metal", Transactions of the ASME, 931-950, (1954)

Dasgupta, A., Oyan, C., Barker, D. and Pecht, M., "Solder creep-fatigue analysis by an energy-partitioning approach", Journal of Electronic Packaging 114, 152-160, (1992)

Desai, C. S., Chia, J., Kundu, T. and Prince, J. L., "Thermomechanical response of materials and interfaces in electronic packaging: Part I - Unified constitutive model and calibration", *Journal of Electronic Packaging* 119, 294-300, (1997)

Deshpande, V. S., Needleman, A. and Vander, G., "Discrete dislocation modeling of fatigue crack propagation", Acta Materialia, v 50, n 4, Feb 25, p 831-846, (2002)

Dundurs, J., "Edge-bonded dissimilar orthogonal elastic wedges under normal and shear loading", ASME Journal of Applied Mechanics 36, 650–652, (1969).

Einstein, A., "Über die von der molekularkinetischen Theorie der Wärme geforderte Bewegung von in ruhenden Flüssigkeiten suspendierten Teilchen", Annalen der Physik 17: 549-560, (1905)

Ellyin, F., "Fatigue Damage, Crack Growth and Life Prediction", Chapman and Hall, New York, (1997)

Erinc, M., Schreurs, P. J. G., Zhang, G. Q. and Geers, M. G. D., "Microstructural damage analysis of SnAgCu solder joints and an assessment on indentation procedures," Journal of Materials Science: Materials in Electronics 16:93-700, (2005)

Fiedler, B. A., Yao, Y., Vaynman, S., Ghosh, G., Keer, L. M. and Fine, M. E., "Pb-Free Sodler Joint Fatigue Crack Initiation and Propagation Related to Electrical, Thermal and Mechanical Loading", Proceeding of SRC Techcon conference, Austin, (2007)

Fine, M. E., Stolkarts, V. and Keer, L. M., "Fatigue crack nucleation assisted by thermal activation", Materials Science and Engineering A: Structural Materials: Properties, Microstructure and Processing, v 272, n 1, Nov, p 5-9, (1999)

Fine, M. E., "Phase transformation theory applied to elevated temperature fatigue", Scripta Materialia, v 42, n 10, May, p 1007-1012, (2000)

Frear, D. R., Jang, J. W., Lin, J. K. and Zhang, C., “Pb-free solders for flip-chip interconnects”, JOM, v 53, n 6, June, p 28-32+38, (2001)

Funabashi, N., Mura, T. and Keer, L. M., “Fatigue Crack Initiation and Propagation in Bonded Sheets”, Journal of Adhesion, v 9, n 3, p 229-235, (1978)

Gan, H. and Tu, K. N., “Effect of Electromigration on Intermetallic Compound Formation in Pb-free solder-Cu interfaces” Electronic components and technology conference (2002)

Gee, S., Kelkar, N., Huang, J. and Tu, K. N., “Lead-Free and PbSn Bump Electromigration Testing”, ASME InterPACK, San Franscisco, CA, (2005)

Ghosh, G., “Elastic properties, hardness and indentation fracture toughness of intermetallics relevant to electronic packaging” J. Mater. Res., Vol. 19, No. 5, May (2004)

Gungor, M. R. and Maroudas, D., “Stress-induced deceleration of electromigration-driven void motion in metallic thin films”, Journal of Applied Physics, v 101, n 6, (2007)

Guo, Q., Cutiongco, E. C., Keer, L. M. and Fine, M. E., “Thermomechanical Fatigue Life Prediction of 63Sn/37Pb Solder”, Journal of Electronic Packaging 114:145-151, (1992)

Gupta, P., “Effect of IMC on Thermal-mechanical Reliability of Lead-Free Solder Interconnections for Flip-Chips”, Master thesis, Georgia Institute of Technology (2004)

Harlow, D. G. and Wei, R.P., “Probabilities of occurrence and detection of damage in airframe materials”, Fatigue and Fracture of Engineering Materials and Structures, v 22, n 5, p 427-436, (1999)

Hauschildt, M., Gall, M., Thrasher, S., Justison, P., Hernandez, R., Kawasaki, H. and Ho, P. S., “Statistical analysis of electromigration lifetimes and void evolution” Journal of Applied Physics, v 101, n 4, p 043523, (2007)

Herring, C., “in the physics of power metallurgy”, (McGraw-Hill, New York), p.143, (1951).
Huntington HB and Grone AR, ‘Current-induced marker motion in gold wires “, J. Phys. Chem. Solids 20, 76 (1961).

Huang, Y., Gong, X. Y., Suo, Z. and Jiang, Z. Q., “Model of evolving damage bands in materials”, International Journal of Solids and Structures, v 34, n 30, Oct., p 3941-3951, (1997)

Huntington, H. B. and Grone, A. R., ‘Current-induced marker motion in gold wires “, J. Phys. Chem. Solids 20, 76 (1961)

Irving, P. E. and McCartney, L. N., “Prediction of Fatigue Crack Growth Rates-Theory, Mechanisms and Experimental Results”, Metal Science, v 11, n 8-9, Aug-Sep, p 351-361, (1977)

Izumi, Y. and Fine, M. E., “Role of Plastic Work in Fatigue Crack Propagation in Metals”, Engineering Fracture Mechanics, v 11, n 4, p 791-804, (1979)

Izumi, Y., Fine, M. E. and Mura, T., “Energy Considerations in Fatigue Crack propagation”, International Journal of Fracture, v 17, n 1, Feb., p 15-25, (1981)

Ju, S. H., Sandor B. I., and Plesha M. E., “Life prediction of solder joints by damage and fracture mechanics”, Journal of Electronic Packaging 118:193-200, (1996)

Kanchanomai, C., Limtrakarn, W. and Mutoh, Y., “Fatigue crack growth behavior in Sn-Pb eutectic solder/copper joint under mode I loading”, Mechanics of Materials, v 37, n 11, November, p 1166-1174, (2005)

Kanchanomai, C. and Mutoh, Y., “Fatigue crack initiation and growth in solder alloys”, Fatigue and Fracture of Engineering Materials and Structures, v 30, n 5, May, Structural Integrity in Electronics, p 443-457, (2007)

Kim, D. H., Elenius, P. and Barrett, S., “Solder joint reliability and characteristics of deformation and crack growth of Sn-Ag-Cu versus eutectic Sn-Pb on a WLP in a thermal cycling test”, IEEE Transactions on Electronics Packaging Manufacturing, v 25, n 2, April, p 84-90, (2002).

Klingbeil, N. W., “A total dissipated energy theory of fatigue crack growth in ductile solid”, International Journal of Fatigue, v 25, n 2, February, p 117-128, (2003)

Knecht, S., and L. R. Fox., “Constitutive Relation and Creep-Fatigue Life Model For Eutectic Tin Lead Solder”, IEEE Transactions On Components Hybrids and Manufacturing Technology 13:424-433, (1990)

Korhonen, T. K., Henderson, D. W. and Korhonen, M. A., “Nucleation and propagation of fatigue damage in near-eutectic Sn-Ag-Cu alloy”, JOM, v 56, n 11, November, p 251-252, (2004)

Kuo, C. G., Sastry, S. M. L., and Jerina, K. L., ”Creep-fatigue life prediction of in situ composite solders”, Metallurgical and Materials Transactions a-Physical Metallurgy and Materials Science 26:3265-3275, (1995)

Kwon, I. B., Fine, M. E., and Mura, T., “Elastic strain energy analysis of the dislocation structures in fatigue”, Acta Metallurgica, v 36, n 9, Sep., p 2605-2614, (1988)

Kwun, S. I. and Fine, M. E., “Fatigue Macrocrack Growth in Tempered HY80, HY130, and 4140 Steels: Threshold and Mid-Delta K Range”, Fatigue of Engineering Materials and Structures, v 3, n 4, p 367-382, (1980)

Lang, M. and Larsen, J. M., “Fatigue crack propagation and load interaction effects in a titanium alloy”, Fatigue and Fracture Mechanics, vol. 30, ASTM STP 1360, 201–213, (1999).

Larson, M. C. and Verges, M. A., “Extending the fatigue life of solder grid array (SGA) electronic packages”, Journal of Electronic Packaging, Transactions of the ASME, v 125, n 1, p 18-23, (2003).

Lau, J. H., “Solder Joint Reliability of Flip Chip and Plastic Ball Grid Array Assembles under Thermal, Mechanical, and Vibrational conditions”, IEEE Transactions VOL. 19, NO 4, NOV. (1996)

Laz, P. J., Craig, B. A. and Hillberry, B. M., “A probabilistic total fatigue life model incorporating material inhomogeneities, stress level and fracture mechanics”, International Journal of Fatigue, v 23, n Suppl. 1, p S119-S127, (2001)

Lee, C. C., Lee, C. C., Chiu, C. C., Chen, C. C., Kuo, F. and Chiang, K. N., “Electromigration Characteristic of SnAg3.0Cu0.5 Flip Chip Interconnection”, Electronic Component and Technology Conference, (2006)

Lee, S. B., and Kim, J. K., “A mechanistic model for fatigue life prediction of solder joints for electronic packages” International Journal of Fatigue 19:85-91, (1997)

Leicht, L. and Skipor A., “Mechanical cycling fatigue of PBGA package interconnects”, International Journal of Microcircuits and Electronic Packaging, v 22, n 1, First Quarter, p 57-61, (1999)

Liang, S. W., Shao, T. L., Chen, C. Y., Everett, C. C. and Tu, K. N., “Relieving the current crowding effect in flip-chip solder joints during current stressing”, Journal of Materials Research, v 21, n 1, January, p 137-146, (2006)

Liaw, P. K., Kwun, S. I. and Fine, M. E., “Plastic work of fatigue crack propagation in steel and aluminum alloys”, Metallurgical Transactions A (Physical Metallurgy and Materials Science), v 12A, n 1, Jan , p 49-55, (1981)

Lin, M. R., Fine, M. E. and Mura, T., “Fatigue Crack Initiation Slip Bands: Theory and Experiments”, Acta Metallurgica, v 34, n 4, Apr, p 619-628, (1986)

Liu, X., Sooklal, V. K., Verges, M. A. and Larson, M. C., “Experimental study and life prediction on high cycle vibration fatigue in BGA packages”, Microelectronics Reliability, v 46, n 7, July, p 1128-1138, (2006)

Lyapunov A.M., “Stability of motion”, Academic Press, New-York and London, (1966)

Manson, S. S., “Behavior of Materials under conditions of thermal stress”, In Heat transfer, a symposium held at the University of Michigan during the summer of 1952. Ann Arbor, MI: Engineering Research Institute, University of Michigan,(1953)

Mars, W. V. and Fatemi, A., “Fatigue crack nucleation and growth in filled natural rubber”, Fatigue and Fracture of Engineering Materials and Structures, v 26, n 9, September, p 779-789, (2003)

Mattila, T. T. and Kivilahti, J. K., “Reliability of lead free interconnects under consecutive thermal and mechanical loadings.” Journal of Electronic Materials, v 35, n 2, February, 2006, p 250-256 , (2006)

McDowell, D. L., “Damage mechanics and metal fatigue: a discriminating perspective”, International Journal of Damage Mechanics, v 8, n 4, Oct., p 376-403, (1999)

McDowell, D. L., Miller, M. P. and Brooks, D. C., “A unified creep-plasticity theory for solder alloys,” Fatigue of Electronic Materials, ASTM STP 1153, pp. 42-59, (1994)

McKittrick, J., Liaw, P. K., Kwun, S. I. and Fine, M. E., “Threshold for Fatigue Macrocrack Propagation in Some Aluminum Alloys”, Metallurgical Transactions A (Physical Metallurgy and Materials Science), v 12A, n 8, Aug. , p 1535-1539, (1981)

Miyazaki, T. and Omata, T., **“**Electromigration degradation mechanism for Pb-free flip-chip micro solder bumps”, Microelectronics Reliability, v 46, n 9-11, Proceedings of the 17th European Symposium on Reliability of Electron Devices, Failure Physics and Analysis, p1898-1903, (2006)

Morrow, J., “Cyclic Plastic Strain Energy and Fatigue of Metals”, In Internal Friction, Damping, and Cyclic Plasticity. Philadelphia: ASTM, (1964)

Mura, T. and Lin, S. C., “Thin Inclusions and Cracks in Anisotropic Media”, Journal of Applied Mechanics, Transactions ASME, v 41 Ser E, n 1, Mar., p 209-214, (1974)

Mura, T., “Three-dimensional constitutive relations and ductile fracture”, Discussion on Section 2, 147-153, North-Holland Publishing Company, (1981)

Mura, T., “Micromechanics of defects in solids (2nd ed.)”, The Netherlands: Martinus Nijhoff, (1991)

Mura, T., “Theory of fatigue crack initiation”, Materials Science & Engineering A: Structural Materials: Properties, Microstructure and Processing, v A176, n 1-2, Mar 31 , p 61-70, (1994)

Nah, J. W., Suh, J. O. and Tu, K. N., “Effect of current crowding and Joule heating on electromigration-induced failure in flip chip composite solder joints tested at room temperature” Journal of Applied Physics 98, 013715 (2005)

Nayeb, H. H. and Yang, P., “Mixed mode I/II fracture and fatigue crack growth along 63Sn-37Pb solder/brass interface”, International Journal of Fatigue 23 S325-335, (2001)

Nguyen, O., Repetto, E. A., Ortiz, M. and Radovitzky, R. A., "A cohesive model of fatigue crack growth", International Journal of Fracture 110: 351–369, (2001)

NIST database for solder properties, Release 4.0 (2002)

Pan, K., Zhou, B. and Yan, Y., "Simulation Analysis of Dynamic Response for CSP under Board Level Drop Test", IEEE Inter. Conf. Electro. Packag. Tech. (2006)

Pao, Y. H., "A Fracture-Mechanics Approach to Thermal Fatigue Life Prediction of Solder Joints", IEEE Transactions On Components Hybrids and Manufacturing Technology 15:559-570, (1992)

Paris, P. C., "Fracture mechanics and fatigue: a historical perspective", Fatigue and Fracture of Engineering Materials & Structures, v 21, n 5, May, p 535-540, (1998)

Prager, W., "A new method of analyzing stresses and strains in work-hardening plastic solids", J. Appl. Mech., Trans. Am. Soc. Mech. Eng.,23, No. 5, 493–496 (1956)

Ren, F., Nah, J. W., Tu, K. N., Xiong, B. S., Xu, L. H. and Pang, J. H. L., "Electromigration induced ductile-to-brittle transition in lead-free solder joints", Applied Physics Letters 89, 141914, (2005)

Rice, J. R., "Mechanics of crack tip deformation and extension by fatigue", ASTM STP 415, 247–311,(1967)

Rice, J. R. and Chuang, T. J., "Energy Variations In Diffusive Cavity Growth", J.AM.CERAM.SOC. J. Am. Ceram. Soc. Vol. 64, no. 1, pp. 46. (1981).

Ritchie, R. O., "Mechanisms of fatigue-crack propagation in ductile and brittle solids", International Journal of Fracture, v 100, n 1, p 55-83, (1999)

Roe, K. L. and Siegmund, T., "An irreversible cohesive zone model for interface fatigue crack growth simulation" Engineering Fracture Mechanics 70 209–232, (2003)

Sematech, "The International Technology Roadmap for Semiconductors: 1999 edition. 1999 ed, Semiconductor Industry Association (SIA). Austin, TX: International Sematech, (1999)

Shang, J. K., Zeng, Q. L., Zhang, L. and Zhu, Q. S., "mechanical fatigue of Sn-rich Pb-free solder alloys", Journal of Materials Science: Materials in Electronics, v 18, n 1-3, March, p 211-227, (2007)

Shangguan, D. K., "Analysis of crack growth in solder joints", Soldering and Surface Mount Technology, v 11, n 3, p 27-32, (1999)

Shi, X. Q., Pang, H. L. J., Zhou, W., and Wang, Z. P., “A modified energy-based low cycle fatigue model for eutectic solder alloy”, Scripta Materialia 41:289-296, (1999)

Seniw, M. E., Conley, J. G. and Fine, M. E., “The effect of microscopic inclusion locations and silicon segregation on fatigue lifetimes of aluminum alloy A356 castings” Materials Science and Engineering A285, 43–48, (2000)

Soboyejo, W. O., Shen, W., Srivatsan, T. S., “An investigation of fatigue crack nucleation and growth in a Ti-6Al-4V/TiB in situ composite”, Mechanics of Materials, v 36, n 1-2, January/February, p 141-159, (2004)

Solomon, H. D., “Fatigue of 60/40 Solder”, IEEE Transactions On Components Hybrids and Manufacturing Technology 9:423-432,(1986)

Stolkarts, V., Keer, L. M. and Fine, M. E., “Damage evolution governed by microcrack nucleation with application to the fatigue of 63Sn-37Pb solder” Journal of the Mechanics and Physics of Solids 47:2451-2468, (1999)

Subrahmanyan, R., Wilcox, J. R. and Li, C. Y., “A Damage Integral Approach to Thermal Fatigue of Solder Joints”, IEEE Transactions On Components Hybrids and Manufacturing Technology 12:480-491, (1989)

Suo, Z. and Hutchinson, J. W., “Interface crack between two elastic layers”, International Journal of Fracture, v 43, n 1, May 1, p 1-18, (1990)

Suo, Z., Wang, W. and Yang, M., “Electromigration instability: Transgranular slits in interconnects” Applied Physics Letter 64(15), 11 April (1994)

Syed, A. R., “Creep Crack-Growth Prediction of Solder Joints During Temperature Cycling - an Engineering Approach”, Journal of Electronic Packaging 117:116-122, (1995)

Towashiraporn, P., Subbarayan, G. and Desai, C. S., “A hybrid model for computationally efficient fatigue fracture simulations at microelectronic assembly interfaces” International Journal of Solids and Structures, v 42, n 15, July, p 4468-4483, (2005)

Thouless, M. D., Yu, H., Zhao, Z. and Yang, W.,” Damage nucleation during electromigration along an isolated interface in an elastic medium”, Journal of the Mechanics and Physics of Solids, v 44, n 3, Mar, p 371, (1996)

Vaynman, S., “Isothermal fatigue of 96.5Pb-3.5Sn solder”, Ph.D. Dissertation, Department of Materials Science and Engineering, Northwestern University, Evanston, IL. (1987)

Vaynman, S. and Zubelewicz, A., “Fatigue Life Prediction For Low-Tin Lead-Based Solder At Low Strains”, Welding Journal 69:S395-S398, (1990)

Vaynman, S. and McKeown S. A., “Energy-Based Methodology For the Fatigue Life Prediction of Solder Materials”, IEEE Transactions On Components Hybrids and Manufacturing Technology 16:317-322, (1993)

Wang, F., Keer, L. M., Vaynman, S. and Wen, S., “Constitutive model and numerical analysis for high lead solders”, IEEE Trans. on Components and Packaging Technology, 27, 718 (2004)

Wang, W., Suo, Z. and Hao, T. H., “A simulation of electromigration-induced transgranular slits”, J. Appl. Phys. 79 (5), 1 March (1996)

Weertman, J., “Theory of fatigue crack growth based on a BCS crack theory with work hardening”, International Journal of Fracture 9(2), pp. 125–131, (1973)

Wen, L. C., and Ronald, G. R., “Comparison of LCC solder joint life predictions with experimental data”, Journal of Electronic Packaging 117:109-115, (1995)

Wen, S., Keer, L. M., and Mavoori, H., “Constitutive And Damage Model For A Lead-Free Solder”, Journal of Electronic Materials, v 30, n 9, September, Lead-Free Solder Materials and Soldering Technologies, p 1190-1196, (2001)

Wen, S., “Thermomechanical fatigue life prediction for several solders”, PhD. Dissertation, Dept. Mech. Eng., Northwestern Univ., Evanston, IL, (2001)

Wen S., Keer L. M., Vaynman S. and Lawson, L. R., “A constitutive model for a high lead solder,” IEEE Trans. on Components and Packaging Technology, vol. 25, pp. 23–31, Mar. (2002)

Whitelaw, R. S., Neu R. W., and Scott, D. T., “Deformation behavior of two lead-free solders: Indalloy 227 and Castin alloy”, Journal of Electronic Packaging 121:99-107, (1999)

Williams, D. R. and Fine, M. E., “Quantitative Determineation on Fatigue Microcrack Growth in SiC Whisker Reinforced 2124 Al Alloy Composites”, Metallurgical Soc Inc, p 639-670, (1985)

Wu, A. T., Tu, K. N., Lloyd, J. R., Tamura, N., Valek, B. C. and Kao, C. R., “Electromigration-induced microstructure evolution in tin studied by synchrotron x-ray microdiffraction” , Applied Physics Letters, v 85, n 13, Sep 27, p 2490-2492, (2004)

Xu, L., Pang, J. H. L., Ren, F. and Tu, K. N., “Electromigration effect on intermetallic growth and Young's modulus in SAC solder joint”, Journal of Electronic Materials, v 35, n 12, December, p 2116-2125, (2006)

Yamada, S. E., “A Fracture-Mechanics Approach to Soldered Joint Cracking”, IEEE Transactions On Components Hybrids and Manufacturing Technology 12:99-104. (1989)
Yang, B., Mall, S. and Ravi, C. K., “A cohesive zone model for fatigue crack growth in quasibrittle materials”, International Journal of Solids and Structures” 38 3927-3944 (2001)

Yang, D., Wu, B. Y., Chan, Y. C. and Tu, K. N., “Microstructural evolution and atomic transport by thermomigration in eutectic tin-lead flip chip solder joints”, Journal of Applied Physics, v 102, n 4, p 043502, (2007)

Yang, Q. D., Shim, D. J. and Spearing, S. M., “A cohesive zone model for low cycle fatigue life prediction of solder joints” Microelectronic Engineering 75, 85–95 (2004)

Yang, W., Wang, W. and Suo, Z., “Cavity and dislocation instability due to electric current”, Journal of the Mechanics and Physics of Solids, v 42, n 6, June, p 897-911, (1994)

Yao, D. and Shang, J. K., “Effect of cooling rate on interfacial fatigue-crack growth in Sn-Pb solder joints”, IEEE Transactions on Components, Packaging, and Manufacturing Technology Part B: Advanced Packaging, v 19, n 1, Feb, p 154-165, (1996)

Yao, Y. and Keer, L. M., “A 3D Finite Element Analysis to Failure of Solder Joint Near the Interface of Intermetallic Compounds and Solder Bulk”, SRC Techcon Conference, Austin, Texas, September (2007)

Yao, Y., Fine, M. E. and Keer, L. M., “An Energy Approach to Predict Fatigue Crack Propagation in Metals and Alloys”, International J. of Fracture, v146, n3, 149-158, Aug., (2007)

Yao, Y., Vaynman, S., Keer, L. M. and Fine, M. E., “Energy Based Micromechanics Analysis on Fatigue Crack Propagation Behavior in Sn-Ag Eutectic Solder”, J. of Electronic Materials, v37, n3,339-346, March, (2008)

Yao, Y., Fiedler, B. A., Keer, L. M., and Fine, M. E., “Electromigration Effect to Void Propagation near the Interface of Solder and Intermetallic Compound” , Proceeding of SRC Techcon conference, Austin, (2008)

Yao, Y., Keer, L. M. and Fine, M. E., “Mechanical and Thermo-Electrical Analysis of Interfacial Failure of Solder Joint”, submitted to IEEE Trans. on Components and Packaging Technology, 2008 (under review)

Yao, Y., Fiedler, A. B., Keer, L. M. and Fine, M. E., “Phase Transform Theory Applied to Fatigue Crack Propagation in Interconnects”, submitted to IEEE Trans. on Components and Packaging Technology, 2008 (under review)

Yao Y., Keer L.M., and Fine M.E., “Electromigration Effect on Pancake Type Void Propagation near the Interface of Solder Bulk and Intermetallic Compound”, submitted to J. of Applied Physics, 2008 (under review)

Ye, H., Basaran, C., and Hopkins, D., “Thermomigration in Pb–Sn solder joints under joule heating during electric current stressing” Applied Physics Letters Volume 82, NUMBER 7 (2003)

Yeh, E. C. C. and Tu, K. N.," Numerical simulation of current crowding phenomena and their effects on electromigration in very large scale integration interconnects" Journal of Applied Physics, v 88, n 10, Nov 15, p 5680-5686, (2000)

Yi, K .S., Cox, B. N. and Dauskardt, R. H., "Fatigue crack-growth behavior of materials in viscous fluid environments. Journal of the Mechanics and Physics of Solids", v 47, n 9, Sep., p 1843-1871, (1999)

Yu, H., Mhaisalkar, S. G., Wong, E. H., Teh, L. K., and Wong, C. C., "Investigation of cure kinetics and its effect on adhesion strength of nonconductive adhesives used in flip chip assembly", IEEE Transactions on Components and Packaging Technologies, v 29, n 1, March, p 71-79, (2006)

Zhang, L., Ou, S., Huang, J. and Tu, K. N., "Effect of current crowding on crack propagation at the interface between intermetallic compound and solder in flip chip solder joints", Applied Physics Letter 88, 012106 (2006)

Zubelewicz, A., Guo, Q., Cutiongco, E. C., Fine, M. E. and Keer, L. M., "Micromechanical Method to Predict Fatigue Life of Solder", Journal of Electronic Packaging 112:179-182, (1990)

Appendix A: Example of ABAQUS code for 3D solder/IMC interconnect mechanical analysis

ABAQUS code for 3D solder/IMC interconnect mechanical analysis using cohesive zone-UCP model (here geometrical descriptions for nodes and elements are omitted)

```
*Heading
** Job name: UCP-cohesive interconnect model
** Model name: UCP-cohesive interconnect model
*Preprint, echo=NO, model=NO, history=NO, contact=NO
**
** PARTS
**
*Part, name=COHESIVE-1
*Node
     1,          0.,          98.,          0.
……
  1586,  -79.8450317,          97.,  -90.7089691
*Element, type=COH3D8
  1,  303,  306,   48,   47,  466,  469,   82,   81
…….
*Nset, nset=_PICKEDSET2, internal, generate
   1,  1586,     1
*Elset, elset=_PICKEDSET2, internal, generate
  1,  748,    1
*Elset, elset=_PickedSet5, internal, generate
  1,  748,    1
** Region: (Section-3-_PICKEDSET2:Picked)
*Elset, elset=_PickedSet5, internal, generate
  1,  748,    1
** Section: Section-3-_PICKEDSET2
*Cohesive Section, elset=_PickedSet5, material=COHESIVE, response=TRACTION SEPARATION,
*End Part
**
*Part, name=DIE-1
*Node
     1,         125.,         100.,          0.
……..
   693,   16.4849625,         110.,    105.32383
*Element, type=C3D8R
```

```
  1, 195, 196, 545, 539,  16,  17, 149, 148
……
416, 689, 489, 488, 664, 533, 143, 142, 503
*Nset, nset=_PICKEDSET2, internal, generate
  1,  693,    1
*Elset, elset=_PICKEDSET2, internal, generate
  1,  416,    1
** Region: (Section-4-_PICKEDSET2:Picked)
*Elset, elset=_I1, internal, generate
  1,  416,    1
** Section: Section-4-_PICKEDSET2
*Solid Section, elset=_I1, material=DIE
1.,
*End Part
**
*Part, name=IMC1-1
*Node
     1,          0.,         100.,          0.
……..
  2379,  -78.8546448,   99.0005951,  -90.1376038
*Element, type=C3D8R
  1,  464,  465, 1751, 1748,   13,   14,  289,  288
……..
1496, 2360, 1196, 1184, 2239, 1727,  223,  222, 1707
*Nset, nset=_PICKEDSET2, internal, generate
   1,  2379,     1
*Elset, elset=_PICKEDSET2, internal, generate
   1,  1496,     1
*Nset, nset=_PICKEDSET3, internal, generate
   1,  2379,     1
*Elset, elset=_PICKEDSET3, internal, generate
   1,  1496,     1
** Region: (Section-1-_PICKEDSET3:Picked)
*Elset, elset=_I1, internal, generate
   1,  1496,     1
** Section: Section-1-_PICKEDSET3
*Solid Section, elset=_I1, material=IMC1
1.,
*End Part
**
*Part, name=IMC2-1
*Node
     1,          0.,         -98.,          0.
……
  2379,  -78.8554688,  -99.0005875,  -90.1368561
```

```
*Element, type=C3D8R
  1,  464,  465, 1751, 1748,   13,   14,  289,  288
……
1496, 2360, 1196, 1184, 2239, 1727,  223,  222, 1707
*Nset, nset=_PICKEDSET2, internal, generate
   1,  2379,     1
*Elset, elset=_PICKEDSET2, internal, generate
   1,  1496,     1
** Region: (Section-2-_PICKEDSET2:Picked)
*Elset, elset=_I1, internal, generate
   1,  1496,     1
** Section: Section-2-_PICKEDSET2
*Solid Section, elset=_I1, material=IMC2
1.,
*End Part
**
*Part, name=SBUSTRATE-1
*Node
     1,        125.,       -120.,          0.
……...
   693,   16.4849625,       -110.,    105.32383
*Element, type=C3D8R
 1, 195, 196, 545, 539,  16,  17, 149, 148
…….
*Nset, nset=_PICKEDSET2, internal, generate
  1,  693,    1
*Elset, elset=_PICKEDSET2, internal, generate
  1,  416,    1
** Region: (Section-5-_PICKEDSET2:Picked)
*Elset, elset=_I1, internal, generate
  1,  416,    1
** Section: Section-5-_PICKEDSET2
*Solid Section, elset=_I1, material=SUBSTRATE
1.,
*End Part
**
*Part, name=SOLDER-1
*Node
     1,          0.,         97.,          0.
…….
 14301,  -10.0929403,  -10.5563126,  -124.465775
*Element, type=C3D8R
   1,   720,   721,  4330,  3934,    13,    14,   355,   354
…….
12800, 11998,  2569,  2540, 11709, 14301,  2669,  2651, 12195
```

```
*Nset, nset=_PICKEDSET2, internal, generate
    1,  14301,      1
*Elset, elset=_PICKEDSET2, internal, generate
    1,  12800,      1
** Region: (Section-6-_PICKEDSET2:Picked)
*Elset, elset=_I1, internal, generate
    1,  12800,      1
** Section: Section-6-_PICKEDSET2
*Solid Section, elset=_I1, material=SOLDER
1.,
*End Part
**
** ASSEMBLY
**
*Assembly, name=Assembly
**
*Instance, name=IMC1-1, part=IMC1-1
*End Instance
**
*Instance, name=IMC2-1, part=IMC2-1
*End Instance
**
*Instance, name=COHESIVE-1, part=COHESIVE-1
*End Instance
**
*Instance, name=DIE-1, part=DIE-1
*End Instance
**
*Instance, name=SBUSTRATE-1, part=SBUSTRATE-1
*End Instance
**
*Instance, name=SOLDER-1, part=SOLDER-1
*End Instance
**
*Nset, nset=uppernodes, instance=DIE-1
  4,   5,   6,   8,  10,  37,  38,  39,  40,  41,  42,  43,  44,  45,  46,  47
……
527, 528, 529, 530, 531, 532, 533
*Nset, nset=lowernodes, instance=SBUSTRATE-1
  1,   2,   3,   7,   9,  11,  12,  13,  14,  15,  16,  17,  18,  19,  20,  21
……..
477, 478, 479, 480, 481, 482, 483
*Elset, elset=_die-low_S2, internal, instance=DIE-1
  1,   2,   3,   4,   5,   6,   7,   8,   9,  10,  11,  12,  13,  14,  15,  16
……
```

349, 350, 351, 352, 353, 354, 355, 356, 357, 358, 359, 360, 361, 362, 363, 364
*Surface, type=ELEMENT, name=die-low
_die-low_S2, S2
*Elset, elset=_IMC1-up_S2, internal, instance=IMC1-1
1, 2, 3, 4, 5, 6, 7, 8, 9, 10, 11, 12, 13, 14, 15, 16
……..
1298, 1299, 1300, 1301, 1302, 1303, 1304, 1305, 1306, 1307, 1308, 1309
*Surface, type=ELEMENT, name=IMC1-up
_IMC1-up_S2, S2
*Elset, elset=_IMC1-low_S2, internal, instance=IMC1-1
342, 343, 344, 345, 346, 347, 348, 349, 350, 351, 352, 353, 354, 355, 356, 357
……
1495, 1496
*Elset, elset=_IMC1-low_S3, internal, instance=IMC1-1
188, 189, 190, 191, 192, 193, 194, 195, 196, 197, 198, 199, 200, 201, 202, 203
……..
1459, 1460, 1461, 1462, 1463
*Elset, elset=_IMC1-low_S4, internal, instance=IMC1-1
221, 222, 223, 224, 225, 226, 227, 228, 229, 230, 231, 232, 233, 234, 235, 236
…….
1338, 1339, 1340, 1341, 1342
*Surface, type=ELEMENT, name=IMC1-low
_IMC1-low_S2, S2
_IMC1-low_S3, S3
_IMC1-low_S4, S4
*Elset, elset=_cohesive-up_S1, internal, instance=COHESIVE-1, generate
1, 748, 1
*Surface, type=ELEMENT, name=cohesive-up
_cohesive-up_S1, S1
*Elset, elset=_cohesive-low_S2, internal, instance=COHESIVE-1, generate
1, 748, 1
*Surface, type=ELEMENT, name=cohesive-low
_cohesive-low_S2, S2
*Elset, elset=_solder-up_S2, internal, instance=SOLDER-1
1, 2, 3, 4, 5, 6, 7, 8, 9, 10, 11, 12, 13, 14, 15, 16
……..
10915, 10916, 10917, 10918, 10919, 10920, 10921, 10922, 10923, 10924, 10925, 10926, 10927, 10928, 10929, 10930
*Surface, type=ELEMENT, name=solder-up
_solder-up_S2, S2
*Elset, elset=_solder-low_S2, internal, instance=SOLDER-1
2901, 2902, 2903, 2904, 2905, 2906, 2907, 2908, 2909, 2910, 2911, 2912, 2913, 2914, 2915,
…….
12519, 12520, 12521, 12522, 12523, 12524, 12525, 12526, 12527, 12528, 12529, 12530

*Elset, elset=_solder-low_S3, internal, instance=SOLDER-1
1601, 1602, 1603, 1631, 1632, 1633, 1661, 1662, 1663, 1691, 1692, 1693, 1721, 1722, 1723,
……
12409, 12410
*Elset, elset=_solder-low_S4, internal, instance=SOLDER-1
1910, 1920, 1930, 1940, 1950, 1960, 1970, 1980, 1990, 2000, 2010, 2020, 2030, 2040,
…….
11490, 11500
*Surface, type=ELEMENT, name=solder-low
_solder-low_S2, S2
_solder-low_S3, S3
_solder-low_S4, S4
*Elset, elset=_IMC2-up_S2, internal, instance=IMC2-1
1, 2, 3, 4, 5, 6, 7, 8, 9, 10, 11, 12, 13, 14, 15, 16
……
1298, 1299, 1300, 1301, 1302, 1303, 1304, 1305, 1306, 1307, 1308, 1309
*Surface, type=ELEMENT, name=IMC2-up
_IMC2-up_S2, S2
*Elset, elset=_IMC2-low_S2, internal, instance=IMC2-1
342, 343, 344, 345, 346, 347, 348, 349, 350, 351, 352, 353, 354, 355, 356, 357
……..
1495, 1496
*Elset, elset=_IMC2-low_S3, internal, instance=IMC2-1
188, 189, 190, 191, 192, 193, 194, 195, 196, 197, 198, 199, 200, 201, 202, 203
…….
1459, 1460, 1461, 1462, 1463
*Elset, elset=_IMC2-low_S4, internal, instance=IMC2-1
221, 222, 223, 224, 225, 226, 227, 228, 229, 230, 231, 232, 233, 234, 235, 236
……..
1338, 1339, 1340, 1341, 1342
*Surface, type=ELEMENT, name=IMC2-low
_IMC2-low_S2, S2
_IMC2-low_S3, S3
_IMC2-low_S4, S4
*Elset, elset=_substrate-up_S2, internal, instance=SBUSTRATE-1
93, 94, 95, 96, 97, 98, 99, 100, 101, 102, 103, 104, 405, 406, 407, 408
409, 410, 411, 412, 413, 414, 415, 416
*Elset, elset=_substrate-up_S3, internal, instance=SBUSTRATE-1
63, 64, 65, 66, 67, 68, 69, 70, 71, 72, 73, 74, 75, 76, 77, 78
…….
311, 312, 365, 366, 367, 368, 369, 370, 371, 372, 373, 374
*Elset, elset=_substrate-up_S4, internal, instance=SBUSTRATE-1
53, 54, 55, 56, 57, 58, 59, 60, 61, 62, 157, 158, 159, 160, 161, 162
…….

```
 393, 394, 395, 396, 397, 398, 399, 400, 401, 402, 403, 404
*Surface, type=ELEMENT, name=substrate-up
_substrate-up_S2, S2
_substrate-up_S3, S3
_substrate-up_S4, S4
** Constraint: IMC1-cohesive
*Tie, name=IMC1-cohesive, adjust=yes
cohesive-up, IMC1-low
** Constraint: IMC2-sbustrate
*Tie, name=IMC2-sbustrate, adjust=yes
IMC2-low, substrate-up
** Constraint: cohesive-solder
*Tie, name=cohesive-solder, adjust=yes
cohesive-low, solder-up
** Constraint: die-IMC1
*Tie, name=die-IMC1, adjust=yes
IMC1-up, die-low
** Constraint: solder-IMC2
*Tie, name=solder-IMC2, adjust=yes
IMC2-up, solder-low
*End Assembly
*Amplitude, name=Amp-1, definition=PERIODIC
1, 3.14, 0., 0.
0., 1.
**
** MATERIALS
**
*Material, name=DIE
*Elastic
131000., 0.3
*Material, name=cohesive
*Elastic, type=traction separation
7e4, 4e4, 4e4
*Damage initiation, criterion=MAXS
8e1, 5e1, 5e1
*Damage evolution, type=energy, mixed mode behavior=bk, power=1.45
0.8, 1.0, 1.0
**
*Material, name=IMC1
*Elastic
96900., 0.309
*Material, name=IMC2
*Elastic
96900., 0.309
*Material, name=SOLDER
```

```
*Elastic
48000., 0.4
*CREEP, LAW=USER
*DEPVAR
4
*Expansion
2.9E-5
*Material, name=SUBSTRATE
*Elastic
131000
**
** BOUNDARY CONDITIONS
**
** Name: bc-lower Type: Displacement/Rotation
*Boundary
lowernodes, 1, 1
lowernodes, 2, 2
lowernodes, 3, 3
lowernodes, 4, 4
lowernodes, 5, 5
lowernodes, 6, 6
** Name: bc-upper Type: Displacement/Rotation
*Boundary
uppernodes, 2, 2
** ----------------------------------------------------------------
**
** STEP: Step-1
**
*Step, name=Step-1, nlgeom=YES, inc=10000
*Static, stabilize=0.0002
0.01, 100., 1.0E-6, 1.
**
** BOUNDARY CONDITIONS
**
** Name: cyclic load Type: Displacement/Rotation
*Boundary, amplitude=Amp-1
uppernodes, 1, 1, 1.
**
** OUTPUT REQUESTS
**
*Restart, write, frequency=0
**
** FIELD OUTPUT: F-Output-1
**
*Output, field
```

```
*Node Output
CF, RF, U
*Element Output, directions=YES
CFAILURE, E, ENER, JK, LE, PE, PEEQ, PEMAG, S, SDEG, STATUS
*Contact Output
CDISP, CSTRESS
**
** HISTORY OUTPUT: H-Output-1
**
*Output, history, variable=PRESELECT
*End Step
SUBROUTINE CREEP(DECRA,DESWA,STATEV,SERD,EC0,ESW0,P,QTILD,
     1  TEMP,DTEMP,PREDEF,DPRED,TIME,DTIME,CMNAME,LEXIMP,LEND,
     2  COORDS,NSTATV,NOEL,NPT,LAYER,KSPT,KSTEP,KINC)
C
      INCLUDE 'ABA_PARAM.INC'
C
      CHARACTER*80 CMNAME
C
      DIMENSION DECRA(5),DESWA(5),STATEV(*),PREDEF(*),DPRED(*),
     1  TIME(2),COORDS(*)
C
C     DEFINE CONSTANTS
C
      AA=0.009
      DD=70.0
      AIWA=0.0
      BB=0.001
      QQ=10000.0
      RT=8.314
      XX_sat=8.0
      miu=7.0
      omig=0.015
      NN=1.2
      YY=0.1
C
c   set initial RR, XX
c
      IF(KSTEP.EQ.1.AND.KINC.EQ.1) THEN
      STATEV(4)=2.0
      STATEV(3)=0.0
      ENDIF
      IF(KSTEP.GE.2.AND.KINC.EQ.1) THEN
      STATEV(4)=STATEV(4)+YY/STATEV(3)
      ENDIF
```

```
      IF(KINC.EQ.1) THEN
      STATEV(1)=STATEV(4)
      STATEV(2)=0.0
      ENDIF
c
c     set FLAG_SIGN (elastic or inelastic)
c
      IF(KINC.EQ.1) THEN
      FLAG_SIGN=0
      ENDIF
c
      RR=STATEV(1)
      XX=STATEV(2)
c
      KK=1.5**0.5*(QTILD-AIWA)-RR
      IF(KK.LT.0) THEN
      DECRA(1)=0
      DECRA(5)=0
      FLAG_SIGN=1
      GOTO 100
      ELSE
      SV=KK
      DFSV=1.5**0.5
      END IF
c
      IF(FLAG_SIGN.EQ.0) THEN
      GOTO 100
      ENDIF


c
c       calculate inelastic strain rate
c
      DECRA(1)=1.5**0.5*AA*(SV/DD)**NN*EXP(BB*(SV/DD)**(NN+1))
     1     *EXP(-QQ/(RT*TEMP))*DTIME
      IF(LEXIMP.EQ.1) THEN
       DECRA(5)=1.5**0.5*AA*NN*(SV/DD)**(NN-1)*(1/DD)*DFSV
     2      *EXP(BB*(SV/DD)**(NN+1))*EXP(-QQ/RT*TEMP)*DTIME
     3      +1.5**0.5*AA*(SV/DD)**NN*EXP(BB*(SV/DD)**(NN+1))
     4      *BB*(NN+1)*(SV/DD)**NN
      5        *(1/DD)*DFSV*EXP(-QQ/(RT*TEMP))*DTIME
      END IF
c
c       calculate XX
c
      CR_rate=DECRA(1)/DTIME
```

```
      XX_rate=miu*CR_rate*(XX_sat-XX)
      XX=XX+XX_rate*DTIME
      STATEV(2)=XX
      STATEV(3)=STATEV(3)+XX_rate*DTIME
      STATEV(1)=STATEV(4)+XX_rate*(1-omig)
c
100   RETURN
      END
```

Appendix B: Apply the Phase Transformation Theory to Ellipsoidal Crack

The assumption of a penny-shaped crack is adopted in this dissertation for simplicity. Phase transformation theory can also be applied to other crack types. Here, the theory is applied to an ellipsoidal crack (Mura 1991), where

$$\Delta W_2 = \frac{4}{3}\pi\sigma^2 a_1 a_2^2 \frac{1-\nu^2}{E \cdot E(k)} \tag{B.1}$$

where a_1 = length of major axis of a ellipsoidal crack;

a_2 = length of minor axis of a ellipsoidal crack;

$E(k)$ is the 2nd kind complete elliptical integral.

$$E(k) = \int_0^{\pi/2} (1 - k^2 \sin^2\phi)^{1/2} d\phi \tag{B.2}$$

where $k^2 = (a_1^2 - a_2^2)/a_1^2$

Substituting Eq. (B.1) into Eq. (3.1), with $A=\pi a_1 a_2$ gives:

$$\Delta W = -\delta(N)\pi a_1 a_2 - \frac{4}{3}\pi\sigma^2 a_1 a_2^2 \frac{1-\nu^2}{E \cdot E(k)} + \gamma\pi a_1 a_2 \tag{B.3}$$

where $\delta(N) = ftN\Delta\sigma\Delta\varepsilon_p$, thus,

$$\Delta W = -ftN\Delta\sigma\Delta\varepsilon_p \pi a_1 a_2 - \frac{4}{3}\pi\sigma^2 a_1 a_2^2 \frac{1-\nu^2}{E \cdot E(k)} + \gamma\pi a_1 a_2 \tag{B.4}$$

By letting $\left(\frac{d}{da_i}\Delta W\right)_{N^*} = 0$, i=1, 2, N^* can be determined.

Calculating $\frac{\partial \Delta W_2}{\partial a_1}$ from Eq. (B.1) gives:

$$\frac{\partial \Delta W_2}{\partial a_1} = \frac{4\pi\sigma^2 a_2^2(1-\nu^2)}{3E}\left\{\frac{1}{E(k)} - \frac{2a_2^2[E(k)-F(k)]}{E^2(k)(a_1^2-a_2^2)}\right\} \tag{B.5}$$

F(k) is the complete elliptical integral of the 1st kind $F(k) = \int_0^{\pi/2}(1-k^2\sin^2\phi)^{-1/2}d\phi$

From Eq. (B.3), $\left(\frac{d}{da_1}\Delta W\right)_{N^*} = 0$ gives:

$$-\frac{4\pi\sigma^2 a_2^2(1-\nu^2)}{3E}\left\{\frac{1}{E(k)} - \frac{2a_2^2[E(k)-F(k)]}{E^2(k)(a_1^2-a_2^2)}\right\} - \pi a_2(ftN^*\Delta\sigma\Delta\varepsilon_p) + \pi a_2\gamma = 0 \tag{B.6}$$

Set $A_1 = \left\{\frac{1}{E(k)} - \frac{2a_2^2[E(k)-F(k)]}{E^2(k)(a_1^2-a_2^2)}\right\}$, N_1^* can be obtained:

$$N_1^* = \frac{E\gamma - 4\sigma^2 a_2(1-\nu^2)A_1}{3Eft\Delta\sigma\Delta\varepsilon_p} \tag{B.7}$$

Similarly, N_2^* can be obtained:

$$\frac{\partial \Delta W_2}{\partial a_2} = \frac{8\pi\sigma^2 a_1 a_2(1-\nu^2)}{3E}\left\{\frac{1}{E(k)} - \frac{a_2^2[F(k)-E(k)]}{E^2(k)(a_1^2-a_2^2)}\right\} \tag{B.8}$$

From Eq. (B.3), $\left(\frac{d}{da_2}\Delta W\right)_{N^*} = 0$ gives:

$$-\frac{8\pi\sigma^2 a_1 a_2(1-\nu^2)}{3E}\left\{\frac{1}{E(k)} - \frac{a_2^2[F(k)-E(k)]}{E^2(k)(a_1^2-a_2^2)}\right\} - \pi a_1(ftN^*\Delta\sigma\Delta\varepsilon_p) + \pi a_1\gamma = 0 \tag{B.9}$$

$$N_2^* = \frac{E\gamma - 4\sigma^2 a_2(1-\nu^2)(\frac{3}{E(k)} - A_1)}{3Eft\Delta\sigma\Delta\varepsilon_p} = N_1^* - \frac{4\sigma^2 a_2(1-\nu^2)(\frac{3}{E(k)} - 2A_1)}{3Eft\Delta\sigma\Delta\varepsilon_p} \tag{B.10}$$

For a conservative prediction, we use minimum value of (N_1^*, N_2^*) to obtain the critical cycle number. From Eq. (B.7) and (B.10),

$$\frac{3}{E(k)} - 2A_1 = \frac{1}{E(k)} + \frac{4a_2^2[E(k)-F(k)]}{E^2(k)(a_1^2-a_2^2)} = \frac{1}{E(k)} - \frac{4a_2^2[F(k)-E(k)]}{E^2(k)(a_1^2-a_2^2)} \qquad \text{(B.11)}$$

From the definition of ellipsoidal crack and elliptic integral, $a_1 > a_2$, $F(k) > E(k) > 0$, thus if $\frac{4a_2^2[F(k)-E(k)]}{E(k)(a_1^2-a_2^2)} < 1$, $N_1^* < N_2^*$, Eq. (B.7) is used to predict the critical failure cycle number; if $\frac{4a_2^2[F(k)-E(k)]}{E(k)(a_1^2-a_2^2)} > 1$, $N_1^* > N_2^*$, Eq. (B.10) is used to predict the critical failure cycle number. It should be noted that if $a_1 = a_2$, the case simplifies to the penny-shaped crack. Phase transformation theory can be applied to other types of cracks if the corresponding value of ΔW_2 is determined.

Appendix C: Considering Electrical Current Effect into Phase Transformation Model

To include electrical current effect in the proposed phase transformation model for crack propagation, the energy release rate G_e due to electrical current concentration at the crack tip needs to be determined. Motivated by the formulation of Thouless et al. (1996), when a crack propagating near the solder/IMC interface, the stress singularity is characterized by a stress intensity factor induced by electrical current as:

$$K_e = \frac{\sqrt{\pi} e \hat{E} (Z_\eta^* - Z_{Sn}^*)}{\Omega} a^{3/2} \ (MPa\sqrt{m}) \qquad \text{(C.1)}$$

where a is the crack length; Z_η^* and Z_{Sn}^* is the effective charge number for IMC and solder, respectively; e is the electron charge (Coulomb). It should be noted that Thouless's argument does not account for void growth, which should be added to the analysis in future research. Eq. (C.1) is similar to the definition of stress intensity factor for mode I crack, and the effect of current is included. Thus, the energy release rate due to electrical current is proposed as:

$$G_e = \frac{K_e^2}{\bar{E}} \ (\text{J/m}^2) \qquad \bar{E} = \frac{E}{1-\nu^2} \text{ for plane strain} \qquad \text{(C.2)}$$

By considering the energy from electrical current, Eq. (3.7) can be rewritten as:

$$\Delta W = -\Delta W_{1a} \Delta A - \Delta W_2 + \Delta W_{1b} \Delta A + \Delta W_3 \Delta A + \gamma_T \Delta A - G_e \Delta A$$

$$\Delta W_{1a}\, dA/dN + \Delta W_2 + G_e\, dA/dN = \Delta W_{1b}\, dA/dN + \Delta W_3\, dA/dN + \gamma_T dA/dN \qquad \text{(C.3)}$$

The proposed phase transformation model can be applied to predict solder/IMC failure including electrical current effect based on Eq. (C.4),

$$\frac{dA}{dN} = \frac{\Delta W_2}{\gamma_T + \Delta W_3 - G_e} \tag{C.4}$$

From the deviation of chapter 3, Eq. (C4) can be written as:

$$\frac{dA}{dN} = \frac{\Delta W_2}{J + U - G_e} \tag{C.5}$$

It should be noted that there are a number of constants in the phase transformation model which need be determined either from the literature, by computation, or by experiment, further research works are need to verify the model with available experimental data.

Appendix D: Numerical Analysis to Electric Packaging under Drop Impact

The drop impact performance of solder joints in electric packaging is a critical concern of semiconductor and electronic product manufacturers. This problem is more serious with the application of lead free soldering, because compared with the traditional SnPb solder alloy, lead free solder alloy have higher rigidity and lower ductibility. The traditional drop test is high cost and time consuming, and it is quite difficult to observe the full dynamic responses during the drop impact. Aim at this problem, the section is focus on numerical analysis of drop impact effect on BGA packaging with the intention of providing the fundamental understanding required to design a reliable electric packaging.

Recently, some finite element simulations were carried out on drop impact reliability study. The dynamic material properties of solder are different from static ones because the dynamic material properties are dependent on strain rate. The solder constitutive model used in finite element simulation will affect stress strain behavior of solder significantly. Assuming solder joints has linear elastic behavior will lead to error predictions. Another method is to consider rate-dependent bilinear plastic model for Sn/Pb solder in finite element simulation of drop impact load. However, rate-dependent stress-strain behaviors of SnAgCu lead-free solder are needed. In this study, finite element modeling and simulation of drop impact were conducted incorporating UCP constitutive models of lead-free solder comprising elastic and rate dependent plastic models. The presence of the IMC layer can affect the drop impact response of the solder joint interface. In this study, the Cu_6Sn_5 IMC layer was incorported in solder interconnects. A 3D finite element model has been developed to simulate the behavior of ball grid array (BGA) electronic packaging under drop impact. An impact analysis procedure coupled with

submodeling technique in ABAQUS/Explicit under version 6.6.3 was established. Numerical analyses were performed to understand the physics of failure in board-level drop impact.

Development of Simplified BGA Packaging Model

The finite element model for the electronic packaging has been developed as shown in Fig. D.1. The silicon die and substrate is connected with representative lead –free solder arrays (6×6 matrix). The solders are protected by the underfill (epoxy) materials, and the whole package is protected by mold compound. Table D.1 gives the material prosperities used in the finite element model (NIST database 2002). Unified creep and plasticity (UCP) model as introduced in Chapter 2 is adopted to predict the plastic and creep behavior of solder joints.

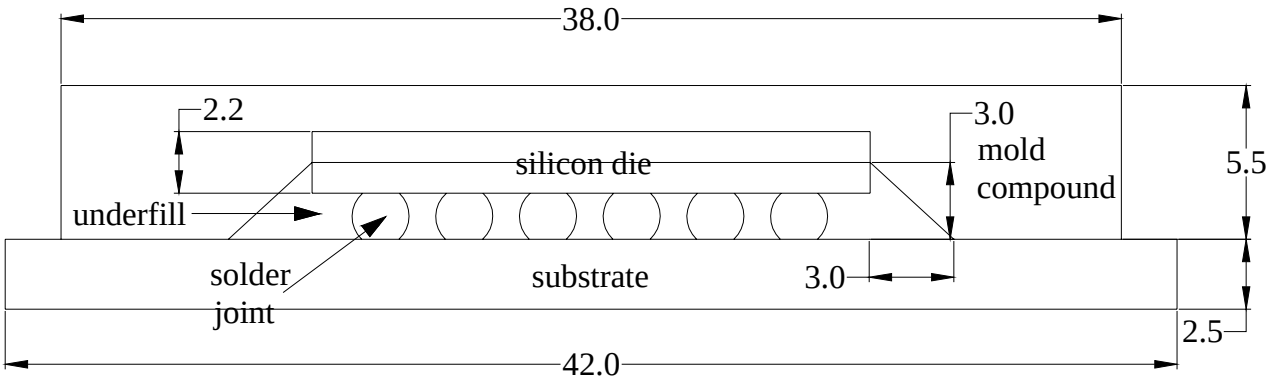
38.0
2.2
3.0
mold
compound
5.5
silicon die
underfill
solder
joint
substrate
3.0
2.5
42.0

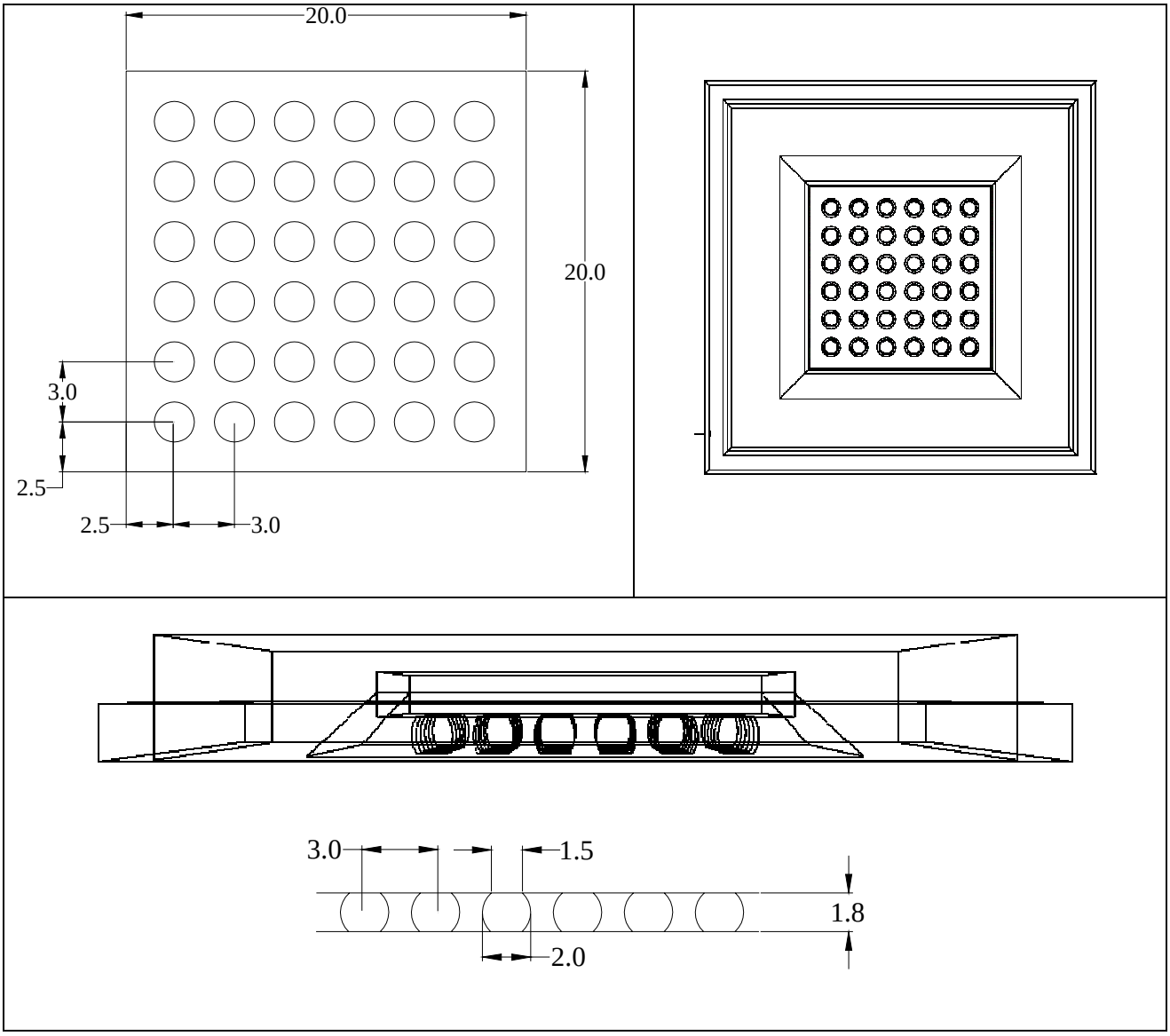
20.0
20.0
3.0
2.5
2.5
3.0
3.0
1.5
1.8
2.0

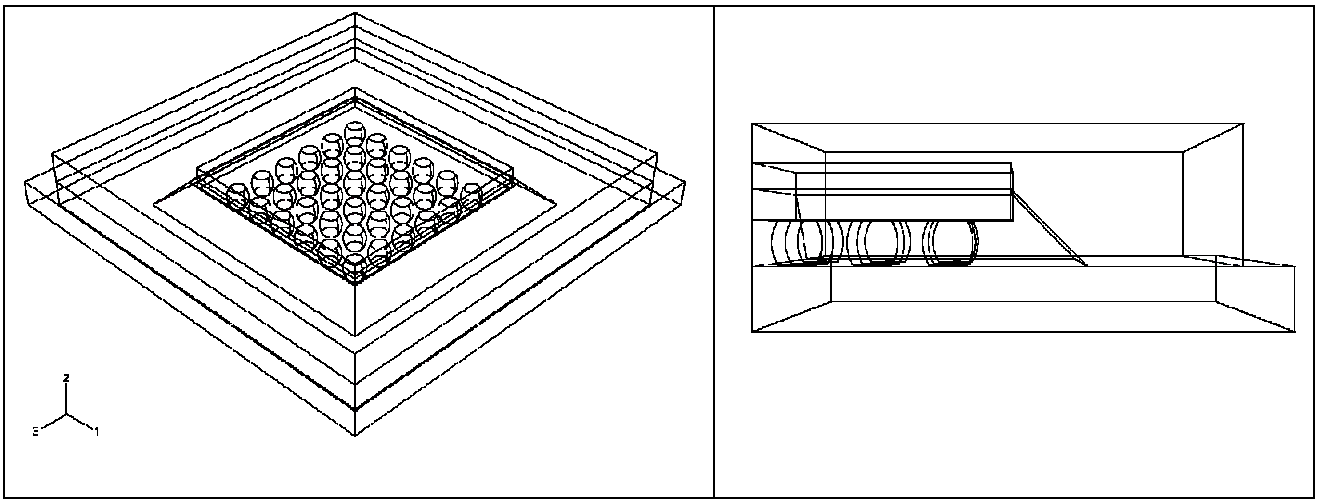

Figure D. 1 Schematic of the simplified packaging model (unit: mm)

Table D. 1 Material properties used in the finite element model (NIST database 2002)

	Density × 10^{-3} (g/mm^3)	Young Modulus (GPa)	Poisson's Ratio	Thermal Expansion Coefficient (/°C)	Temperature (°C)
Silicon die	2.33	162	0.23	2.8e-6	0
	2.33	150	0.23	2.8e-6	50
	2.33	140	0.23	2.8e-6	100
Solder	7.50	44.8	0.37	2.4e-5	0
	7.50	43.2	0.37	2.4e-5	20
	7.50	36.8	0.37	2.4e-5	100
	7.50	34.5	0.37	2.4e-5	130
Cu_6Sn_5	8.28	96.9	0.309	1.63e-5	25
Underfill	1.0	10	0.333	2.31e-5	25
	1.0	9.7	0.329	2.31e-5	50
	1.0	8.1	0.306	2.31e-5	125
	1.0	7.0	0.296	2.31e-5	150

A periodic temperature load has been applied to the package firstly; since the packaging is a symmetric structure, the von Mises stress distribution of one quarter of the package and the solders is shown in Fig. D. 2.

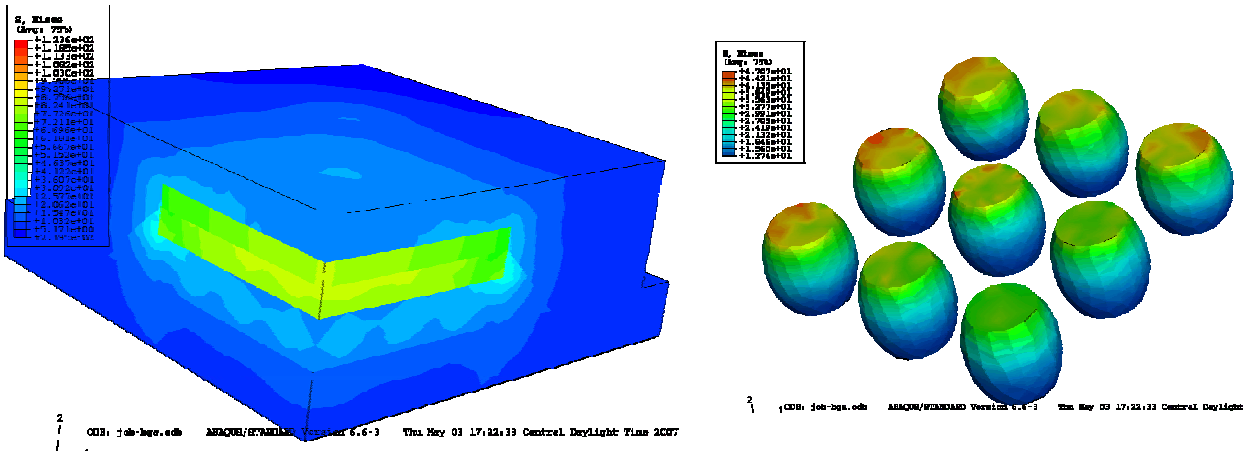

Figure D.2 von Mises stress distribution predicted from the proposed model

Dynamic Analysis to BGA Packaging

For nonlinear dynamic analysis problems, the "modal projection method" is used in ABAQUS (ABAQUS manual 2006). The basis of the method is to use eigenmodes of the linear system (extracted from an eigenfrequency analysis) as a set of global Ritz functions. The basic equation for the equilibrium statement, written as the virtual work principle is: (ABAQUS manual 2006)

$$\int_{V^0} \boldsymbol{\tau}^c : \delta\varepsilon dV^0 = \int_S \mathbf{t}^T \cdot \delta\mathbf{v} dS + \int_V \mathbf{f}^T \cdot \delta\mathbf{v} dV \qquad \text{(D.1)}$$

where τ^c and ε are any conjugate pairing of material stress and strain measures; the Cauchy stress matrix $\boldsymbol{\sigma}$ at a point of S is defined by $\mathbf{t} = \mathbf{n} \cdot \boldsymbol{\sigma}$; $\mathbf{f}$ is the body force per unit of current volume at any point within the volume of material under consideration; $\delta\mathbf{v}$ is the test function,

which is compatible with all kinematics constraints. **t**, **f**, and **σ** are an equilibrium set, i.e., $\mathbf{t} = \mathbf{n} \cdot \boldsymbol{\sigma}$, $(\frac{\partial}{\partial \mathbf{x}}) \cdot \boldsymbol{\sigma} + \mathbf{f} = 0$, $\boldsymbol{\sigma} = \boldsymbol{\sigma}^T$.

The finite element approximation to equilibrium equation is:

$$M^{NM}\ddot{u}^M + I^N - P^N = 0 \qquad \text{(D.2)}$$

where $M^{NM} = \int_{V_0} \rho_0 \mathbf{N}^N \cdot \mathbf{N}^M dV_0$, M^{NM} is the consistent mass matrix, $I^N = \int_{V_0} \boldsymbol{\beta}^N : \boldsymbol{\sigma} dV_0$,

I^N is the internal force vector, and $P^N = \int_S N^N \cdot \mathbf{t} dS + \int_V N^N \cdot \mathbf{F} dV$, P^N is the external force vector.

F is externally body force; N is shape function; ρ_0 is reference density; V_0 is reference volume; β_N is a matrix that depends, in general, on the current position, *x*, of the material point being considered. The matrix β_N that defines the strain variation from the variations of the kinematic variables is derivable immediately from the interpolation functions once the particular strain measure to be used is defined.

The time step depends on the smallest element size in the explicit time integration. In current research, the element size of model has a large variation for different materials. If the time step size is set to default, the total solution time will take a few days. It is necessary to use the mass-scaling technique increasing the minimum time step to shorten the solution time. But a longer time step will induce negative element volume and imprecise results. For example, some high frequency components in the dynamic responses can not be carried out by modeling. A scale factor of 2.0 and a time step size of 2×10^{-2} s are applied in current model for ensuring a stable solution and reducing solution time.

A predefined velocity field is applied to simulate different drop heights, for example, if the packaging drops from 1.5m height, the predefined velocity is 5.42m/s. The step time is set to be 5×10^{-5} second. Lead free solder is susceptible to brittle crack because of relatively higher elastic modulus, so stress criteria is suitable for investigating the drop impact reliability of lead free solder joint. The stress of solder balls is induced by mechanical shock during drop impact. Figure D.3 shows the von Mises stress distribution of the representative BGA packaging and ball grid array solder joints when drop to the ground from 1.5m height. It is found that the bottom solders especially the corner one has the highest von Mises stress. This indicates that the outermost solder joint of package corner has the highest peeling stress, and the stress concentration is along the solder/package pad interface. Thus, the outermost solder ball is more susceptible to brittle fracture than other solder balls. Therefore, the sacrificial balls could be located at the outermost of package corner instead of the functional balls, which may be useful to protect the functional balls in drop test.

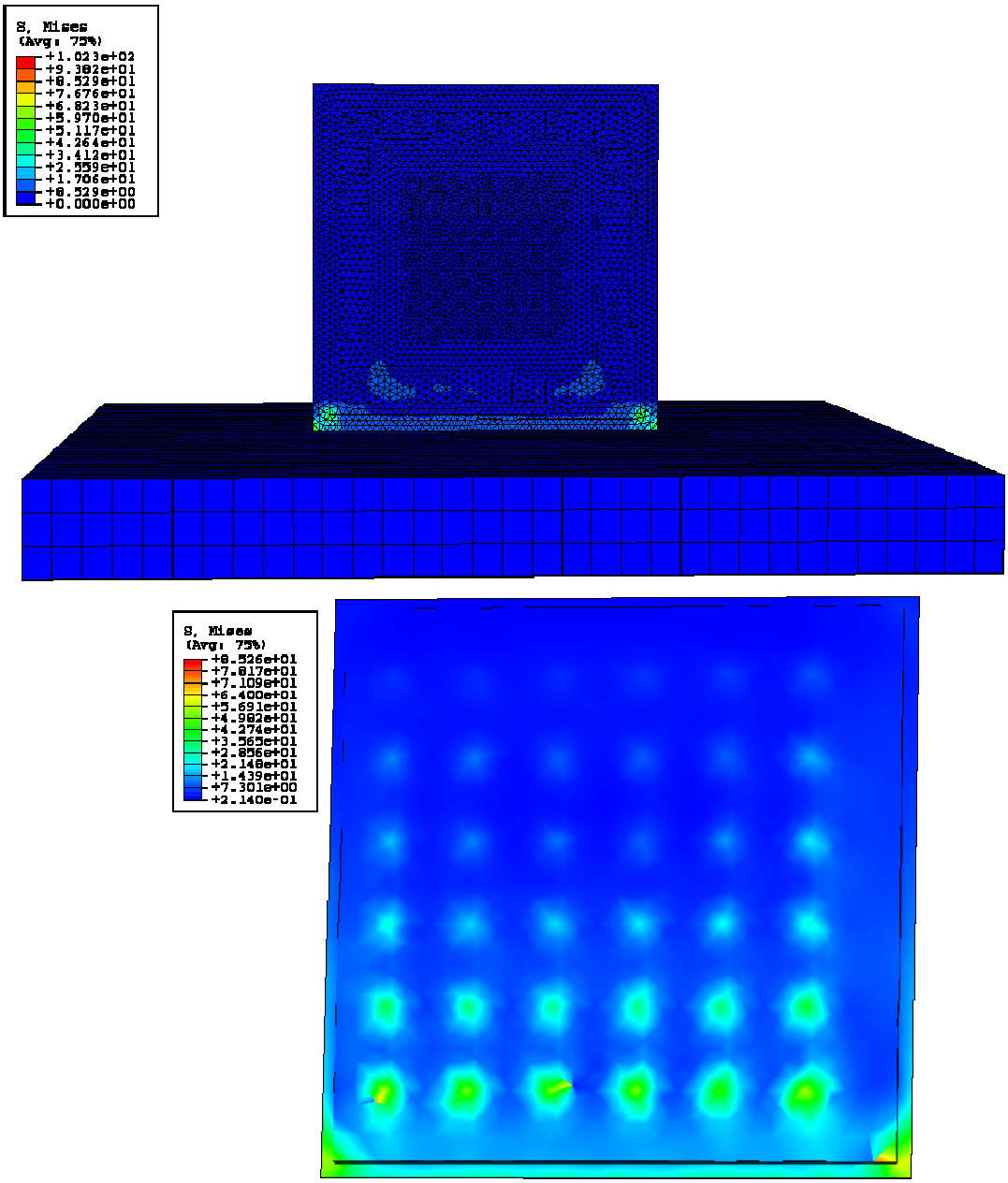
S, Mises
(Avg: 75%)
+1.023e+02
+9.382e+01
+8.529e+01
+7.676e+01
+6.823e+01
+5.970e+01
+5.117e+01
+4.264e+01
+3.412e+01
+2.559e+01
+1.706e+01
+8.529e+00
+0.000e+00
S, Mises
(Avg: 75%)
+8.526e+01
+7.817e+01
+7.109e+01
+6.400e+01
+5.691e+01
+4.982e+01
+4.274e+01
+3.565e+01
+2.856e+01
+2.148e+01
+1.439e+01
+7.301e+00
+2.140e-01

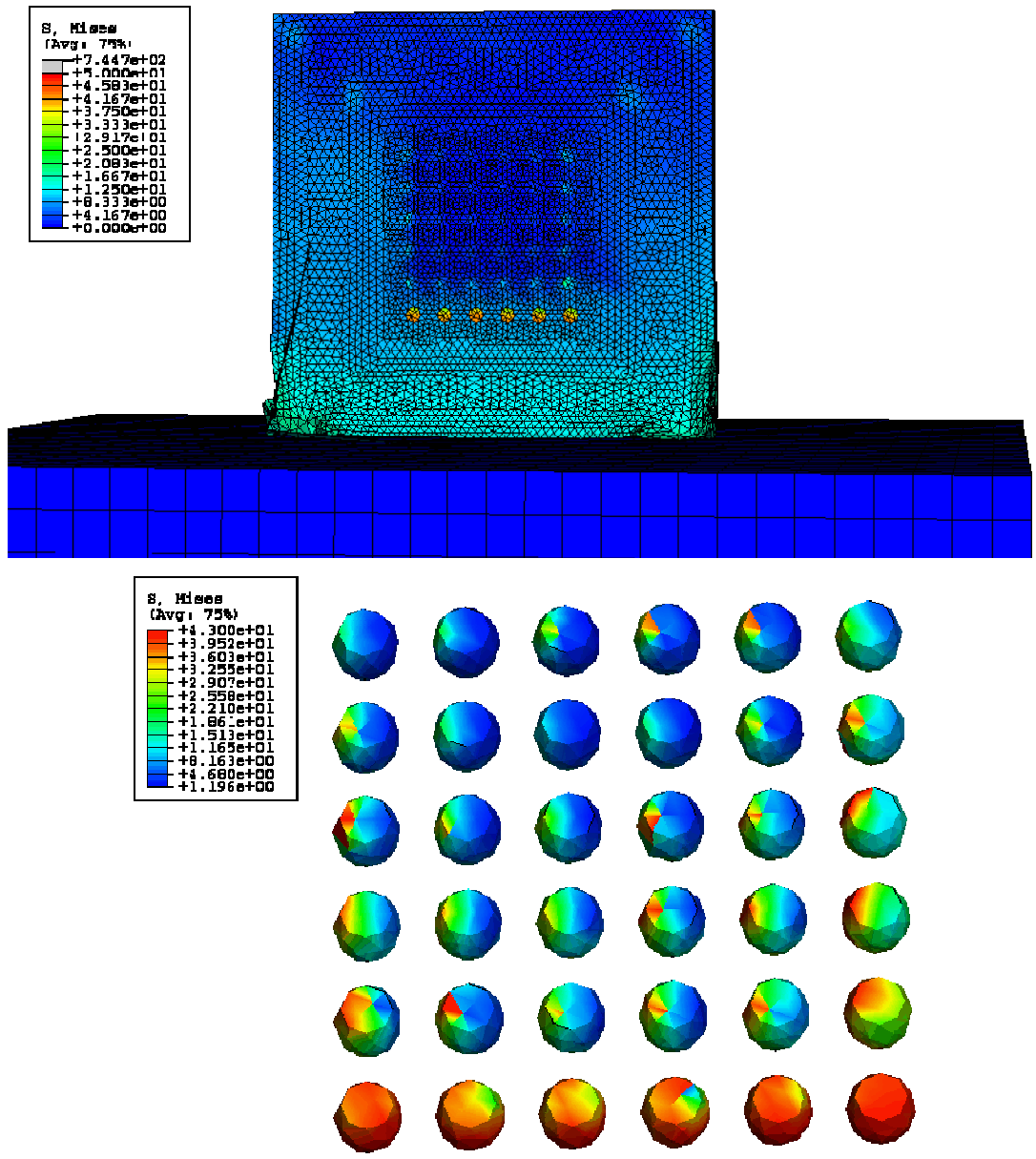

Figure D.3 von Mises stress distribution of the packaging when drop to the ground from 1.5m height

From the UCP-cohesive model developed in Chapter 2 for solder joints, the interconnect can be failure caused by solder/IMC interfacial crack nucleation and propagation under drop impact. In current research, a drop test model was established and the dynamic responses of lead

free solder joint were studied. The mechanical shock is the main failure mechanism of solder joint during drop impact. The maximum stress is observed at the outermost corner solder joint. The susceptible failure location is concluded at the interface between the solder and intermetallic compound based on the stress criteria. The current model can be used to compare the drop impact performance of different components and solder alloys, which can be used to guide the proper selection of component and optimize the layout of BGA electric packing. The results from the current model can be further applied directly to other sub-models for better analyzing the actual failure location of solder joints. A drop life evaluation equation of lead free solder joint based on the normal stress criterion can be further developed. Based on the developed model, the behavior of electric packaging and different types of solder interconnects under drop impact can be predicted with corresponding material parameters determined from experiment.

VITA

Yao Yao

Born on June 27, 1978, Zun Yi, Gui Zhou Province, China

DEGREES

Ph.D. in Structure, Theoretical and Applied Mechanics, Civil and Environmental Engineering, Northwestern University, Evanston, IL, USA, December 2008

M.S. in Civil Engineering, Nanyang Technological University, Singapore, April 2002

B.S. in Civil Engineering, Tongji University, Shanghai, China, July 1999

PUBLICATIONS

Yao Y., Vaynman S., Keer L.M., and Fine M.E., "Energy Based Micromechanics Analysis on Fatigue Crack Propagation Behavior in Sn-Ag Eutectic Solder", J. of Electronic Materials, v37, n3,339-346, March, 2008

Yao Y., Fine M.E., and Keer L.M., "An Energy Approach to Predict Fatigue Crack Propagation in Metals and Alloys", Inter. J. of Fracture, v146, n3, 149-158, Aug., 2007

Yao Y., Fiedler B.A., Keer L.M., and Fine M.E., "Fatigue Crack Propagation Behavior of Sn-Ag-Cu Solder Interconnects ", submitted to IEEE Trans. on Components and Packaging Technology, 2008 (under review)

Yao Y., Keer L.M., and Fine M.E., "Mechanical and Thermo-Electrical Analysis of Interfacial Failure of Solder Joint", submitted to ASME J. of Electronic Packaging, 2008 (under review)

Yao Y., Keer L.M., and Fine M.E., "Electromigration Effect on Pancake Type Void Propagation near the Interface of Solder Bulk and Intermetallic Compound", submitted to J. of Applied Physics, 2008 (under review)

Yao Y., Fiedler B.A., Keer L.M., and Fine M.E., "Electromigration Effect to Void Propagation near the Interface of Solder and Intermetallic Compound" , Proceeding of SRC Techcon conference, Austin, 2008

Fiedler B.A., Yao Y., Vaynman S., Ghosh G., Keer L.M., and Fine M.E., "Pb-Free Solder Joint Fatigue Crack Initiation and Propagation Related to Electrical, Thermal and Mechanical Loading", Proceeding of SRC Techcon conference, Austin, 2007

Yao Y. and Keer L.M., "Cohesive Zone Modeling and Finite Element Analysis to Intermetallic in Solder Connects", Proceeding of SRC Techcon conference, Austin, 2007